DEVELOPMENT OF DEMOUNTABLE STRUCTURAL ELEMENTS FOR A SUSTAINABLE CONSTRUCTION APPROACH BASED ON GREEN CONCRETE UTILIZING RECYCLED CONSTRUCTION DEMOLITION WASTE

SÜRDÜRÜLEBİLİR BİR İNŞAAT STRATEJİSİ İÇİN GERİ DÖNÜŞÜMLÜ İNŞAAT YIKIM ATIĞI KULLANILARAK ELDE EDİLEN YEŞİL BETONDAN ÜRETİLEN SÖKÜLEBİLİR YAPISAL ELEMANLARIN GELİŞTİRİLMESİ

ŞABAN AKDUMAN

ASSOC. PROF. DR. ALPER ALDEMİR
Supervisor

Submitted to
Graduate School of Science and Engineering of Hacettepe University
as a Partial Fulfillment to the Requirements
for be Award of the **Degree of Doctor of Philosophy**
in Civil Engineering

2025

ABSTRACT

DEVELOPMENT OF DEMOUNTABLE STRUCTURAL ELEMENTS FOR A SUSTAINABLE CONSTRUCTION APPROACH BASED ON GREEN CONCRETE UTILIZING RECYCLED CONSTRUCTION DEMOLITION WASTE

ŞABAN AKDUMAN

Doctor of Philosophy, Department of Civil Engineering
Supervisor: Assoc. Prof. Dr. Alper ALDEMİR
May 2025, 230 pages

The urgent demand for sustainable solutions in the construction industry, driven by environmental concerns and seismic safety requirements, has led to increasing interest in alternative materials and structural systems. This thesis presents a comprehensive experimental investigation into the structural performance, seismic behavior, and reusability potential of precast reinforced concrete elements incorporating geopolymer concrete made from construction and demolition waste (CDW).

The research comprises four integrated studies. The first study evaluates four different demountable column base connections design by investigating the seismic performance and damage characteristics of moment-resisting bolted joints under different axial compression ratios. Its primary aim is to identify the optimal connection design that balances strength, ductility, and energy dissipation for seismic applications. The second study experimentally assesses seismic performance of fully demountable column base connection systems for CDW-based geopolymer concrete columns. Six half-scale specimens, three demountable and three monolithic, were tested under reversed cyclic lateral displacements and three levels of constant axial load. The study compares failure modes, load–displacement behavior, ductility, energy dissipation, stiffness degradation, and curvature distributions between the two connection types. The third study evaluates the seismic behavior of an innovative demountable connection system for reinforced concrete columns featuring bolted dry joints, subjected to combined axial and cyclic lateral loading. Its performance is compared to that of conventional monolithic connections. Six half-scale specimens, half with bolted connections, half monolithic, were tested under axial compression ratios of 0.10, 0.20, and 0.30. The investigation focused mainly on evaluating failure mechanisms, damage characteristics, and seismic response. The results emphasize the influence of axial load intensity and reinforcement detailing on plastic hinge formation and damage progression. The fourth study explores the feasibility of constructing demountable precast buildings using CDW-based geopolymer concrete under real-life field conditions, highlighting both technical challenges and sustainability benefits.

Experimental results demonstrate that CDW-based geopolymer concrete provides structural performance comparable to that of conventional concrete. Furthermore, the dry-type demountable connections exhibited adequate ductility and strength under seismic loading while enabling disassembly and reuse. These findings confirm the potential of geopolymer concrete as a low-carbon, high-performance alternative to Portland cement and emphasize the role of connection design in supporting circular construction strategies.

This research contributes to the growing body of knowledge on sustainable prefabricated construction by integrating innovative materials with advanced structural detailing, offering new pathways for resilient, reusable, and environmentally responsible building systems.

Keywords: Geopolymer columns, Construction and demolition waste (CDW), Seismic performance, Damage assessment, Demountable connection, Sustainable Construction

ÖZET

SÜRDÜRÜLEBİLİR BİR İNŞAAT STRATEJİSİ İÇİN GERİ DÖNÜŞÜMLÜ İNŞAAT YIKIM ATIĞI KULLANILARAK ELDE EDİLEN YEŞİL BETONDAN ÜRETİLEN SÖKÜLEBİLİR YAPISAL ELEMANLARIN GELİŞTİRİLMESİ

ŞABAN AKDUMAN

Doktora, İnşaat Mühendisliği Bölümü
Tez Danışmanı: Doç. Dr. Alper ALDEMİR
Mayıs 2025, 230 sayfa

Çevresel kaygılar ve deprem güvenliği gereklilikleriyle şekillenen inşaat sektöründe sürdürülebilir çözümlere duyulan acil ihtiyaç, alternatif malzemelere ve yapısal sistemlere yönelik ilgiyi giderek artırmıştır. Bu tez, inşaat ve yıkım atıklarından (CDW) üretilen jeopolimer beton kullanılarak imal edilen prefabrik donatılı beton elemanların yapısal performansı, sismik davranışı ve yeniden kullanılabilirlik potansiyelini kapsamlı bir deneysel çalışma ile ortaya koymaktadır.

Araştırma dört bütünleşik çalışmadan oluşmaktadır. Birinci çalışmada, farklı eksenel basınç oranları altında moment aktaran cıvatalı birleşimlerin sismik performansı ve hasar karakteristikleri incelenerek dört farklı sökülebilir kolon-temel bağlantı tasarımı değerlendirilmiştir. Bu çalışmanın temel amacı, deprem etkilerine karşı dayanım, süneklik ve enerji sönümleme kapasitesini dengeleyen en uygun bağlantı detayını belirlemektir. İkinci çalışma, CDW bazlı jeopolimer beton kolonlar için geliştirilen tamamen sökülebilir kolon-temel bağlantı sistemlerinin sismik performansını deneysel olarak incelemektedir. Üçü sökülebilir, üçü monolitik olmak üzere altı adet yarı ölçekli numune tersinir çevrimsel yatay yüklemeye ve üç farklı sabit eksenel yüke tabi tutulmuştur. Çalışmada, bağlantı tipleri arasında göçme şekilleri, yük–deplasman davranışı, süneklik, enerji sönümleme, rijitlik bozulması ve eğrilik dağılımları karşılaştırılmıştır. Üçüncü çalışma, cıvatalı kuru birleşim elemanlarına sahip yenilikçi bir sökülebilir kolon bağlantı sisteminin, birleşik eksenel ve çevrimsel yatay yükler altındaki sismik davranışını değerlendirmektedir. Bu bağlantının performansı geleneksel monolitik bağlantılarla karşılaştırılmıştır. Üçü cıvatalı, üçü monolitik olmak üzere altı adet yarı ölçekli numune, 0.10, 0.20 ve 0.30 eksenel basınç oranları altında test edilmiştir. Çalışma, özellikle göçme mekanizmaları, hasar karakteristikleri ve sismik yanıtın değerlendirilmesine odaklanmıştır. Elde edilen sonuçlar, eksenel yük seviyesinin ve donatı detaylandırmasının plastik mafsal oluşumu ve hasar gelişimi üzerindeki etkisini vurgulamaktadır. Dördüncü çalışma ise, CDW bazlı jeopolimer beton kullanılarak gerçek saha koşullarında sökülebilir prefabrik bir yapının inşa edilebilirliğini incelemekte; teknik zorlukları ve sürdürülebilirlik faydalarını ortaya koymaktadır.

Deneysel sonuçlar, CDW bazlı jeopolimer betonun geleneksel betonla karşılaştırılabilir yapısal performans sağladığını göstermektedir. Ayrıca, kuru tip sökülebilir bağlantılar, sismik yüklemeler altında yeterli süneklik ve dayanım sergilemiş; aynı zamanda sökülüp yeniden kullanılabilme imkânı sunmuştur. Bu bulgular, jeopolimer betonun Portland çimentosuna düşük karbon salınımlı, yüksek performanslı bir alternatif olabileceğini doğrulamakta; bağlantı tasarımının döngüsel inşaat stratejilerindeki kilit rolünü vurgulamaktadır.

Bu çalışma, yenilikçi malzemeleri gelişmiş yapısal detaylarla bir araya getirerek sürdürülebilir prefabrik yapılaşma alanındaki bilgi birikimine katkı sağlamakta; dayanıklı, yeniden kullanılabilir ve çevresel açıdan sorumlu yapı sistemleri için yeni yaklaşımlar sunmaktadır.

Anahtar Kelimeler: Geopolimer kolonlar, İnşaat ve yıkım atıkları (İYA), Hasar değerlendirmesi, Sismik performans, Sökülebilir bağlantı, Sürdürülebilir inşaat

ACKNOWLEDGEMENT

Foremost, I would like to express my deepest gratitude to Assoc. Prof. Dr. Alper ALDEMİR, whom I have always felt by my side throughout every stage of this dissertation. I regard him as more than an academic advisor. His extensive experience and solution-oriented guidance have supported me immensely. With his humble attitude toward students, helpfulness, and fairness, he will always remain a role model in my academic and personal life.

Besides my advisor, I would also like to thank Prof. Dr. Erdem CANBAY, Prof. Dr. Barış BİNİCİ, Prof. Dr. Berna UNUTMAZ, and Assoc. Prof. Dr. Mustafa Abdullah SANDIKKAYA for their valuable time and insightful feedback.

I sincerely thank Erol TOSUN, a devoted technician in the laboratory, who treated our problems as his own. His responsibility, sincerity, and empathy made him more than a colleague, like an elder brother. May Allah bless him.

I also thank my friend Rafet AKTEPE, with whom I have shared the same office and laboratory for years, for his valuable support throughout this process. His contributions undoubtedly deserve more than just words of thanks.

I would like to express my gratitude to Prof. Dr. Mustafa ŞAHMARAN, the principal investigator of the project.

Additionally, I would like to acknowledge the financial support provided by the Scientific and Technological Research Council of Türkiye (TÜBİTAK - 218M102, Horizon 2020 - 869336 and 894100, and BİDEB - 2211).

Finally, I extend my heartfelt love and respect to my precious family. I have always felt their affection and compassion by my side through every challenge in life. In particular, I am deeply grateful to my mother, Fatma AKDUMAN, a true symbol of selfless devotion who dedicated her life to her children. Her presence has always been a source of strength for me. I also express my love to my dear wife and our two sons, Zübeyir and Abdurrahman. The hope of being with them both in this world and in the eternal paradise is my greatest consolation and prayer.

ŞABAN AKDUMAN

TABLE OF CONTENTS

LIST OF TABLES

LIST OF FIGURES

SYMBOLS AND ABBREVIATIONS

Symbols

Ca(OH)2	Calcium Hydroxide
Na2SiO3	Sodium Silicate
NaOH	Sodium Hydroxide

Abbreviations

BCC	Beam-column connection
BFS	Blast Furnace Slag
CBJ	Column Base Joint
CC	Conventional Concrete
CDW	Construction Demolition Wastes
CIP	Cast-in-Place Columns
CMC	Conventional Concrete Monolithically Connected Column
CPC	Conventional Portland Cement Concrete
CVC	Conventional Vibrated Concrete
CW	Concrete Waste
DC	Demountable Connected Column
DfD	Design for Disassembly
DRFDBJ	Dry-Connected Rotational Friction Dissipative Beam-To-Column Joint
EDC	Energy Dissipation Capacity
EDS	Energy Dissipation Segment
FA	Fly Ash
GBFS	Ground Granulated Blast Furnace Slag
GMC	Geopolymer Concrete Monolithically Connected Column
GPC	Geopolymer Concrete
GW	Glass Waste
HB	Hollow Brick

LCA	Life Cycle Assessment
MC	Monolithically Connected Column
MSI	Material Sustainability Index
NEDS	Non-Dissipative Segment
NPCF	Precast Concrete Frame System
OPC	Ordinary Portland Cement
PSJ	Prefabricated Steel Joints
RCA	Recycled Concrete Aggregate
RCB	Red Clay Brick
RCDW-GC	CDW-Based Geopolymer Concrete
ROPC-C	Reinforced OPC Concrete
RT	Roof Tile
SEM	Scanning Electron Microscopy
SHS	Square Hollow Sections
TEC2018	Turkish Earthquake Code (TEC2018)
TPCA	Turkish Precast Concrete Association
UHPFRC	Ultra-High-Performance Fiber-Reinforced Concrete
UHTCC	Ultra-High Toughness Cementitious Composite
XRD	X-ray Diffraction Analysis
XRF	X-Ray Fluorescence

INTRODUCTION

1.1. General

With significant technological advancements and a rapid increase in global population, building stocks have reached unprecedented levels. The rapid growth of the construction industry, while impressive, has led to heightened consumption rates and the rapid depletion of natural resources. Ignoring this issue will inevitably result in the exhaustion of these resources over time. Therefore, the manufacturing of concrete and the quality of materials utilized in construction have become crucial, considering the universal use of concrete in a variety of structures around the world.

With the increasing visibility of climate change effects, sustainability has emerged as a major concern not only in daily life but also within the construction industry. Concepts such as green buildings and sustainable construction have become increasingly prominent, emphasizing the need to evaluate building systems from a broader perspective. Sustainable construction involves assessing buildings across their full lifecycle, from design and construction to operation, maintenance, and eventual demolition, through environmental, economic, social, and health-based lenses. Challenges in sourcing raw materials are expected to increase the significance of sustainable construction practices moving forward.

Sustainable construction does not merely focus on the building phase; It also includes the extraction of raw materials, their transportation, the production of construction materials, the operation and maintenance of buildings, as well as their deconstruction at the end of life. This holistic approach is called the cradle-to-grave Life Cycle Assessment (LCA). However, in recent years, scholars have criticized cradle-to-grave models for overlooking post-demolition material reintegration into the economy. Consequently, the cradle-to-cradle LCA model has gained traction, advocating for the reuse of materials, recycling, and efficient deconstruction to achieve circular construction.

Building construction, use, and demolition stages result in high energy consumption, carbon emissions, and significant waste generation. CDW represents one of the most environmentally impactful by-products of the construction environment. Globally, CDW accounts for approximately 10–30% of total waste [1], with even higher figures reported in urbanized regions, 60% in Chicago, 50% in the UK, and 37% in Hong Kong [2]. In the United States alone, demolition waste comprises around 48% of total CDW (U.S. EPA, 1998). According to Transparency Market Research, the annual volume of CDW is projected to double by 2025, reaching 2.2 billion tons worldwide. Due to their bulk and weight, these wastes require substantial landfill space. Nonetheless, the majority of CDW holds significant potential for recycling and direct reuse, as reported by Peng et al. [3].

Construction debris can be reincorporated into building systems either after appropriate processing or directly reused without treatment. Although direct reuse without reprocessing offers significant energy savings, it requires careful design for disassembly (DfD) during the initial construction phase. This process, known as deconstruction, allows for the recovery of valuable materials, reduces landfill waste, and minimizes environmental impacts (U.S. EPA, 2008). Demountable buildings offer further advantages such as:

- Scalability, facilitating quick expansion or reduction;
- Relocatability, allowing components or systems to be transferred to new sites [4].

In contrast, conventional reinforced concrete (RC) or current precast concrete framing systems often necessitate complete demolition even when only a few structural elements suffer irreparable damage. Medium-level seismic damage may be technically repairable, but time-consuming and costly restoration efforts often render buildings functionally obsolete [5]. For these reasons, designing RC components to be demountable is of critical importance in sustainable construction.

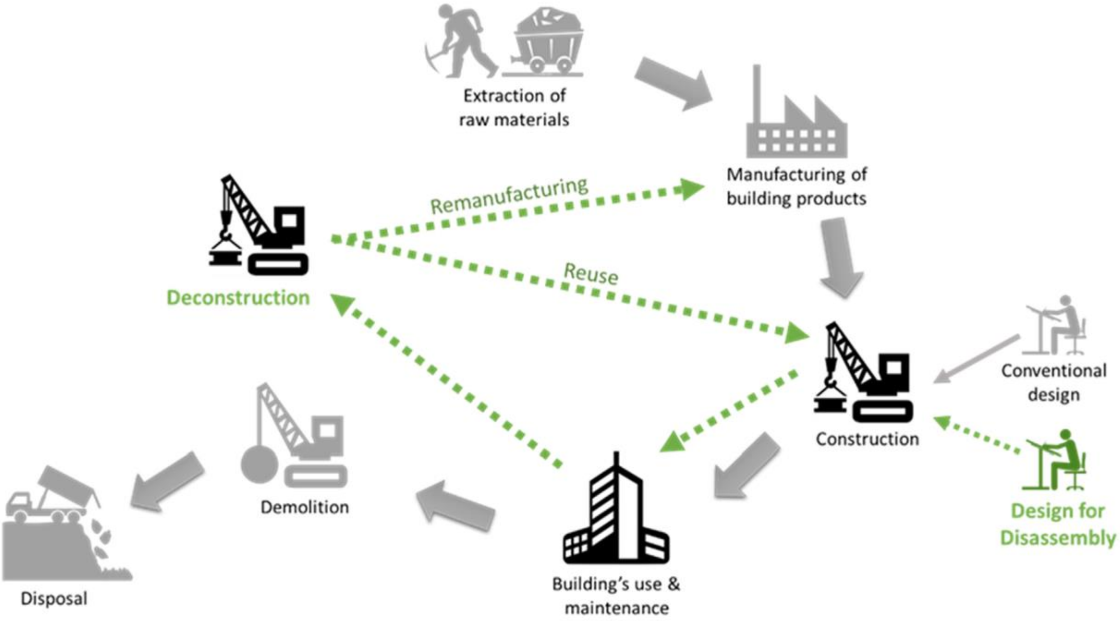

Figure 1.1 Design for disassembly in the building lifecycle [6]

As emphasized above, effective management of waste generated during demolition and repair is crucial for sustainable development. Therefore, designing concrete structures to be demountable holds significant potential for reducing environmental impact. To facilitate demountability, such structures should be prefabricated and connected using dry connections rather than permanent bonding materials.

Prefabricated structural components can be mechanically joined using bolted pins, welds, reinforcing bars, and joints filled with mortar or concrete. Various types of joints are used globally in precast structures, including monolithic, emulative, and dry mechanical connections. Among these, emulative joints, which rely on mortar, are not suitable for disassembly. In contrast, dry bolted connections, secured using bolts and nuts, are far more suitable for repeated assembly and disassembly.

1.2. Objective and Scope

This study aims to experimentally assess the structural performance, seismic performance, and sustainability potential of precast concrete elements made from geopolymer concrete derived from CDW. That is, this research evaluates the feasibility of utilizing CDW-based geopolymer concrete (GPC) as a sustainable and structurally dependable substitute for conventional Portland cement concrete (CPC). Special emphasis is placed on its application in demountable prefabricated structural systems designed for disassembly and reuse, enabling post-earthquake repair and minimizing material waste. The research additionally emphasizes creating and experimentally validating new dry connections for beam-to-column, column-to-foundation, and slab-to-beam configurations, aimed at ensuring ductile seismic performance, facilitating replacement, and improving structural resilience. By combining material innovation with connection design, the research contributes to advancing eco-efficient construction practices and circular economy strategies in seismic-prone regions.

In the scope of this study, a full-size demountable building prototype was designed and constructed using structural elements produced from geopolymer concrete incorporating recycled CDW. The study systematically evaluated constructability, connection detailing, structural reusability, and environmental benefits within the framework of sustainable and circular construction practices. As part of the experimental program, multiple demountable column specimens with varying connection configurations were fabricated and subjected to reversed cyclic loading. Comparative analyses were performed between geopolymer and conventional concrete, as well as between monolithic and demountable systems. Key performance metrics were examined to assess the structural viability and resilience of demountable precast systems in seismic applications, including load-carrying capacity, energy dissipation, stiffness degradation, and component reusability.

Finally, the results of these experimental studies were utilized to construct a full-scale, demountable precast building in real-world conditions in Türkiye. This practical implementation not only validated laboratory results but also offered valuable insights into constructability, logistical challenges, and sustainability outcomes when using CDW-based geopolymer concrete in actual construction settings. Additionally, the study included a contextual evaluation of Türkiye’s current CDW recycling strategies, identifying key areas for improvement and policy enhancement.

Through these interconnected research efforts, the study delivers a comprehensive understanding of how CDW-based geopolymer concrete can be effectively integrated into sustainable construction systems. It bridges the gap between material innovation and structural engineering practice, while also advancing circular economy principles in the construction sector by introducing reusable, demountable structural components.

1.3. Organization of Thesis

This thesis consists of several chapters, with each focusing on a particular element of the research concerning geopolymer concrete and demountable structures systems. The organization of the thesis reflects the chronological development of the work.

Chapter 1 – Introduction

This chapter outlines the reasons for the study, identifies the research problem, and highlights the importance of utilizing geopolymer concrete made from construction and demolition waste (CDW) in precast structures systems. It also outlines the research objectives, and scope.

Chapter 2 – Literature Review

An extensive review of existing studies on geopolymer concrete, CDW utilization, prefabricated systems, demountable connections, and seismic performance of reinforced concrete elements is provided. This chapter establishes the theoretical background and identifies the research gap addressed in the thesis.

Chapter 3 – Experimental Program

The materials, specimen details, instrumentation, and test setup used in the experimental studies are described. Monolithic and demountable test elements are introduced, produced with conventional and geopolymer concrete. Details of the column, beam, slab, and connection geometries are included, along with testing protocols.

Chapter 4 – Experimental Results and Discussions

This chapter is based on three peer-reviewed scientific articles and focuses on the core experimental outcomes and discussions of the study, particularly the seismic performance of the test specimens. Key parameters examined include failure modes and crack propagation, load-displacement behavior, displacement ductility, energy dissipation capacity, stiffness degradation, moment-curvature relationships, the influence of axial load, plastic hinge characteristics, and overall damage assessment.

First, the experimental results and seismic performance of the demountable column-to-foundation connections are presented by integrating the relevant findings from all three articles. Following this, brief summaries of the beam-to-column and slab-to-beam connection tests are provided, as these components were designed as pinned connections and evaluated accordingly.

Chapter 5 – Full-Scale Application and Field Performance of a Demountable System

The case study presents the designing, constructing, and evaluating a full-scale demountable precast building prototype using GPC produced from CDW. Building upon the findings of the previous experimental studies, this research validates the practical feasibility of using CDW-based GPC and demountable connection systems under real-world construction conditions. The study investigates constructability, connection performance, and on-site assembly challenges, while also conducting a comprehensive sustainability assessment.

Chapter 6 – Conclusions and Recommendations

The final chapter outlines the key findings of the thesis, assesses the research objectives, and offers suggestions for future research in geopolymer concrete, sustainable construction, and demountable structural design.

1.4. Overview of Thesis

Based on the aforementioned information, a more energy-efficient and environmentally friendly alternative for structural elements could be achieved by the utilization of demountable precast elements with construction and demolition (C&D) waste-based geopolymer concrete. This approach not only reduces waste, CO_2 emissions, and energy consumption associated with Portland cement production and demolition activities, but also promotes sustainability in the construction industry by enabling the reuse and relocation of structural elements. To address this opportunity, the study is structured into four interlinked research phases:

In the first phase, four novel demountable column-to-foundation connections made from CDW-based geopolymer concrete were developed and tested under constant axial load and reversed cyclic lateral displacements. Their seismic responses were compared against a monolithic benchmark to assess lateral stiffness, energy dissipation, ductility, failure modes, and moment-curvature behavior.

The second phase focused on the effects of axial compression ratio on the seismic performance of demountable column-base joints made with CDW-based geopolymer concrete. A set of six half-scale specimens, three monolithic and three demountable, were tested under cyclic lateral displacement with three different axial load levels (10%, 20%, and 30%). Observations included changes in load-displacement behavior, ductility, energy dissipation, stiffness degradation, and moment-curvature response, providing insight into how axial force variations affect damage development and overall performance.

In the third phase, similar tests of second study were replicated using conventional concrete to isolate the material-based effects and better understand the influence of geopolymer binder systems on joint behavior. Comparative evaluations between monolithic and bolted specimens were carried out with emphasis on stiffness retention, damage morphology, and energy dissipation capacity. Moreover, this phase explored damage assessment procedures critical to post-event rehabilitation, highlighting the practical importance of joint detailing in performance-based seismic design.

The final phase translated the laboratory findings into a real-world full-scale eco-friendly demountable building application. This novel structure, constructed entirely from sustainable CDW-based geopolymer precast elements, was designed and assembled according to cradle-to-cradle design principles. For the first time, the practicality and scalability of a reusable structural system composed of demountable prefabricated components was validated under realistic construction conditions. This phase also included a comprehensive sustainability analysis covering embodied energy, CO_2 emissions, and practical guidelines for implementing such systems in Turkey. Challenges and opportunities in the local construction context, from waste handling to industrial-scale adoption of prefabrication, were examined.

Together, these four phases present a holistic framework for sustainable structural design, merging green material development, seismic performance validation, and scalable construction strategies, positioning demountable geopolymer-based precast systems as a forward-looking solution to environmental and engineering challenges in modern construction.

LITERATURE REVIEW

2.1. Introduction

Concrete structures are typically designed to remain functional for decades. However, due to changing usage requirements, demographic shifts, or damage caused by severe loadings such as earthquakes and extreme winds, these structures often require adaptation or replacement before the end of their service life. Conventional cast-in-place and precast reinforced concrete systems are largely monolithic, leading to full or partial demolition when modifications are needed. This process results in significant economic loss and generates large volumes of construction and demolition waste (CDW) [7]. Therefore, the construction industry is shifting toward demountable and reusable systems to enhance sustainability and reduce environmental impact.

Precast concrete connections, particularly at critical joints, are often the weakest points in the structure during seismic events [7]. These connections are generally categorized as "wet" (requiring on-site concrete casting) or "dry" (not requiring concrete placement on-site). While wet connections are straightforward to implement, they are not demountable. Dry connections, often formed with bolted joints, offer advantages in terms of fast assembly, reusability, and ease of disassembly for repair or relocation purposes [7].

In addition to enhancing structural reusability, reducing the environmental burden of Portland cement production is critical. Cement manufacturing is responsible for approximately 7% of global CO_2 emissions, with about 0.59 tons of CO_2 released per ton of cement produced [8]. In 2021 alone, cement production reached 4.3 billion metric tons globally [8]. Geopolymer concrete, made from alkali-activated industrial by-products such as fly ash, blast furnace slag, and silica fume, offers a promising alternative to conventional cement by significantly lowering the carbon footprint [9-11]. However, rising demand for these mainstream by-products and their regional availability raise concerns regarding future feasibility [12-14].

As an alternative source material, CDW has recently garnered attention for its potential in geopolymer concrete production. It is estimated that approximately 10 billion tons of CDW are generated annually worldwide [15-17]. Although promising research findings exist regarding CDW-based geopolymer mortars and pastes [18-20], most studies have remained at the laboratory scale and focus on basic properties such as compressive strength and shrinkage. To enable real-world implementation, further research is needed on the structural behavior of full-scale elements produced from CDW-based geopolymer concrete.

The importance of such research has become even more pronounced in the aftermath of recent seismic disasters. On February 6, 2023, two successive major earthquakes with moment magnitudes of Mw = 7.7 and Mw = 7.6 struck Pazarcık and Elbistan (Kahramanmaraş), resulting in the collapse or severe damage of over 260,000 buildings and more than 50,000 casualties across 11 provinces in Türkiye [21]. Investigations revealed that many of these failures were caused by inadequate detailing and poor performance of reinforced concrete columns and column base joints (CBJs) [22]. Moreover, these disasters produced a vast quantity of CDW, posing risks to public health, the environment, and the economy if not properly managed [23].

Given these factors, developing seismically resilient, demountable column base joints using CDW-based geopolymer concrete has become an urgent priority. Several researchers have explored CBJ alternatives to improve structural safety under seismic loads [24-31]. Integrating such joint systems with sustainable materials like CDW-based geopolymers presents a unique opportunity to address both seismic resilience and environmental sustainability in modern construction.

Given the pressing need to reduce the environmental footprint of the construction industry and enhance structural resilience against seismic events, the development and adoption of alternative binders and innovative structural systems have gained significant momentum in recent years. In particular, the integration of CDW-based geopolymer concrete with demountable precast systems presents a promising pathway toward both sustainability and structural adaptability. To comprehensively address these interrelated challenges, the following literature review explores the state-of-the-art developments in low-carbon binder technologies, the use of recycled materials in concrete production, and the evolution of demountable connection systems. This extensive review aims to provide a solid foundation for understanding the current scientific and technical advancements that inform the experimental and analytical phases of this study.

2.2. Concrete Composition

This section presents a review on conventional concrete and geopolymer concrete made from construction and demolition waste, highlighting its promise as a more sustainable construction option given the environmental consequences of conventional cement-based materials.

2.2.1. Ordinary Portland cement and Conventional Concrete

Concrete plays a vital role in the construction industry worldwide. However, its production process has significant environmental implications, as it utilizes significant natural resources and emits greenhouse gases that contribute to global warming.

Portland cement stands as the most consumed material globally after water, owing to its widespread availability, low-cost production, and shapeability in its fresh state. These advantages have made Portland cement a fundamental component across a wide range of construction applications, comprising structures such as buildings, bridges, and tunnels, both infrastructure and superstructure systems.

However, expanding its use into diverse environmental and structural contexts has revealed several material-related durability issues. Among the most critical are its low resistance to acidic and sulfate environments, its vulnerability to alkali-silica reactions (ASR), and the occurrence of shrinkage and thermal cracking. To mitigate these challenges and ensure reliable performance under various conditions, several international standards have been established. Standards such as ISO 679, ASTM C595, and ASTM C150/C150M define the compositional limits, strength classes, durability criteria, and testing protocols for Portland cement, thereby ensuring quality assurance on a global scale [32, 33].

Portland cement typically consists of three major components, among which the ratio of water to cement is an important factor in determining the mechanical characteristics of the resulting concrete. Although a certain amount of water is required for hydration and workability, excess water adversely affects concrete’s properties, particularly compressive strength and durability.

In recent years, two major innovations have significantly improved the performance of high-strength concretes. The first involves the incorporation of extremely fine, reactive materials such as nanosilica, which fill microvoids in the cement matrix, thereby increasing the density and reducing porosity. The second development addresses workability issues by introducing admixtures, commonly referred to as plasticizers and superplasticizers, that enhance workability without increasing water content. These advancements enable the creation of high-performance concretes that exhibit enhanced robustness and resilience by optimizing combinations of chemical and mineral additives.

From an environmental perspective, the impacts of Portland cement are substantial. To produce one ton of Portland cement, around 1.5 tons of raw materials are needed, emitting almost one ton of CO_2, accounting for an estimated 5–8% of global human-made CO_2 emissions [32, 34]. Among the most critical environmental consequences of cement production are CO_2 emissions and water resource consumption, both of which contribute significantly to air pollution and ecological degradation. The current atmospheric CO2 concentration of 400 ppm could be reached by the end of the century, according to recent studies [35], even without taking into account industrial or technological growth.

Moreover, cement production emits not only CO_2 but also other harmful pollutants including carbon monoxide (CO),sulfur dioxide (SO_2), nitrogen oxides (NO_x), and trace heavy metals. These emissions primarily originate from the high-temperature kiln operations inherent in clinker production.

Furthermore, Cement costs make up more than 45% of total expenses in traditional concrete production, as noted by [36]. Additionally, the production of concrete necessitates energy-intensive aggregate extraction processes that generate substantial waste. Moreover, the production of concrete requires substantial amounts of water, presenting a specific challenge in regions with limited access to fresh water resources [37]. Recognizing the importance of sustainability and increasing awareness of global warming, the construction industry has been actively seeking alternative materials [38].

While the widespread use of Portland cement has facilitated enormous progress in modern construction, its environmental drawbacks necessitate urgent action. Recognizing this, the development of alternative, low-impact binder systems is no longer optional but essential for sustainable construction practices. As such, the search for and adoption of eco-friendly cement alternatives has become a scientific and environmental imperative.

2.2.2. Geopolymers as Alternative Binders

In the 1970s, J. Davidovits coined the term geopolymer to explain binder systems that were created by reacting aluminosilicate-based powders with alkaline solutions [39, 40]. The development of these materials began as heat-resistant alternatives created in response to major fires that occurred in European countries. In the beginning, they were utilized to safeguard carbon fiber composites against high temperatures and to provide fire-resistant coatings for wooden structures. As time passed, the superior strength and reliability performance of geopolymers, particularly those produced from fly ash (FA) activation, contributed to a growing interest in these materials within the construction industry[40, 41].

Geopolymers are materials composed predominantly of amorphous or semi-crystalline aluminosilicate chains, formed through the reaction of aluminosilicate-rich raw materials with alkaline solutions. This process fundamentally involves the polymerization of Si–O–Al bonds within the silico-aluminate framework [40].

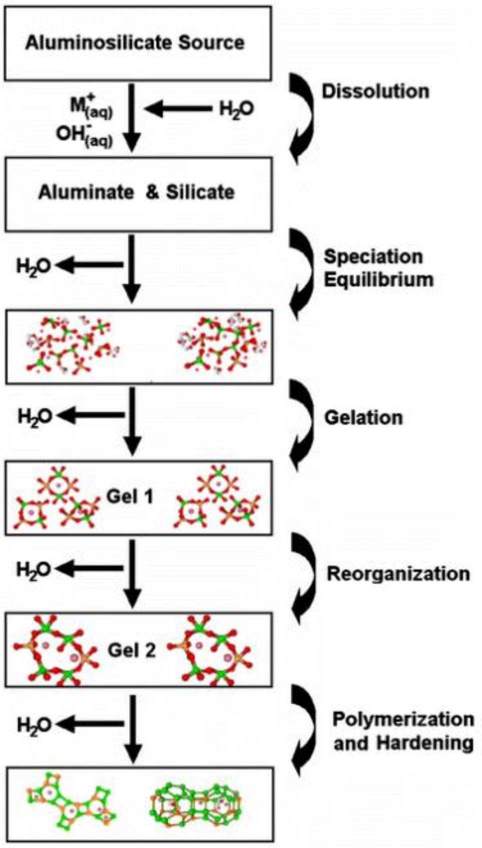

Figure 2.1 Geopolymerization procedure (modified from Davidovits [42])

Thanks to their excellent chemical stability, thermal resistance, and mechanical strength, geopolymers were initially adopted as an option to traditional concrete in environments exposed to fire or aggressive chemical agents. Commonly used binders in geopolymer synthesis include fly ash, metakaolin, and ground granulated blast furnace slag (GGBFS). Among these, metakaolin is frequently preferred due to its high reactivity; however, its energy-intensive production has prompted the search for more sustainable alternatives [42].

In contrast, fly ash has become a major research focus in geopolymer production as it results from thermal power plant by-product formation and its availability in desired properties, avoiding the intensive energy consumption needed for cement manufacturing. In this context, two main classes of fly ash have been extensively studied: Class C (high-calcium) and Class F (low-calcium). Fly ash has become a favored binder component in geopolymer systems because it can enhance workability, improve resistance to chemical attack, and significantly increase fire resistance. [43]

Compared to fly ash, GGBFS is notable in geopolymer generation for its capacity to attain early-age strength [44]. GGBFS is typically obtained as a by-product from an iron-steel factory. Rapid cooling of molten slag creates a reactive substance with high concentrations of calcium oxide (CaO), silicon dioxide (SiO_2), and aluminum oxide (Al_2O_3), all of which contribute significantly to the binding properties of the geopolymer matrix. Unlike FA-based geopolymers, which often necessitate high temperatures for curing, GGBFS-based geopolymers can generally cure at ambient temperature. Also, geopolymers produced with GGBFS exhibit high resistance against acid, sulfate, and chloride ion attacks. Due to the intrinsic characteristics of the resulting gel structure, they typically display lower porosity and reduced permeability [45].

Li and Liu investigated the impact of GGBFS on the performance of FA-based geopolymers. By incorporating only 4% GGBFS into the total binder content, the geopolymer mixture attained compressive strengths of 50 MPa and 70 MPa after 14 days of curing at 30 °C and 70 °C, respectively. To analyze the role of slag in enhancing mechanical performance, the researchers employed Fourier-transform infrared (FTIR) spectroscopy, X-ray diffraction (XRD), and additional microstructural techniques. The results from XRD and FTIR analyses indicated that the inclusion of GGBFS led to the formation of more amorphous phases and significantly accelerated the reaction kinetics of the raw materials, thereby contributing to the superior early strength performance of the geopolymer [46].

Gruskovnjak et al. conducted a comparative analysis of the hydration properties of alkali-activated slag versus conventional Portland cement systems. They examined the variation in hydration products observed in both systems by employing sophisticated microstructure analysis methods like scanning electron microscopy (SEM) and XRD. Their findings indicated that calcium silicate hydrate (C–S–H) forms more rapidly in alkali-activated slag due to the accelerated dissolution of sodium metasilicate in the alkaline environment. However, this rapid initial reaction alters the long-term hydration kinetics of the slag, resulting in lower late-age strength development compared to systems based on Portland cement [45].

Conventional concrete and geopolymer concrete have two distinct hardening mechanisms: hydration and geopolymerization. Despite this difference, both can achieve similar compressive strengths with adequate curing. This causes differences in parameters such as hydration products, setting time, pore structure, and drying shrinkage. Yet, literature research demonstrates that geopolymer concretes not only outperform Portland cement concretes in terms of eco-friendly [20] but also have comparable drying shrinkage in the same classes, better resistance to acid and chemical attacks due to its binder system is devoid of C_3A, similar or more densely packed and interconnected pore structure with smaller pore sizes, which can lead to higher durability and lower permeability [47-49]

2.2.3. Alkali Activation in Geopolymer Binders

When developing geopolymer binders, the selection and proportioning of alkaline activators are as critical as the characteristics of the precursor material. These activators function by chemically stimulating aluminosilicate precursors through alkali hydroxide and alkali silicate compounds. Among these, potassium and sodium-based activators are generally found to deliver the most effective performance in both categories. Due to their high solubility, up to 20 mol, sodium and potassium hydroxides provide significant adaptability in the design of geopolymer mixtures [50]. Alkaline silicates, although their pH values are similar to those of hydroxides, tend to demonstrate greater overall alkalinity. Although hydroxides contribute to a rapid increase in pH during the initial phases of the reaction, the addition of silica from silicate solutions can sustain or elevate this pH level over time [51].

Jimenez and Puertas [52] examined the strength development and hydration behavior in alkali-activated slag cement systems using different combinations of alkali activators. In their study, three specific activator blends, comprising sodium silicate, sodium hydroxide, and sodium carbonate, were formulated, maintaining Na_2O content at 4% of the total binder. Their findings highlighted that slag dissolution rate is directly influenced by the pH environment, with values above 12 enhancing reactivity. Moreover, once the pH exceeds this threshold, the setting and strength development become highly dependent on the characteristics of the anions present in the activator, which interact with calcium ions released during slag hydration to form stable products.

In another study, Wang et al. [53] explored various parameters affecting the mechanical performance of geopolymer binders. Their results emphasized that curing conditions and factors such as liquid-to-slag ratio, silicate modulus, activator type, and particle fineness played a dominant role. Sodium silicate was identified as the most efficient activator across all test conditions. Optimal values were determined for several parameters: Na_2O dosage between 3.0% and 5.5%, solution-to-slag ratio between 0.38 and 0.45, and fineness of the slag varies from 4000 to 5500 cm^2/g.

Dombrowski et al. [54] focused on the impact of calcium content in FA-based geopolymers. Their experimental results demonstrated that adding calcium hydroxide at varying dosages significantly affected the gel structure, reaction kinetics, and mechanical strength. Notably, an 8% addition of $Ca(OH)_2$ resulted in the highest mechanical performance and was effective under ambient conditions and at elevated curing temperatures.

2.2.4. Use of Construction and Demolition Wastes in Geopolymer Production

The construction sector remains a major consumer of natural resources, consequently producing large volumes of construction and demolition waste. CDW represents the largest share of solid waste worldwide, leading to considerable environmental and economic issues. Yazdani et al. [55] emphasized that the effective management, recycling, and reuse of CDW at the local level is essential for sustainable development.

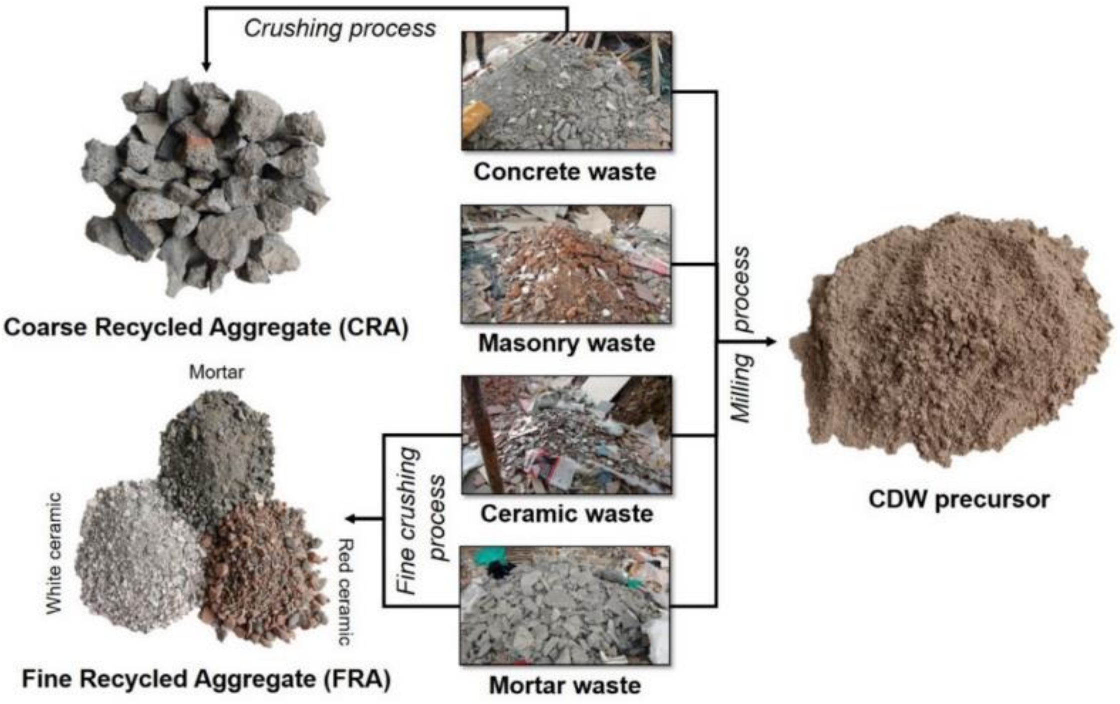

Figure 2.2 CDW precursor and recycled aggregates (adapted from Robayo-Salazar et al. [56])

Figure 2.3 Steps involved in converting CDW precursors into CDW concrete (adapted from Robayo-Salazar et al. [56])

Despite these concerns, the literature remains relatively limited regarding the utilization of CDW in geopolymer and other structural materials. Most research has focused on the flexural and shear performance of geopolymer beams. For instance, Akduman et al. [57] investigated beams produced entirely from CDW-derived binders, using recycled glass, brick, and concrete waste. They reported that their flexural strength showed similarity to traditional concrete. Four-point bending tests demonstrated ductile cracking patterns and structurally viable behavior.

Similarly, Aldemir et al. [23] explored the shear behavior of geopolymer beams made with CDW. The study showed that recycled aggregate significantly affected crack propagation and damage mode, especially at lower shear span-to-depth (a/d) ratios, where shear failure became dominant.

Curing conditions are a significant factor impacting the mechanical performance of geopolymers made from CDW. Ulugöl et al. [18] assessed the microstructural development of binders made from diverse CDW types under both ambient and elevated temperature curing. Notably, Samples that included hollow bricks and were cured at 115 °C for 24 hours reached compressive strengths greater than 45 MPa. FTIR and XRD analyses confirmed the formation of an amorphous aluminosilicate gel, indicating enhanced geopolymerization under optimized alkaline activation.

The consensus across these studies is that with appropriate precursor combinations, Si/Al ratios, and curing conditions, CDW-based geopolymers can perform on par with or even surpass ordinary Portland cement (OPC) concretes. Tan et al. [58] demonstrated that blending CDW with supplementary cementitious materials, including fly ash, metakaolin, silica fume, and GGBFS, yields high-performance binders. In particular, metakaolin enhanced the aluminum content, strengthening the gel formation in low-pH systems, while GGBFS improved both mechanical strength and chemical resistance.

In terms of chemical durability, Vafaei et al. [59] reported that geopolymers synthesized from CDW-based bricks and slag displayed superior resistance to hydrochloric acid compared to OPC concrete. After 24 weeks of acid exposure, only superficial damage was observed, highlighting the potential for long-term durability of CDW-based geopolymers in challenging environments.

Fořt et al. [60] conducted a sustainability assessment on CDW-based geopolymers and found that using 70% brick waste in the binder matrix yielded compressive strengths comparable to Portland cement paste. Additionally, the production process required 45% less energy and resulted in 72% fewer greenhouse gas emissions, highlighting its potential to reduce carbon emissions and encourage circularity of materials in construction industry.

From a structural engineering perspective, CDW-based geopolymer concretes have also demonstrated mechanical properties comparable to OPC concrete. Sumajouw et al. [61] experimentally evaluated reinforced geopolymer concrete columns produced with fly ash and confirmed that current structural design codes (e.g., ACI) can be effectively applied to these elements.

Sarker [62] assessed the applicability of Popovics' (1973) stress–strain model for low-calcium FA-based geopolymer concrete (GPC). The results indicated that with slight modifications, the model could predict the mechanical behavior of geopolymer concrete with reasonable accuracy.

Mo et al. [63] concluded that GPC used in structural components does not compromise load-bearing capacity and can be safely designed using existing code provisions.

Albitar et al. [64] examined columns and beams manufactured with FA and granulated lead smelter slag under ambient curing. The findings indicated behavior similar to OPC concrete under axial and eccentric loading. However, they also observed that some analytical methods overestimated the load capacity, suggesting the need for revised design frameworks.

Tran et al. [65] highlighted that GPC beams displayed a brittle failure mode characterized by explosive top-crushing, resulting in reduced residual deformation compared to OPC beams. Nevertheless, the incorporation of steel fibers improved cracking resistance, post-cracking stiffness, ductility, and load-bearing capacity.

Saranya et al. [66] assessed the axial load-bearing capacity of stub columns made with GGBS and dolomite-based geopolymer concrete. They found that the geopolymer alternative reduced construction costs by approximately 28% compared to OPC with equivalent compressive strength.

Pham et al. [67] developed a finite element (FE) model to predict the moment–curvature performance and cracking patterns of geopolymer concrete beams reinforced with low-calcium fly ash and GGBFS. The model closely matched the results of four-point bending tests.

Neupane and Hadigheh [68] applied sodium hydroxide-free geopolymer binders in prestressed concrete beams and found improved serviceability and higher load-carrying capacity relative to OPC systems, suggesting the viability of geopolymer alternatives in prestressed applications.

Saranya at al. [69] and Mao at al. [70] explored the seismic response of geopolymer beam-column joints under cyclic reversal loading. Their studies confirmed that the joints maintained acceptable deformation capacity and energy dissipation performance.

Finally, Albidah [71] proposed a strut-and-tie predictive model to assess the shear behavior of deep geopolymer beams composed of metakaolin and fly ash. The study demonstrated that varying steel fiber content and stirrup ratios significantly influenced shear strength, with validated predictions against experimental results.

2.2.5. Using Recycled Concrete Aggregate in Geopolymer

The construction industry consumes natural resources day by day and creates significant amounts of CDW [30]. CDW, which is both heavy and bulky, is a significant source of municipal solid waste, constituting 10% to 30% of the total waste landfilled [1]. However, a large portion of construction demolition waste has a high potential for recycling and reuse [72].

Nevertheless, limited research has been performed to examine the structural performance of CDW-based geopolymer concretes at reinforced structural elements. Shi et al. [73] tested the structural behavior of geopolymeric concrete-filled steel tubes utilizing recycled material. The load capacity decreased with the increase of recycled aggregate percentage, whereas an improvement in the peak deformation value and the ductility index under axial load was observed.

The effect of recycled aggregates on the bending behavior of GPC beams and the optimum replacement percentage of recycled aggregates for GPC was examined by Kathirvel and Kaliyaperumal [74]. Kathirvel and Kaliyaperumal [74] stated that ductility and deflections of GPC beams risen with the increasing percentage of recycled concrete aggregate in GPC, and the optimum loading capacity increase was 22.5%, observed at a 75% replacement level.

Akduman et al. [75], and Aldemir et al. [23] experimentally investigated the structural performance of reinforced geopolymer concrete beams produced from CDW-based materials, including recycled aggregates, waste masonry units (e.g., red clay brick, roof tile, hollow brick, etc.), and glass. The studies stated that the use of recycled aggregates had little effect on the load capacities of OPC and geopolymer concrete samples. Still, they reduced approximately normalized energy dissipation capacities by 30%, and the performance of code predictions (TS500 [76] and ACI318 [77]) is very low. Thus, researchers suggested using an increased factor of safety for tested specimens.

According to Ferreira et al. [78], CDW-based RCAs have higher water absorption, a more porous structure, and consequently lower density [79] than standard aggregates resulting from old adhesion mortar. This causes RCA-containing concretes to have slightly lower performance regarding compressive strength, workability, modulus of elasticity, density, and permeability compared to normal aggregate-containing concretes. Treatments such as increasing the mixing water or pre-saturation of RCAs may be effective to overcome the workability losses of RCA-containing concretes [80].

Some studies have reported that concretes containing 100% RCA may have lower compressive strength in the range of 20-25% than concretes containing normal aggregates [81, 82], while other studies have indicated that there are no appreciable variations in the compressive strength and several other characteristics of concretes including RCA and that variables such the quality, type, crushing factor, and pre-treatment of RCA are decisive [83, 84].

In addition to the environmental concerns associated with PC preparation and aggregate quarrying, traditional concrete structures lack high durability and tend to deteriorate over time due to various mechanical, chemical, and environmental factors. This decline frequently results in structural demolition and produces large quantities of waste concrete and masonry units.

Additionally, with the rapid growth of urban populations and developing economies worldwide, demand for new construction and demolition of buildings before their end has increased considerably. Unfortunately, demolition at the end of a building's service life generates an incredible amount of solid waste. Similarly, the construction of new buildings and the remediation of existing buildings also generate a large amount of solid waste.

The construction and demolition of the building can be considered the largest producer of solid waste globally. If not properly managed, this waste, which often ends up in landfills and may contain toxic substances, presents dangers to human wellbeing and the environment around it [85]. Therefore, appropriate handling of CDW is crucial to ensure environmental, social, and economic benefits.

Consequently, finding suitable solutions for managing waste concrete has become a subject of debate. Researchers have begun exploring methods to recycle waste concrete, such as crushing it to obtain recycled aggregates of different sizes. However, the challenge lies in determining effective applications for these recycled aggregates. Generally, coarse RCAs are used in simple technology applications like pavements and non-structural fillings [86].

Akbarnezhad et al. [87] highlighted that the mechanical performance of RCA-based concrete is greatly affected by the quantity of residual mortar attached to the surface of the RCA particles. A higher volume of this adhered mortar results in a more porous structure and decreases compressive strength due to the creation of weaker secondary interfacial transition zones (ITZ) between the old mortar and the new cement matrix, as shown in **Figure 2.4**. The adhered mortar also brings to an raise in the water absorption capacity by approximately 4–5%, resulting in a higher porosity, reduced density, and increased permeability, all of which negatively affect the overall durability of RCA-based concretes.

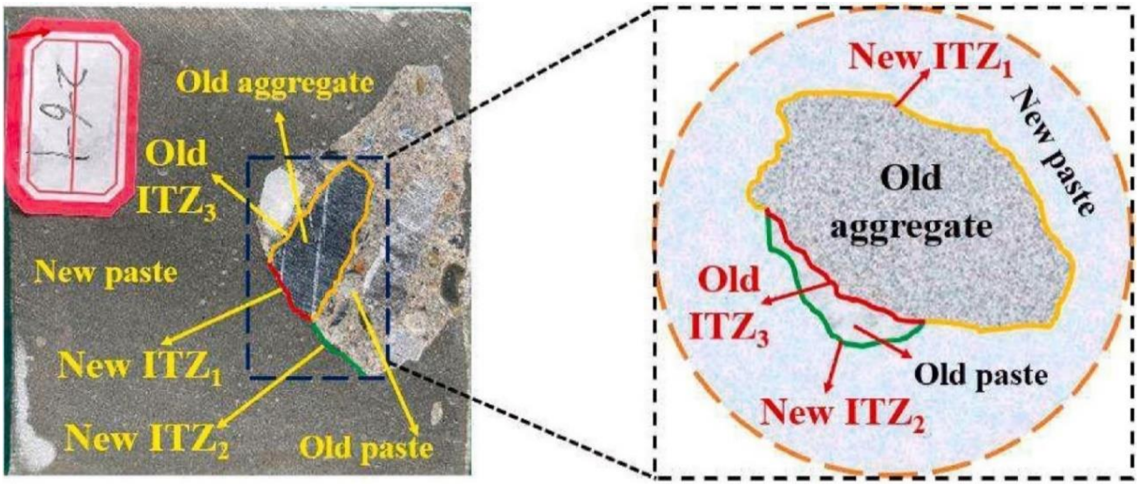

Figure 2.4 Interfacial Transition Zone (ITZ) [88]

To address these drawbacks, Akbarnezhad et al. [87] proposed a microwave-assisted technique for enhancing RCA quality. This method exploits the differing electromagnetic properties of the mortar and aggregate components; the adhered mortar heats up more rapidly than the natural aggregate, leading to thermal stress at the interface and enabling partial detachment of the mortar. This selective removal enhances the mechanical characteristics of the concrete by producing cleaner aggregates.

Additionally, Li et al. [89] created a technique named the Two-Stage Mixing Approach (TSMA) to enhance the interfacial bond between RCA and the new paste. Initially, RCA is combined with cement, creating a thin layer of fresh paste that coats the old aggregate before the other ingredients are incorporated. This pre-coating promotes the denser and more homogenous ITZ, reducing the local porosity and calcium hydroxide concentration, which results in increased compressive strength and reduced permeability of the concrete.

The general outcome of the work conducted up to this point indicates that geopolymer concrete with CDW-based RCA exhibits structural behavior identical to that of OPC concrete of the same grade. Conversely, geopolymer concrete's ductility, energy dissipation capacity (EDC), and ultimate load capacities depend on the proportion of CDW-based materials used. While specific studies indicate that incorporating RCAs into geopolymer concrete might influence structural performance, the environmental consequences of CDW make it essential to substitute natural aggregates with RCAs, if possible. Performance concerns can be effectively mitigated through various enhancement techniques.

Some enhancement techniques are listed below to mitigate the drawbacks associated with RCA usage:

- Use of high-range superplasticizers to boost workability despite higher water demand.
- Restricting the substitution rate of natural aggregate with RCA to manage strength reduction.
- Preferential use of coarse RCA has less adhered mortar per unit of surface area.
- The inclusion of FA in the mix, refines the pore structure and enhances long-term strength.
- Combining RCA with natural sand to improve particle grading and reduce voids.
- Pre-saturation of RCA to minimize the undesired absorption of mixing water during hydration.
- Carbonation of the RCA facilitates chemical reaction between the calcium hydroxide (CH) and calcium silicate hydrate (C-S-H) phases present in the adhered old mortar and atmospheric CO_2, resulting in the formation of stable calcium carbonate ($CaCO_3$) and silica gel.
- Selection of RCA produced from lower-strength concrete is more brittle and tends to hold less mortar during crushing.
- Crushing using jaw crushers, which can produce cleaner, more uniformly graded aggregates.

2.3. Structural Element Connection Type

In precast structures, the joints (i.e., connections) are often regarded the weakest components and are primarily responsible for the occurrence of severe damage, and in some cases, progressive collapse failures in these structures [90-97]. Precast joints could be formed using “wet methods”, which require on-site concrete casting, or “dry methods”, which do not require any on-site concrete casting. The use of on-site concrete casting “wet methods” is generally straightforward to employ but increases construction time and requires proper quality assurance measures. On the other hand, using dry methods for precast joints is easier to install, time efficient, and could be disassembled for reuse or rehabilitation [30].

2.3.1. Wet Connection

Wet connections, which utilize site-cast concrete to bond precast structural components, have historically been an essential method in precast concrete construction. These connections provide various engineering and practical benefits, particularly their capacity to create monolithic-like behavior between adjacent elements, thereby enhancing continuity, structural integrity, and stiffness. In seismic contexts, well-detailed wet connections can offer outstanding energy dissipation and ensure that failure modes occur away from the joint interface, which enhances the overall ductility and resilience of the structure. Additionally, wet joints promote greater geometric flexibility and can compensate for tolerances, which is especially advantageous in intricate structural designs where dimensional discrepancies might otherwise cause performance challenges. Their adaptability to site-specific reinforcement detailing also enables better integration with in-situ construction elements like slabs and foundation systems. For many years, wet precast connections have been considered the preferred choice in high seismic risk areas, where moment-resisting frames and rigid structural systems are necessary. Wet connections remain a reliable and widely accepted option in precast concrete design, thanks to their robust performance under both axial and lateral loads, along with their compatibility with conventional construction methods.

Among various wet connection types, grouted sleeve (GS) connections are widely adopted due to their ability to imitate the load transfer performance of monolithic cast-in-place joints, while also offering significant advantages in terms of ease of assembly and on-site efficiency [98]. In these systems, large-diameter longitudinal reinforcement projecting from precast columns (PC) is inserted into sleeves embedded in the foundation, which are then filled with high-strength grout via designated inlet and outlet ports.

However, since these sleeves are typically located near the potential plastic hinge region, they tend to increase local stiffness and restrict ductile behavior, resulting in unfavorable failure modes on the basis of seismic loading. To defeat this limitation, recent studies have proposed shifting the plastic hinge zone upward, beyond the sleeve region, to promote more reliable and ductile deformation patterns. Additionally, enhancements such as modified splicing details, the use of high-strength reinforcement, and alternative anchorage configurations have been investigated to achieve controlled cracking and improved energy dissipation.

Ghayeb et al. [98] previously indicated that the formation of plastic hinges can be adversely affected when they occur within the stiff region of grouted sleeves. To overcome this challenge, Haber et al. [99] suggested a design approach that shifts the plastic hinge region above the grouted sleeve as shown in **Figure 2.5**, aiming to enhance both the plastic rotation capability and the overall ductile performance of the connection. The relocation of this hinge was accomplished by using transition splicing techniques and incorporating high-strength steel reinforcement in the connecting footing element.

To evaluate the effectiveness of this technique, two 0.42-scale precast column specimens were evaluated under slow cycling lateral loading, in conjunction with uniaxial tensile tests. The experimental outcomes confirmed that the proposed connection provides enhanced ductility matched to traditional cast-in-place (CIP) columns and previously examined grouted sleeve (GS) connection details. Both experimental and analytical approaches to moment-curvature analyses were utilized to inform design implications and to develop a simplified estimation method for estimating the deformation capacity of precast columns with GS joints and strategically adjusted plastic hinge locations.

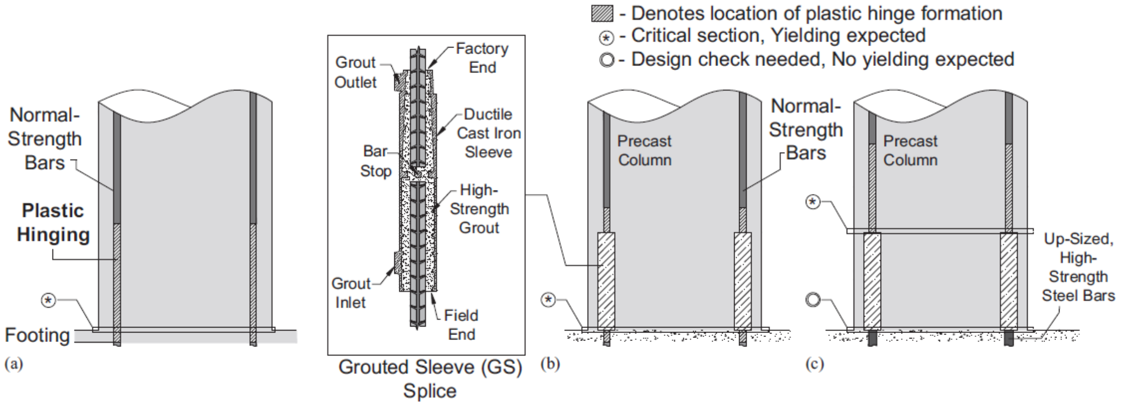

Figure 2.5 Locations of plastic hinges for traditional and precast columns: (a) traditional monolithic column; (b) standard Grouted Sleeve connection; (c) Grouted Sleeve connection featuring shifted hinge detailing. [99].

In the experimental investigation of Fan et al. [100], they investigate the impact of employing high-strength reinforcement with large diameters in column-to-foundation connections of prefabricated concrete structures, an area relatively unexplored in prior research. Three full-scale test specimens were prepared: one with grouted sleeve connections (PC-S), another with grouted corrugated duct connections (PC-C), and a cast-in-place monolithic specimen (CIP) used as a reference, as shown in **Figure 2.6**. All specimens were exposed to pseudo-static cyclic loading to evaluate their ductility, EDC, and failure mechanisms. Among the three, specimen PC-C demonstrated the best ductility performance, reaching a maximum lateral drift of 5.5%. In contrast, specimen PC-S experienced premature failure due to longitudinal bar buckling and stirrup rupture. While all specimens exhibited similar EDC up to a 3.5% drift ratio, the CIP specimen outperformed the others at higher drift levels. The PC-C specimen displayed notable pinching in its hysteresis response, primarily attributed to bond-slip between the reinforcing bars and the grout in the grooved ducts. Although PC-S showed more stable hysteretic behavior, it failed earlier due to local reinforcement instability. Ultimately, both prefabricated connection types exhibited structural responses comparable to monolithic systems. However, the findings emphasize the need for enhanced reinforcement, such as denser stirrup spacing above sleeves and ducts, increased lap splice lengths, and higher-performance grouting materials, in regions prone to localized damage.

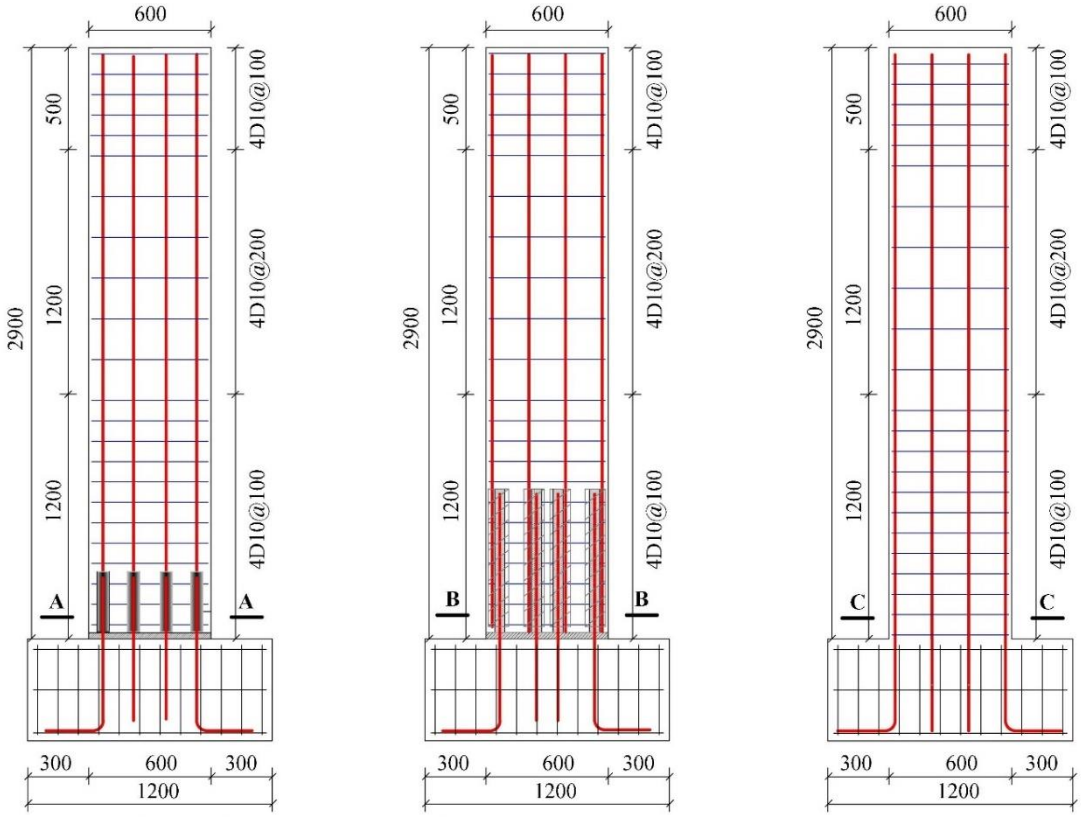

(a) Specimen PC-S
(b) Specimen PC-C
(c) Specimen CIP

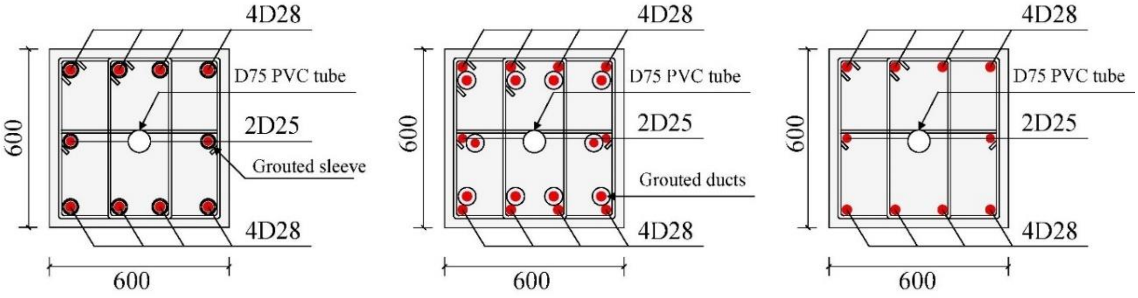

(d) A-A section
(e) B-B section
(f) C-C section

Figure 2.6 Details and configurations of test specimen reinforcements (Dimensions in mm) [100]

As discussed above, wet connections in precast concrete construction offer several advantages, including their ability to provide structural continuity and compatibility with traditional construction techniques. Many studies in the resource have highlighted the effectiveness of these connections in achieving monolithic-like behavior and facilitating robust load transfer between precast elements. However, despite these benefits, wet connections present significant limitations when evaluated in the context of modern construction priorities, particularly with respect to sustainability, adaptability, and resilience.

A growing body of research has revealed several critical disadvantages of wet joint method that compromise their long-term performance and alignment with circular construction strategies. Wet connections are typically non-demountable, which directly conflicts with the increasing demand for reusable and modular construction systems. Their reliance on on-site work prolongs construction timelines and introduces quality control issues, especially in projects with complex geometries or under adverse weather conditions. Moreover, these connections can become critical points of weakness in seismic applications due to the lack of mechanical continuity in reinforcement, potentially resulting in brittle failure or progressive collapse.

Aktepe et al. [30] emphasize that, unlike dry or demountable systems, wet connections do not allow for disassembly or easy repair, rendering them less suitable for structures that may require future modification. Additionally, the inherent rigidity of wet joints makes them vulnerable to damage accumulation under cyclic lateral loads, thereby reducing their energy dissipation capacity and overall ductility.

These limitations highlight the urgent need for transitioning toward dry and demountable connection systems, particularly in the development of sustainable and reusable structural components such as those utilizing geopolymer concrete.

2.3.2. Dry Connection (Bolted Demountable Connection)

Dry connections, often realized through bolted mechanical joints, offer a series of compelling advantages over traditional wet connections in precast concrete construction. The most significant benefit is their demountability, enabling structural components to be disassembled, reused, or replaced without damage. This property aligns directly with the fundamentals of design for disassembly (DfD) and supports circular construction practices by reducing demolition waste and extending the lifecycle of structural elements. Additionally, dry connections are typically faster to install due to the absence of on-site casting, formwork, and curing time requirements. These characteristics make them especially suitable for fast-track construction, particularly in urban or seismic-prone regions where construction efficiency and adaptability are critical. From a maintenance perspective, dry systems facilitate easy inspection and repair, which is often unfeasible in wet systems. Furthermore, when integrated with geopolymer concrete elements, dry connections significantly reduce embodied carbon and promote resource-efficient construction.

Several recent experimental and numerical studies have demonstrated that properly detailed dry precast joints can exhibit seismic performance comparable to monolithic systems, especially under combined lateral and axial cyclic loading. For instance, Senturk et al. [101] and Pul et al. [27] developed bolted column-base and beam-column connections (BCC) that displayed stable hysteresis behavior, satisfactory ductility, and high energy dissipation capacity. In comparative tests with monolithic connections, some dry systems even exhibited higher lateral load capacity and stiffness retention, particularly when the connections were reinforced with steel plates and well-distributed anchorage systems. The cyclic loading results also indicated that plastic hinge formation could be effectively guided away from the connection region, thereby reducing concentrated damage and improving post-earthquake reparability. These findings confirm that demountable systems can be considered reliable for seismic applications, provided they are supported by robust design detailing and proper reinforcement anchorage strategies.

Some researchers have investigated the behavior of various types of precast RC bolted beam-to-column [101-107] and RC bolted column-to-column [24, 108-111] joints in buildings. The precast structures' connections are the most important areas that can sustain significant damage from earthquakes [27]. In order to obtain desired performance level in precast concrete structures to transfer forces (i.e., shear, moment, and axial load), connections should be carefully designed. Several demountable connection techniques have been proposed for the connection of precast concrete structures.

Aninthaneni and Dhakal [112] proposed floor-to-floor, floor-to-beam, beam-to-column, column-to-column, and column-to-foundation steel-based demountable joints for fully demountable PC frame building methods.

Senturk et al. [101] and Pul et al. [27] developed monolithic-like PC beam-column and column-foundation connections fabricated based on bolts and steel plates. Detailed numerical and experimental studies were performed on the developed connections to investigate their cyclic behavior, curvature distributions, failure modes, energy dissipation capacities, and ductility. It was found that the suggested precast connections might offer structural behavior that is either equal to or better than that of monolithic connections.

Nascimbene and Bianco [26] examined the seismic behavior of a demountable column-to-foundation joint relying on the mechanical interlock between steel shoes embedded in the column base and anchor bolts extending from the foundation, emphasizing the performance of the welded interface between steel shoes and reinforcement.

Zhou et al. [29] proposed a demountable steel-concrete composite connection for possible use in column-pile cap joints in the precast pier. A bolted flange plate-based demountable column-to-column joint for concrete structures has been suggested by Chen et al. [110] and experimentally and numerically investigated to determine seismic performance. Torra-Bilal et al. [107] examined both analytically and through testing the performance of multiple hybrid beam-to-column connections featuring diverse detailing strategies for use in precast moment-resisting frames under cyclic load reversals.

Fan et al. [113] numerically compared the shear performance of thick precast shear walls with in-situ casting walls. Additionally, in recent decades, artificial intelligence and machine learning techniques have been developed by researchers to design, predict effective strength, and inspect reinforced concrete products [114-116].

In the study conducted by Ye et al. [117], a composite BCC was produced in line with the strong-column to weak-beam design principle as shown in **Figure 2.7**. The proposed connection incorporates steel I-beams and cladding plates to enhance energy dissipation capacity while maintaining structural integrity. Experimental findings showed that the mechanical behavior of the connection matched that of conventional in-situ reinforced concrete joints. Notably, energy dissipation was predominantly concentrated in the steel I-beam and cladding plate regions, thereby reducing energy accumulation in the column and contributing to a safer and more resilient structural system.

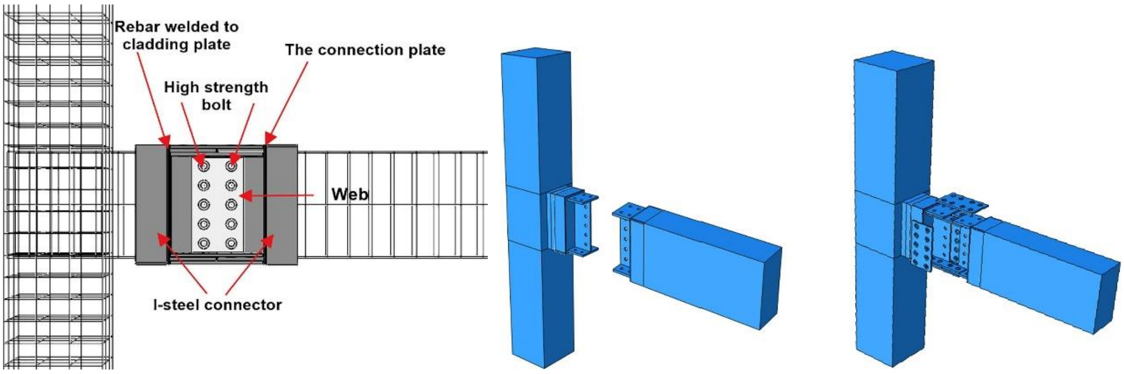

Figure 2.7 Column-beam connection proposed by Ye et al. [117].

In the research by Nzabonimpa et al.[118], They designed a steel–concrete composite connection in accordance with the provisions of AISC 358 for the steel components as shown in **Figure 2.8**. The proposed dry-type beam–column system was developed to achieve complete moment transfer in reinforced concrete structures, utilizing high-strength bolts, steel end plates, and anchor reinforcement for moment transmission. A common challenge in such systems is the insufficient stiffness of the end plates relative to the beams, which can lead to local buckling. To address this, the study investigated the mechanical behavior of connections by varying the thickness of the end plates and comparing them with conventional in-situ reinforced concrete beam–column joints. The results indicated that the specimen with a 45 mm-thick end plate exhibited mechanical performance similar to that of conventional cast-in-situ connections.

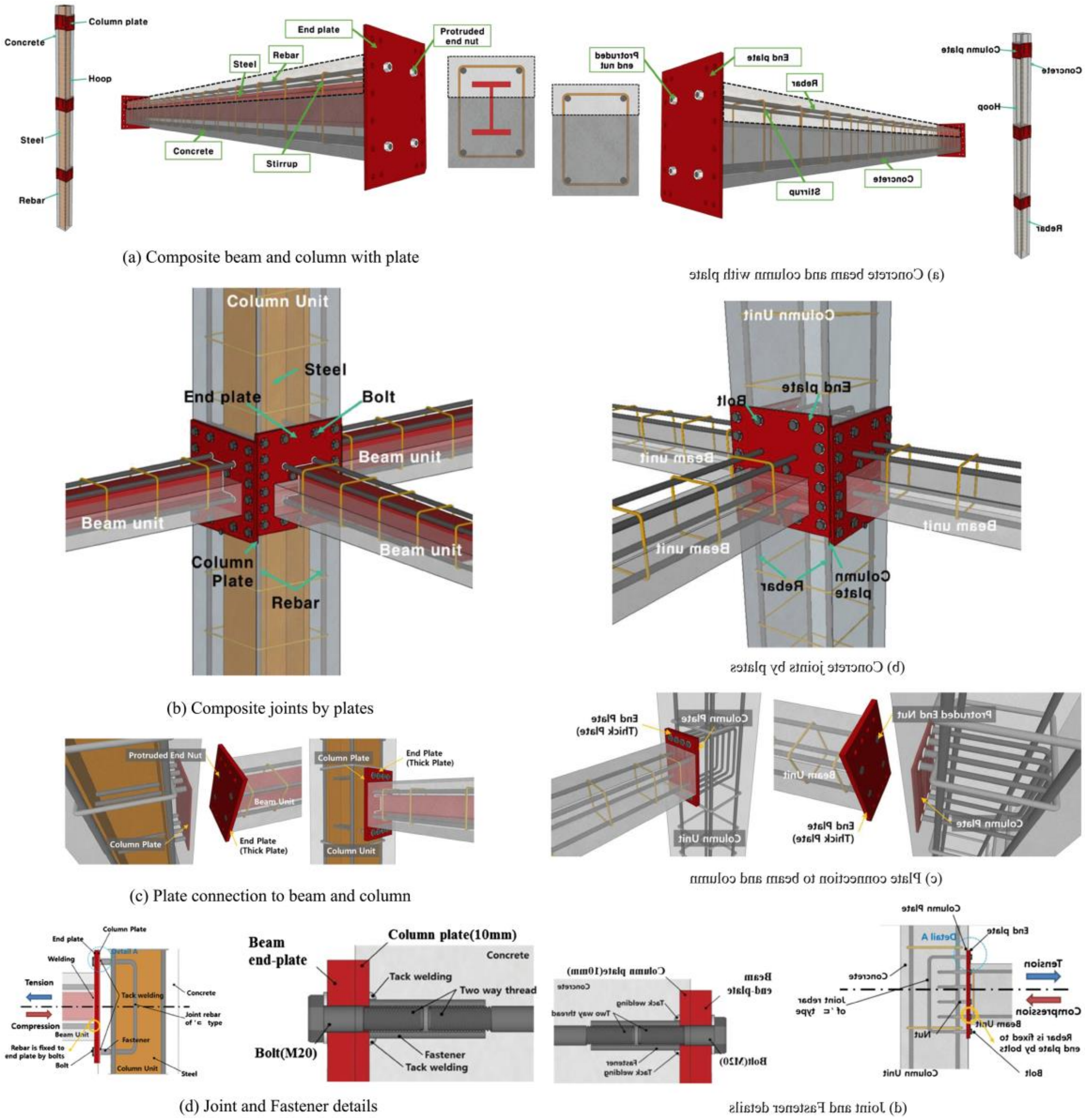

(a) Composite beam and column with plate

(b) Composite joints by plates

(c) Plate connection to beam and column

(d) Joint and Fastener details

Figure 2.8 Various kinds of composite beam-column connections proposed by Nzabonimpa et al. [118].

As reported by Aninthaneni et al. [119], a similar approach was adopted by employing an end plate to carry-over moments from the column to the beam using high-grade bolts, as shown in **Figure 2.9**. Gusset plates were utilized to enhance the rigidity and rotational stiffness of the end plate. Particular attention was given to ensuring that the end plate remained within the elastic range subjected to quasi-static cyclic loading and that its strength exceeded the ultimate capacity of the beam. Following the analysis of the observed hysteretic curves and energy dissipation capacities, the proposed connection exhibited structural performance comparable to, or even exceeding, that of traditional ductile monolithic beam-column joints. This enhanced performance can be attributed to the stress distribution mechanism, where stresses propagate progressively from the upper part of the beam end plate, rather than accumulating solely at a localized plastic hinge region, as typically seen in conventional ductile systems. Post-test observations showed a notable presence of horizontal cracks in the upper area of the base plate.

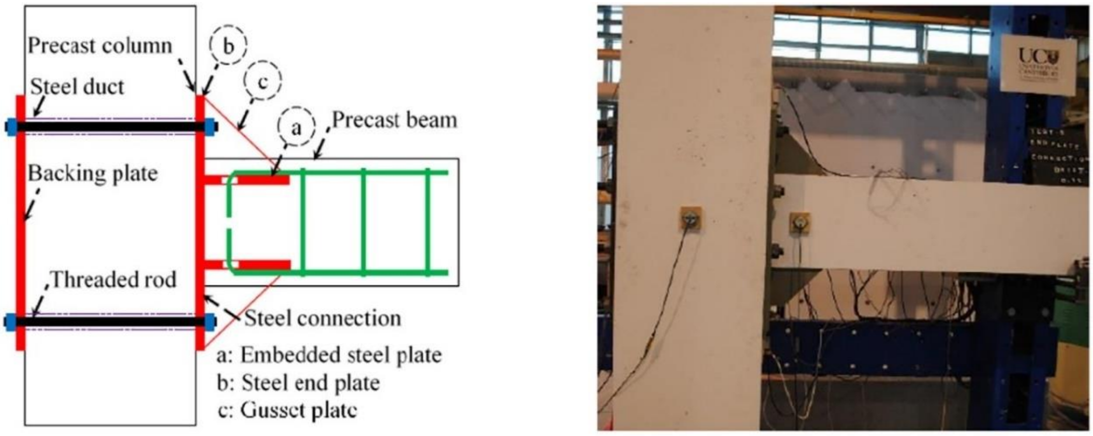

(a) Schematic layout of the connection

(b) A sub-assembly with the end plate connection

Figure 2.9 Beam-column joint details proposed by Aninthaneni et al. [119].

In the study of Zhou et al., a composite column-to-foundation connection was explicitly developed for application in demountable precast concrete structures. The connection incorporates a centrally perforated steel base plate, designed to facilitate force transmission and disassembly as shown in **Figure 2.10**. To enhance both the rigidity and rotational stiffness of the base plate, gusset plates were installed on both the interior and exterior faces. High-strength bolts and pre-stressed anchor rods were employed to secure the assembly. Under pseudo-static loading tests, all specimens exhibited typical flexural failure patterns. Notably, the connection steel plates and bolts remained undamaged and within the elastic range throughout the loading process. External stiffening plates and modified perforbond connectors demonstrated excellent performance transferring loads between the concrete column and the steel end plate.

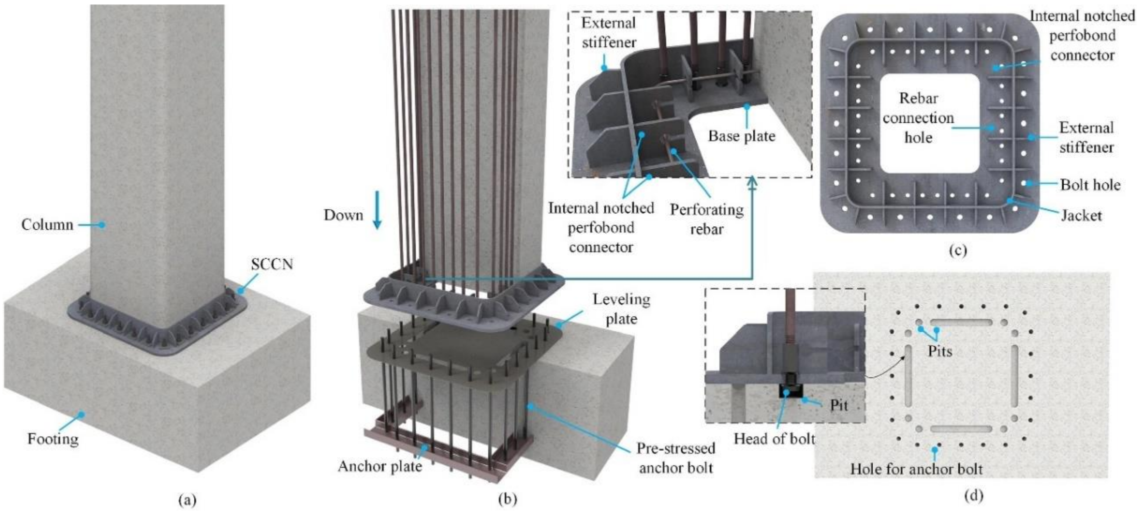

Figure 2.10 Novel demountable column-foundation connection [120].

According to the outcomes stated by Senturk et al. [101], this study investigates an innovative demountable precast beam-to-column joint developed to facilitate rapid and cost-effective repair by enabling the replacement of damaged structural components following seismic events. Unlike conventional approaches, this system employs rivet-headed reinforcing bars integrated into specially engineered end-plate assemblies, as shown in **Figure 2.11.** A set of six full-scale specimens, differing in beam length and longitudinal reinforcement ratio, underwent testing under a steady axial load equal to 10% of the column strength using a quasi-static cyclic lateral loading protocol. Their performance was analyzed with respect to ductility, rigidity, and observed damage patterns. Results demonstrated that the demountable specimens exhibited up to 34% greater ultimate lateral displacement and ductility compared to their monolithic counterparts. However, no notable distinction was seen between the two systems regarding initial stiffness and lateral load-bearing capacity. Specimens with higher longitudinal reinforcement ratios (2%) showed superior ductility and energy dissipation. Furthermore, while damage in demountable connections was distributed along the beam rather than concentrated at the connection region, damage in monolithic connections was localized at the joint, confirming that the proposed design aligns with the strong column–weak beam theory recommended in guidelines.

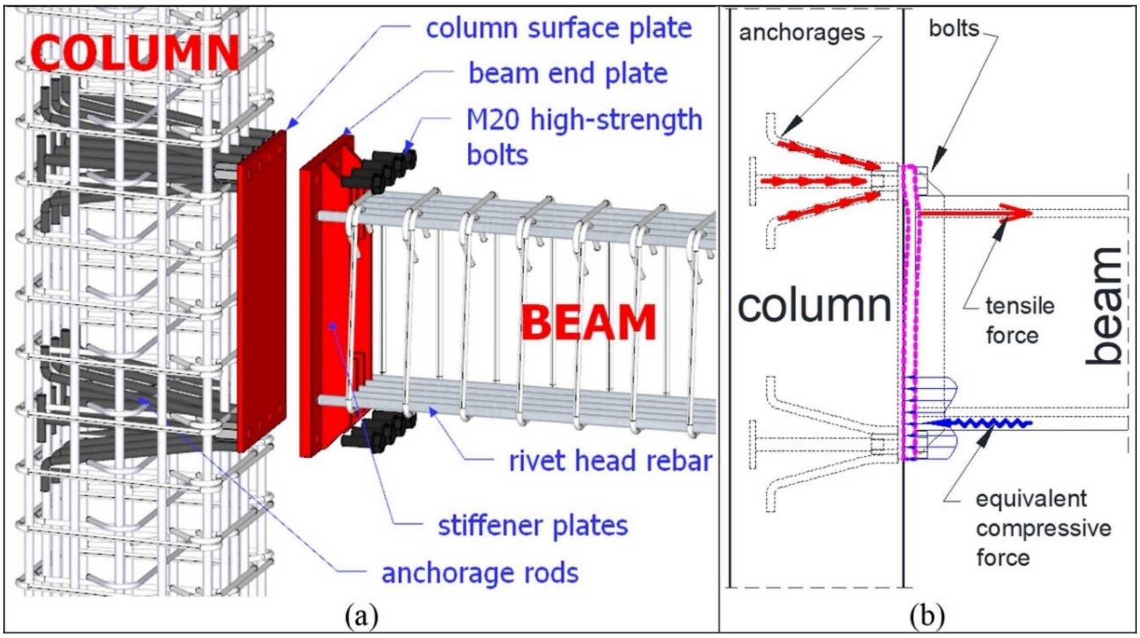

Figure 2.11 Proposed connection system details [101].

In the study conducted by Lu et al. [25], eight full-size RC columns with base connections were evaluated to assess a novel approach to structural repair. Unlike conventional demountable systems that require the full replacement of damaged columns after an earthquake, this method aims to restore structural functionality more rapidly and economically by replacing only the damaged steel fuse plates and padding blocks located at the interface region, as shown in **Figure 2.12**. The objective is to ensure no damage occurs in the RC column body. The experimental program was conducted in two stages: in the primary stage, samples were subjected to lateral drift up to 2%, after which the damaged components were replaced and the tests were resumed up to 4% drift. The key test parameters included the cross-sectional area of the steel fuse, the type of infill material of the padding block, and the axial load ratio. The results indicated that irreversible damage was limited solely to the replaceable steel fuses and padding blocks, with all other structural elements staying within their elastic limits. After component replacement, specimens were able to regain their original load-carrying capacities. The specimen with a larger fuse area and higher axial load demonstrated the highest lateral strength. Furthermore, the specimen utilizing ultra-high toughness cementitious composite (UHTCC) as the infill material of the padding block exhibited superior energy dissipation performance. However, pinching behavior was observed in the hysteretic loops beyond 3.33% drift due to local buckling. Overall, the proposed connection achieved structural performance in load transfer, moment capacity, and stiffness comparable to conventional monolithic systems.

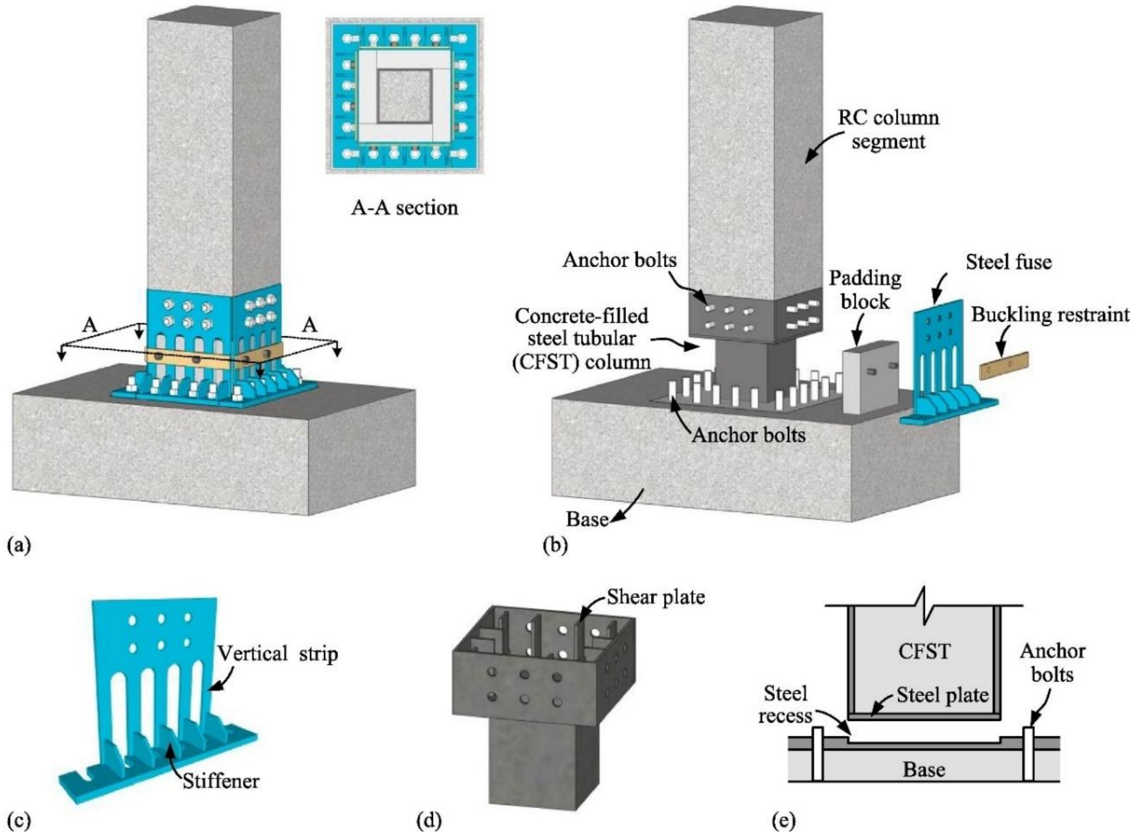

Figure 2.12 Details of the prefabricated column-base connection [25]

Nzabonimpa et al. [121] presented a novel approach in their research. This research aims to develop a simple, fast, and cost-effective demountable column system that can directly substitute conventional reinforced concrete columns in numerous types of structural use cases. In the proposed system, each end of the PC is equipped with steel connection plates. Three different types of mechanical joints were designed and tested in full-scale specimens: (1) a filler-plate type utilizing bent longitudinal rebars, (2) embedded nut-type column plates, and (3) a thick stacked filler plate configuration as shown in **Figure 2.13**. All threaded nuts were tightened to a 600 N·m torque and enclosed within the filler plate for enhanced load transfer and protection. While the filler-plate connection with bent rebars incurs additional labor costs due to bar bending or thicker filler plates, the embedded nut configuration requires precision drilling and machining, increasing fabrication costs. These disadvantages highlight areas for future optimization.

Experimental results confirmed that, when designed with sufficient stiffness, the end plates enabled the demountable columns to achieve structural behavior comparable to that of monolithic systems. Moreover, by optimizing plate thickness and bolt layout, the connection system can be made more efficient and economically viable for practical applications.

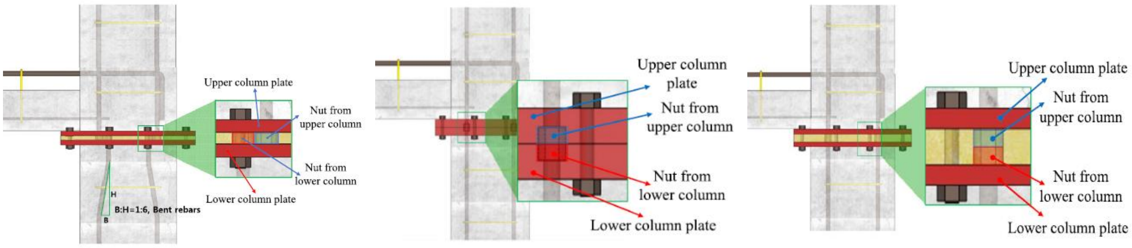

Figure 2.13 Type of connections proposed by Nzabonimpa et al. [121].

Li et al. [122] revealed a composite steel beam-to-column connection system for use in prefabricated structures, utilizing low yield strength steel (LYP100) to enable controlled energy dissipation during seismic events. The primary goal of the design is to guarantee that the reinforced concrete columns and beams remain within the elastic range by concentrating inelastic deformations within specially engineered energy-dissipating steel elements. Four full-scale samples were tested under quasi-static cyclic loading, including three prefabricated steel joints (PSJ) configurations and one monolithic reference specimen, as shown in **Figure 2.14**. The tests investigated the influence of the EDS length and the non-dissipative segment (NEDS) thickness on joint performance. In contrast to the monolithic specimen, the PSJ systems exhibited superior ductility and EDC. In the PSJ specimens, damage was confined exclusively to the steel joints, while the concrete components remained undamaged. An increase in NEDS thickness led to higher moment capacity but reduced energy dissipation. Conversely, a longer EDS improved ductility but slightly reduced load-bearing capacity. Among the tested configurations, PSJ-1 exhibited the highest energy dissipation capacity (64% greater than the monolithic specimen), while PSJ-2 achieved the highest lateral load capacity (14% greater). This research underscores the efficacy of the suggested PSJ system in maintaining the integrity of concrete members during seismic events by localizing damage to replaceable low-yield steel dampers. This modular design facilitates faster and more cost-effective post-earthquake repair and recovery, contributing to greater resilience and environmental efficiency of the structure.

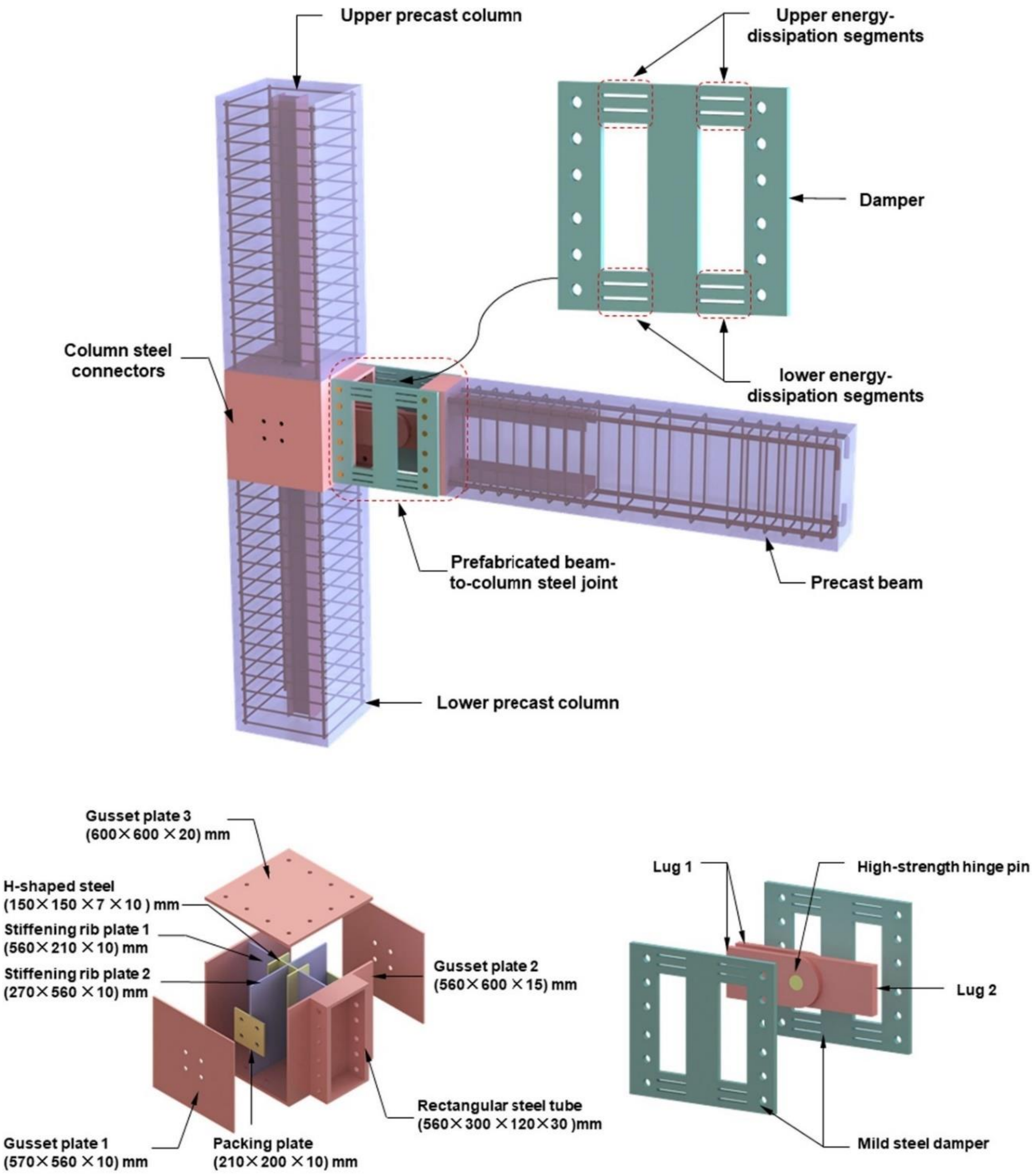

Column steel connectors

Beam-to-column steel joint

Figure 2.14 Prefabricated steel joint (PSJ) configurations of prefabricated beam-to-column steel joint. [122].

Zhang et al. [123], similar to previous research, prepared two test specimens: one cast-in-situ reference specimen and one incorporating a dry joint connection. Seismic behavior was evaluated through pseudo-static cyclic loading, with findings indicating that the dry joint behaved comparably to the monolithic counterpart. Consistent with the 'weak beam–strong column' design principle, damaging in the dry joint sample was primarily focused in the steel components of the beam, while the column remained intact.

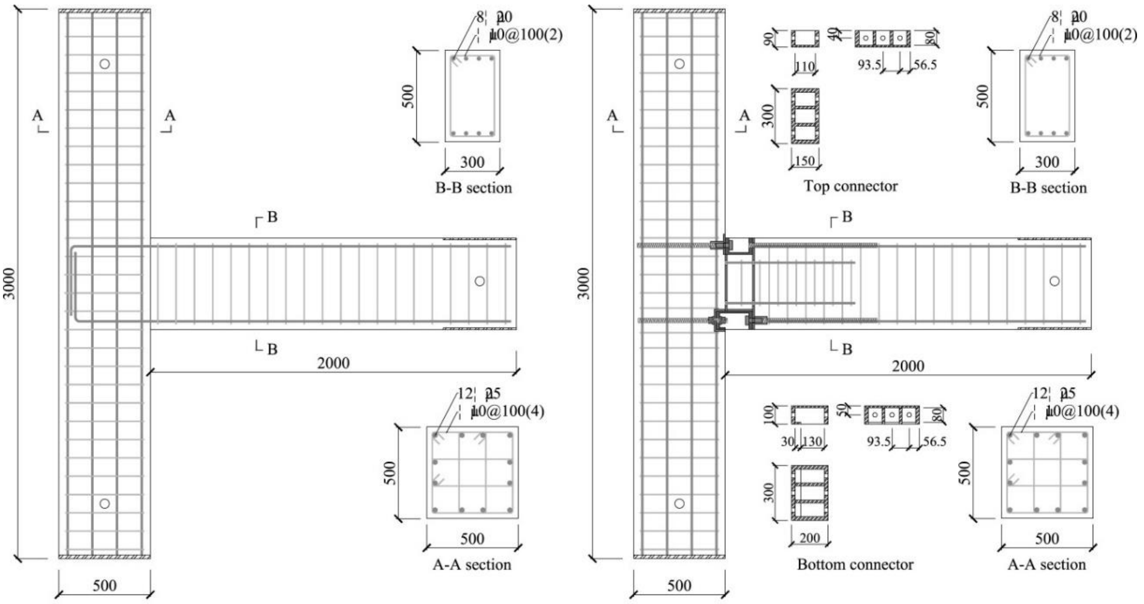

（a）CJ （b）PJ

Figure 2.15 Connection proposed by Zhang et al. [123].

Yang et al. [124] developed a novel dry-connected rotational friction dissipative beam-to-column joint (DRFDBJ) aimed at controlling seismic damage via energy dissipation, as shown in **Figure 2.16**. Unlike conventional precast systems that rely on plastic hinge formation in wet or dry joints, the proposed precast concrete frame system (NPCF) dissipates seismic energy through controlled friction at the connection interface, without inducing damage to the main structural components. The study involved nonlinear time-history analyses of 300 frame models, and the results showed that the system effectively minimized both story drift and damage concentration. A regression-based relationship between the sliding moment ratio (ρ) and the number of stories (ns) was established in accordance with current code provisions, enabling practical design applications. Validation on 5-7 story buildings confirmed that the proposed system reduced maximum interstory drift ratios by 13% to 24% compared to monolithic reference structures. The findings demonstrate that seismic performance can be significantly enhanced by adjusting the frictional resistance in the DRFDBJ using post-tensioned bolts, allowing energy dissipation to be tailored based on building height and expected seismic moment demand. This project marks a major improvement in creating resilient, removable, and maintenance-free structural systems for areas vulnerable to earthquakes.

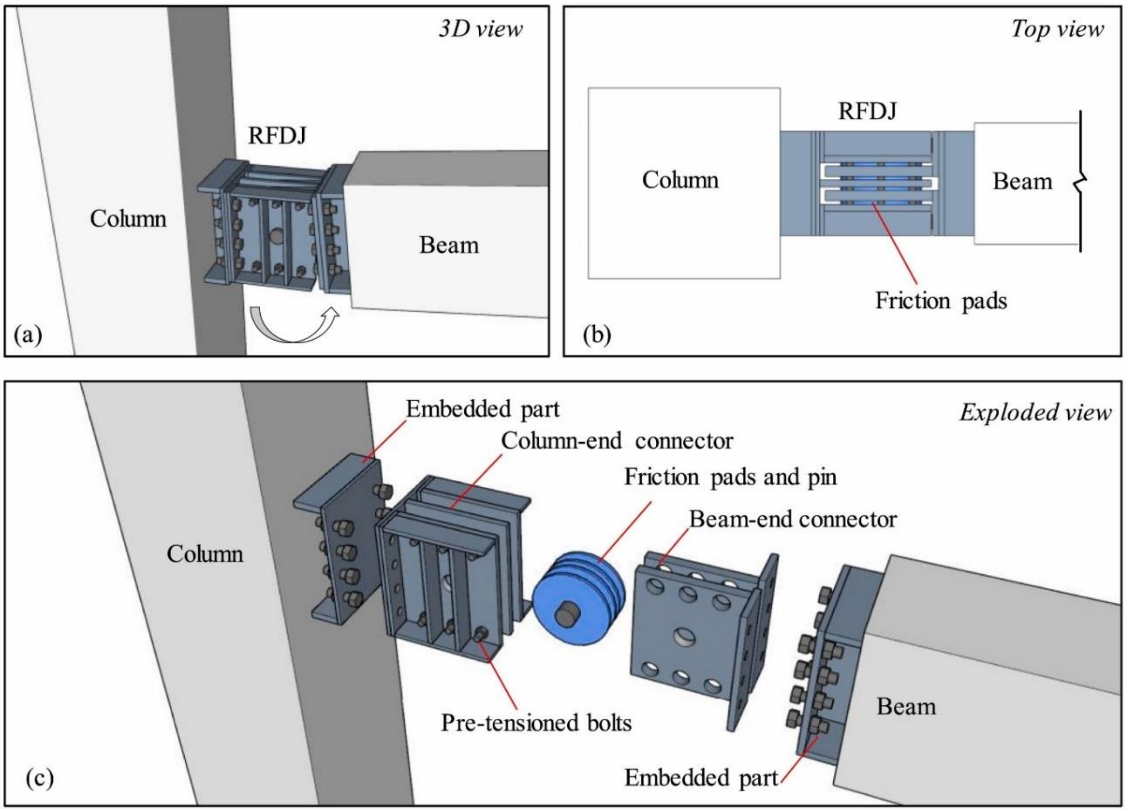

Figure 2.16 Configuration of DRFDBJ proposed by Yang et al. [124].

Dowel shear connections are a commonly used method for connecting beams to columns in precast concrete construction [92]. This preference is mainly due to the numerous advantages that dowel-type connections offer, including rapid and easy on-site assembly, minimal labor requirements, reduced sensitivity to adverse weather conditions, and enhanced transportability of structural elements. These features make dowel shear connections especially favorable for modern prefabricated systems where efficiency and modularity are critical.

Typically, in dowel shear connections, beams are manufactured with holes that align with the column's protruding threaded rods (dowels). These rods are fastened with bolts, and the annular voids between the dowels and holes are subsequently filled with grout to ensure mechanical interlock and load transfer. Although grout is used in limited quantities, the presence of mortar classifies these joints as semi-dry connections, as they do not fully meet the criteria for dry, fully demountable systems.

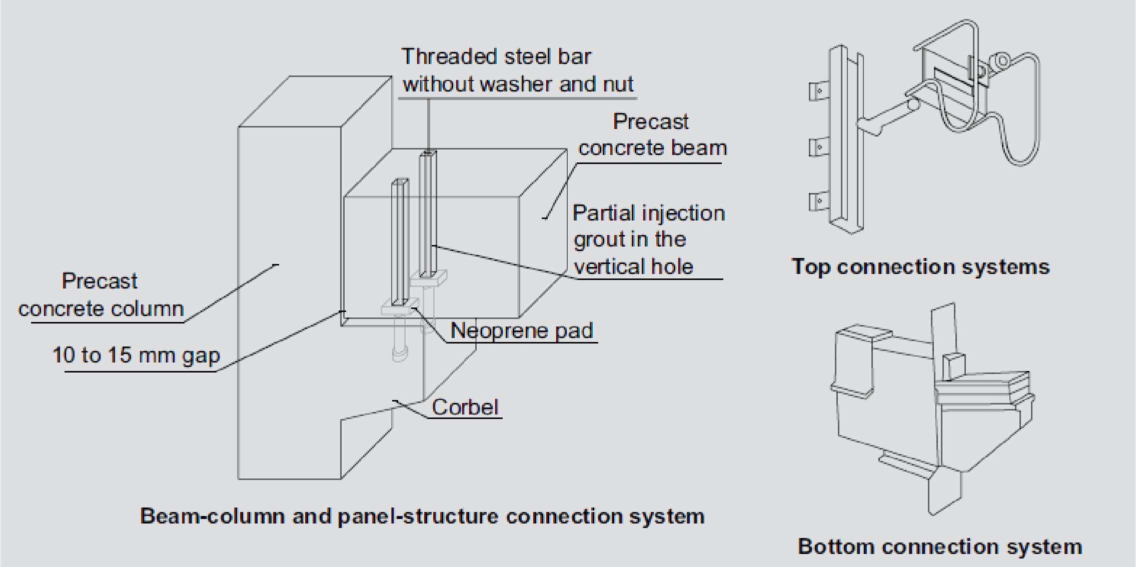

Figure 2.17 Typical pin shear beam-column connection [125]

Psycharis and Mouzakis [126] conducted an in-depth study on the shear ductility and load-bearing behavior of dowel-type beam-column joints under monotonic and cyclic shear forces. The research emphasized the effects of several design variables, such as dowel diameter (D), quantity of dowels, concrete cover thickness along and across the beam axis, and grout compressive strength, as shown in **Figure 2.18**. The results indicated that connections with low d/D ratios exhibited significantly lower tensile resistance than compressive resistance, under monotonic and cycling loading. This behavior was attributed primarily to the premature cracking of the concrete cover surrounding the dowels. Moreover, the connections subjected to cyclic loading demonstrated less than half the strength compared to those tested under monotonic loading conditions. Despite this reduction, the authors noted that adequate concrete cover around the dowels was critical in achieving satisfactory shear ductility during cyclic testing. Additionally, the application of high-strength grout contributed substantially to improved joint performance. Specifically, it enhanced the bond strength, reduced slippage, and increased ductility, strengthening the connection’s overall response under cyclic loading.

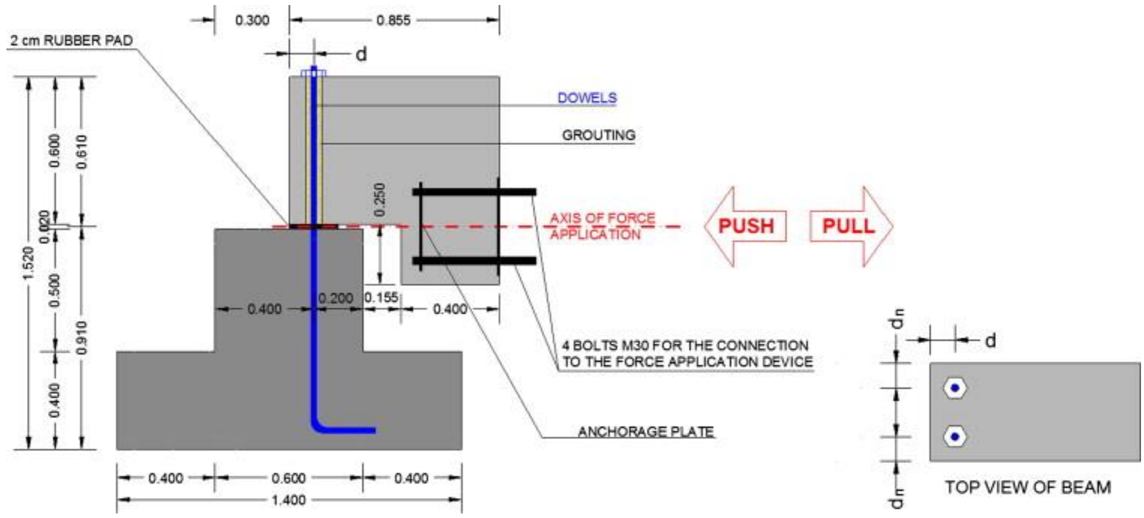

Figure 2.18 General layout of the specimens. [126]

Magliulo et al. [127] conducted a numerical investigation on the shear resistance of dowel-type beam-to-column connection as illustrated in **Figure 2.19**, assessing the effects of different geometric and material variables. The numerical results were validated by comparing them with experimental data, confirming the accuracy of the model. The study revealed that when the concrete cover thickness in both front and lateral directions is less than approximately 6–7 times the dowel diameter, concrete splitting failures are likely to occur under both tensile and compressive loading conditions. Furthermore, it was noted that lateral splitting tends to occur more frequently when the side concrete cover is equal to or smaller than the front cover. In contrast, concrete cracking was predominantly observed in the bottom zone under compressive loading only when the lateral cover exceeded the front cover. These findings underscore the importance of appropriately detailing concrete cover in dowel connections to avoid premature brittle failures and ensure adequate performance under multidirectional load demands.

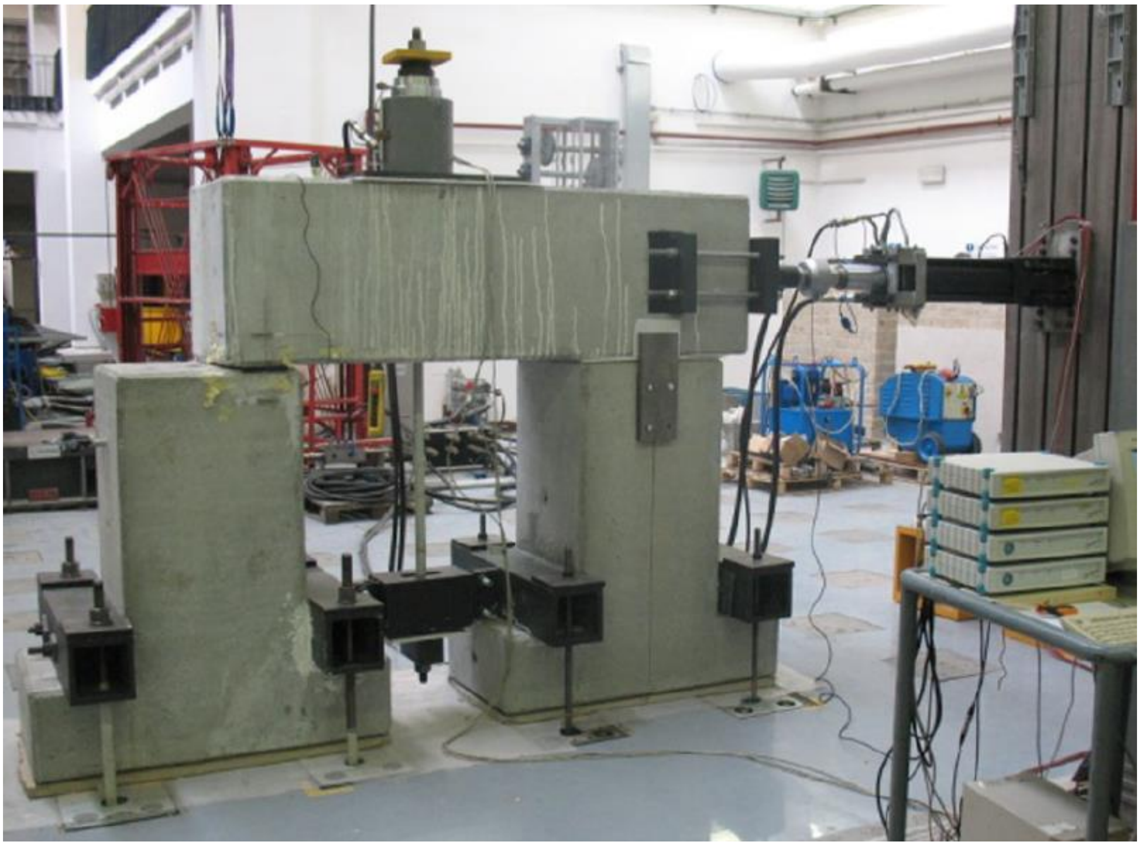

Figure 2.19 Shear test experimental setup [127]

As part of the SAFECAST Project, Bournas et al. [128] and Negro et al. [129] executed full-scale pseudo-dynamic experiments on a three-story precast concrete building designed with four different layout arrangements. The research aimed to assess the seismic behavior of various dry mechanical joints, including slab-to-slab, slab-to-beam, wall-to-structure, column/wall-to-foundation, and beam-to-column connections, with particular emphasis on the response of beam-column joints and floor diaphragms.

Two distinct beam-to-column connection types were utilized across different configurations:

- Dowel-type pinned beam-to-column connection (representing a hinged joint),
- Innovative emulative moment-resisting beam-to-column connection (mimicking monolithic behavior).

The experimental consequences emphasized the significance of connection style and diaphragm stiffness in governing global seismic behavior. The moment-resisting connections demonstrated improved energy dissipation and inter-story drift control compared to the pinned counterparts, especially under higher seismic intensities.

In a related study, Brunesi et al. [125] tested a 0.75 scale, two-bay, three-story precast frame under pseudo-static cyclic loading. To examine the impact of cladding on the seismic response of pinned dowel-type BCCs, two frame configurations were constructed: one with PC cladding panels and one without. While appropriate structural detailing was found to reduce local damage at connection points and corners, the overall seismic response of this frame typology was deemed insufficient. The system exhibited a nearly elastic–brittle global behavior, a consequence of the structural scheme and limitations inherent to the dowel-type connection system. As a result, the study concluded that such precast solutions should be avoided in high seismic hazard regions.

Aguiar et al. [130] explored the mechanical strength of dowels used in dowel-type shear connections through a combined experimental and theoretical investigation. A total of 15 test specimens as presented in **Figure 2.20** were designed to assess various parameters, including dowel diameter, dowel inclination, concrete compressive strength, and the presence of axial load applied perpendicular to the interface. The findings demonstrated that increasing dowel inclination enhanced shear capacity, while axial compression significantly influenced the performance of inclined dowels. These observations underscore the necessity of incorporating realistic boundary conditions in both design and testing of dowel-based connections.

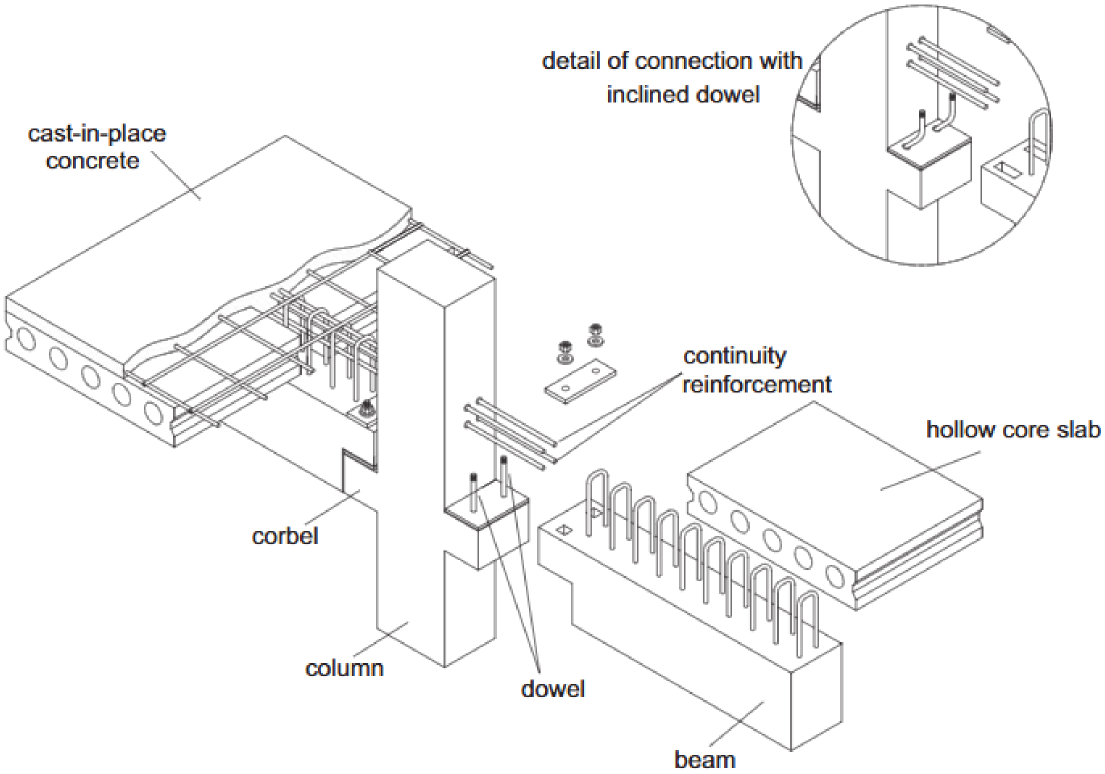

Figure 2.20 BCC with perpendicular and inclined dowels [130]

In the study by Zoubek et al. [131], both tests and simulations were performed to examine the behavior of dowel-type shear connections under cyclic and monotonic loading. A validated finite element model was created in ABAQUS, grounded in the experimental findings. The findings from the study revealed that:

- BCC strength is highly based on the plastic hinge depth;
- Under cyclic loading, a lower plastic hinge depth resulted in significantly reduced strength;
- The inclusion of neoprene buffers was effective in enhancing connection capacity;
- When excessive rotation occurred between the beam and the column, cyclic strength was observed to drop by 15–20%.

Building on this work, Kremmyda et al. [132] developed a three-dimensional FE model to simulate the characteristics of dowel-type connections under both monotonic and cyclic shear loads. This model was validated against experimental results, which confirmed the presence of expected failure mechanisms such as localized concrete crushing around the dowels and bending yield of the steel dowels. Analytical observations indicated that:

- Plastic hinges tended to form near the beam-column interface with an approximate length of 5–10 cm;
- Under cyclic loading, hinge zones were shorter than in monotonic loading scenarios;
- As hinge length decreased, connection strength diminished;
- Transverse reinforcement at the beam's base and the column's top significantly influenced joint performance.

Later, Kremmyda et al. [133] conducted a parametric numerical study to develop a predictive formula for evaluating the cyclic strength of dowel-type connections. Their findings showed that the failure mode shifted toward brittle behavior when the concrete cover thickness around the dowels was insufficient. However, including reinforcement confinement around the dowels transformed the failure mechanism from brittle behavior to ductile response. The study also revealed that:

- Monotonic strength was approximately twice the cyclic strength;
- The strength of the joint was proportionally impacted by the square root of the material strengths (grout, concrete, steel);
- The number of dowels affected the capacity linearly, while dowel diameter had a quadratic effect;
- Increasing the thickness of the elastomeric buffer reduced peak strength but increased the ultimate displacement capacity;
- The ratio of concrete cover to dowel diameter influenced strength beyond a critical threshold.

Kang and Lee [134] presented a full-size experimental investigation of non-emulative precast concrete BCC incorporating post-tensioned bolts as observed in **Figure 2.21**. Five beam-to-column specimens were analyzed under reversed cyclic lateral displacements to evaluate their seismic efficiency. The test matrix included two monolithic connections as reference specimens, allowing for direct performance comparison with the precast alternatives. The study focused on main variables such as connection size, anchor nut diameter, and whether post-tensioning bars were used. Experimental findings revealed that the precast connections outperformed the monolithic ones regarding ductility and deformation capacity, demonstrating the potential for increased displacement resilience. However, the precast systems exhibited relatively lower EDC and were more prone to pinching effects under cyclic loading. Despite these limitations, the yielding mechanism of the anchorage bars and the observed high lateral drift capacity supported the conclusion that such precast beam-to-column connections could achieve satisfactory seismic behavior when used as a component of a moment-resisting frame system. The results contribute valuable insights into developing demountable and reparable structural systems for seismic regions.

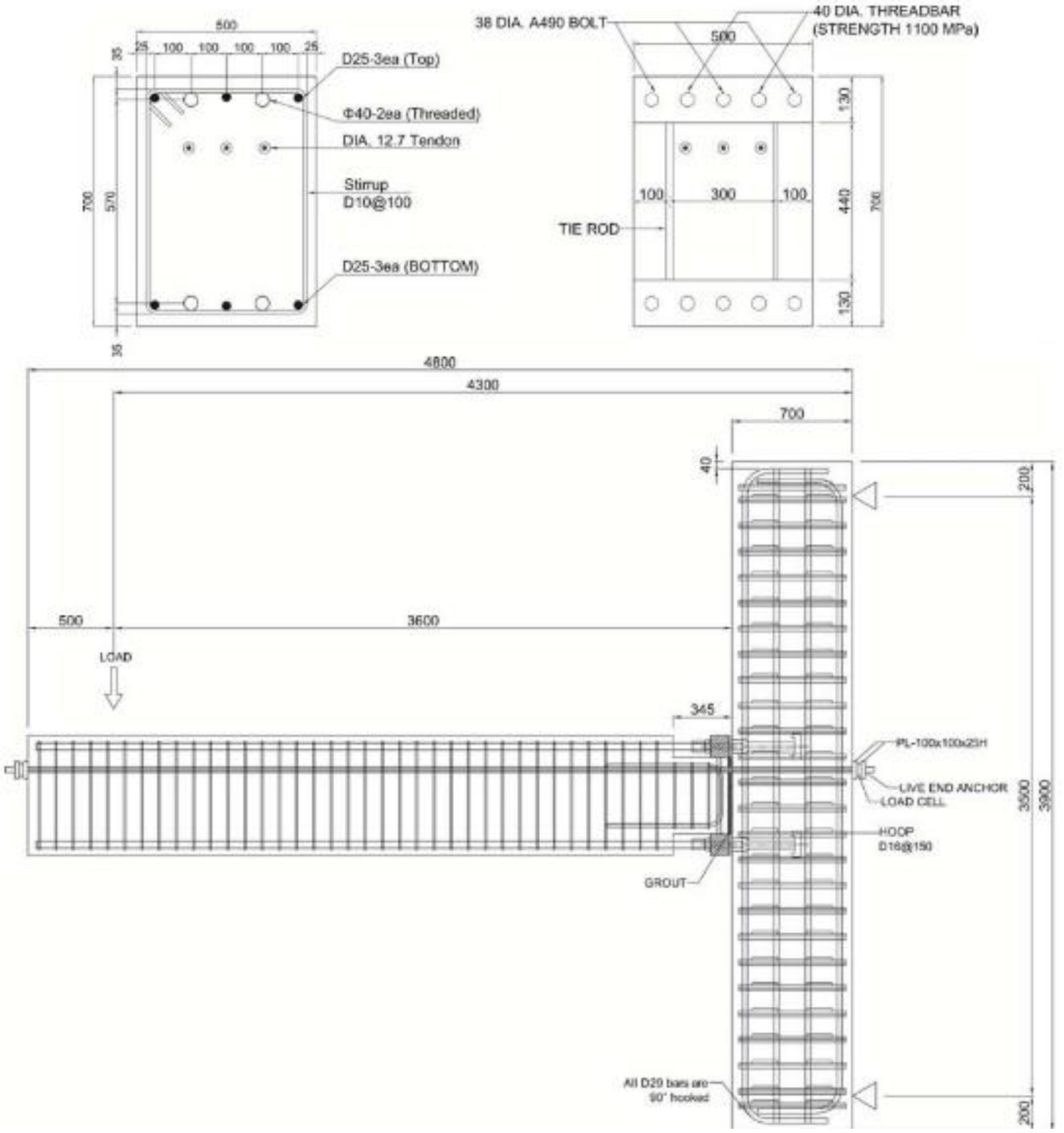

Figure 2.21 Specimen drawing details [134].

Aninthaneni and Dhakal [5] proposed a series of demountable steel connection types, comprising steel plates, angles, hollow sections, and bolts, for use in prefabricated structural systems. Their study discussed these connection types' practical applicability, advantages, and limitations under the context of structural demountability and post-earthquake reparability.

In the subsequent experimental study, Aninthaneni et al. [135] examined the seismic performance of three different dry steel BCCs as depicted in **Figure 2.22** under quasi-static cyclic loading. The tests aimed to evaluate the proposed systems' load resistance, deflection capacity, and EDC.

Among the tested configurations, Type 1 steel connection demonstrated superior structural performance, primarily due to its direct load path from the beam to the connection interface, which reduced stress concentrations and enhanced rotational stiffness. This behavior contrasted with the other connection types, where indirect force transmission mechanisms led to reduced overall efficiency. Based on experimental observations, the authors concluded that the precast concrete elements could reproduce the behavior of a cast-in-place RC frame closely interconnected through well-designed demountable steel joints. These findings highlight the potential of dry mechanical steel connections in achieving both seismic resilience and ease of post-event repair in modular construction systems.

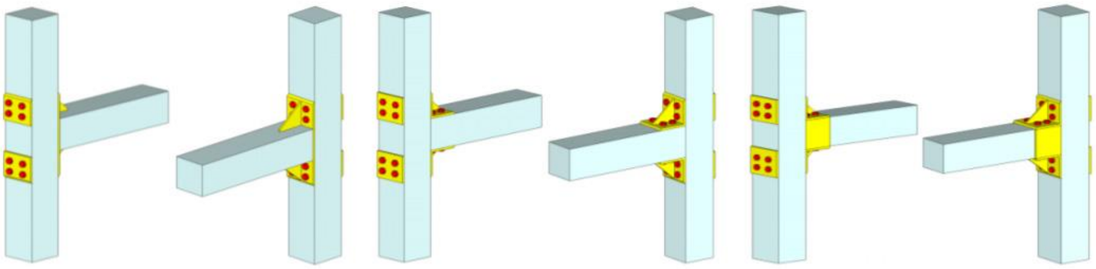

Figure 2.22 Dry steel beam-column connection types [135]

Navarro-Rubio et al. [136] concentrated on assessing the eco-efficiency and optimization prospects of prefabricated construction through the analysis of a newly introduced dry precast BCC as presented in **Figure 2.23** under various durability and service scenarios. The study incorporated a comprehensive assessment that included structural performance (via numerical modeling), optimization potential (in terms of material procurement, construction scheduling, and financial expense), and environmental concern, assessed using Life Cycle Assessment (LCA) methodologies. Numerical simulations involving incremental static loading demonstrated that, while the proposed dry connection exhibited lower structural performance compared to monolithic connections, it successfully met the required structural limit states. This indicates its suitability for practical implementation under specified design conditions. Moreover, the structural optimization analysis revealed that the proposed connection system significantly reduced labor hours and task duration by approximately 80% and shortened the overall construction timeline by 60%.

The reuse of prefabricated elements further contributed to a notable reduction in cumulative economic costs over the building's lifecycle. These findings emphasize the potential of dry mechanical joints not only in facilitating demountability and reuse but also in enhancing economic viability and environmental sustainability in prefabricated concrete construction.

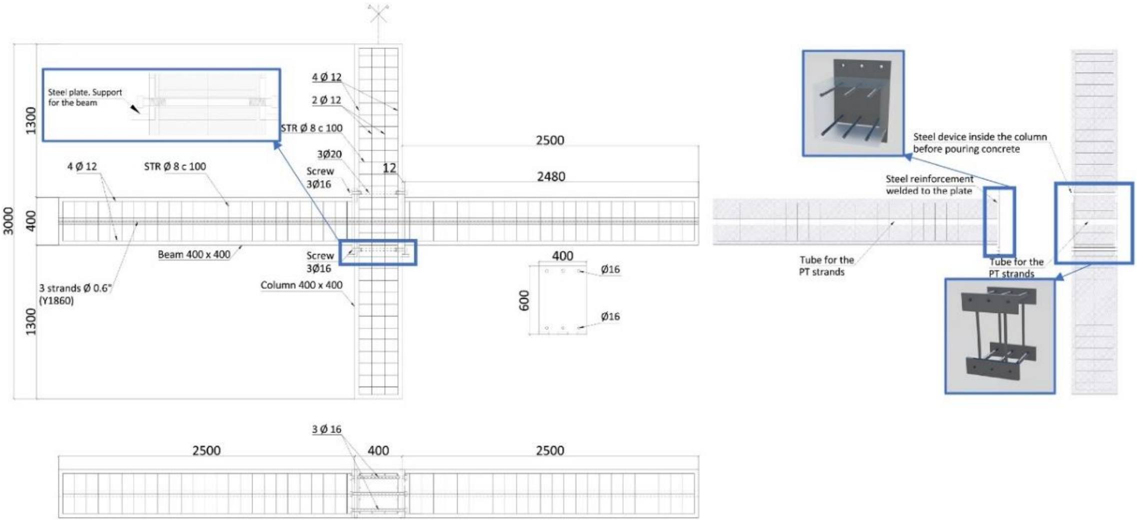

Figure 2.23 Steel beam-column connection types [136]

Baghdadi et al. [137] developed, tested, and numerically analyzed five innovative dry beam-to-beam and three dry BCC, inspired by traditional woodworking techniques and interlocking wooden puzzles as illustrated in **Figure 2.24**. These novel connection geometries aimed to facilitate demountability while maintaining structural integrity under service and ultimate loads.

The complex joint geometries were realized using 3D-printed molds, into which Ultra-High-Performance Fiber-Reinforced Concrete (UHPFRC) with self-compacting and reinforced properties was cast. To enhance the mechanical efficiency of the samples, post-tensioning was applied to the concrete segments before subjecting them to flexural loading. Experimental findings revealed that in beam-to-column configurations, failure occurred away from the contact region, i.e., in the beam itself, once the beam's flexural capacity was exceeded. This result confirmed the robustness and reliability of the proposed dry joints under loading, demonstrating their potential for use in modular and demountable precast concrete systems.

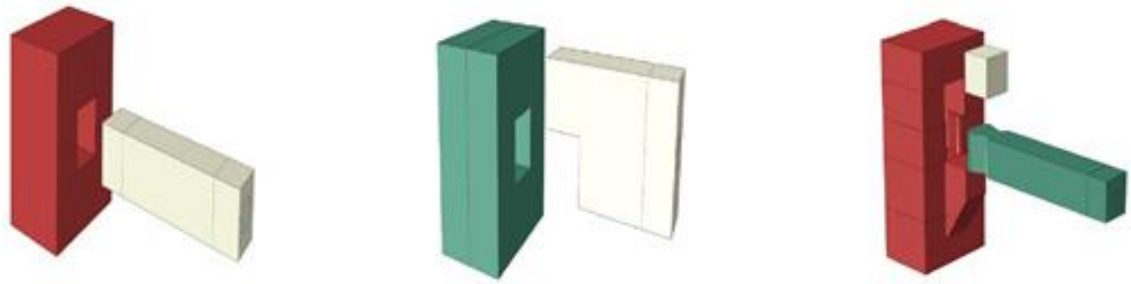

Figure 2.24 Different type of beam column connection [137]

Bao and Li [138] introduced an innovative structural concept inspired by LEGO blocks as demonstrated in **Figure 2.25**, wherein interlocking concrete units were fabricated from bendable (ductile) concrete and connected through dry joints without adhesives or mortar. The proposed system was designed for rapid assembly, easy disassembly, and reusability, features that align with sustainable and demountable construction principles.

The authors constructed a pedestrian bridge prototype using these interlocking concrete units to validate their concept. The assembled bridge was subjected to post-tensioning via prestressed tendons to enhance structural integrity and minimize crack formation under load. Mechanical testing demonstrated that the bridge exhibited adequate stiffness and load-bearing capacity, verifying its viability for pedestrian use. Following the tests, the entire structure was disassembled and reconfigured, showcasing its adaptability for reuse in various structural frameworks. The study emphasized that this LEGO-inspired construction technique offers a more environmentally friendly alternative to conventional building methods due to its ease of assembly, disassembly, and reconfiguration, as well as its potential to reduce construction waste and extend material lifecycles.

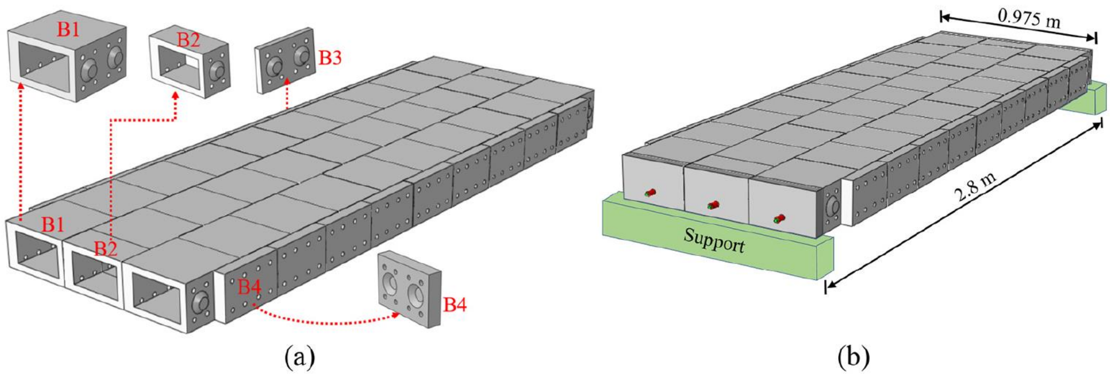

Figure 2.25 Drawing of a pedestrian bridge made of building blocks inspired by Lego [138]

Zhou et al. [139] explored the structural design and robotic assembly of interlocking concrete blocks inspired by LEGO construction principles as illustrated in **Figure 2.26**, aimed explicitly at potential applications in lunar habitat construction. The study focused on developing modular, dry-joint concrete units that could be assembled without the need for formwork or wet materials, making them highly suitable for use in extraterrestrial environments where traditional construction methods are not feasible.

The proposed lunar shelter system was evaluated under extreme environmental conditions, such as low gravity and high thermal fluctuations, and demonstrated satisfactory structural performance. Moreover, the study successfully implemented automated robotic assembly techniques, which enabled high-precision placement and alignment of the modular blocks. This robotic construction approach supports autonomous building capabilities, reducing human involvement and increasing construction efficiency in remote or hazardous environments. The findings highlight the potential of LEGO-inspired modular dry construction not only for Earth-based sustainable applications but also for future off-planet habitats, where rapid, reusable, and automated building systems are essential.

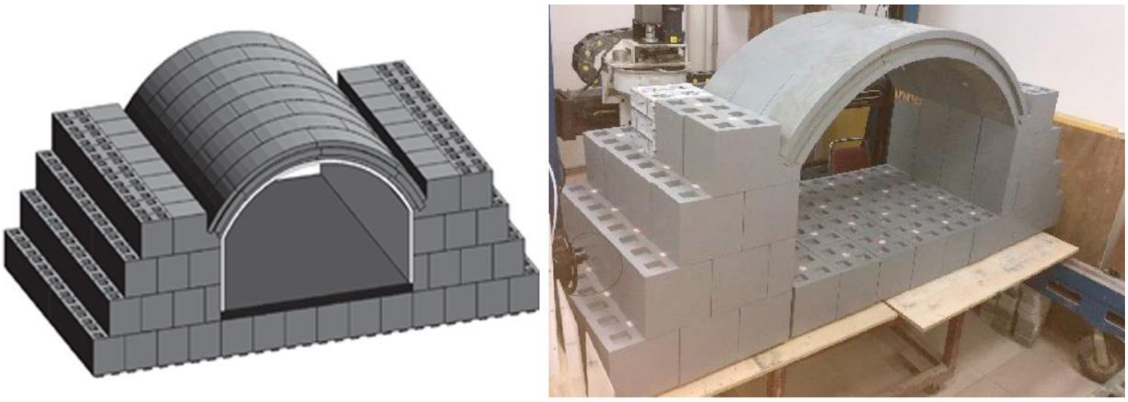

Figure 2.26 LEGO-inspired modular dry construction [139]

As evidenced by the review of existing studies above, a limited number of full-scale experimental research focus on the structural feasibility and building efficiency of demountable RC systems through dry mechanical connections [140]. While several studies have investigated BCC under monotonic and cyclic loads, dry column-to-foundation connection details are notably absent in current research.

Nevertheless, it may be inferred that specific beam-to-column dry connection mechanisms, such as those developed by Pul and Şentürk [141] and Aninthaneni et al. [142], could be adapted for column-to-foundation applications. These studies provided promising results for dry connections using bolted steel interfaces and mechanical joints, which, if appropriately reconfigured, may also offer viable solutions for foundation-level demountable designs.

The integration of dry-type connections with CDW-based geopolymer concrete represents a critical advancement toward sustainable prefabrication practices. Geopolymer concrete, particularly when produced using recycled aggregates and construction and demolition waste (CDW), offers considerable environmental benefits by significantly reducing CO_2 emissions, energy consumption, and natural resource depletion. Nevertheless, the use of alkali-activated binders introduces logistical and handling challenges for in-situ applications, positioning precast production with dry connections as the most feasible and scalable construction method. This combination not only eliminates site-related limitations but also enables the fabrication of fully reusable structural components, as demonstrated by recent full-scale pilot implementations. In this regard, dry connections serve as a transformative mechanism that bridges the gap between laboratory-scale material innovation and real-world modular construction solutions. Especially in seismic zones, where the possibility of structural reconfiguration or post-earthquake retrofitting is high, the ability to assemble and disassemble structural members without compromising performance becomes both a technical requirement and an environmental imperative.

While the existing literature provides valuable insights into the behavior and benefits of dry connection techniques in precast concrete systems, most studies have focused on conventional Portland cement-based materials, with limited research addressing their integration with geopolymer concrete, particularly those incorporating CDW. Furthermore, earlier works have predominantly emphasized structural performance, often overlooking aspects such as demountability, reusability, and practical constructability. To address these gaps, the present study introduces a novel experimental investigation into fully demountable structural connections fabricated with CDW-based geopolymer concrete. Unlike prior research, this study not only evaluates the seismic behavior and energy dissipation characteristics of the proposed systems under cyclic loading but also highlights their potential for easy assembly and disassembly, long-term durability, and reuse, all aligned with circular construction principles. Half-scale specimens were tested under displacement-controlled loading regimes and benchmarked against conventional monolithic and wet-connected counterparts. The outcomes of this research contribute a meaningful step toward the development of structurally viable and environmentally sustainable prefabricated systems.

EXPERIMENTAL PROGRAM

This chapter presents a comprehensive description of the materials, test setup, and experimental procedures employed in the column, beam, and slab tests. The geometrical properties of the specimens, reinforcement configurations, fabrication process, components of the loading setup, and the loading protocols are systematically outlined to ensure the reproducibility and accuracy of the experimental data.

Since the target of this study is a low-rise building, lateral stiffness is provided solely through the columns. Given that the column-to-foundation connection are designed as fixed supports, while the beams and slabs are modeled as pinned connections, the majority of the study will concentrate on the design and experimental investigation of demountable column connections. The beam and slab systems will be addressed only briefly.

3.1. Prototype Structure

The structural plan presented below corresponds to a single-story building constructed in the Ankara region. As a reference specimen, column S107 was selected.

According to TS500, the clear spacing between bars in columns must not be less than 1.5 times the bar diameter, 4/3 of the maximum aggregate size, or 40 mm, whichever is greater. Therefore, when the dimensions of the column and reinforcement are scaled down by a factor of 1/2, a new column cross-section detail will be designed to meet these requirements and to facilitate construction. In designing the new cross-section, particular attention will be given to ensuring that the interaction diagram of the scaled column remains identical to that of the primary, and that the reinforcement percentage is preserved as closely as possible.

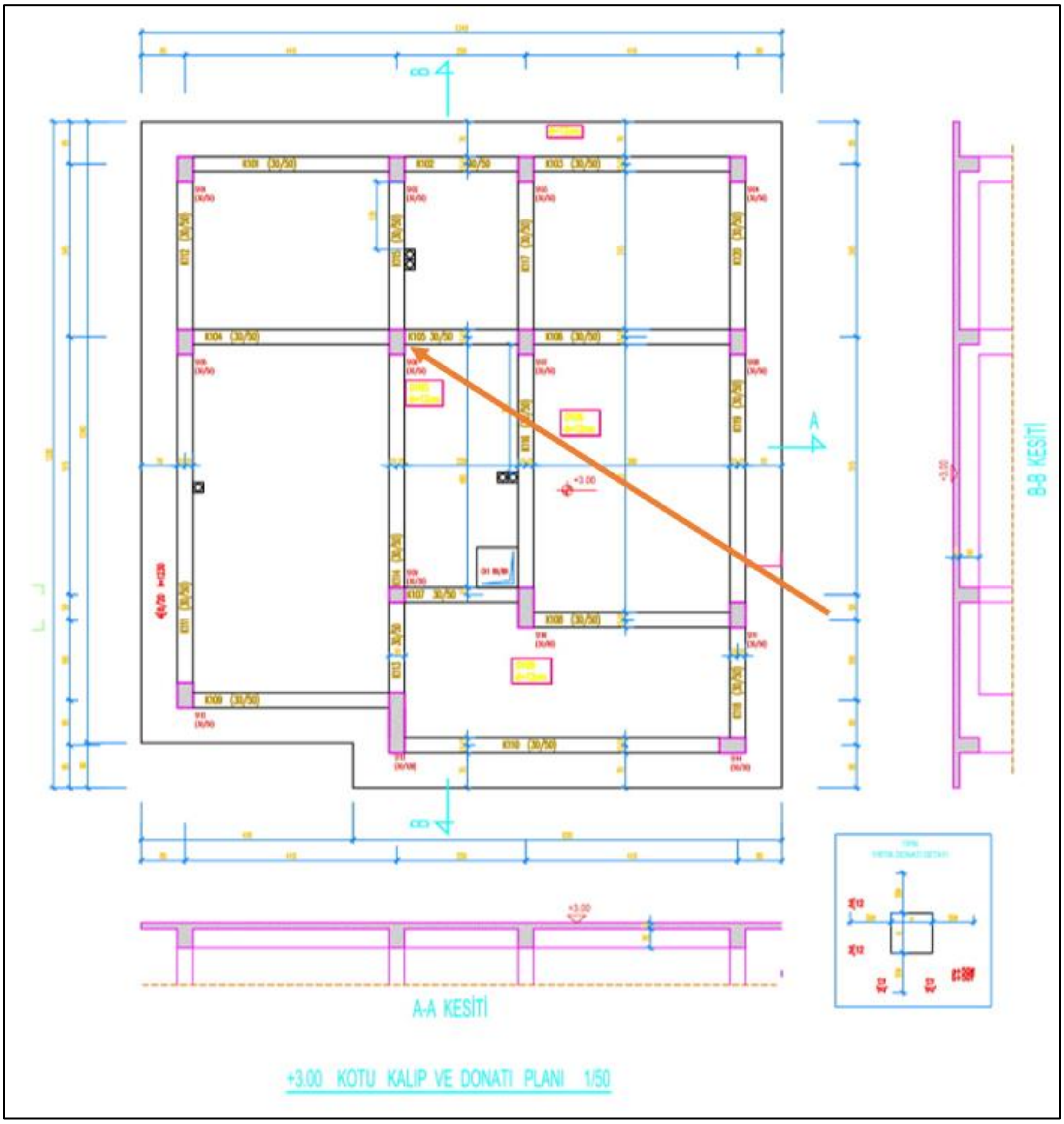

Figure 3.1 Formwork and reinforcement plan +3.00 elevation

The building under investigation is situated on a Z4-class soil characterized by weak and loose ground conditions. For the experimental study, column S107 was selected as the test specimen. The column will be tested in the strong axis direction, where its moment capacity is maximized. The column height is set to 3 meters. To examine the influence of axial loading, three different normalized axial load levels will be applied during testing: $P/(A_g*f_{ck})$: 0.0, 0.1, 0.2, 0,3. These load ratios are selected to represent varying levels of axial force typically encountered in structural applications.

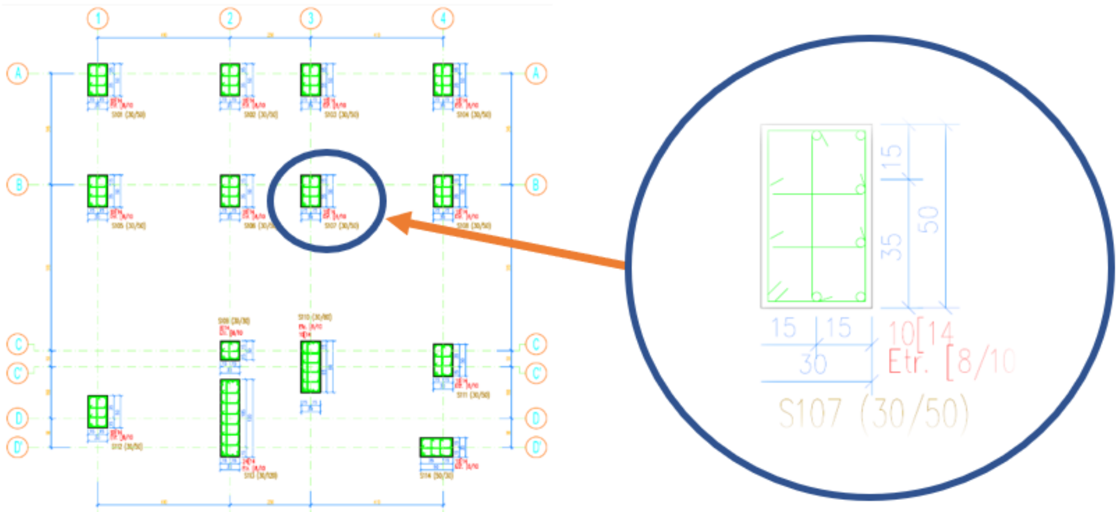

Figure 3.2 Selected S107 column reinforcement detail

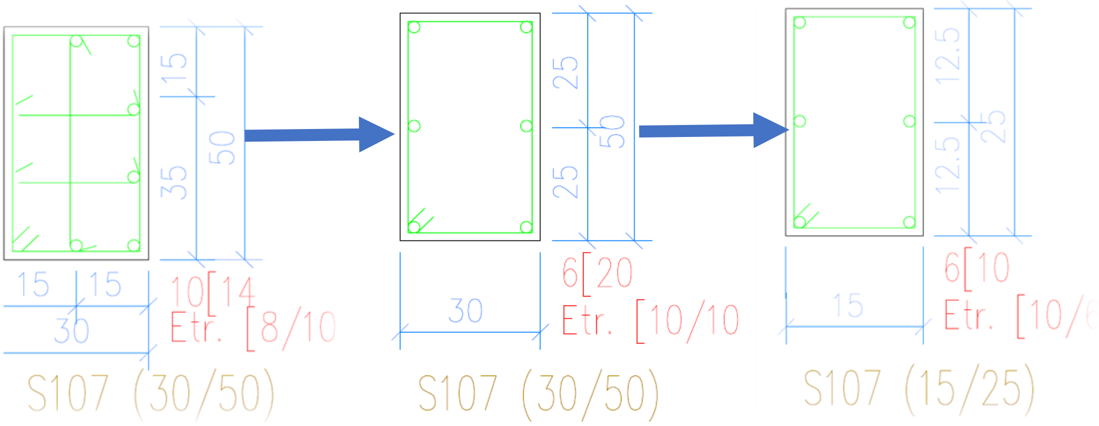

a) Reference column b) Modified column c) Test column scaled with 0.5

Figure 3.3 Scaling of test column reinforcement detail

The reinforcement detailing of the modified column is demonstrated in the picture above. According to the Turkish Seismic Code (TEC2018), if the spacing between longitudinal reinforcement bars is less than 25 times the bar diameter (25d), the use of tie wires may not be required, so to simplify construction and improve workmanship, tie wires were intentionally omitted in this design. When the reinforcement used for stirrups in the original column is considered, the overall reinforcement ratios of both sections have been adjusted to remain closely comparable.

The interaction diagrams were calculated using the SAP2000 software. In the SAP2000 modeling, the concrete material was specified as C25, and the yield strength of the reinforcement was assumed to be 420 MPa. Since these material properties were implemented identically to both columns, any potential difference in their actual strengths did not lead to inconsistencies in the comparative analysis.

A_0f_c= 300*500*25/1000=3750 kN (axial load capacity)

P/ A_0f_c =0.1=375 kN

P/ A_0f_c =0.2=750 kN

P/ A_0f_c =0.3= 1125 kN

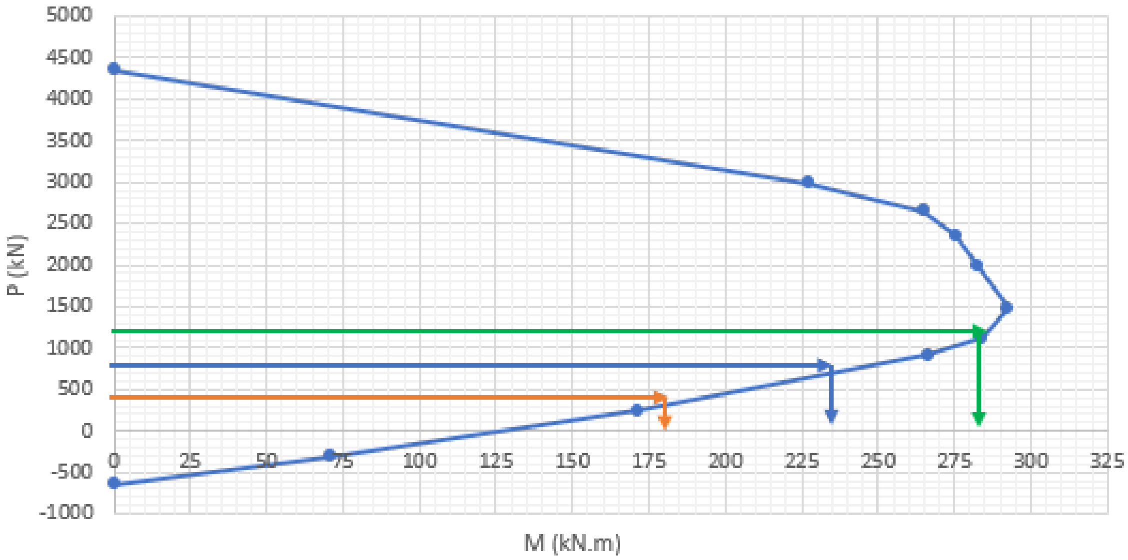

Figure 3.4 Selected S107 column axial load-moment response diagram in strong direction

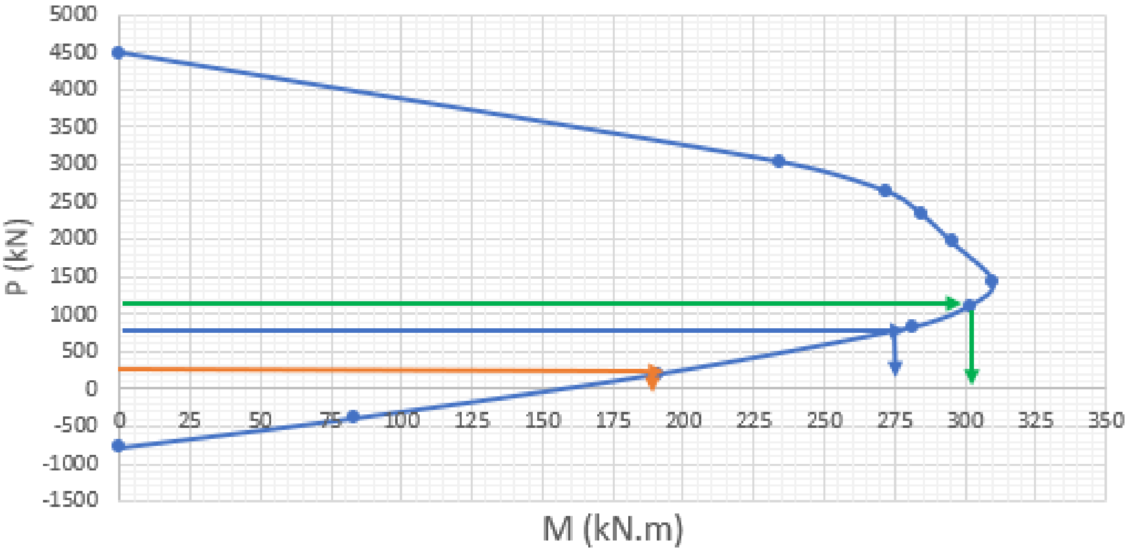

Figure 3.5 Modified column axial load-moment response diagram in strong direction

As shown in the two graphs above, a comparison between the modified column and the S107 column indicates that the modified column exhibits slightly higher capacity. This approach ensures a conservative design while also avoiding excessive overdesign.

All geometric lengths and reinforcement bar diameters of the test column were scaled down by a factor of 0.5. Although 5 mm diameter stirrups were initially specified, 6 mm bars were used instead due to the limited availability of 5 mm bars and their brittle and hard-to-handle nature. The mechanical characteristics of the selected reinforcement bars were verified through tensile tests, and the results confirmed that the bars were suitable for use and closely matched the intended design parameters.

3.2. Experimental Study on a Demountable Column Base Connection for Green Concrete

This section presents the experimental program, which combines three separate studies related to the design and testing of demountable columns.

3.2.1. Material properties

3.2.1.1. CDW Based Geopolymer Concrete

3.2.1.1.1. Background of geopolymer concrete mixture

The development of novel construction materials that are environmentally friendly has the potential to significantly reduce greenhouse gas emissions, optimize the utilization of CDW, enhance the durability of structures, improve material recyclability, and foster sustainable development. Despite several studies yielding positive results in the realm of CDW recovery [19, 20, 30], these approaches have not gained widespread acceptance in the construction industry due to lack of accurate information and trust, variability of quality and reluctance of final consumers. On the other hand, the generation of tremendous amounts of CDW, the negative impacts of the Portland cement production on the environment, and green transformation initiatives increasingly push the CDW to participate in the circular economy in the construction sector. In this context, novel geopolymer concrete mixtures were designed with the use of various CDW-based materials as the precursor and aggregate phase. The detailed methodology and results of the developed CDW-based geopolymer concretes are presented in following sections.

3.2.1.1.2. Precursors

Building demolition typically generates large volumes of construction and demolition debris, including masonry elements (such as red clay bricks (RCB), hollow bricks (HB), and roof tiles (RT)), along with concrete (C) and glass (G) waste. These CDW materials were collected from a demolition site in Turkey. CDWs were first exposed to the grinding process via a jaw crusher for early size reduction. Then they were ground via a ball mill for 60 min to bring the particle size to a suitable fineness for the geopolymerization. Visuals of the CDW materials in raw and milled states, as well as their corresponding particle size distributions, were presented in Error! Reference source not found. and **Figure 3.7**, respectively. According to **Figure 3.7**, the masonry units demonstrated comparable fineness due to the same crushing and grinding process, while G was the coarsest material. Considering the fact that grinding CDWs without separation will be advantageous in terms of energy intake and discharge in their future use for mass production, no extraordinary regard was paid to bringing the CDWs to the same fineness degree. In addition, F-class FA and GGBFS were also utilized in the composition.

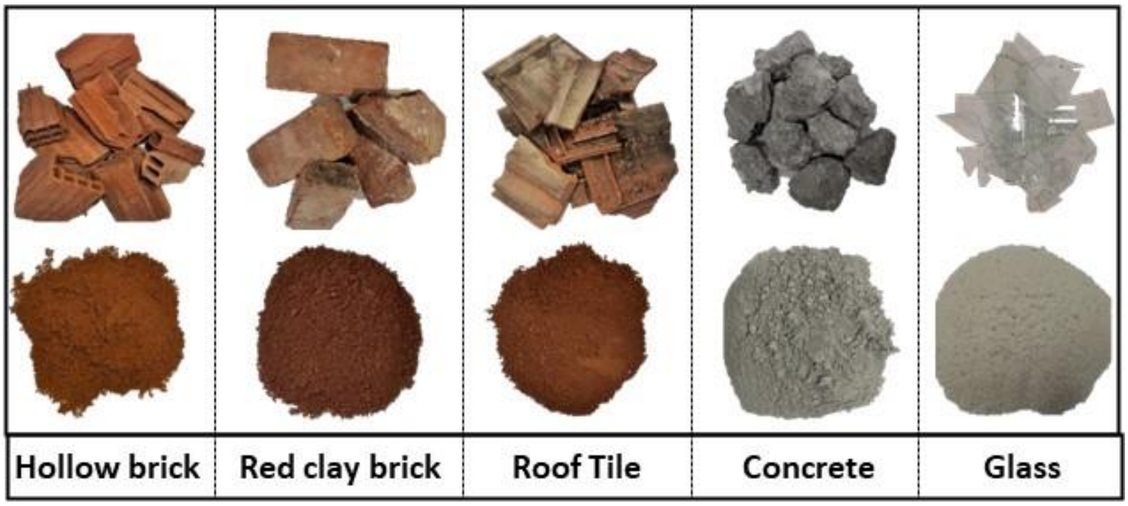

Figure 3.6 Images of the CDW-based materials.

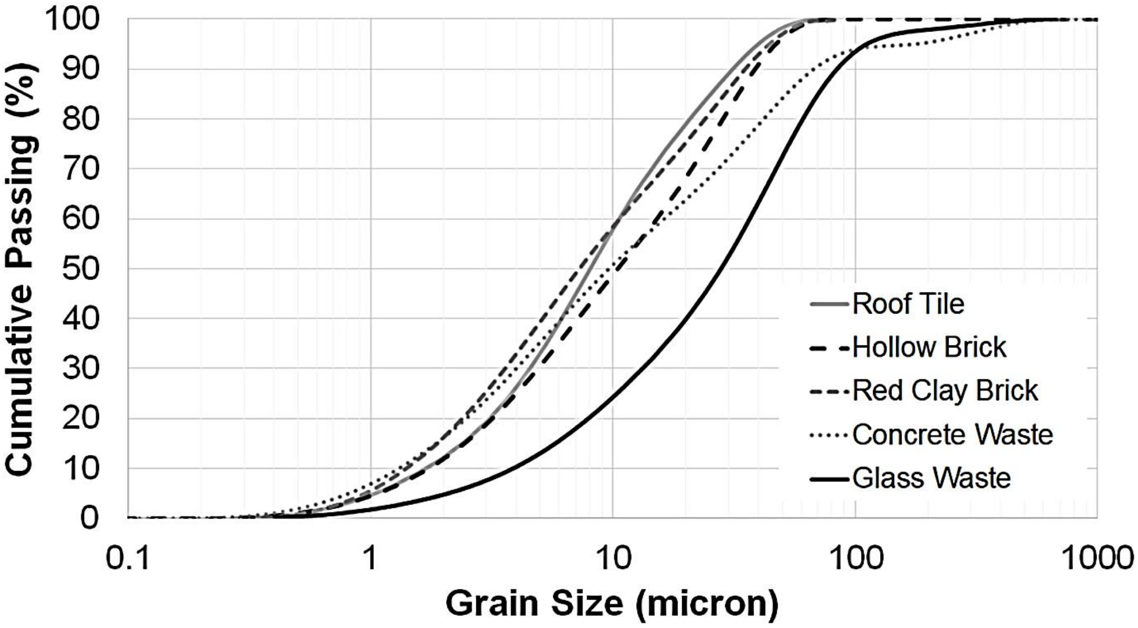

Figure 3.7 Particle size distributions of the CDW-based materials.

The chemical composition of CDWs was defined by performing XRF analysis with the wavelength of 0.1–50 Å and laser diffraction technique with the size range sensitivity of 0.02–2000 µm on the oven-dried powders, and the outcomes are presented in **Table 3.1**. As can be seen in **Table 3.1**, the chemical composition of the masonry units, especially the amount of Al_2O_3, SiO_2, and Fe_2O_3, is very suitable in terms of geopolymerization reactions. On the other hand, while the G has the highest amount of SiO_2 among other CDWs, it was determined that C contains a high amount of SiO_2 and CaO.

Table 3.1 Chemical composition of the precursors (units are in %).

Materials	SiO_2	Al_2O_3	Fe_2O_3	CaO	MgO	SO_3	TiO_2	K_2O	Na_2O	LoI*
HB	39.7	13.8	11.8	11.6	6.45	3.40	1.65	1.55	1.45	7.80
RCB	41.7	17.3	11.3	7.69	6.49	1.41	1.57	2.66	1.15	7.96
RT	42.6	15.0	11.6	10.7	6.26	0.71	1.82	1.60	1.60	7.49
C	31.6	4.76	3.50	31.3	5.12	0.92	0.24	0.71	0.45	20.9
G	66.5	0.93	0.25	10.0	3.93	0.24	0.06	0.20	13.6	4.15
FA	60.1	21.4	7.41	0.99	1.82	0.22	0.94	2.91	0.99	2.61
GGBFS	32.1	11.2	0.62	36.1	5.64	1.21	1.07	0.83	0.31	9.09

*: Loss on ignition.

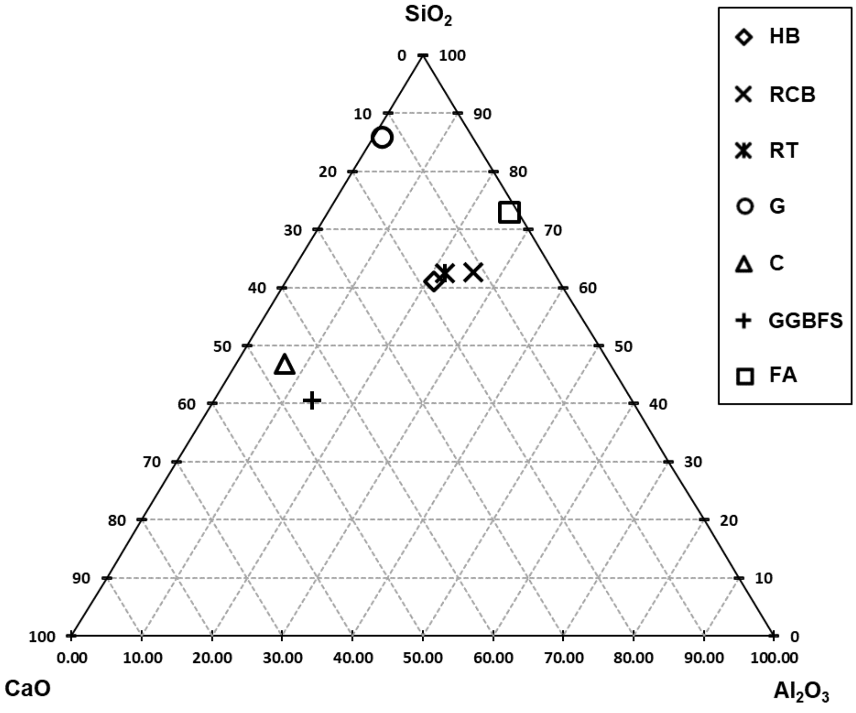

Figure 3.8 Ternary diagram of CDW-based materials according to their chemical composition.

100% RCA achieved from the grinding of concrete waste via a jaw crusher was used in the mixtures. RCA was crushed into coarse RCA (CRCA) and fine RCA (FRCA) by adjusting various jaw crusher openings to ensure an ideal gradation curve. In addition, the physical characteristics of RCA utilized in this research are given in **Table 3.2**.

Table 3.2 Physical properties of the RCA.

Property	**RCA size (mm)**	
	16.00-4.75	**4.75-0.00**
Dry specific gravity (g/cm^3)	2.23	1.86
SSD* specific gravity (g/cm^3)	2.32	2.11
Apparent specific gravity (g/cm^3)	2.46	2.51
Water absorption (%)	4.20	13.8
Loose unit weight (g/cm^3)	1.22	1.44
Dense unit weight (g/cm^3)	1.35	1.58

*: Saturated surface dry

Sodium hydroxide (NaOH), sodium silicate (Na_2SiO_3), and calcium hydroxide ($Ca(OH)_2$) were employed as alkaline activators in the geopolymer concrete production process. NaOH was solid and in flake shape with a 98% purity grade, and $Ca(OH)_2$ was also solid and in pulverized shape and had a purity grade of 87%. Na_2SiO_3 was in liquid form with a boiling point of 40. In addition, city water was used as the water phase of the geopolymer compositions.

The mixture ratios of all constituents in the CDW-based geopolymer concrete are detailed in **Table 3.3**. In CDW-based GPC design, the use of CDWs in mixed form rather than single-use was made considering the following purposes: i) better simulation of actual field conditions where the CDWs are in mixed/unseparated form, ii) providing the formation of different geopolymeric gel structures that will enhance strength due to the varied chemical composition of CDWs, and iii) instead of dumping some CDWs into landfills, providing the optimum valorization of each type of CDW. The mixture proportions were determined based on the authors' previous studies [18, 19, 23]. The geopolymer mixtures were produced by next steps: (i) NaOH flakes were dissolved in water to prepare the solution, which was then left to stabilize at room temperature for a day, accounting for workability reduction caused by the heat released during the exothermic reaction [143], (ii) dry mixture including CDW-based precursors, FA, GGBFS and RCAs were mixed in a 50-liter capacity mixer until the obtain homogeneous dry mixture, (iii) later on, the NaOH solution was slowly added to the mixer in 60 seconds and mixed for an additional 120 seconds, (iv) liquid Na_2SiO_3 was slowly added to the mixer in 60 seconds and mixed for an additional 120 seconds, (v) powder $Ca(OH)_2$ was added to the mixer and the admixture operation was finalized after the additional 120 seconds of blending. At the end of the blending phase, the prepared mixtures were placed into different formworks detailed following sections and cured in ambient conditions until the testing age.

Table 3.3 Proportions of ingredients for CDW-based GPC.

Mixture proportion (kg/m^3)												
HB	**RCB**	**RT**	**G**	**C**	**GGBFS**	**FA**	**$Ca(OH)_2$**	**NaOH**	**Na_2SiO_3**	**FRCA**	**CRCA**	**Water**
150	200	250	100	100	150	50	50	112	224	500	500	202.15

3.2.1.1.3. Alkali Activators

One of the critical parameters in the formulation of geopolymer concrete (GPC) compositions is the type and intensity of alkaline activators. In this study, three distinct activator systems were examined by varying their concentrations and combinations to identify the most effective activator type and phase composition. The mixtures exhibiting superior mechanical properties were selected as the basis for the final GPC formulations. $Ca(OH)_2$, NaOH, and Na_2SiO_3 were utilized due to their strong alkaline characteristics and their ability to establish a highly basic environment conducive to geopolymerization. Sodium hydroxide contributes to the dissolution of reactive species such as SiO_2, Al_2O_3, and CaO by providing the high alkalinity required for initiating the geopolymerization action. Sodium silicate supplies significant amounts of soluble silica (SiO_2) and sodium oxide (Na_2O), enhancing gel formation and accelerating the reaction kinetics. Additionally, calcium hydroxide improves the mechanical performance of the matrix by contributing to the development of secondary calcium silicate hydrate phases (C-S-H) and calcium aluminosilicate hydrate (C-A-S-H) gels, thereby strengthening the overall geopolymeric structure.

Based on extensive preliminary investigations aimed at optimizing the alkaline activator composition, the molarity of NaOH was chosen as 8 M. Na_2SiO_3 was incorporated at a dosage corresponding to twice the mass of sodium hydroxide. Additionally, $Ca(OH)_2$ was contained in the mixtures at 5% of the total binder content. In the context of geopolymer concrete incorporating recycled aggregates derived from CDW, the fine aggregates exhibited varying characteristics such as water absorption capacity, porosity, and the presence of adherent cementitious particles. Therefore, different aggregate gradations and binder-to-aggregate ratios were evaluated. Following extensive preliminary testing, a binder-to-aggregate ratio of 1:1 was adopted for the optimized mix design [18, 19]. The finalized geopolymer concrete mixture proportions are summarized in **Table 3.3** while further details can be found in the recent studies conducted by Yıldırım et al. [19] and Ulugöl et al. [18].

(a) NaOH (b) Na_2SiO_3 (c) $Ca(OH)_2$

Figure 3.9 Alkali Activators utilized in the mix design of CDW-based GPC

In certain cases, $Ca(OH)_2$ was also included along with NaOH and Na_2SiO_3 as an additional activator. The primary motivation behind incorporating calcium-based elements into geopolymer systems was to enhance the compressive strength levels achievable under ambient conditions**.** According to the collective research efforts of the authors in geopolymer designs, a specific mixture design was determined for geopolymer concrete that allows for the highest possible evaluation of CDW components, ensuring optimal structural performance [23, 75, 144, 145]. Furthermore, the selection of alkali-activator designs took into account environmental and cost considerations, ensuring that performance aspects such as efflorescence, porosity, and shrinkage are satisfactorily addressed at a structural level. Especially the efflorescence, the development of white salt deposits on material surfaces, can occur in alkali-activated materials due to excessive alkali ions reacting with airborne CO_2. It's influenced by factors like soluble silicates, unreacted alkalis, and the material's structure. Minimizing efflorescence involves reducing alkali leaching and promoting a denser matrix. In a previous study, the authors investigated efflorescence in CDW-based geopolymers and found that using GBFS and sodium silicate significantly reduced efflorescence by enhancing compressive strength and decreasing porosity [20].

3.2.1.1.4. Aggregates

The aggregate component of the geopolymer concrete mixes was obtained by crushing construction and demolition waste with a jaw crusher. Recycled aggregates were produced solely through pre-crushing and separated into different size fractions using sieves with varying mesh sizes. In producing geopolymer concrete, the largest particle size of recycled aggregates was restricted to Dmax = 16 mm, in accordance with the Fuller-Thompson ideal gradation curve (**Figure 3.10**). No additional treatment or enhancement procedures were applied to the recycled aggregates.

To enable a direct comparison between GPC and conventional vibrated concrete (CVC), the aggregate gradation was selected to be consistent across both mixture types. This approach also allows for a more precise evaluation of the influence of natural versus RCAs on the overall concrete strength.

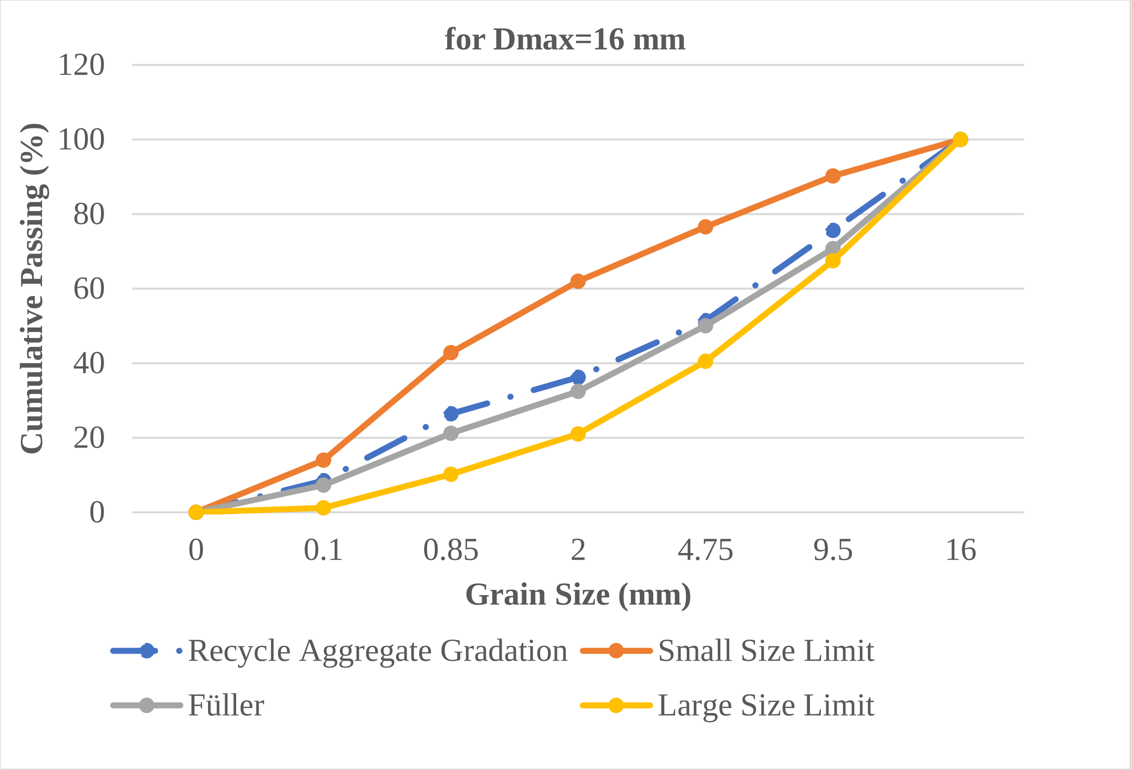

Figure 3.10 The gradation curve of the recycle aggregate with Fuller-Thompson ideal gradation curve

3.2.1.1.5. Mechanical Properties of CDW-Based Geopolymer Concrete

Following the casting process, the mixtures were cured under ambient conditions until the day of testing. The developed mixture underwent tests for compressive strength (ASTM C109), drying shrinkage (ASTM C157), water absorption (ASTM C642), chloride ion penetration (ASTM C1202), and porosity (mercury intrusion porosimetry test). The 28-day test results for CDW-based geopolymer concrete are presented in **Table 3.4**. As it is widely known, CDW-based materials generally have lower reactivity compared to mainstream waste materials. Although the calcination process can enhance the pozzolanic activity of CDW-based materials, it is not considered a viable alternative due to the additional environmental and cost burdens it imposes [146]. Additionally, while CDW-based geopolymers can achieve high mechanical performance through heat curing, this approach presents disadvantages such as additional labor and costs, making ambient curing a more favorable option [147]. Therefore, as demonstrated in this study, the aim was to activate CDW-based materials in a high pH solution using partially high molarity sodium hydroxide, while reactive Si ions were provided to the system through sodium silicate. Moreover, the incorporation of a small amount of calcium hydroxide facilitated the formation of calcium-based gels and led to improvements in mechanical performance. Furthermore, the addition of 15% GBFS and 5% FA prevented early-age strength loss and provided adequate workability without the need for additional water [148]. As a result of the geopolymer studies conducted by the authors, the development of CDW-based geopolymer concrete resulted in the successful completion with 34.2 MPa compressive strength, 3874 με drying shrinkage, 8.6% water absorption, 9.8% porosity, and 2390 C chloride ion penetration properties at 28 days, as shown in **Table 3.4**. In the subsequent stages of the study, the detailed mixture design of CDW-based geopolymer concrete that is considered to be used for the fabrication of all structural elements is given in **Table 3.3**.

Table 3.4 28-day mechanical and durability properties of CDW-based geopolymer concrete

	Compressive strength (MPa)	Drying shrinkage (με)	Water absorption (%)	Porosity (%)	Chloride ion penetration (C)
Geopolymer Concrete	34.2	3874	8.6	9.8	2390

3.2.1.2. Conventional Concrete

OPC CEM I 42,5 R grade was utilized for the monolithic and bolted specimens. The water-to-cement ratio was 0.67. Quantities of the ingredients of the OPC concrete are listed in **Table 3.5**.

Table 3.5 Mixing ratios of the OPC concrete

Fine aggregates (kg/m^3)	Coarse aggregate (kg/m^3)	Cement (kg/m^3)	Water (kg/m^3)	Water/Cement (%)
917.3	917.3	316.4	211.9	67

The compressive strengths of OPC were evaluated through compression tests on cube specimens measuring 150 × 150 × 150 mm for each batch. These specimens were cured under ambient conditions, utilizing the sprinkling method, plastic sheets with wet blankets, or a curing pool, in the identical environment as the test samples.

The gradation curve of the aggregates used in conventional concrete mixtures is presented in the graph below. The aggregates were sourced from two quarries and classified as fine and coarse. Aggregates passing through the 4.75 mm sieve were categorized as fine aggregates, while those retained on the 13 mm sieve were considered coarse aggregates. The maximum particle size (D_{max}) of the coarse aggregates utilized in the experiments was 16 mm. These aggregates were obtained by crushing natural white stone using jaw crushers. The aggregates' water absorption capacity was generally less than 2%, indicating good quality and low porosity.

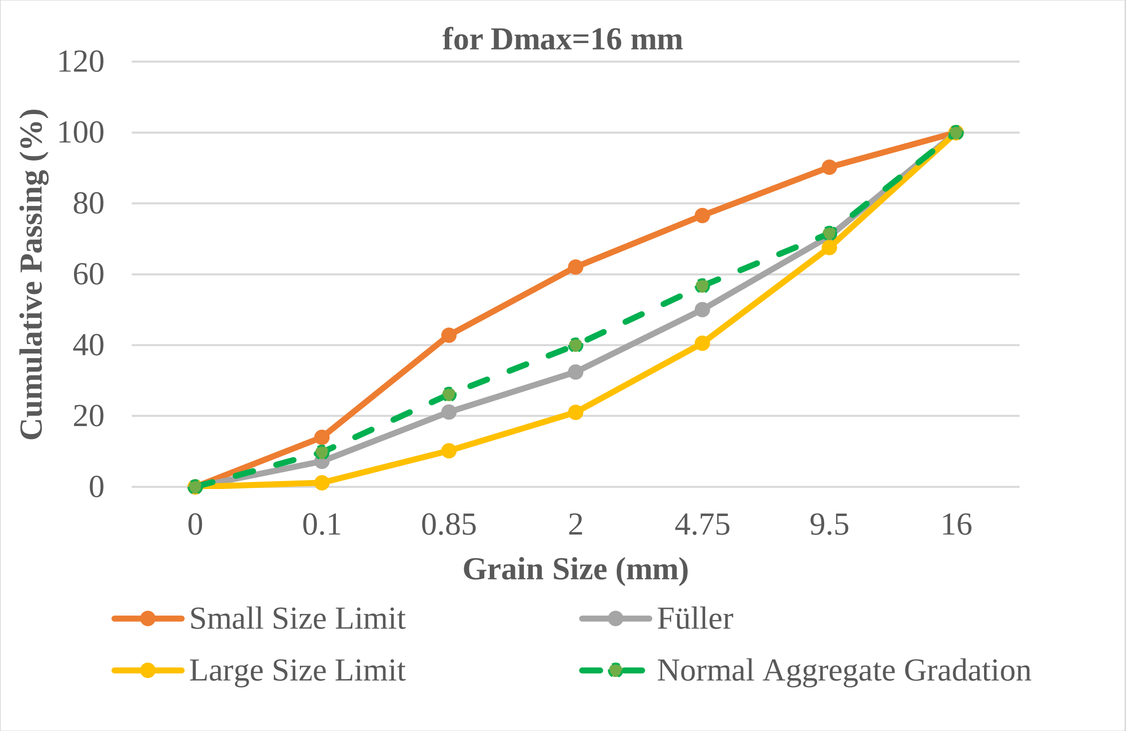

Figure 3.11 The gradation curve of the normal aggregate with Fuller-Thompson ideal gradation curve

3.2.2. Compressive and Splitting-Tensile Strength of Test Sample

Alongside the fabrication of the column samples, 150 mm cubic specimens were produced to evaluate their compressive strength. In accordance with ASTM C39 [88], a loading speed of 0.30 MPa/s was applied throughout the compressive cubic specimen tests.

Additionally, the characteristic compressive stress–strain response of the CDW-based geopolymer concrete was obtained from a displacement-controlled compression test using an extensometer on three cylindrical specimens (200 mm height × 100 mm diameter), as illustrated in **Figure 3.12**. In **Figure 3.12**, it is evident that the strain associated with ultimate strength is approximately 0.002, similar to CVC concrete, while the ultimate strain remains unspecified ~0.0035.

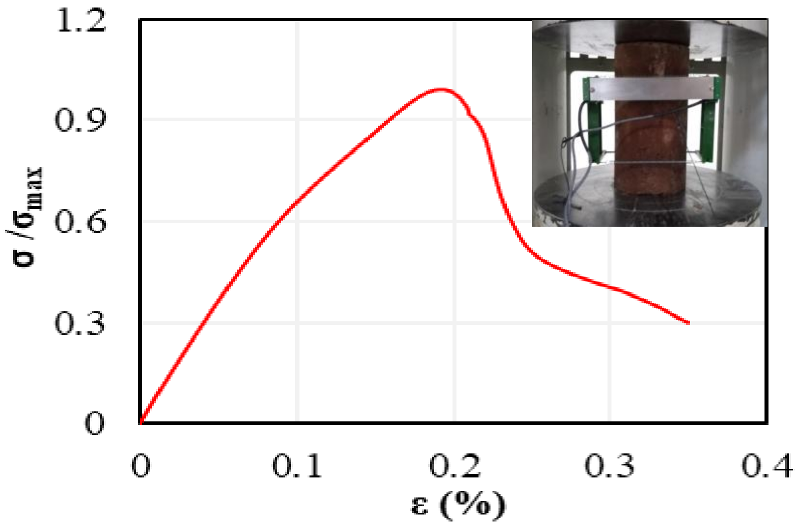

Figure 3.12 Typical stress – strain curve of the developed CDW-based geopolymer concrete.

The tensile strength of concrete (f_{ct}), which is rarely determined by direct tensile tests, can be calculated approximately by dividing the splitting tensile strength ($f_{ct,sp}$) by 1.50 [76]. The splitting tensile strength, $f_{ct,sp}$ was calculated using **Eq. (3.1)**.

$$f_{ct,sp} = \frac{2P_{ct}}{\pi L_{ct} D_{ct}} \tag{3.1}$$

where P_{ct} refers to the maximum applied load on the cylinder in the test, and L_{ct} (300mm) and D_{ct} (150mm) refer to the length and diameter of the cylinder specimen, respectively.

Table 3.6 Compressive and splitting-tensile strength of the column samples of fully demountable column base connections study

Properties	**Monolithic Specimen**	**Demountable Specimen**	
Samples	**GMC**	**GDC1-GDC3**	**GDC4**
Concrete cube compression strength, MPa	27.00	34.90	31.20
Concrete splitting tensile strength, MPa	2.61	-	2.60

Table 3.7 Compressive and splitting-tensile strength of the column samples of structural performance of CDW-based geopolymer concrete columns study

Properties	**Monolithic Specimen**	**Demountable Specimen**
Samples	**GMC**	**GDC**
Concrete cube compression strength, MPa	27.00	31.20
Concrete splitting tensile strength, MPa	2.61	2.60

Table 3.8 Compressive and splitting-tensile strength of the column samples of damage characteristics and seismic response of demountable RC column base joints study

Properties	**Monolithic Specimen**	**Demountable Specimen**
Samples	**CMC**	**CDC**
Concrete cube compression strength, MPa	28.60	30.20
Concrete splitting tensile strength, MPa	3.32	3.54


S-1203-02
S-1203-01
S0602-04
S0602-05
A2
A1
A16

Figure 3.13 Cube and cylinder specimens test

3.2.3. Reinforcing Steel Bars

In practical applications, longitudinal reinforcement in columns typically consists of 14–18 mm diameter deformed bars, while 8 mm diameter bars are commonly used for stirrups due to their ease of bending and shaping. When the S107 reference column model was scaled to half of its original dimensions, the equivalent stirrup diameter was not commercially available and could only be sourced as a custom-manufactured hard steel product. However, due to the brittle nature of hard steel, which can restrict plastic hinging and potentially cause sudden failure, it was deliberately excluded from use in this experimental study.

Instead of other options, plain round bars with a 6 mm nominal diameter were used as stirrups, while 10 mm deformed bars were applied for longitudinal reinforcement, and 14 mm deformed bars were placed in the foundation. The tensile strengths of the reinforcement bars and steel plates used in the experiment are presented below. Each reinforcement specimen was extracted from a different bar to ensure representative results. In line with relevant standards, tensile tests were carried out at the Materials Laboratory of METU. The tensile strength of steel bars was determined by tensile tests carried out using a Universal Testing Machine. Three specimens were taken from each of the bar types, which have a different diameter, to be used in the tensile test. All obtained material properties are summarized in **Table 3.9**.

Table 3.9 Tensile properties of the reinforcement bars and stee

	Specimen No	Diameter (mm)	Nominal Area (mm²)	Yield Strength (MPa)	Ultimate Strength (MPa)
Ɵ6	1.00	6.42	32.37	327.40	451.00
	2.00	6.52	33.39	329.40	449.30
	3.00	6.48	32.98	333.50	448.80
	Average	**6.47**	**32.90**	**330.10**	**449.70**
Ɵ10	1.00	10.40	84.95	459.10	724.00
	2.00	10.10	84.12	449.30	699.00
	3.00	10.38	83.62	460.80	726.80
	Average	**10.29**	**84.20**	**456.40**	**716.60**
Ɵ14	1.00	14.32	161.06	490.51	620.90
	2.00	14.22	158.81	484.84	623.40
	3.00	14.27	159.93	493.96	625.30
	Average	**14.30**	**159.90**	**489.80**	**623.20**
Steel plate				**235.00**	**360.00**

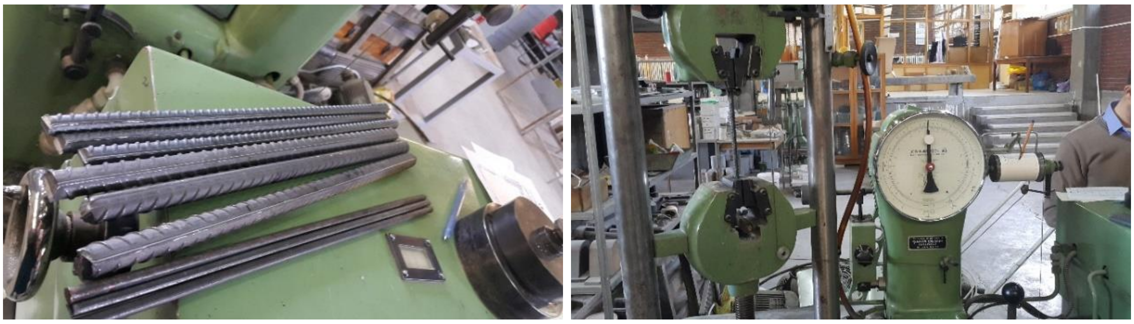

Figure 3.14 Tensile test of reinforcement bars

3.2.4. Methodology

3.2.4.1. Preparation of Mixtures

The preparation of GPC specimens was conducted through a straightforward mixing process. Initially, the dry powder constituents, including the binder and calcium hydroxide, were individually weighed with a precision of 0.1 g and transferred into a 50-liter Hobart mixer. These components were blended for approximately five minutes to achieve a uniform mixture.

At the same time, sodium hydroxide was dissolved in water and left to cool at ambient temperature for a full day. Once the solution reached room temperature, it was gradually mixed with the dry components. Liquid sodium silicate, known for its rapid setting, was added after ensuring uniform mixing, helping to limit mixing duration. The final mix was stirred for three more minutes and directly transferred into molds.

Figure 3.15 NaOH solution preparation

Figure 3.16 Preparation of the geopolymer mixture and casting into molds

Moreover, the conventional concrete mixture was prepared using a 250-liter capacity mixer. Before mixing, a minimal quantity of water was used to wet the interior of the mixing equipment. The aggregates and cement were then added in the specified proportions and mixed for approximately five minutes. After achieving a uniform dry mix, the remaining water was added gradually according to the predetermined ratio. The consistency and workability of the mixture were visually assessed to ensure that the slump was within acceptable limits. Without delay, the newly mixed concrete was placed into the molds. A vibrator was used to ensure proper compaction and eliminate air voids. Finally, the surface of the concrete was leveled using an appropriate finishing tool and left to cure under ambient conditions.

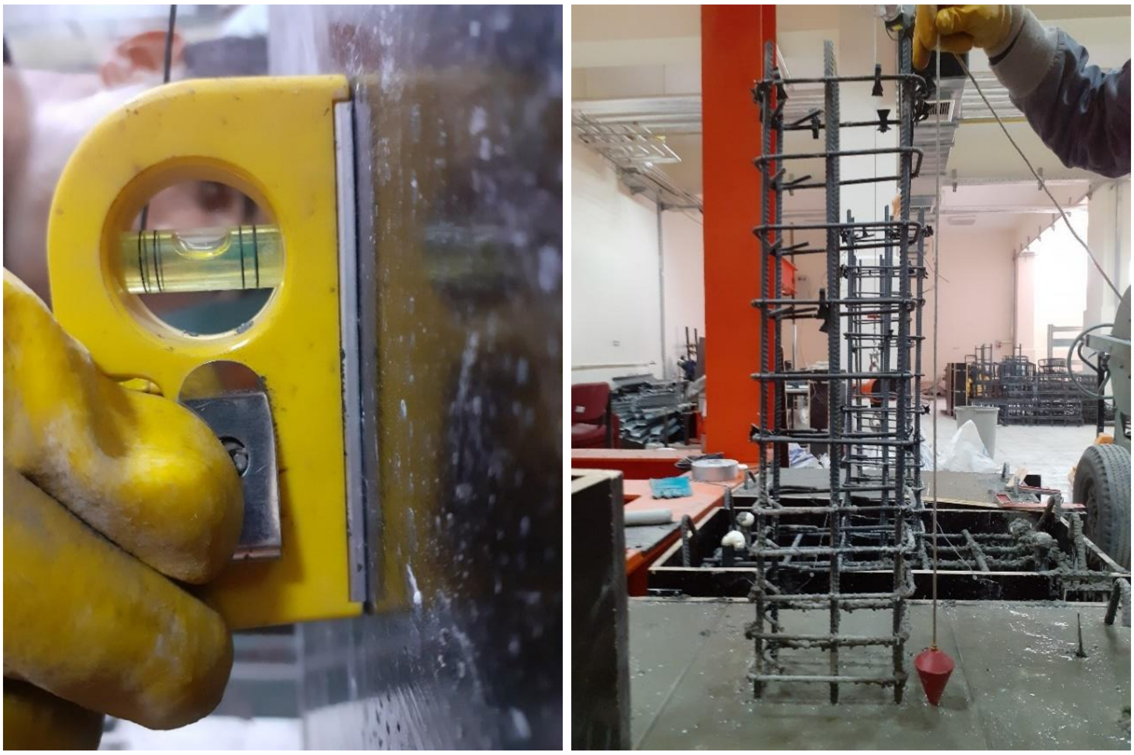

Figure 3.17 Preparation of the concrete mixture and adjusting the column plumb

3.2.4.2. Curing Conditions

Column specimens, with cube and cylinder samples, were demolded one day after casting and subsequently cured in a water tank. This curing method was employed to prevent moisture loss, minimize drying shrinkage, and support the continuation of geopolymerization reactions. In contrast, conventional concrete samples underwent moisture curing under sheltered conditions until the day of testing.

Figure 3.18 Curing of geopolymer demountable columns

Figure 3.19 Curing of geopolymer monolithic columns with a drip system

3.2.5. Test specimens

As part of the experiment, demountable columns were designed to create a "Lego-like" construction system that allows for disassembly and reassembly. For comparison and reference, conventionally cast-in-place columns with similar strength properties were produced using traditional concrete, followed by the production of geopolymer columns under identical conditions.

The experimental specimens were classified into two main categories: monolithic columns and demountable columns. Each category was further subdivided based on the type of concrete used, either conventional or geopolymer. In the monolithic group, seven columns were cast, including four made of conventional concrete and three made of geopolymer concrete. One of the monolithic samples was evaluated without axial loading and was primarily intended for use in beam design evaluation.

Also, five different column connections were developed and tested to find the best column design. These connection types were evaluated in terms of performance, and the best-performing configuration was selected. After optimizing its details, three demountable columns were produced using conventional concrete and three using geopolymer concrete, resulting in six demountable test specimens.

In addition, a test foundation incorporating threaded rod (tie-rod) connections was specifically designed and constructed to facilitate the testing of all demountable columns. During the preparation of the foundation formwork, various demountable connection alternatives were initially evaluated. Based on these evaluations, a threaded rod configuration was selected for anchoring the column bases, as it offered advantages in terms of both cost-effectiveness and ease of fabrication.

The reinforcement and geometrical details of the columns are obtained by scaling down the ground-story column of the RC building designed according to the recent Turkish Earthquake Code (TEC2018) [149]. The scale factor is considered to be 0.5 due to the limitations of the testing facility. Thus, the tested rectangular column has a width of 150 mm and a height of 250 mm (i.e., 150 × 250 mm rectangular section). Columns reinforced with six 10-mm-diameter deformed longitudinal steel rebars, corresponding to a reinforcement ratio of 1.26%. In addition, 6-mm-diameter plain steel bars are employed as lateral reinforcement (i.e., to increase shear capacity and provide a confinement effect along the column height). Lateral bars are bent 135 degrees at both ends as per TEC2018. The spacing of lateral reinforcement is taken as 50 mm at the confinement zone, whose height is equal to 250 mm. Beyond the confinement zone, the spacing of lateral reinforcement is doubled to 100 mm. The nominal concrete covers to all reinforcement are adjusted to be at least 15 mm in the column and 25 mm in the foundations. The column geometry and reinforcement configuration were kept identical across all test specimens to enable straightforward comparison.

The labeling of the test specimens was carried out as shown in the table below.

GMC	Geopolymer Concrete Monolithically Connected Column
CMC	Conventional Concrete Monolithically Connected Column
GDC	Geopolymer Concrete Demountable Connected Column
CDC	Conventional Concrete Demountable Connected Column

3.2.5.1. Specimens description of Fully Demountable Column Base Connections Study

This study aims to develop easily mountable, demountable, and inexpensive connections for geopolymer concrete structural elements. Four different types of bolted demountable connections (DC) are designed and manufactured. Additionally, one monolithic connection and one foundation are also manufactured.

3.2.5.1.1. Monolithic specimens

The test foundation has a 500 × 400 mm rectangular cross-section with a 1000 mm length. The foundation includes symmetric reinforcement using four 14 mm diameter deformed steel bars in both longitudinal and transverse directions. The foundation is produced from high-strength conventional concrete to minimize damage during testing. To carry over load from the column to the foundation, eight 14-mm-diameter threaded bars are embedded in the foundation before casting. After the casting, the upper surface of the foundation, which contacts the column base plate, is adjusted with the help of an angle grinder without damage to the steel rods to provide a flat contact surface for connections. On the other hand, the flatness deviation between the column base plate and the top surface of the foundation is also monitored by adding a thin elastomeric pad between the foundation and column. GMC1 consists of a monolithically connected geopolymer concrete column and geopolymer concrete foundation. The GMC1 foundation shares similar reinforcement details and size with the test foundation, and the total height of the column is 930 mm.

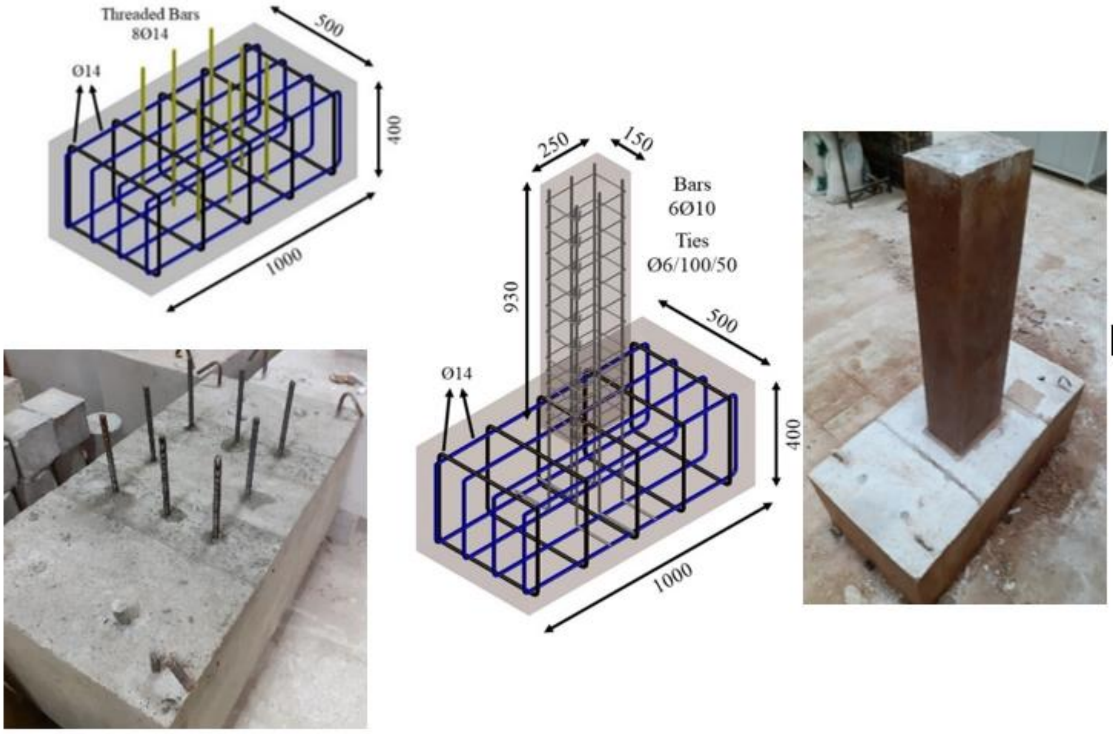

Figure 3.20 Reinforcement details and general views of the monolithically connected specimen (GMC1) and test foundation.

Figure 3.21 Formwork guide for end plate of demountable column

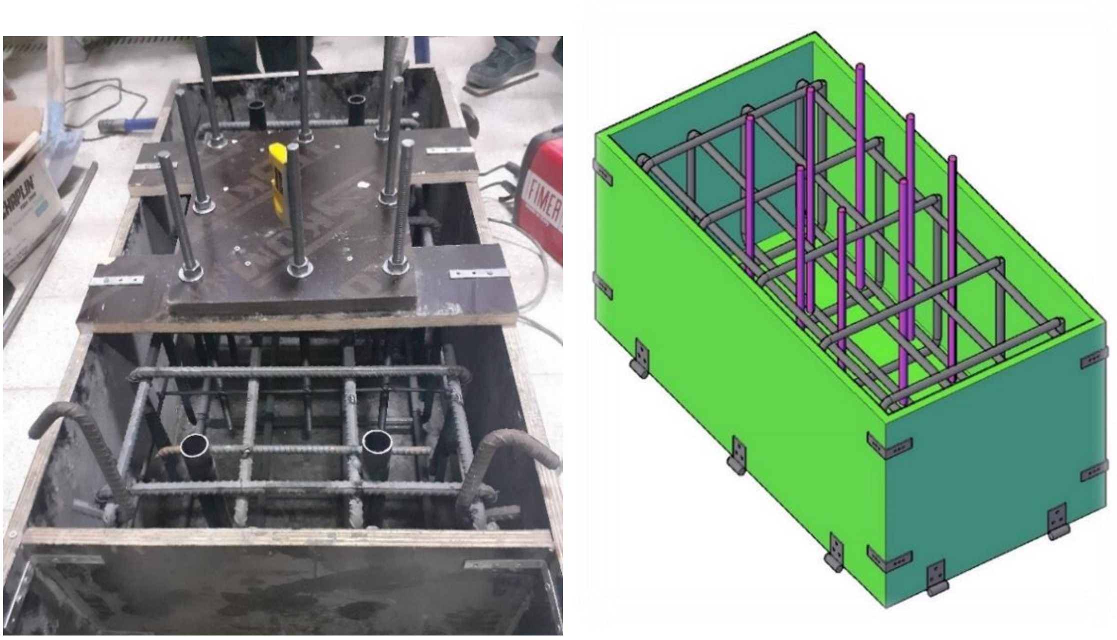

Figure 3.22 Foundation formwork for demountable column

As shown in the figure above, the threaded rods were placed into the Lego foundation using a positioning guide, and their vertical alignment was ensured using a spirit level.

Figure 3.23 Vertical alignment of threaded rods

To prevent any potential misalignment during casting, the vertically adjusted threaded rods, aligned using a spirit level and secured with nuts, were tack-welded in place. According to TS500 provisions, the embedded length of the threaded rods within the concrete was set to 300 mm. Their exposed sections were covered with steel pipes to protect the rods from potential impact damage and prevent contamination during casting.

In this setup, to ensure that no damage would occur during testing, the rods were deliberately overdesigned to provide an additional safety margin.

Figure 3.24 Details of foundation with threaded rods and elastomer application

3.2.5.1.2. Demountable specimens

In the design stage of DC1-DC3 specimens, the idea is to generate an easy-to-apply and feasible connection without a significant need for steel. Because the structural elements are produced from fully recycled materials (i.e., CDW-based geopolymer), generating a base connection with a large amount of recycled material is astonishing at the preliminary design stage. Although these connection designs could be prone to having premature base cracking and crushing concentrated at the joint, the idea about enhancing the recycling ratio of the structural component deserves an experimental observation. Nevertheless, the main idea behind the specimen DC4 is to create an easy-to-apply, feasible, and high-performance connection using steel plates. The design parameters for each connection type are summarized in **Table 3.10**.

Table 3.10 Summary of design parameters for each connection type

Connection	RC Footing (w × h × t)	Steel Base Plate (w × h × t)	Reinforcements in RC Footing	Base Connection Bolts	Steel Jacketing
DC1	290 × 390 × 55	N/A	8Φ6 paralel to short direction 6Φ10 paralel to long direction	8Φ14	N/A
DC2	300 × 400 × 30	N/A	Rectangular steel grille with a 30 × 30 mm square grids (2 × 30 mm steel plates in strong direction and 6-mm-diameter round bars in weak direction)	8Φ14	N/A
DC3	300 × 400 × 30	N/A	Rectangular steel grille with a 30 × 30 mm square grids (2 × 30 mm steel plates in strong direction and 3 × 30 mm steel plates in weak direction)	8Φ14	N/A
DC4	N/A	250 × 350 × 10	N/A	8Φ14	3 × 50 mm steel plate

Design of Connection DC1

The first type of demountable connection, DC1, is produced from steel bars with different diameters and has a 290 × 390 × 90 mm rectangular prism shape, as shown in **Figure 3.25**. Six rebars with a diameter of 10 mm are used along the short direction, whereas eight 6 mm diameter flat bars are utilized along the long direction. To decrease the connection height, steel bars in strong and weak directions are designed to be two pieces: top and lower steel bars, and the top bars are welded to the lower bars. 18 mm diameter bolt holes welded to the steel bars in order to conform to threaded bars in the test foundation. The ends of the longitudinal bars are bent 90 degrees and welded the lower bars.

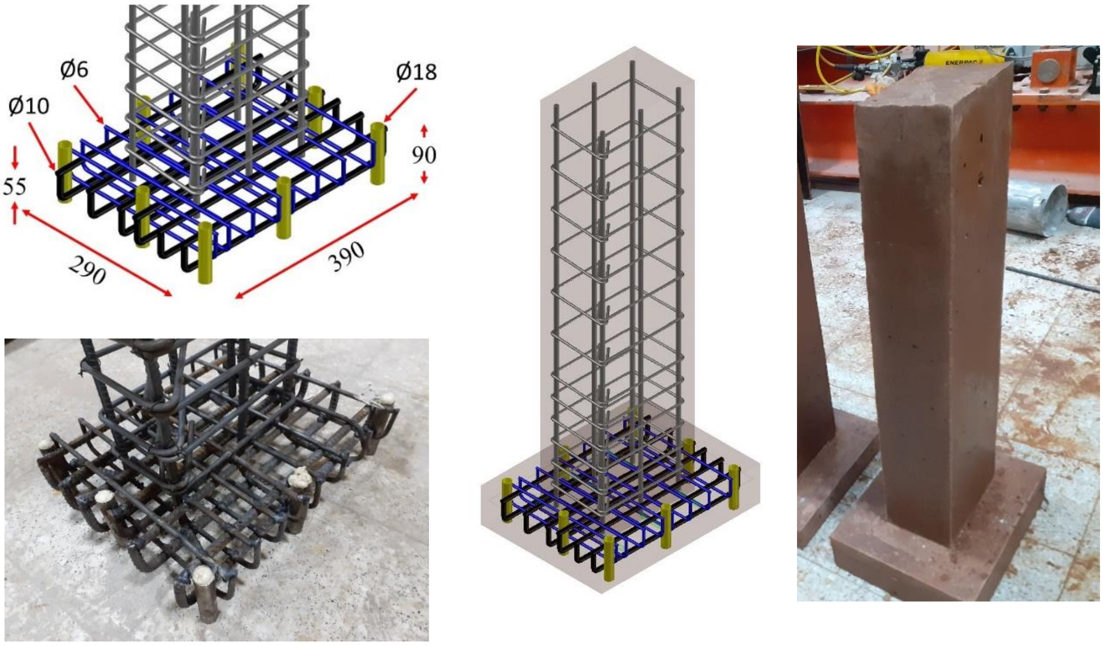

Figure 3.25 Reinforcement details in connection region and general views of the DC1 specimen.

Design of Connection DC2

In the design of specimen DC2, a rectangular grille with square grids whose grid dimensions are equal to 30 × 30 mm is used. The grille has a width of 300 mm, a length of 400 mm, and a height of 30 mm. The grille consists of 2-mm-thick 30-mm-high steel plates and 6-mm-diameter round bars in strong and weak directions, respectively. Steel plates and round bars are spot-welded to each other. At their ends, the longitudinal rebars are bent at a right angle and attached to the steel plates by welding. Reinforcement configurations and general illustrations of specimen DC2 are provided in **Figure 3.26**.

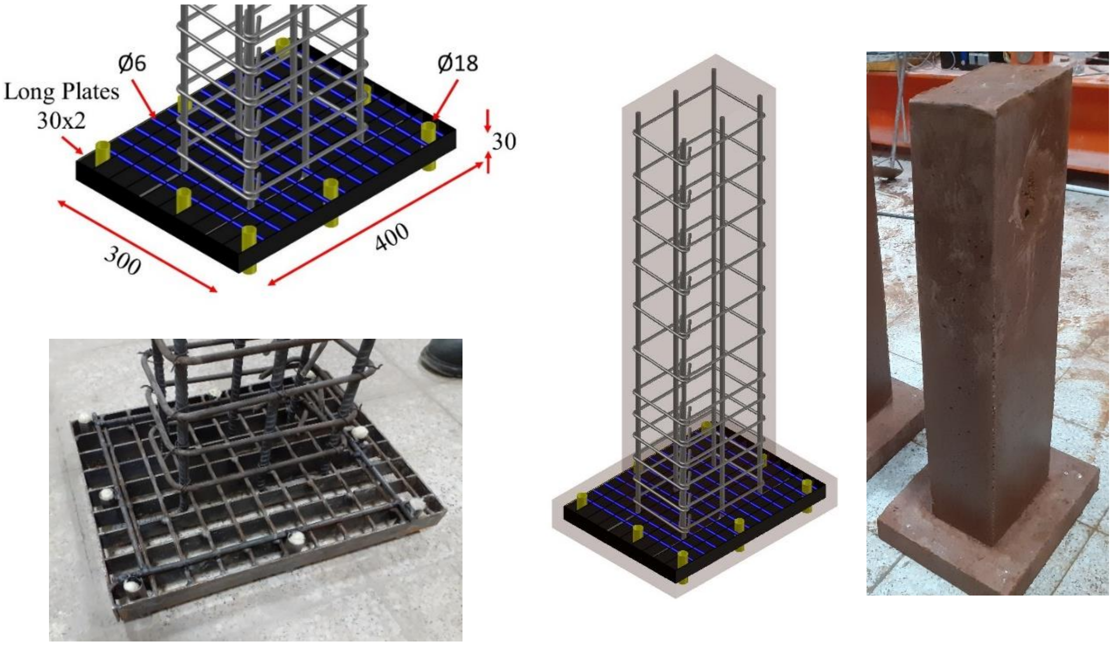

Figure 3.26 Reinforcement details in the plastic hinge region and general views of the DC2 specimen.

Design of Connection DC3

The demountable connections DC3 and DC2 are similar, with the exception that 20 × 3 mm steel plates are used in the weak direction instead of round bars. Steel plates in the weak and strong axes are spot-welded to each other. The reinforcement details and general views of specimen DC3 are shown in **Figure 3.27.**

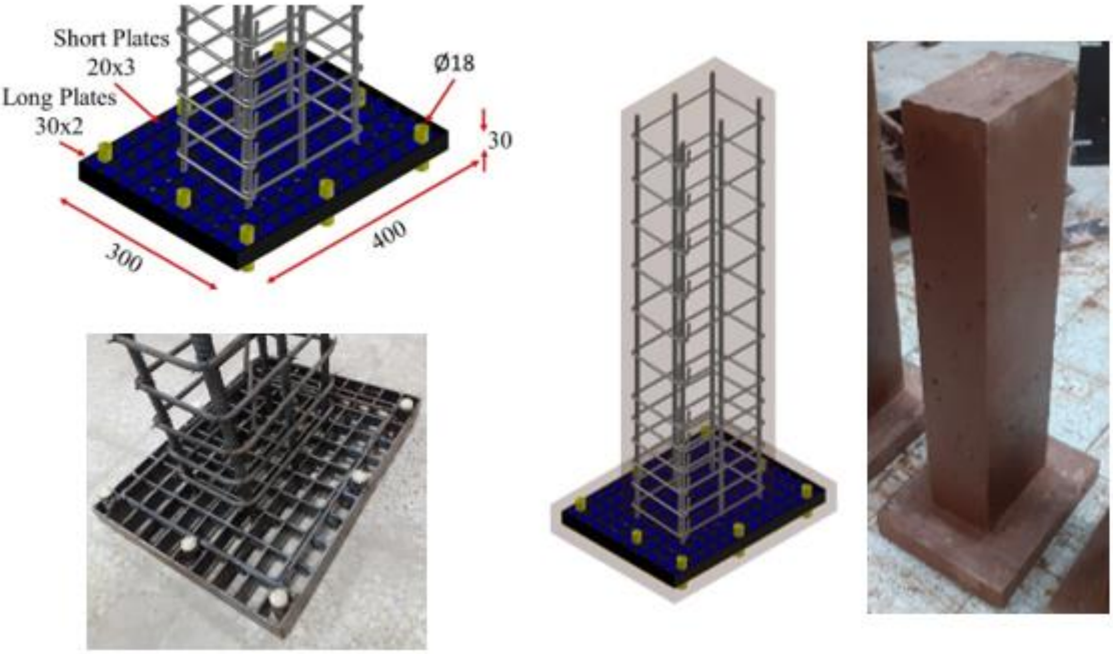

Figure 3.27 Reinforcement details in connection region and general views of the DC3 specimen.

Design of Connection DC4

Specimen DC4 is based on anchoring columns’ longitudinal rebars to the steel end plate and assembling to the test foundation using high-strength bolts. 250 × 350 × 10 mm steel plate is used to form the connection base. The 50–mm–high and 3-mm-thick steel plates are welded to the end plate to avoid joint splitting caused by poor adhesion between concrete and steel (i.e., serving as jacketing). 8-mm-thick triangular stiffeners of 50 × 50 mm are welded to the end plate and the steel jacket to increase the stiffness of the connection. The purpose of these stiffeners is to transmit shear forces from the column to the end plate and restrict the rotation demand at the column base. To carry out the load transmit among the end plate and the column in a safer manner, eight pieces of 250-mm-long 8-mm-diameter threaded steel bars (i.e., anchorage rods) are also used and bent 30 degrees toward the concrete core. All reinforcements and threaded steel rods are welded to the steel plate. Thus, 9-mm-diameter and 13-mm-diameter holes are drilled using a metal laser cutting machine on the expected location of the longitudinal rebars and anchorage rods. The countersinking operation is performed on drilled holes in the end plate to increase the welding area (i.e., groove welding). Anchorage rods and longitudinal rebars are welded to countersink holes, and the bottom surface of the end plate is ground so that a smooth surface is obtained. The geometry and reinforcement details of specimen DC4 are shown in **Figure 3.28**.

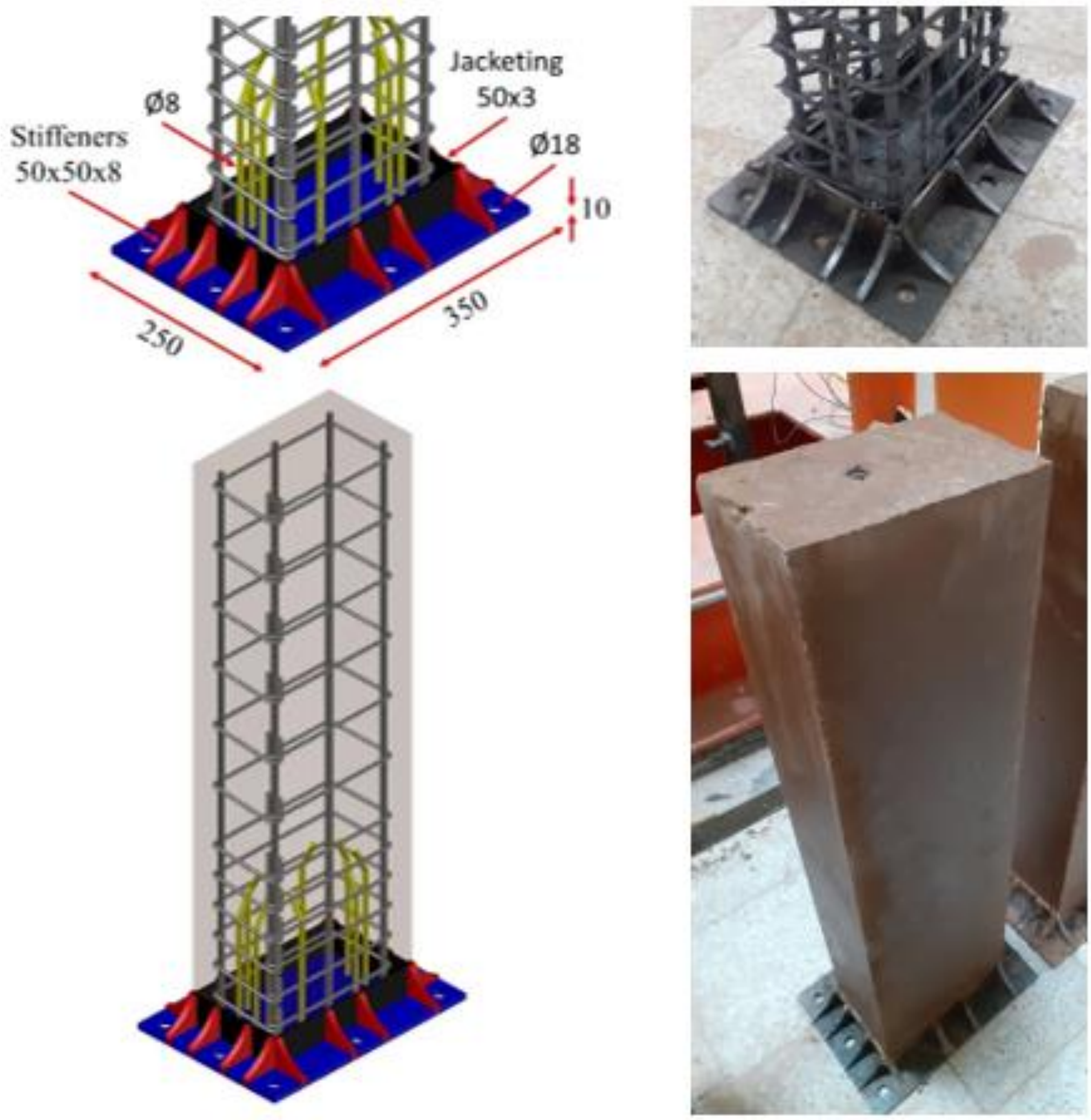

Figure 3.28 Reinforcement details in connection region and general views of the DC4 specimen.

Figure 3.29 Details of demountable column 4 (DC4)

3.2.5.2. Specimens description of Structural Performance of CDW-Based Geopolymer Concrete Columns Study

In this study, six specimens, three monolithic and three demountable specimens, were produced from CDW-based geopolymer concrete.

Since the geopolymer concrete is denser and more viscous, the vibrator process was used at closer intervals and for a longer time than the OPC concrete specimens. Test samples were demolded for curing, depending on their size: demountable specimens were kept in the curing pool, while the monolithic and foundation specimens were wrapped with a blanket and plastic cover. Additionally, the monolithic and foundation specimens were cured by watering twice a day for the first week and once a day until the test day.

The test specimens were labeled according to the connection type (MC and DC refer to monolithic and demountable connection, respectively), and axial compression ratio (i.e., $N_{applied} / (A_g \times f_{ck})$ = 0.10, 0.20, or 0.30). For instance, the test specimen labelled “GMC-0.30” indicates a specimen with geopolymer concrete monolithic connection subjected to an axial compression ratio of 0.3.

3.2.5.2.1. Monolithic specimens

The geometrical and reinforcement details of the monolithic specimen are shown in **Figure 3.30**. Three monolithic specimens were produced to compare the effectiveness of the demountable column connections. The cross-section dimensions and height of the columns were 150 × 250 mm ($b \times h$) and 930 mm, respectively. Four pipe profiles were also left in the foundation to provide holes for rod anchors, allowing easy fixing of test specimens to the reaction frame. The production steps of the monolithic specimen are given in **Figure 3.31**.

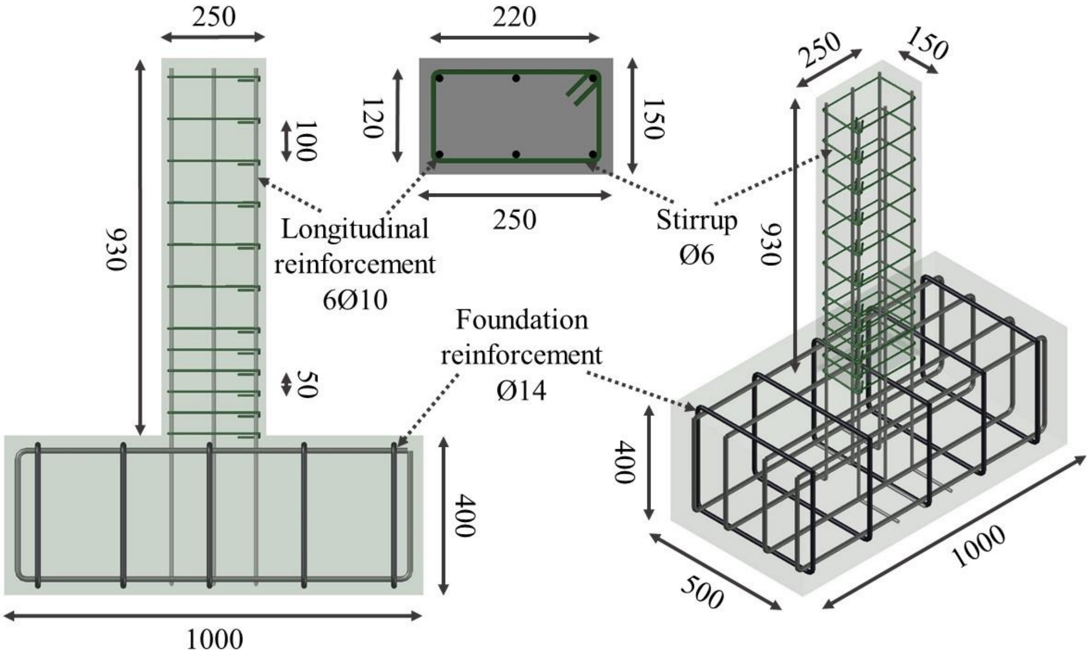

Figure 3.30 Details of the monolithic specimen (unit: mm)

(a) b) (c)

Figure 3.31 Details of the fabrication of the monolithic specimen: (a) reinforcement skeleton, (b) after concrete casting in the foundation, and (c) after concrete casting in a column.

3.2.5.2.2. Demountable specimens

To test demountable specimens, the same test foundation was used. The foundation's size and reinforcement details were the same as the monolithic specimen's foundation.

The demountable specimens could be categorized as column and connection parts. The arrangement of reinforcements and dimensions of a column of the demountable specimens was similar to that of the column of the monolithic specimens. In this study, used novel demountable connection was the same as DC4. The details of the fabrication of the demountable specimen are given in **Figure 3.32**.

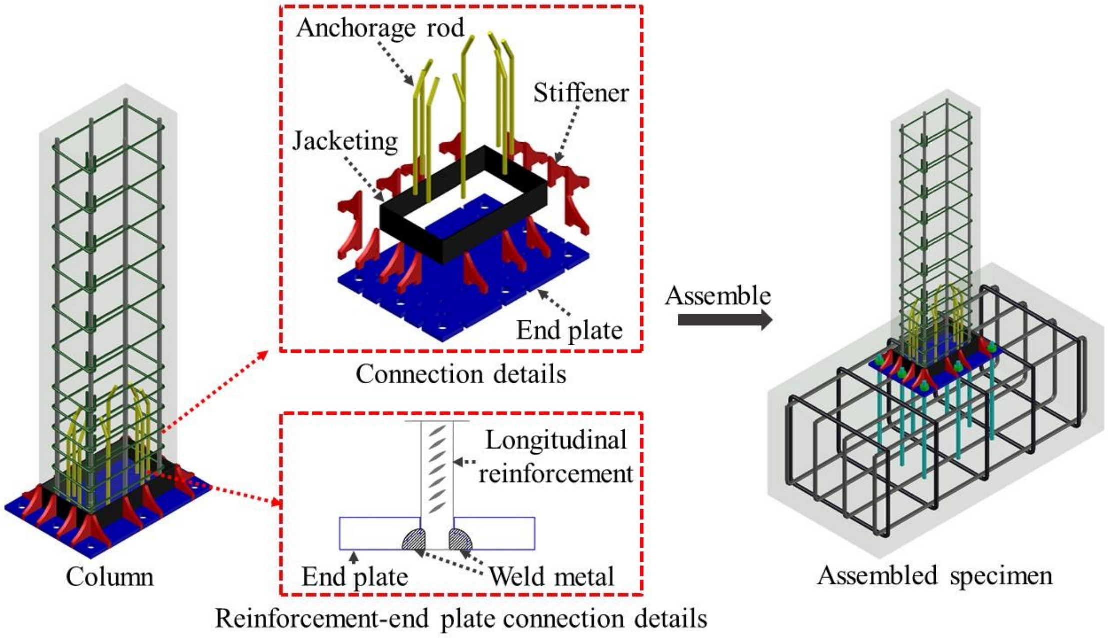

Figure 3.32 Details of the demountable specimen.

The main idea behind the demountable specimen is based on anchoring the longitudinal reinforcements of the columns to the steel end plate and then assembling a reinforced geopolymer concrete column onto the testing foundation using high-strength nuts. The loads that come from the column are transferred to the foundation through the steel end plate, and then to eight 14-mm-diameter threaded rods. The main advantages of this demountable connection can be categorized as feasibility, high structural performance, and ease of application, achieved through the utilization of steel plates and threaded rods.

(a) (b) (c) (d)

Figure 3.33 Details of the fabrication of the demountable specimen: (a) manufacturing of the connection, (b) before concrete casting, (c) after concrete casting, and (d) assembled specimen.

3.2.5.3. Specimens description of Damage Characteristics and Seismic Response of Demountable RC Column Base Joints Study

For this study, a total of six specimens were prepared using Ordinary Portland Cement (OPC), consisting of three monolithic specimens and three bolted specimens manufactured according to the design of DC4. Additionally, one foundation made of OPC concrete was used specifically for testing the bolted specimens.

The test specimens were labeled according to their joint type and their axial compression ratio. The joint type could be a monolithic joint (MC) or a bolted joint (DC). Additionally, the axial compression ratio, denoted as $N_{applied}$ / (A_g × f_{ck}), could be 0.10, 0.20, or 0.30. For example, a test specimen labeled as "CMC-0.30" indicates a conventional concrete monolithic specimen subjected to an axial compression ratio of 0.3.

3.2.5.3.1. Monolithic specimens

The geometric and reinforcement details of the monolithic specimen can be seen in **Figure 3.34**. The production steps of the monolithic specimen are illustrated in **Figure 3.35**.

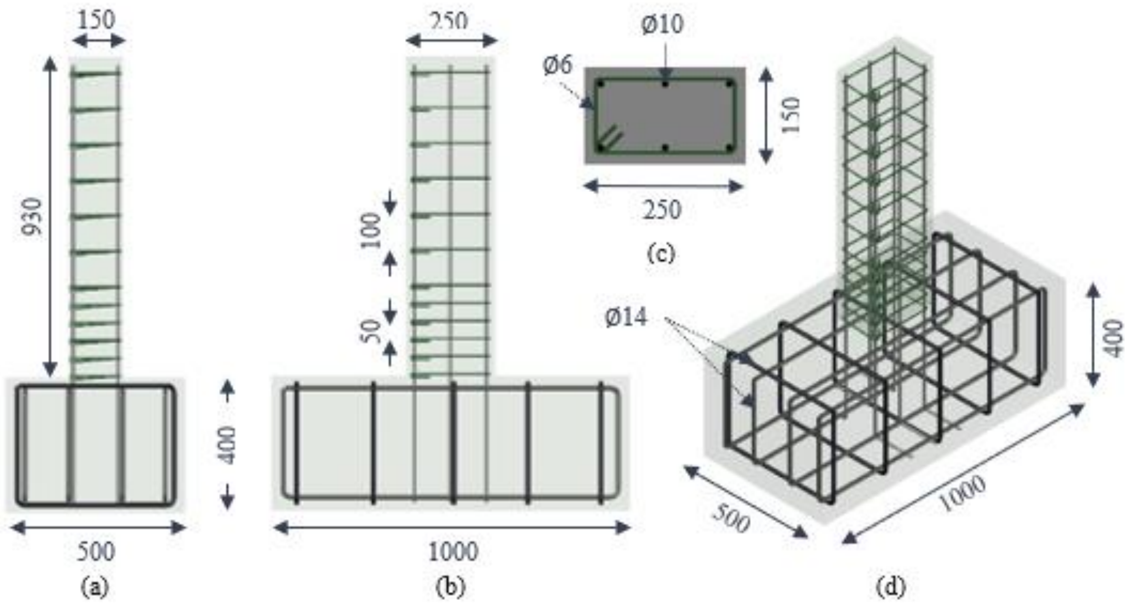

Figure 3.34 Details of the monolithic specimen: (a) side view, (b) front view, (c) cross-sectional view, and (d) isometric view (unit: mm)

(a) (b) (c) (d)

Figure 3.35 Details of the production of the monolithic specimen, (a) reinforcement skeleton (b) placement into the mold and concreting; (c) concreting; (d) assembled column on the test setup

3.2.5.3.2. Demountable specimens

In this study, used novel demountable connection was the same as DC4. The details of the fabrication of the demountable specimen are given in **Figure 3.37**.

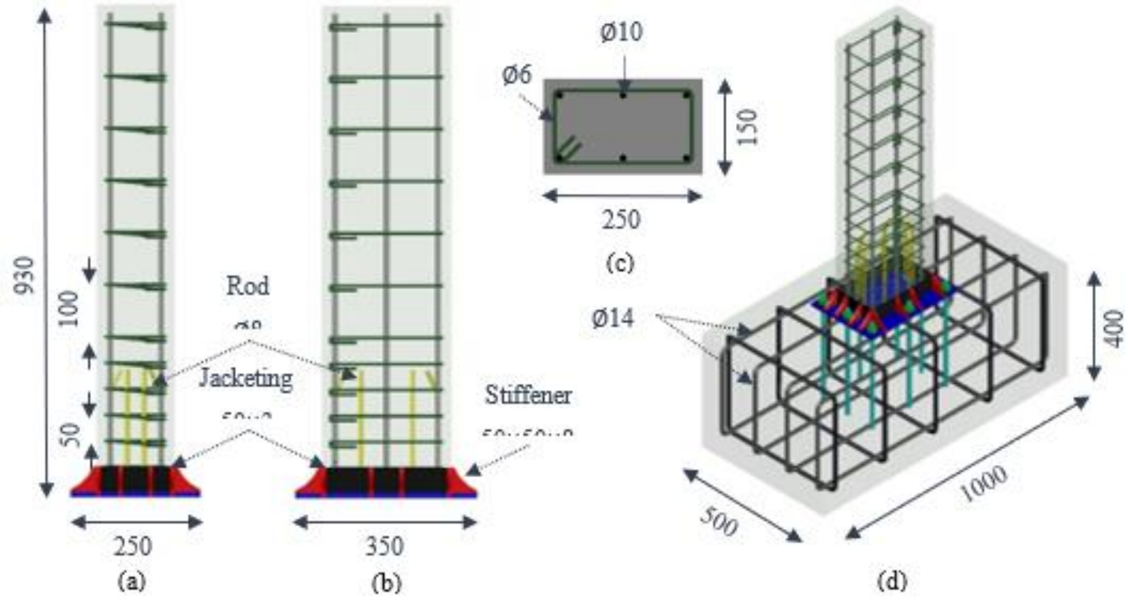

Figure 3.36 Details of the bolted specimen: (a) front view, (b) side view, (c) cross-sectional view, and (d) assembled specimen (unit: mm)

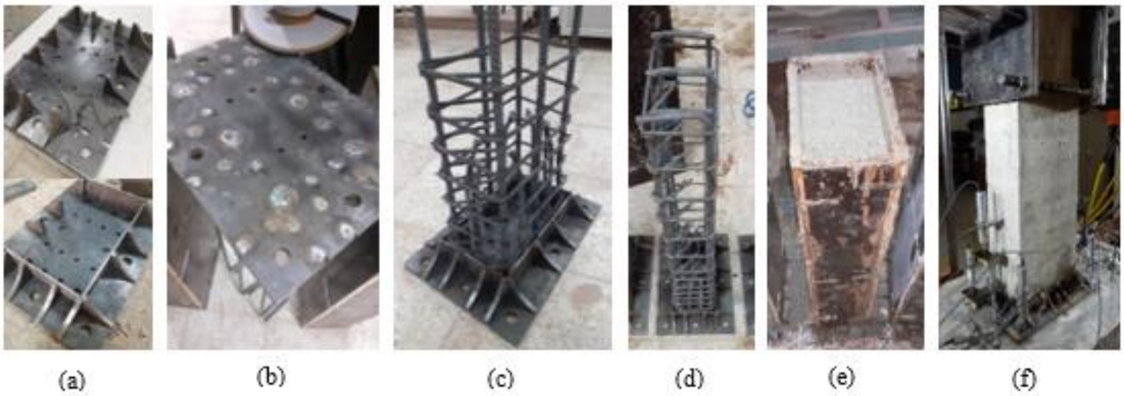

Figure 3.37 Details of the production of bolted specimen: (a) welding of the joint parts, (b) end plate smoothing, (c) fabricated joint, (d) making reinforcement skeleton, (e) placement into the mold and concreting, and (f) assembled column on the foundation

3.2.6. Test setup and Instrumentation

The tests were conducted on a steel reaction framework, as shown in **Figure 3.38**. Four high-strength threaded rods securely fastened the foundation of the test specimens to the reaction frame.

Two slippage stoppers were employed to restrain the foundation to prevent slippage. The reaction frame was equipped with a hydraulic actuator featuring a 333 mm stroke and a 750 kN load capacity for lateral reversed-cyclic loading.

Hinges were installed at both ends of the hydraulic cylinders to prevent eccentric loading. A cantilever setup applied a constant axial load (N) along the column's axis through the post-tensioning of two steel rods without inducing first- or second-order moments.

The steel rods were post-tensioned using a second hydraulic cylinder with a capacity of 600 kN, which reacts against the test frame and transmits the bar force to the column. Load cells capable of 600 kN, featuring a dual-action mechanism, were installed beneath the hydraulic cylinders to monitor and record the applied load.

Thin elastomeric pads were placed between the hydraulic cylinder and the top of the sample to reduce the flatness error between the contacted steel plate and the concrete surface.

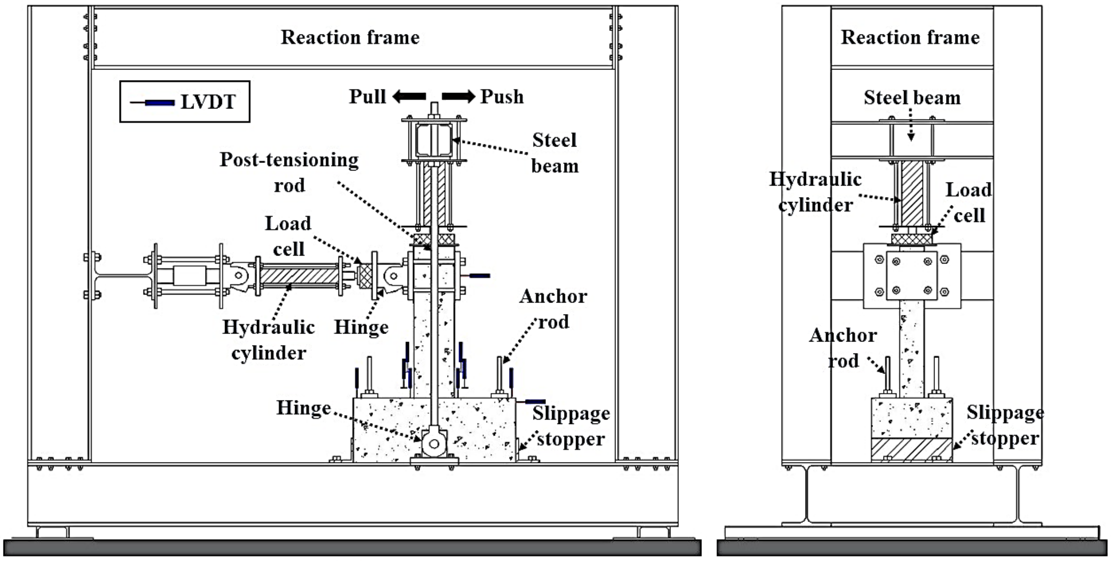

(a) (b)

Figure 3.38 Details of the test setup: (a) front view and (b) side view

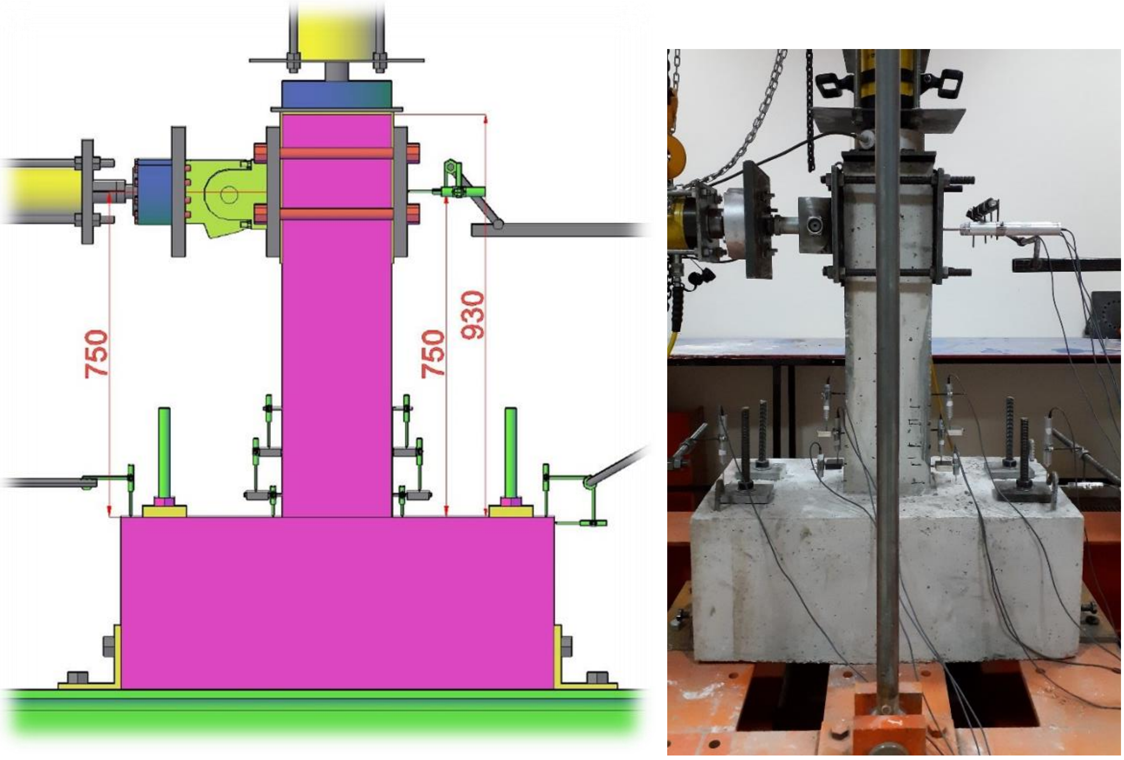

Figure 3.39 Side views of the column

The figure above indicates that the lateral actuator exerts a load on the column at a height of 750 mm. Attached to the clevis at the end of the hydraulic actuator is a 300 × 300 mm steel plate, with a matching steel plate positioned on the opposite side of the column to promote uniform loading. Despite the overall height of the column being 930 mm, the lateral load is specifically applied at the 750 mm mark.

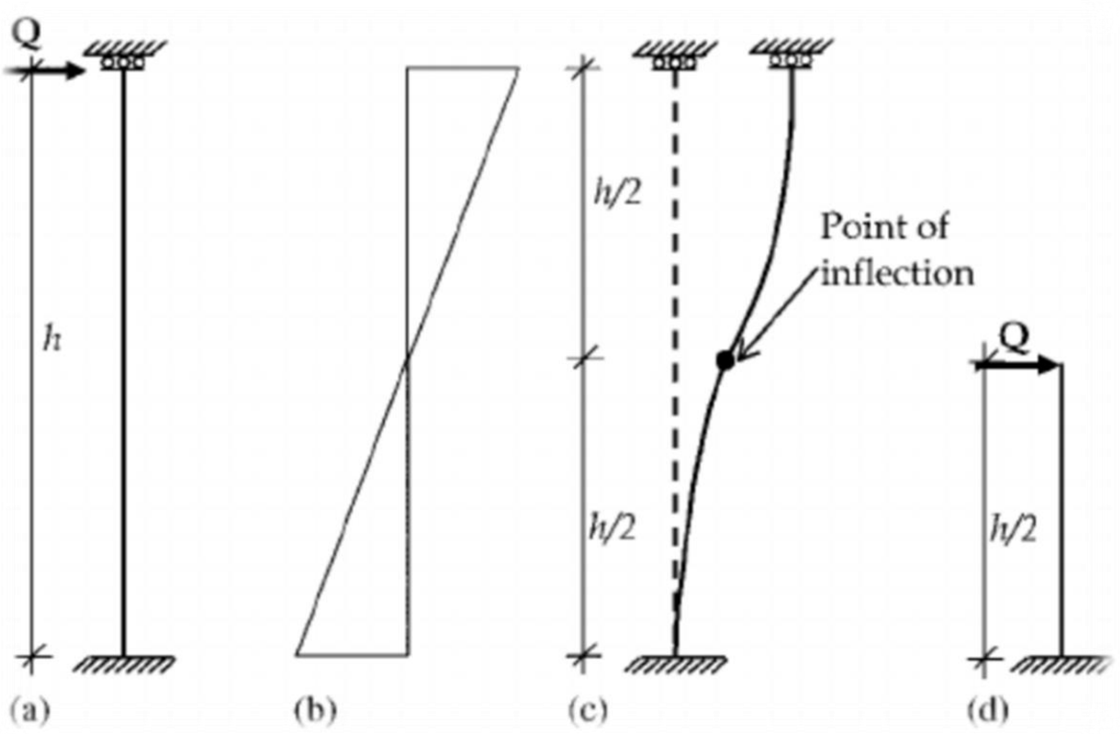

Figure 3.40 Point of inflection

Conducting the test at a height of 750 mm accurately represents the loading condition on the full-scale prototype building column, which has a height of 3000 mm. The rationale behind this scaling is illustrated in the figure above.

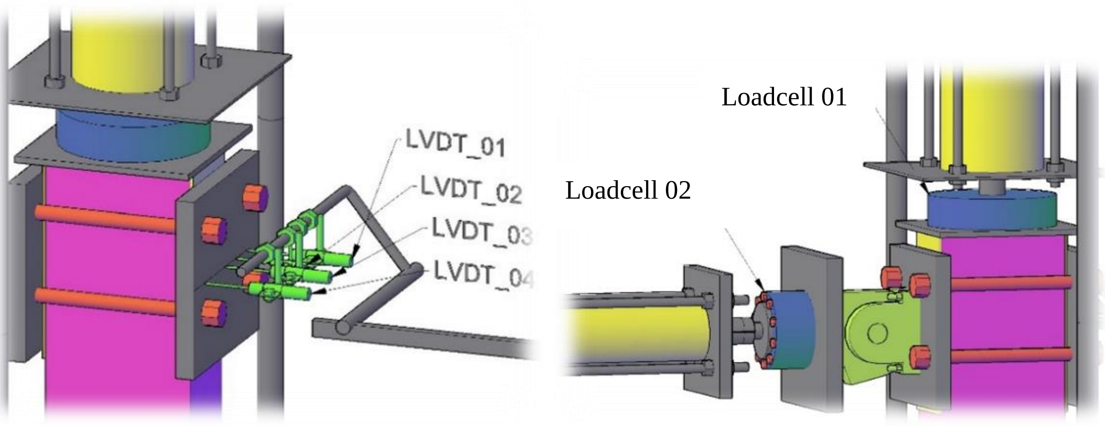

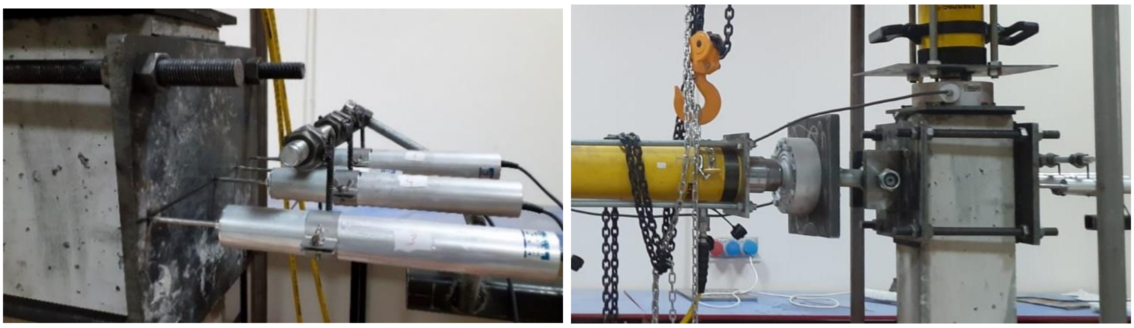

Figure 3.41 LVDT and loadcell arrangement detail

The images above show the details of the LVDT placements. Four LVDTs were installed at the top of the column. LVDT_01 and LVDT_04 were used to verify whether the column experienced any rotational movement during testing. LVDT_02 served as the primary device for displacement control; in other words, the experiment utilized displacement control derived from the measurements of LVDT_02.

The LVDTs used in this setup had a stroke capacity of 100 mm and were positioned to account for up to 6% lateral drift, which equates to 45 mm of lateral displacement at the column's top. Additionally, LVDT_03, with a 50 mm stroke capacity, was included in the system as a reference sensor to validate the readings of the 100 mm LVDTs.

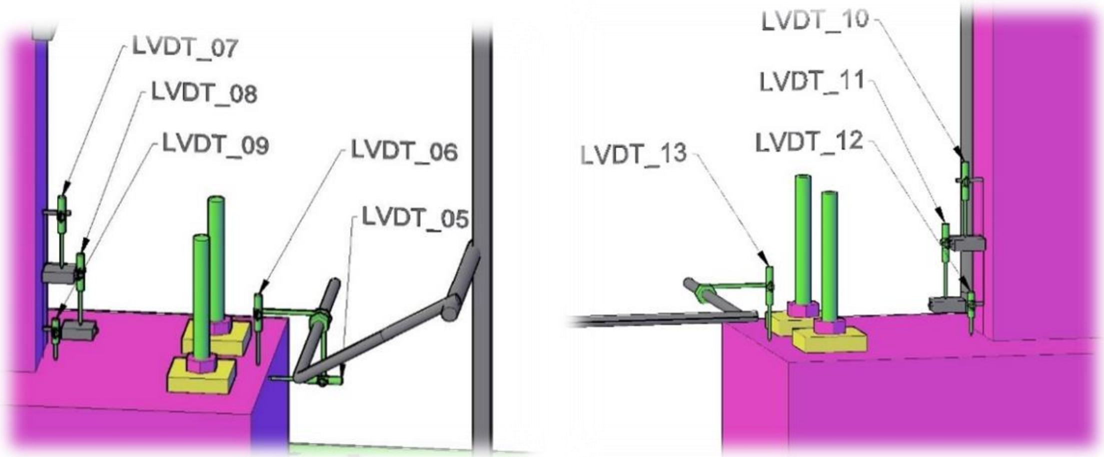

Figure 3.42 LVDT and fixing threaded rod arrangement detail

These images illustrate the LVDTs located at the column's base and within the foundation. Six LVDTs were strategically placed at the lower section of the column to accurately measure localized deformations in the confinement area. Additionally, LVDT_05 was integrated into the system to monitor any lateral slip or movement of the specimen during testing.

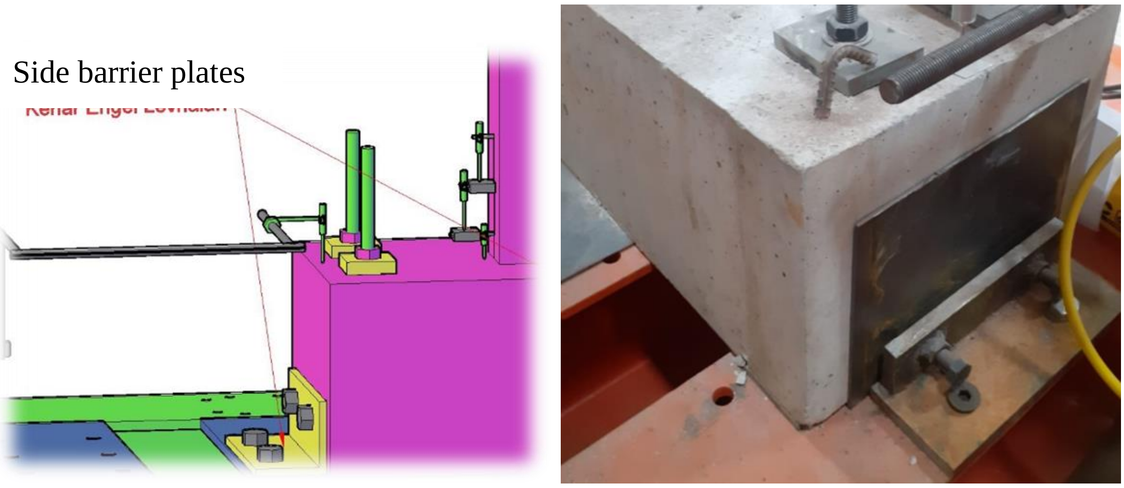

Figure 3.43 Side barrier plates

To prevent lateral sliding, edge restraint plates were used. One side of each plate was fixed to the lower beams, while the other side was tightened against the specimen using screws.

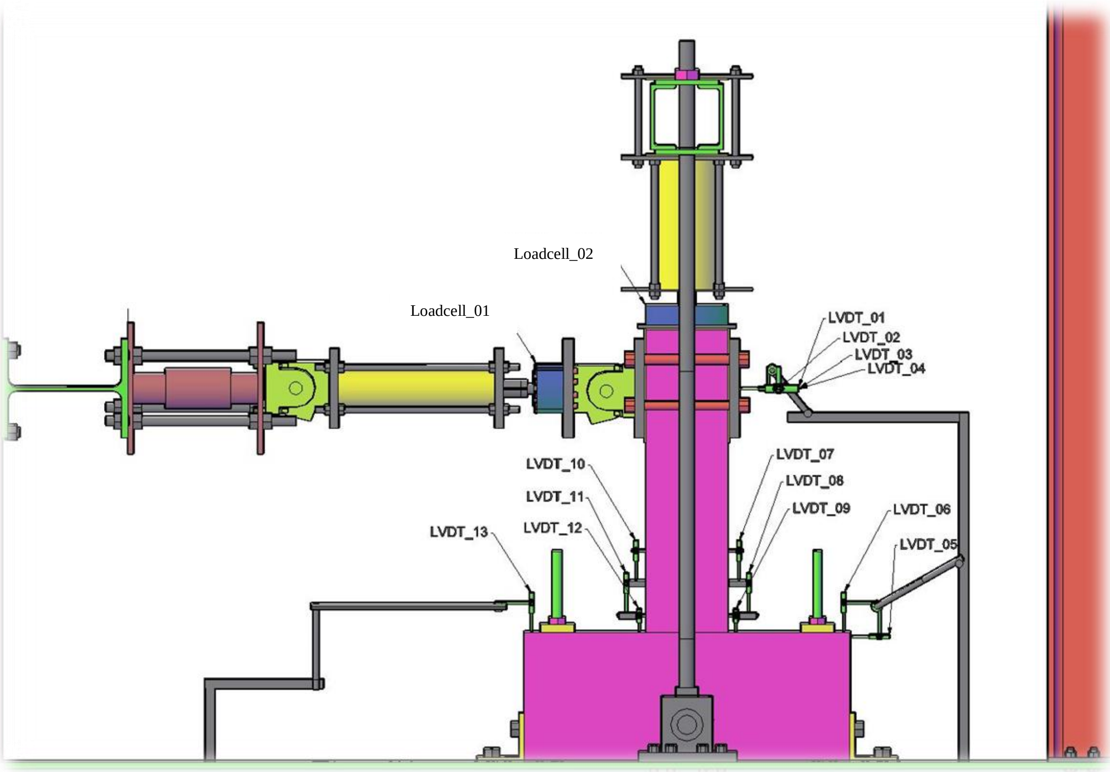

Figure 3.44 LVDT labeling

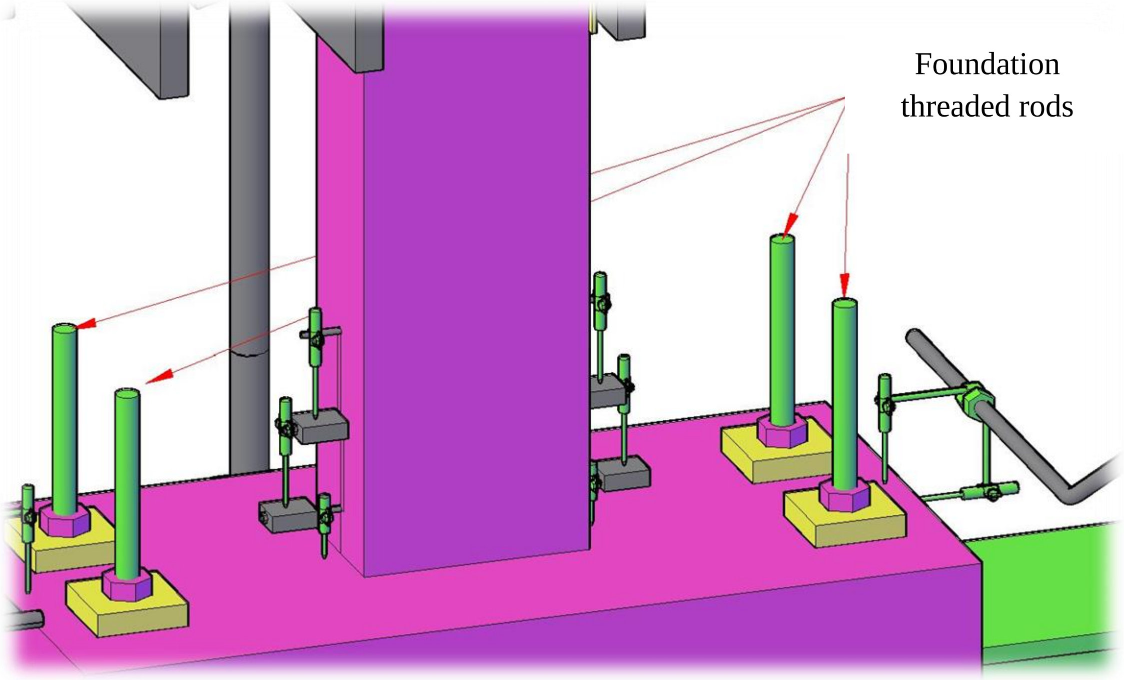

Figure 3.45 Details of foundation threaded rod

To prevent upward rotational displacement of the foundation during testing, four 24 mm diameter threaded rods were utilized. The lower ends of these rods were anchored to the supporting beam beneath the setup using nuts. At the top ends, each rod was secured with a 20 mm thick steel washer, measuring 100 × 100 mm, and fastened with nuts. Even a slight rotational movement at the base of the specimen could lead to significant measurement errors during the experiment. Consequently, two LVDTs were positioned at both ends of the foundation to monitor and ensure the accuracy of the test outcomes.

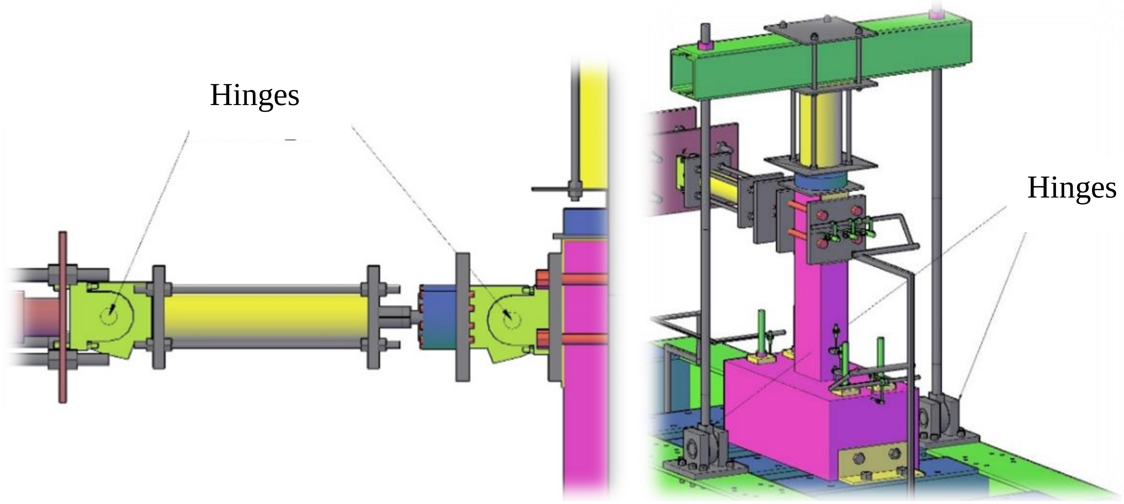

Figure 3.46 Details of hinges

During lateral loading, the hydraulic actuator is subjected to potential buckling due to the column's circular motion around its plastic hinge region. To mitigate this risk, two hinges (also known as rod end bearings) were installed on both sides of the lateral actuator. This configuration allows the actuator to follow the column's movement path, enabling smooth force transmission in the intended lateral direction.

Similarly, two additional hinges were incorporated to ensure that the vertical actuator used for axial loading can displace in sync with the column's lateral motion while maintaining vertical load application. The vertical load is transmitted through robust steel rods connected to these bearings, forming a closed system that permits controlled vertical displacement in coordination with lateral deformation.

3.2.7. Testing procedure

The test specimens, including monolithic and demountable types, are subjected to lateral loading at a height of 750 mm from the base, specifically in the strong axis direction, to address the more critical scenarios. The reversed-cyclic loading protocol follows the guidelines set forth in the ACI 374.2R-13 [150]. The loading protocol consists of double-cycle lateral drifts of 0.10%, 0.25%, 0.50%, 0.75%, 1.00%, 1.50%, 2.00%, 2.50%, 3.00%, 3.50%, 4.50%, and 6.00%, consisting of 24 cycles (**Figure 3.47**). An axial load, equal to 10% of the column's axial load-bearing capacity, calculated from the compressive strength of geopolymer concrete and the gross sectional area, is applied at the start of the test and maintained for its duration, except in the case of GDC1. The testing involves using cyclic lateral and constant axial loads at the upper end of the specimens until a reduction of at least 20% in ultimate capacity is observed [150, 151].

The explanation for no axial load applied during the testing of GDC1 is that the specimen GDC1 is designed to be a reinforced concrete footing serving as a column base connection. This connection was intended to be superior as far as economic concerns are taken into consideration. However, this connection is more critical for the early cracking of the concrete footing under lateral load demands. For this purpose, this specimen is first tested under no axial load, which results in more rigorous test conditions. However, the GDC1 specimen failed due to early cracking at the RC footing level, and the tested column showed no signs of plastic hinge formation. Consequently, no further testing was performed on this type.

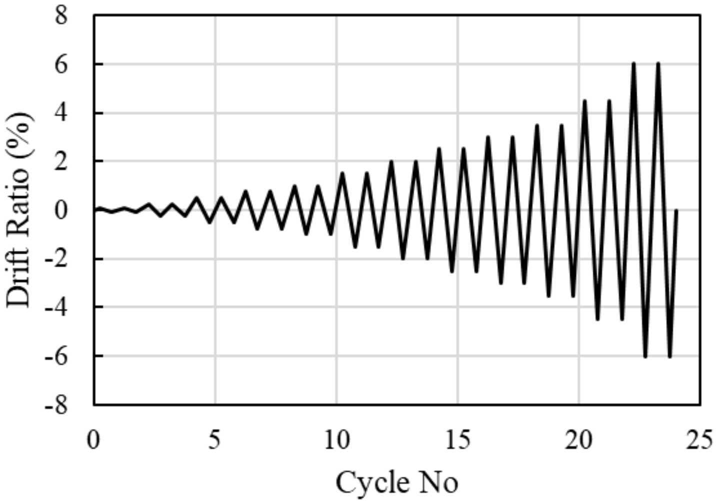

Figure 3.47 Loading protocol.

3.2.8. Data processing

The lateral displacement measured at the upper part of the column using LVDTs D_{1-4} comprises both the lateral displacement caused by the foundation's sliding and overturning as well as the columns' net displacement. To obtain the net lateral displacement (δ_{net}) of columns, the lateral displacements due to the foundation's sliding ($\delta_{sliding}$) and overturning ($\delta_{overturning}$) should be subtracted from the measured lateral displacement ($\delta_{measured}$). The computation for the net lateral displacement is outlined in **Eqs. (3.2** and **(3.3**.) The symbols used in **Eq. ((3.3)** are illustrated in **Figure 3.48**. Then, the drift ratio, Δ, is evaluated based on the ratio of the net lateral displacement to the clear span of the column (i.e., L=750 mm), as calculated in **Eq. (3.4)** Additionally, for demountable specimens, the relative displacement between the steel end plate and the foundation was calculated with the help of two LVDTs that measure lateral displacement of the steel endplate and the foundation. The maximum observed relative lateral displacement between the steel end plate and the concrete foundation was recorded for specimen GDC-0.30, and approximately 0.8 mm at 3.0% drift ratio. The measured maximum magnitudes of the relative displacement for demountable specimens were too lower than the measured lateral displacement, so the relative displacement was deemed negligible for calculations.

$$\delta_{net} = \delta_{measured} - \delta_{sliding} - \delta_{overturning} \quad \textbf{(3.2)}$$

$$\delta_{net} = (DT_2 + DT_3)/2 - DT_{11} - (DT_{13} - DT_{12}) \times h'/w_{12-13} \quad \textbf{(3.3)}$$

$$\Delta = \delta_{net}/L \times 100 \quad \textbf{(3.4)}$$

where h' refers to the height of DT_{1-4} from the base of the foundation.

To ensure accuracy when applying an axial load (*N*), it’s important to adjust the lateral load (P) depending on where the axial load is applied. If the upper part of the column is moved laterally, the post-tensioning rods become slanted and generate an additional lateral load. To obtain the net lateral load, this additional lateral load due to the axial load must be subtracted from the applied lateral load, using **Eq. (3.5**)

$$P_{net} = P - N\,\delta_{net}/h \quad \textbf{(3.5)}$$

where h refers to the vertical distance between the base of the foundation and the top of the column where the axial load is applied.

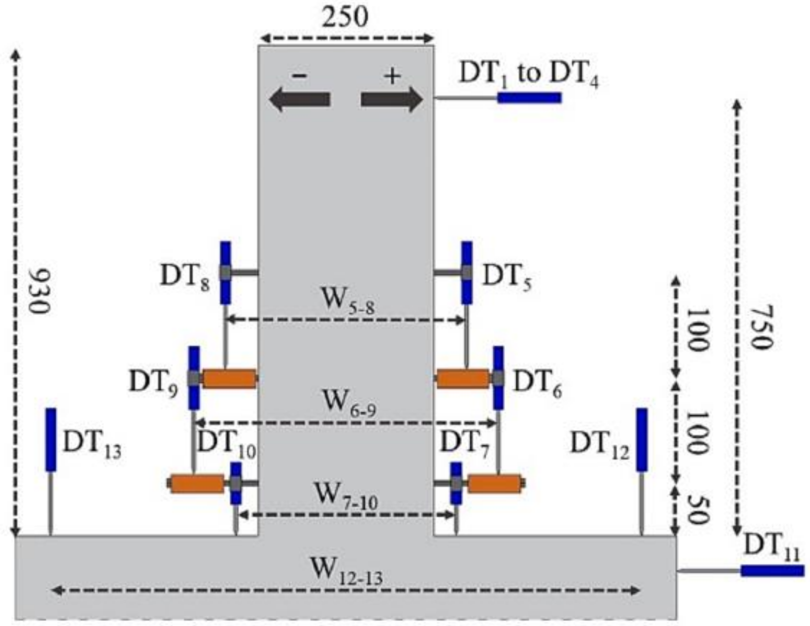

Figure 3.48 Arrangement of the LVDTs (unit: mm).

Some of the performance parameters including cyclic displacement ductility and effective stiffness are calculated based on the principle of an equivalent energy elastic-plastic (EEEP) determined as per ASTM E2126 [151] from the envelope curves of the specimens. In this principle, the load – displacement curve is represented by two lines. The slope of the first line (i.e., elastic portion) is found by drawing a line between origin and the point on the curve with an ordinate of $0.40P_{max}$. Then, the area of the curve and the bilinearized representation is tried to be matched by changing P_y. It should be noted that, in this calculation, the end point of the test curve is taken as $0.80P_{max}$ as per ASTM E2126. In summary, ASTM E2126 recommends the well-established equivalent energy method to be used to calculate the drift ratios and the loads that caused yielding.

3.3. Beam-to-column connection

3.3.1. Material properties

In order to accurately assess the structural performance of the demountable cantilever beam specimen subjected to a bending test, the mechanical properties of the constituent materials were determined. These include the compressive strength of concrete and the yield and ultimate strengths of reinforcing steel.

3.3.1.1. Concrete

The concrete mix used in the slab specimen was designed for a target compressive strength of C30/37. Standard 150 mm × 150 mm × 150 mm cube specimens were prepared and cured under same conditions of beam specimens. In order to reduce the curing time, CEM I 52.5 R type high-strength cement was used with a water-to-cement ratio of 0.50 and a superplasticizer. The beam specimens reached sufficient compressive strength approximately 10 days after casting and were subsequently subjected to testing. The average compressive strength of three specimens was found to be around the 40 MPa.

3.3.1.2. Reinforcing Steel

S420 grade reinforcement was used in the production of the beam specimens.

Steel plates used in the production of the specimens have a nominal yield strength of 235 MPa and an ultimate strength of 360 MPa.

3.3.2. Test specimens

The beam-to-column connection was designed as a simple support that restrains both in-plane and out-of-plane deflections, while allowing rotational movement under gravity loading. To investigate the performance of this connection detail, one reinforced concrete

(RC) column and three RC beams were fabricated using conventional concrete and structural steel components.

The column had cross-sectional dimensions of 400 × 400 mm and a height of 1000 mm. It was reinforced with eight 16 mm diameter longitudinal bars, and 10 mm diameter stirrups placed at 50 mm spacing in the confinement zone and 100 mm spacing above. To enhance the shear transfer capacity and facilitate the beam connection, the upper 500 mm of the column was encased with perforated steel plates. Beneath these plates, 100 × 100 × 10 mm equal angle sections were welded with stiffeners to resist shear forces effectively.

At the beam–column interface, a steel socket, fabricated from thick steel angle profiles, was welded onto the perforated steel plates to enable a more efficient and precise on-site connection and to minimize deflection under load. This socket served both as a guide for beam placement and as a structural component to distribute loads.

The fabrication stages of the column head are illustrated in the images below. During construction, 100 × 100 × 10 mm L-profiles were installed to support the seating of the beams. These L-profiles were reinforced at each beam-bearing point with four 10 mm-thick stiffener plates, ensuring local load-bearing capacity.

Considering the brittle behavior of welds, particularly under seismic or impact loading, additional reinforcement was introduced using three high-strength threaded rods (tie rods) of 24 mm diameter at each beam support location. These tie rods enhanced the mechanical connection between the L-profiles and the concrete core of the column. The tie rods were designed to carry shear forces independently in case the welds became insufficient. Nuts were placed on both ends of each rod to prevent pull-out failure under tensile loading.

Some of the steel plates used in the column head were manufactured with perforations or internal voids to reduce the volume of steel used and to minimize air entrapment during casting, which can compromise bond strength. Additional channel sections and angle profiles were welded from the interior face of the column head to ensure alignment and facilitate beam installation. These profiles were installed with a slight downward slope to eliminate the risk of binding or misalignment during the placement process.

Finally, a cover plate was welded on top of the column head assembly, unifying all steel components and ensuring full load transfer between the beam and column through the integrated steel connection system.

Figure 3.49 Details of demountable column head

Primarily produced beam specimen shown in the figure below was designed using the same reinforcement and steel plate configuration as in the actual column design of DC 4, with the only difference being that the surface in contact with the column was made flat for overlapping. However, this design was later abandoned for use in the beam elements. The primary reasons were the difficulty in aligning and fixing the holes on the bottom plates of the columns and the impracticality of ensuring proper alignment of seven such holes for each beam connection across the entire structure. As a result, the beams were redesigned to function with pin-type connections to simplify assembly and improve constructability

Figure 3.50 Details of primarily produced demountable beam specimen

The other two demountable beam specimens are designed as a pin-type connection. Beams with cross-sectional dimensions of 300 × 500 mm and a length of 1800 mm was produced with six longitudinal reinforcements of 20 mm in diameter and stirrups of 10 mm in diameter. The end of the beams was surrounded by steel plates and longitudinal reinforcements welded to the end plate. In the first demountable beam design, 8 mm-thick base plates were used to weld jacket plates. Additionally, 8 mm inner plates were welded to the interior face of the beam, and the longitudinal reinforcement bars were welded directly to these inner plates. However, this design encountered significant limitations. The base plate extended 5 cm beyond the beam edges on each side, and due to spatial constraints, especially the closeness to the steel plate located at the column top, it was not feasible to position the beam closely against the column edge. As a result, the beam width had to be at least 15 cm shorter than the column width in that direction, which proved structurally and practically inadequate. Consequently, this beam configuration was deemed unsuccessful.

As shown in the images below, the final pin-type demountable beam design did not extend beyond the beam edges and offered a more compact and effective solution. In this design, the steel channel sections used for the connection were carefully dimensioned so that their width did not exceed that of the beam, making them compatible with the steel plates placed at the top of the column.

At the ends of the beam, T-profiles were utilized. These were designed to allow limited displacement while still enabling some moment transfer. A thick steel plate was welded across the top of the T-profiles to enhance their connection both to each other and to the beam web, improving the transfer of shear forces.

At the lower portion of the beam, 8 mm and 10 mm thick steel plates were first welded to the base, followed by welding of longitudinal reinforcement bars to their outer faces. To confine the concrete in the joint region, thin jacket plates were placed around the longitudinal bars, enclosing the concrete and enhancing the connection’s strength and ductility. This configuration was ultimately adopted in the final structure.

Figure 3.51 Preparation of pin-type demountable beams

The main body of the demountable beam is presented in the image below. Several key connection details are visible here, which were specifically designed to enable the pin-type connection of slab elements to the beam. Thin steel plates with a thickness of approximately 3–4 mm was incorporated to serve as guides for the anchor bolts and to enhance the reliability of load transfer between the slabs and the beam.

Inside the beam, two nuts were welded together in a stacked configuration to form an internally threaded anchor. Reinforcing bars were welded around this threaded insert to ensure the effective transfer of vertical loads. The ends of these bars were bent to reduce the required anchorage length. The bending was designed to be minimal in length to prevent complications during assembly.

The primary purpose of this connection design is to resist uplift forces on the slabs during seismic events and to prevent differential vertical movement. This ensures that the slabs move integrally with the beam and are protected from dynamic impact forces that may result from mutual collision.

During assembly, it is essential to place an elastomeric layer between the beam and the slab to absorb potential vibrations and accommodate minor deformations, further enhancing the structural resilience of the system.

Figure 3.52 Structural details of beam body with pin-type slab connection via tie rods

3.3.3. Test setup and instrumentation

The test setup was designed to investigate the flexural and shear behavior of demountable reinforced concrete (RC) beam-to-column connections under monotonic vertical loading. The beam-to-column connection was constructed as a slip-in (socketed) system without any mechanical fasteners, simulating a demountable assembly. The supports were configured as pinned connections, allowing free rotation while restraining translational movements.

A clear span of 1600 mm was maintained between the support points. The RC beam specimen was subjected to a concentrated point load applied at end-span through a hydraulic actuator. The actuator, with a stroke capacity of 333 mm and a maximum load capacity of 750 kN, was mounted on a rigid steel reaction frame. To avoid unintended eccentric loading, hinge joints were placed at both ends of the hydraulic cylinder, allowing self-alignment during load application. A steel bearing plate was used at the loading point to ensure uniform stress distribution on the concrete surface.

A total of 15 Linear Variable Differential Transformers (LVDTs) were strategically placed along the specimen to capture local and global deformations. These displacement transducers were used to measure:

- Rotational deformations at the beam ends and near the plastic hinge zone,
- Flexural displacements in the plastic region and mid-span,
- Relative slip between the beam specimen and column head and column head to ground surface,
- Rotational deformation column head

The LVDTs were fixed to rigid frames or steel bases independent from the beam, ensuring that measurements reflected true structural behavior rather than setup movement. Additional instrumentation included a load cell integrated with the actuator and a high-speed data acquisition system.

Below figures shows the complete test setup and instrumentation layout used in the beam-to-column connection test.

Figure 3.53 Flexural test setup of the demountable beam to column connection

The shear capacity of the designed column head was assessed using a steel beam in the loading setup. No displacement transducers (LVDTs) were utilized in this test; instead, the applied shear force was recorded solely through the load cell integrated with the actuator.

Figure 3.54 Shear test setup of the column head

3.3.4. Testing procedure

The beam specimen was tested under displacement-controlled loading to evaluate the flexural strength. Loading was applied monotonically, targeting to see pin like behavior at the supports with the minor crack at beam body.

Prior to the main test, a small preload of approximately 5 kN was applied to ensure proper seating of the beam and the actuator. The load was subsequently increased until the target displacement was observed. Throughout the test, the applied load, vertical displacement, and LVDT readings were continuously recorded.

Special attention was given to the development of:

- Flexural cracks in the plastic region,
- Relative movement at the support and connection zones,

Visual inspection and photographic documentation were conducted at each load increment. The LVDT readings were monitored in real time to detect the crack propagation and to validate failure mechanisms.

The bending and shear capacity of the beam-to-column connection were separately tested by bending and shear tests, respectively. Under bending, the beam-to-column connection illustrated sufficient rotation and bending capacity with minor cracking in the beam and limited deformations in the steel socket (as illustrated at below figures). The shear capacity of the connection was determined by applying shear load on the equal angle profile which transferred shear loading from beam to column, with the help of an I-shaped steel profile.

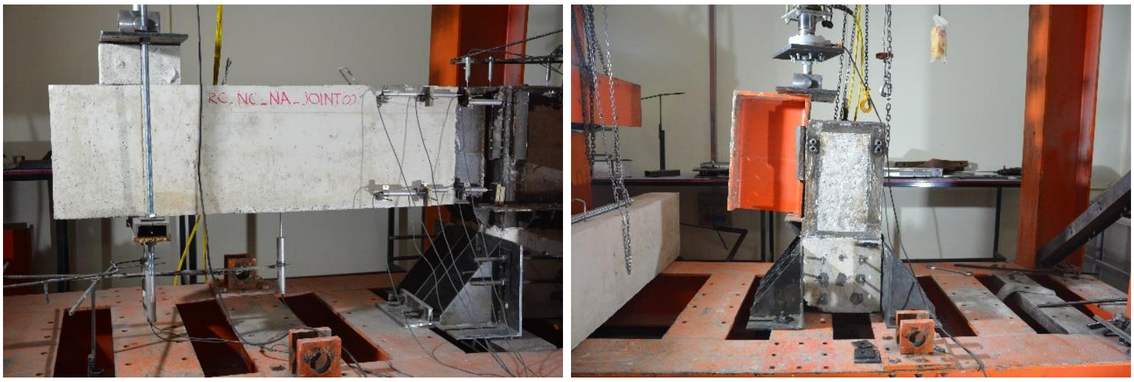

3.3.5. Data processing

The raw data collected from the load cell and LVDTs were post-processed using Excel to evaluate the structural response of the beam. Data processing steps included:

- Noise filtering using a low-pass digital filter to eliminate signal fluctuations,
- Derivation of load-displacemen curves and identification of ultimate points,
- Calculation of rotational deformations based on differential LVDT readings on the top and bottom surfaces of the beam
- Tracking of curvature distribution across the plastic hinge region

In addition, energy dissipation capacity was estimated by integrating the area under the load-displacement curve. Crack development and failure modes were correlated with

LVDT readings to ensure consistency between mechanical data and physical observations.

3.4. Slab-to-beam connection

3.4.1. Material properties

To accurately assess the structural performance of the demountable slab specimen subjected to a three-point bending test, the mechanical properties of the constituent materials were experimentally determined. These include the compressive strength of concrete, the yield and ultimate strengths of reinforcing steel, and any additional materials used in demountable connections, such as bolts or plates.

3.4.1.1. Concrete

The concrete mix used in the slab specimen was designed for a target compressive strength of C30/37. OPC CEM I 42,5 R grade was utilized for the specimens. The water-to-cement ratio was 0.5. Standard 150 mm × 150 mm × 150 mm cube specimens were prepared and cured under the same conditions as slab specimens. The compressive strength test was carried out at 28 days in accordance with TS EN 12390-3. The average compressive strength of three specimens was found to be around 37 MPa.

3.4.1.2. Reinforcing Steel

Tensile tests were performed on samples taken from the same batch of reinforcement used in the column specimen, following the procedures specified in TS EN ISO 6892-1. Details of the tensile strength of the reinforcement bars are given in the previous column chapter.

In the support connections, grade 8.8 bolts were used, with a nominal yield strength of 640 MPa and ultimate strength of 800 MPa. Also, steel plates used in the support have the nominal yield strength of 235 MPa and ultimate strength of 360 MPa.

3.4.2. Test specimens

To explore the capacity of the proposed demountable slab-to-beam connection system, a test specimen consisting of a reinforced concrete slab and two supporting beams was produced using conventional concrete. The slab element was cast with dimensions of 200 mm in depth, 800 mm in width, and 3670 mm in length. To enable mechanical connection to the beams, four steel square hollow sections (SHS), each measuring 50 × 50 mm in cross-section and 200 mm in height, were embedded within the slab during casting. These profiles served as designated anchoring points for the tie rods. 10 mm diameter reinforcement bars were used throughout the specimen. Along the longitudinal direction, a total of 14 bars were placed at 100 mm spacing, both at the top and bottom faces. In the transverse direction, 10 mm bars were placed at 150 mm spacing. As shown in the figures below, additional reinforcement was provided near the support regions to enhance shear capacity and ensure more effective transfer of support reactions at the connection zones.

Figure 3.55 Details of demountable slab

3.4.3. Test setup and instrumentation

The three-point bending test was conducted in the structural engineering laboratory to investigate the flexural behavior of the demountable slab specimen. The specimen was simply supported at both ends and subjected to a monotonic vertical load applied at mid-span using a hydraulic actuator.

The slab was connected to the beam using grade 8.8 threaded steel rods with a diameter of 24 mm, along with square washers measuring 80 × 80 × 10 mm. The threaded rods were positioned such that the edge distance was 120 mm along the long axis and 100 mm along the short axis of the slab to ensure sufficient concrete cover and anchorage performance.

During assembly, a rubber sheet was placed at the junction of the beam and the slab. This was done to minimize the effect of surface irregularities and to improve contact behavior under loading. The overall connection design allowed the slab to be demountable while ensuring sufficient load transfer and rotational flexibility.

A hydraulic cylinder with a stroke capacity of 333 mm and a maximum load capacity of 750 kN was affixed to the reaction frame to apply the vertical force through a steel loading head. Hinges were installed at both ends of the hydraulic cylinder to prevent eccentric loading.

The load was applied with a 98 mm wide plate through a line that crosses the slab in a transverse direction at mid-length of the slab. The displacements of different locations on the slab were recorded with the help of LVDTs.

Instrumentation included the following components:

- Load cell integrated with the hydraulic actuator to record the applied load.
- Nine LVDTs (Linear Variable Differential Transformers): three located directly under the mid-span, two placed symmetrically at quarter-span points to measure deflections, two LVDTs located to measure the tilting of the beam supports, and two located to measure the separation of the beam and slab at the supports.
- A high-resolution camera was positioned at the front side to document crack development throughout the test.

All sensors were connected to a data acquisition system recording data at a sampling rate of 10 Hz. The test setup and instrumentation layout are shown at below.

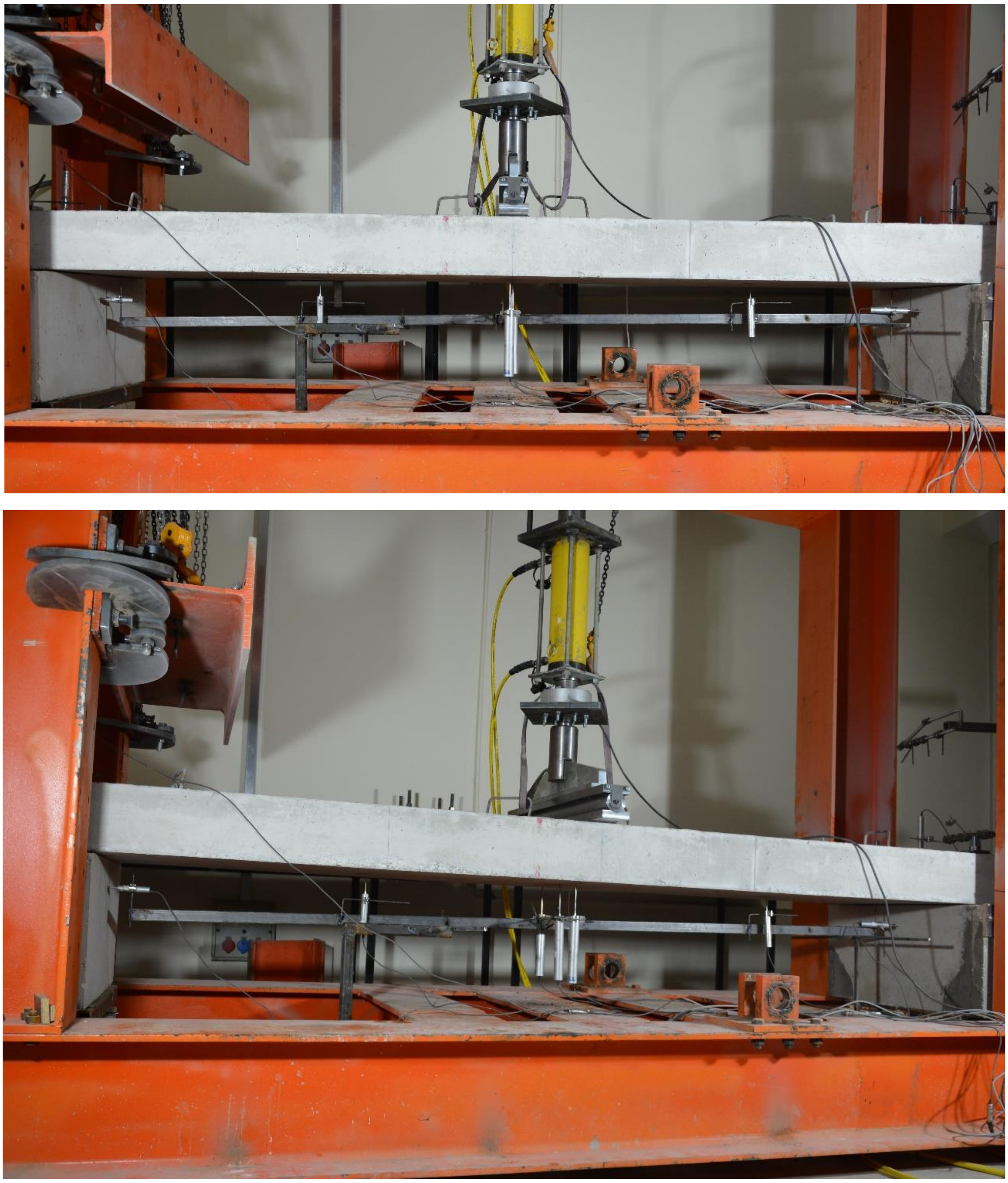

Figure 3.56 Test setup of the demountable slab

Figure 3.57 Details of the demountable slab test setup

3.4.4. Testing procedure

The test was carried out under monotonic displacement-controlled loading. The vertical displacement was applied through the hydraulic actuator, following standard experimental procedures for flexural testing of concrete elements.

Before starting the actual test, the system was calibrated, and a small preload of 2–5 kN was applied to ensure full contact between the supports and the specimen. Following this, displacement was applied continuously until visible cracking, yielding of reinforcement, and ultimately failure of the slab occurred. Key observations were recorded throughout the test, including:

- Initial cracking load
- Crack propagation
- Concrete crushing
- Failure mode (flexural, shear, or combined)

Photographs were taken periodically to document the formation and progression of cracks.

The test was terminated by excessive deflection beyond L/240, where L is the clear span of the specimen.

3.4.5. Data processing

The raw data obtained from the loadcell and LVDTs were processed to evaluate the structural behavior of the slab. The data were exported to Excel for further analysis.

The following steps were carried out:

- Filtering: Raw signals were checked for noise and, if necessary, smoothed using a moving average filter.
- Load-displacement curve: A primary graph showing the applied load versus end-span deflection was plotted to evaluate ultimate capacity.
- Crack pattern analysis: Using photographic evidence and visual inspection, the number, location, and width of cracks were identified and documented.

EXPERIMENTAL RESULTS AND DISCUSSION

This chapter draws upon three peer-reviewed journal articles and presents the main experimental findings of the study, with a particular focus on the seismic performance of the tested specimens. The analysis covers key parameters such as failure modes, crack patterns, load-displacement behavior, displacement ductility, energy dissipation, stiffness degradation, moment-curvature relationships, axial load effects, plastic hinge development, and overall damage evaluation.

The chapter begins with a detailed assessment of the experimental results for demountable column-to-foundation connections, combining relevant findings from all three articles. It then provides concise overviews of the beam-to-column and slab-to-beam connection tests, which were designed as pinned connections, so they were evaluated shortly.

4.1. Development and investigation of demountable column base connection

In this section, the seismic performance results of three complementary experimental studies are collectively evaluated to provide a comprehensive understanding of demountable **column**-base systems constructed with sustainable concrete. In the first study's name is **Fully Demountable Column Base Connections Design**. In that study, various column base configurations were tested to identify the most effective design under cyclic loading. The configuration demonstrating the best performance was then selected for further investigation. The second study's name is **Structural Performance of CDW-Based Geopolymer Concrete Columns.** In that study, the selected novel column base design with CDW-based geopolymer was tested under different axial load conditions and compared to a monolithic counterpart to assess its robustness and load-bearing capacity. The third study's name is **Damage Characteristics and Seismic Response of Demountable RC Column Base Joints**. In that study, similar tests were conducted using conventional concrete to evaluate the repeatability of the findings and to compare the seismic behavior of monolithic and demountable specimens. Additionally, the damage characteristics of the specimens were analyzed in detail. Across all studies, critical performance parameters such as failure modes, load-displacement behavior, energy dissipation capacity, stiffness degradation, and moment–curvature response were examined to comprehensively assess the structural efficiency and reusability of the proposed demountable systems.

4.1.1. Mode of failure and crack propagation

Understanding the failure mechanisms and crack propagation behavior of structural systems is essential for assessing the seismic performance and ductility of precast and demountable elements. In this context, three independent studies investigated the failure patterns of various column-base connection assemblies developed with sustainable concrete, aiming to explore innovative and reusable joint strategies under cyclic loading.

Failure states are identified as cracking, cover concrete crushing, core concrete crushing, and footing failure. In the first study, detailed observations of crack propagation and damage mechanisms in columns with different base connection details were reported, highlighting the influence of anchor arrangements and confinement on structural integrity. The second study analyzed the damage progression in various demountable joint configurations, noting distinct crack trajectories depending on joint flexibility and axial loading conditions. Finally, the third study presented experimental evidence on the failure modes of demountable assemblies under cyclic loading, emphasizing connection details can significantly influence plastic hinge formation and energy dissipation capacity.

4.1.1.1. Fully Demountable Column Base Connections Design

The failure state of the specimens in the first study is shown in **Figure 4.1** at the end of all tests. Failure of specimen GMC1 is concentrated at the column-foundation joint, where cracks and concrete crushing occur. The first crack during the test of specimen GMC1 is observed at a drift ratio of 0.50% near the column-foundation joint. When displacement levels increase, the number and size of cracks increase and are distributed along the column. The cracks in the joint between the column and foundation widen at a 2.00% drift ratio. When the drift ratio reaches 2.50%, concrete crushing is noted in the corner of the column-foundation joint. Beyond a 2.50% drift ratio, the concrete crushing in this area escalates and spreads. Importantly, there was no recorded buckling in the longitudinal rebars throughout the test.

The failure states of specimens GDC1 to GDC3 are similar, where limited cracks appear in the area where the plastic hinge is desired to form during the test which induce that large deformation in the column footing. At the column-footing joint, the size of cracks increases as displacement levels increase. The concrete cover of the footings is crushed (i.e., footing concrete between column and bolt locations). This can be attributed to the load transfer mechanism of the column footing, which carries the load from the column that is subsequently transferred to the foundation, which does not have sufficient rigidity. So, plastic hinge formation is not observed in specimens GDC1 to GDC3.

(a) (b) (c) (d) (e)

Figure 4.1 Failure states of specimens: (a) GMC1, (b) GDC1, (c) GDC2, (d) GDC3, and (e) GDC4.

The formation of cracks, cover concrete crushing, core concrete crushing, and longitudinal rebar buckling is observed in specimen GDC4. The first crack appears on the tension side at the drift ratio of 0.50%. When displacement levels increase, the number and size of cracks increase. The first concrete crushing and the first core concrete crushing occur at the drift ratios of 2.50% and 3.50%, respectively. The initial buckling of the longitudinal rebars with a half wavelength of 50 mm on the column is observed at a 4.50% drift ratio. The plastic hinge of 200 mm long occurred at the zone that starts from the steel jacket to the end of the anchorage rods. This can be attributed to the effect of the anchorage rods, which carries part of the load that is subsequently transferred to the reinforcement bars. Additionally, the steel jacket is able to offset the plastic hinge formation from the column joint and prevents joint openings and concrete crushing at this zone. **Figure 4.2** demonstrates the damage progression of specimen GDC4.

(a) (b) (c) (d)

Figure 4.2 Damage progression of the GDC4 at drift ratios of: (a) 0.50%, (b) 2.00%, (c) 3.00%, and (d) 4.50%.

The failure modes of the specimens GDC1, GDC2, and GDC3 are similar to each other and observed due to insufficient flexural rigidity of the column footing. Therefore, the plastic deformations focused on a small area in conjunction of the column with the footing, as shown in **Figure 4.3**(a), and seismic performance parameters (e.g., maximum lateral load capacity) of the specimens are governed by the footing performance. On the other hand, specimen GDC4 exhibits ductile behavior with column hinging. The column's base plate has sufficient flexural rigidity so that the column experiences cracking, concrete spalling and crushing, and longitudinal rebar buckling, resulting in high energy absorption, and high maximum lateral load capacity (**Figure 4.3**(b)). In addition, the use of the anchorage rods leads to an increase in plastic deformations including concrete spalling and crushing, which spread over a longer area than its monolithic counterpart.

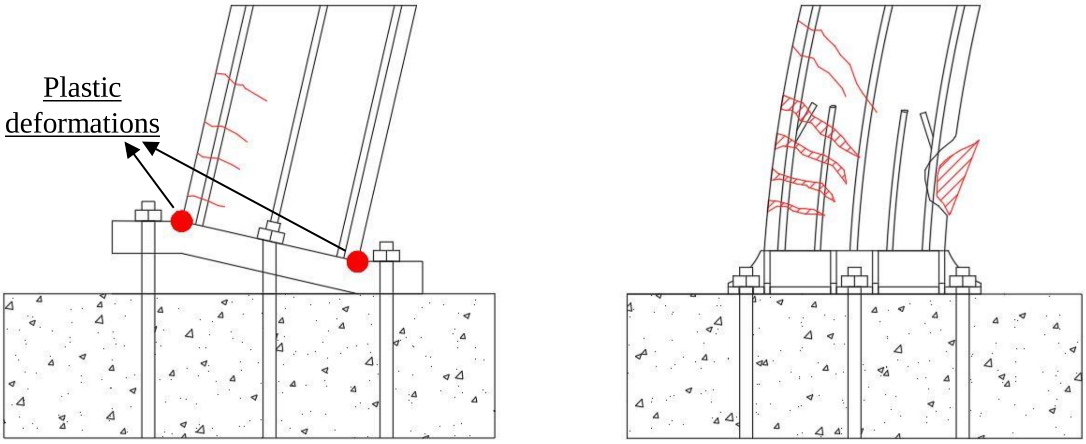

(a) (b)

Figure 4.3 Schematic representation of the observed failure mechanism of specimens: (a) GDC1, GDC2, and GDC3, and (b) GDC4.

4.1.1.2. Structural Performance of CDW-Based Geopolymer Concrete Columns

In the second study, the crack propagation and observed failure modes of the CDW-based geopolymer concrete monolithic specimens are presented in **Figure 4.4**. All cracks in monolithic specimens were distributed on the column. Cracks, concrete crushing and spalling, and core crushing were observed through the testing of monolithic specimens.

For specimen GMC-0.10, the first fine horizontal cracks appeared at the columns' end when the drift ratio reached Δ=-0.50%. When the displacement continued to increase, the existing cracks gradually expanded and the number of cracks increased. The number of cracks in the push and pull directions were nearly equal to each other. At the same time, limited slight and short cracks were observed at the surface of the columns that were 250 mm above the foundation. The maximum positive and negative lateral load capacities were obtained at Δ=2.23% and Δ=-2.83%, respectively, leading to the concrete crushing. When the drift ratio reached Δ=-3.50%, significant concrete crushing, and spalling occurred at the edges of the specimen. The confined concrete zone of the specimen started to crush at drift ratios of Δ=4.50%, resulting in the failure of the specimen. In addition, no buckling occurred at the longitudinal reinforcements.

The crack propagation and failure mode of the specimen GMC-0.20 with a 20% axial compression ratio were similar to that of the GMC-0.10. The first fine horizontal cracks occurred at the tension zone when the drift ratio was equal to Δ=-0.50%. The maximum positive and negative lateral load capacities of the specimen were, respectively, obtained at Δ=2.29% and Δ=-1.95%, then reduced due to concrete crushing and spalling. At the end of the first and second cycles of Δ=3.50%, the specimen failed due to the crushing of the confined concrete zone.

The last monolithic specimen, GMC-0.30 with a 30% axial compression ratio, showed similar crack progression and failure to the other monolithic specimens. The first fine horizontal cracks were observed at Δ=-0.50%. The maximum positive and negative lateral load capacities of the specimen were, respectively, obtained at Δ=2.29% and Δ =-1.91% but this capacity decreased afterward because of concrete crushing and spalling. The specimen failed due to the spreading of concrete crushing to the confined concrete zone at the end of cycles of Δ=3.50%.

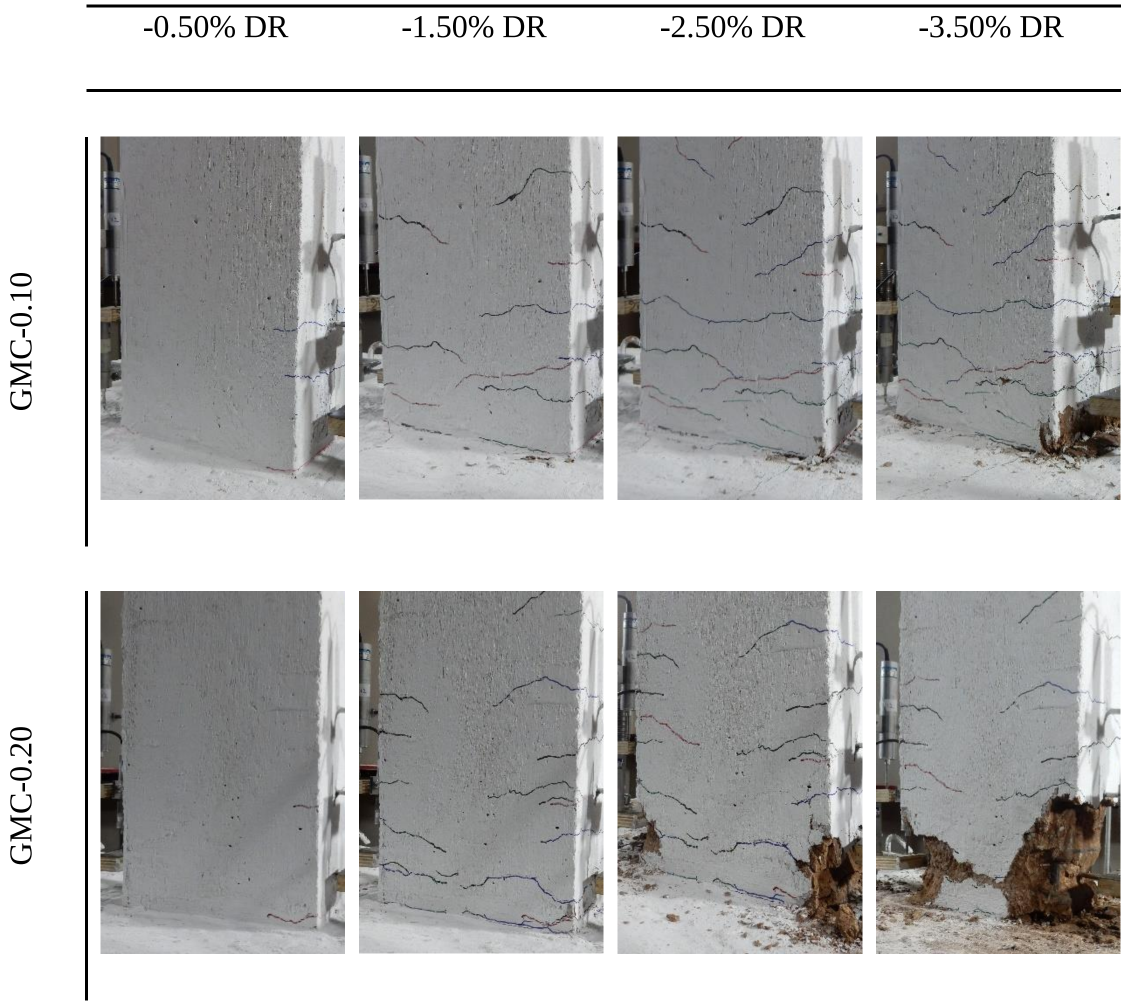

Figure 4.4 Observed failure modes at the monolithic specimens.

CDW-based geopolymer concrete demountable specimens exhibited typical reinforced concrete response with horizontal cracks, followed by diagonal crack propagation, concrete crushing and spalling and eventually buckling of the longitudinal rebars (as shown in **Figure 4.5**).

The first fine horizontal cracks of the specimen GDC-0.10 with a 10% axial compression ratio occurred at the tension zone which is above the steel jacketing when Δ=0.50%. Then fine horizontal cracks widened and propagated in an inclined direction having an angle of 45° to the center of the section. The maximum positive and negative lateral load capacities were, respectively, obtained at Δ=2.19% and Δ=-1.64%, with concrete crushing and spalling occurred on the edges of the column. When the drift ratio reached Δ=-3.50%, concrete crushing and spalling started to expand from the edge to the inner side of the specimen. GDC-0.10 (as depicted in **Figure 4.5**). The significant buckling of longitudinal reinforcements in compression sides of the specimen GDC-0.10 at Δ=4.50% and Δ=-4.50% resulted in the failure of the specimen.

Specimen GDC-0.20 with a 20% axial compression ratio showed a similar progression of crack and failure modes to the specimen GDC-0.10 at different drift ratios. The first fine horizontal cracks occurred at the tension zone when the drift ratio was equal to Δ=0.75%. Then, horizontal cracks spreaded over the plastic hinge zone and became wider. The thickness of the crack was relatively less than that of specimen GDC-0.10. The maximum positive and negative lateral load capacities of the specimen were, respectively, obtained at Δ=1.93% and Δ=-1.83%, then reduced due to concrete crushing and spalling. When the drift ratio reached Δ=-2.50%, significant concrete spalling occurred and most of the cracks were interconnected with each other. The confined concrete zone started to crush at both sides of the specimen GDC-0.20 at the end of the first and second cycles of Δ=3.00%. Buckling of longitudinal reinforcements at the compression zone of the specimen occurred when Δ=3.50% and Δ=-3.50%, resulting in the failure of the specimen.

The last demountable specimen, GDC-0.30 with a 30% axial compression ratio, showed similar crack progression and failure to the other demountable specimens. The first fine horizontal cracks were observed at Δ=0.75%. After the second cycle of Δ=1.50%, concrete crushing with limited size occurred in corners that are above the steel jacketing of the specimen. The maximum positive and negative lateral load capacities were obtained at Δ=1.87% and Δ=-1.48%, respectively, leading to significant concrete crushing and spalling. When the drift ratio reached Δ=-2.50%, concrete core crushing occurred at both sides of the specimen GDC-0.30. The concrete crushing and spalling spread over all edges of the specimen when the drift ratio reached Δ=3.00%. At the same time, the specimen failed due to concrete core crushing followed by a buckling of longitudinal reinforcements at the compression zones.

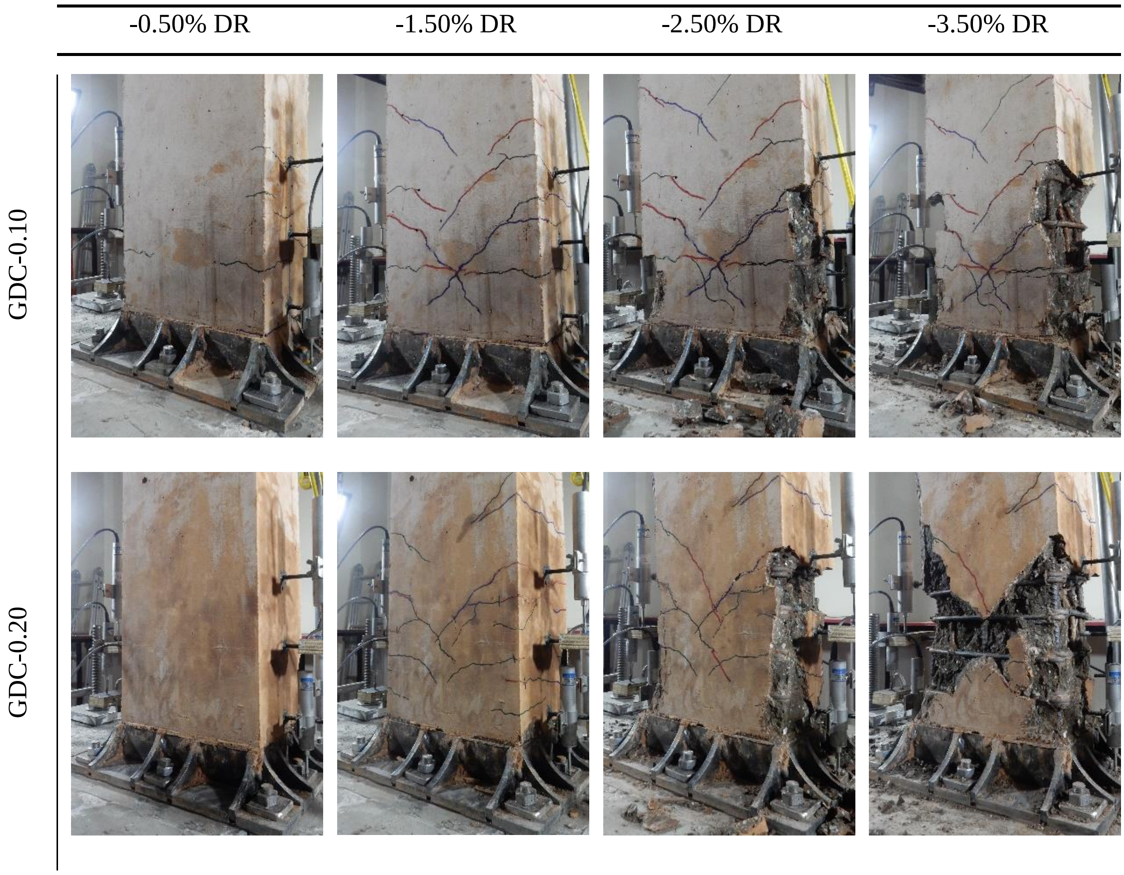

Figure 4.5 Observed failure modes at the demountable specimens.

4.1.1.3. Damage Characteristics and Seismic Response of Demountable RC Column Base Joints

When the failure modes of conventional concrete monolithic specimens were examined, cracks, concrete crushing and spalling, concrete core crushing, and longitudinal rebar buckling were observed sequentially, as shown in **Figure 4.6**. For specimen CMC-0.10, the first fine crack occurred at a drift ratio of 0.50%. The amount and size of the cracks increased in the confinement zone, especially between 0-150 mm above the top of the foundation. There were approximately the same number of cracks with similar thicknesses on both sides of the columns. The maximum positive and negative lateral load capacities were achieved at drift ratios of Δ=1.44% and Δ= -0.98%, respectively, resulting in the occurrence of wider cracks and concrete crushing. When the drift ratio reached Δ=2.50%, the thickness of the crack in the tension side of the column increased to nearly 1.5 mm. At a second cycle with a drift ratio of Δ=-3.00%, significant concrete crushing, and spalling were observed on both sides of the specimen. The confined concrete zone of the specimen started to crush at a drift ratio of Δ=3.50%, resulting in the buckling of longitudinal rebar with a half-wavelength of approximately50 mm at a drift ratio of Δ=4.50%.

The propagation of cracks and the observed failure modes in specimen CMC-0.20 were similar to those in specimen CMC-0.10. The initial fine horizontal cracks appeared in the tension zone when the drift ratio reached Δ=0.50%. The specimen reached its maximum positive and negative lateral load capacities at Δ=1.38% and Δ=-1.37% respectively, then decreased due to concrete crushing and spalling. The observed number of cracks was more than that of CMC-0.10, whereas the thickness of the cracks was less. When the drift ratio reached Δ=2.50%, the crushed and spalled area expanded from the edges to the center of the column’s sides. At the end of the first and second cycles with a drift ratio of Δ=-3.50%, the confined concrete zone on both sides of the specimen CMC-0.20 began to experience crushing. The specimen failed when the drift ratio reached Δ=4.50% and Δ=-4.50% due to the buckling of longitudinal rebar in the compression sides.

The last monolithic specimen with a 30% axial compression ratio, CMC-0.30, experienced similar crack progression and failure to the other monolithic specimens. The first fine horizontal cracks were observed at Δ=-0.50%. The maximum positive and negative lateral load capacities were achieved at drift ratios of Δ=1.36% and Δ= -0.97%, respectively, resulting in the occurrence of concrete crushing and spalling at the edges of the column. When the drift ratio reached Δ=2.00%, the crushed and spalled area expanded from the edges to the center of the column’s sides. The confined concrete zone on both sides of the specimen started to crush at a drift ratio of Δ=2.50%. The specimen failed when the drift ratio reached Δ=3.00% and Δ=-3.00% due to the buckling of longitudinal rebar in the compression sides. Concrete crushing and spalling occurred in the middle sections of both the front and back faces of the columns, in contrast to the other monolithic specimens.

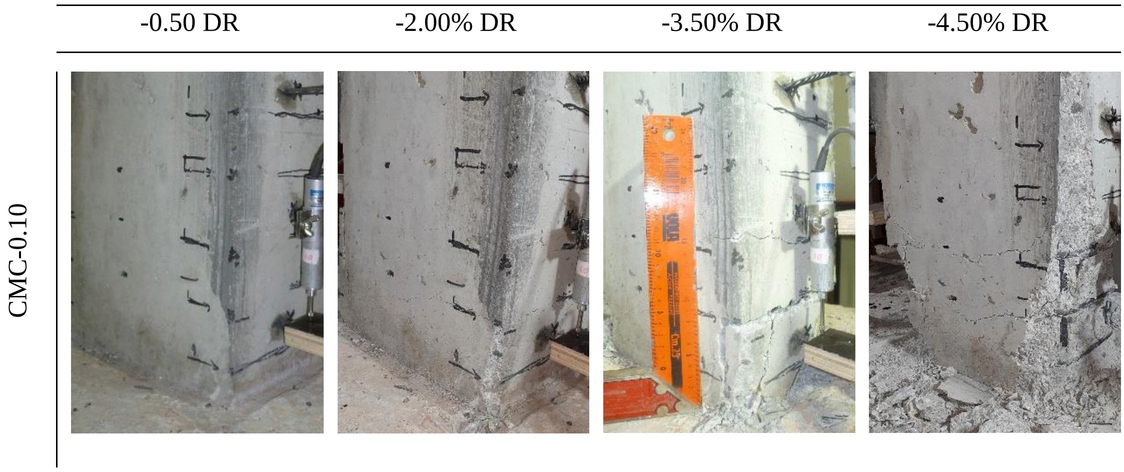

Figure 4.6 Damage progression in the monolithic specimens with increasing drift ratio

Bolted specimens exhibited similar damage progression to monolithic specimens, beginning with horizontal cracks and propagating of horizontal cracks to the center of the section with an angle of 45°, concrete crushing, and spalling, and finally buckling of the longitudinal rebars (as illustrated in **Figure 4.7**).

For specimen CDC-0.10, the first fine horizontal cracks occurred at the tension zones which are above the steel jacketing when a drift ratio reached -0.50%. Then, with an increasing drift ratio, the fine horizontal cracks expanded and elongated diagonally at an angle of 45° relative to the center of the section. The maximum positive and negative lateral load capacities, respectively, occurred at Δ=1.86% and Δ=-1.90% due to the concrete crushing. At the end of the first and second cycles of Δ=2.50%, significant concrete crushing, and spalling occurred on the edges of the column. When the drift ratio reached Δ=3.50%, the confined concrete zone of the specimen started to crush, leading to the buckling of the longitudinal rebar with a half-wavelength of ~50 mm at the end of the first cycle of Δ=4.50%. The observed damages accumulated in the sides of the columns where started from steel jacketing and ended at about 250 mm above the steel base plate.

The formation of damages including the progression of cracks, concrete crushing and spalling, and buckling of longitudinal rebars of specimen CDC-0.20 were similar to those in specimen CDC-0.10. The initial fine horizontal cracks appeared in the tension zone when the drift ratio reached Δ=-0.50%. The specimen reached its maximum positive and negative lateral load capacities at Δ=1.84% and Δ=-1.89% respectively, then capacity decreased due to concrete crushing and spalling at the edges of the column. At the end of the first and second cycles with a drift ratio of Δ=-3.00%, the confined concrete zone on both sides of the specimen began to experience crushing. The specimen failed when the drift ratio Δ=4.50% and Δ=-4.50% due to the buckling of longitudinal rebars in the compression sides.

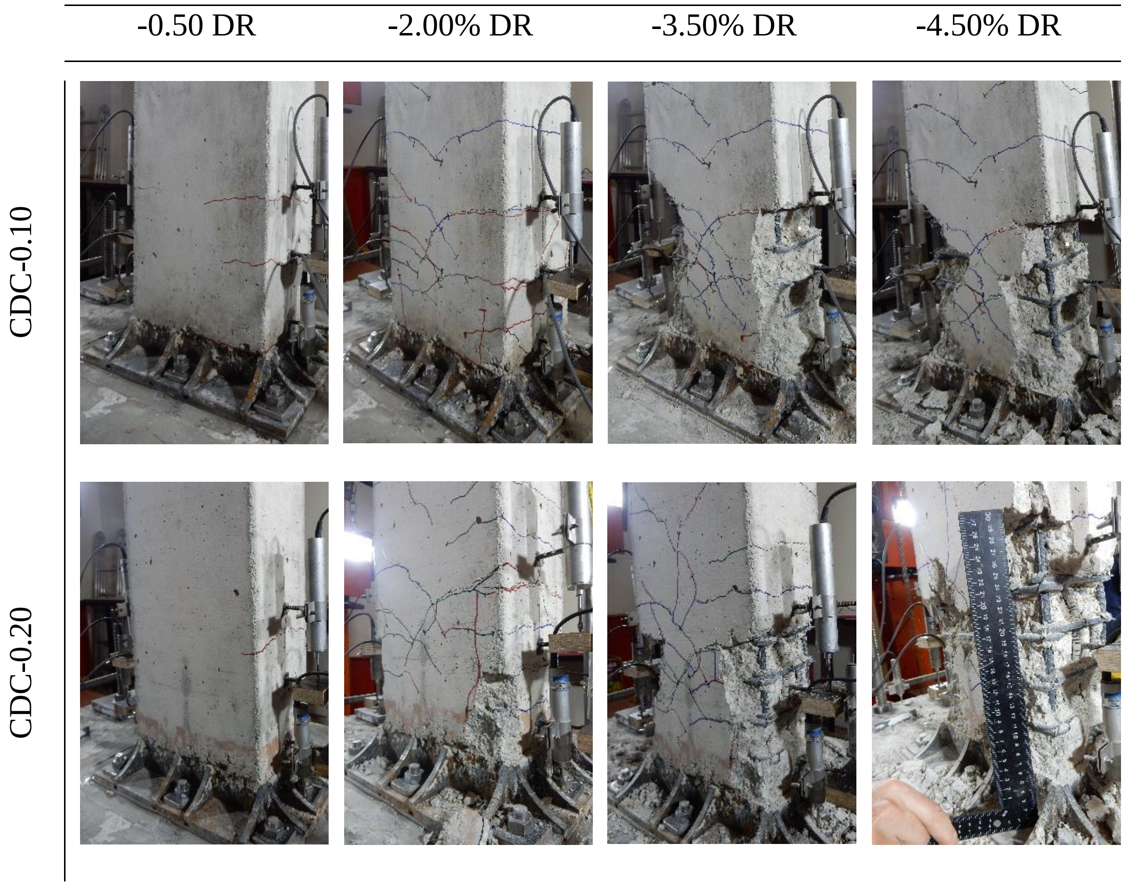

Figure 4.7 Damage progression in the bolted specimens with increasing drift ratio

The last bolted specimen with a 30% axial compression ratio, CDC-0.30, showed the first fine horizontal crack when the drift ratio is equal to Δ=0.75%. The maximum positive and negative lateral load capacities were achieved at drift ratios of Δ=1.33% and Δ= -1.55%, respectively, resulting in the occurrence of concrete crushing and spalling at the edges of the column. When the drift ratio reached Δ=2.00%, the crushed and spalled area expanded from the edges to the center of the column’s sides. The confined concrete zone on both sides of the specimen started to crush at a drift ratio of Δ=2.50%. The specimen failed when the drift ratio reached Δ=3.50% and Δ=-3.50% due to the buckling of longitudinal rebar in the compression sides. Similar to the monolithic counterpart, concrete crushing, and spalling occurred in the middle sections of both the front and back faces of the columns.

The damage progression due to applied axial and lateral loadings on columns could be observed in four possible failure zones, including the foundation area, demountable columns’ connection parts, column area, and combination of the foundation and columns areas. The demountable connection parts showed sufficient performance under the loadings so the demountable columns’ connection zone showed no deformation or damage throughout the testing. All deformation and damage progression concentrated on the columns’ end approximately 190 mm long. Similarly, damage progression occurred on the column end with a relatively short length for monolithic specimens. On the other hand, the demountable specimens experienced more concrete spalling and crushing with a longer area than the monolithic specimens. That can be attributed to the anchorage rods that improved the deformation capacities by spreading out deformations along its length. The depth of the anchorage rods comply with the ACI318 standard. Therefore, the length of the anchorage rod was decided on the design loads calculated for each anchorage rod and the use of the equations given in ACI 318.

4.1.2. Load-displacement curves

Understanding the lateral load–displacement response of structural systems is essential to assess their stiffness, strength, ductility, and overall seismic performance. In this context, three separate studies evaluated the behavior of demountable and monolithic column systems under cyclic lateral loading.

4.1.2.1. Fully Demountable Column Base Connections Design

In this study, **Figure 4.8** displays the hysteretic curves for all specimens, derived from calibrated measurements of lateral load and displacement, offering insight into their cyclic response characteristics. The blue curves in **Figure 4.8**, i.e., envelope curves, obtained by connecting the peak points of the first hysteretic loop under each loading cycle, shown in **Figure 4.9**. The hysteretic and envelope curves for all specimens are used to obtain performance parameters that have been separately summarized in **Table 4.1**. When the lateral load-displacement responses of the specimens are analyzed, the specimen GDC4 have, on average, 22% higher maximum lateral load capacity P_{max} in both axes than the monolithic counterpart, which can be attributed to more robust loading transfer between the base and the longitudinal reinforcements due to the welding. On the other hand, specimens GDC1 to GDC3 exhibit less maximum lateral load capacity than the monolithic counterpart, in especially the maximum lateral load capacity of specimen GDC1 is approximately half of the monolithic one. The main reason for observing less lateral capacity from specimen GDC1 can be due to the absence of the axial load. Additionally, nominal lateral load capacity of the column ($P_{n,a}$) and lateral load that corresponds to the yielding of the longitudinal reinforcements ($P_{y,a}$) were analytically predicted and included in **Figure 4.8.** As can be seen, all specimens except monolithic one have shown less maximum lateral load capacity than their predicted nominal capacities. The observation of less maximum lateral load capacity than the predicted nominal capacity for specimen GDC4 can be attributed to the effectiveness of the anchorage rods is low due to not continuing through the length of the columns while main reason of observing less lateral capacity than the predicted nominal capacity for specimens GDC1, GDC2, and GDC3 can be due to the premature failure of the column footing. Lastly, it has been noted that all specimens exhibit sufficient maximum lateral load capacity to cause yielding in the longitudinal reinforcements of the columns.

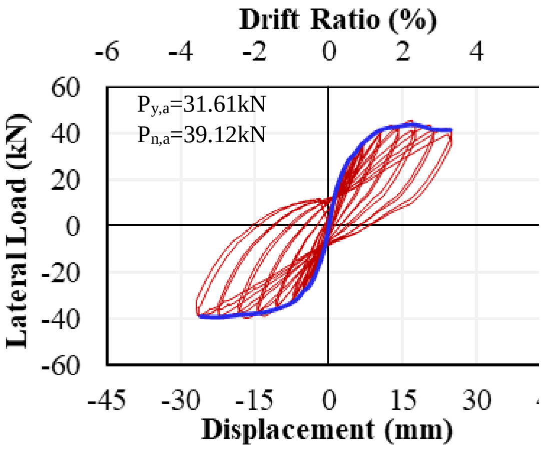

(a) - GMC1

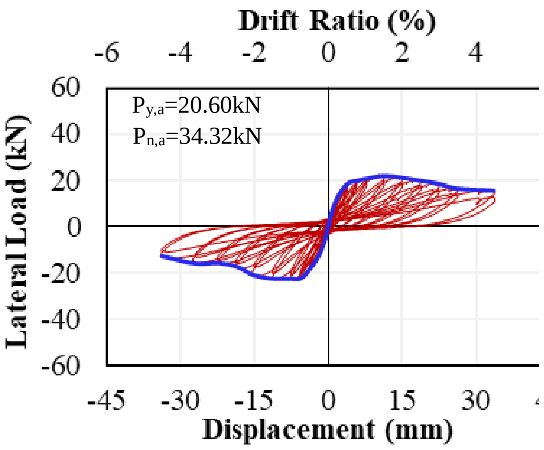

(b) - GDC1

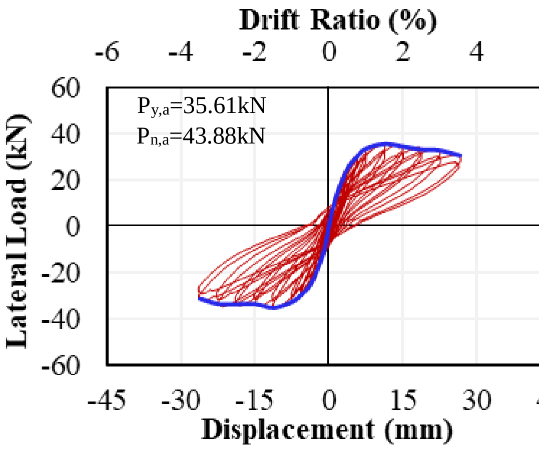

(c) - GDC2

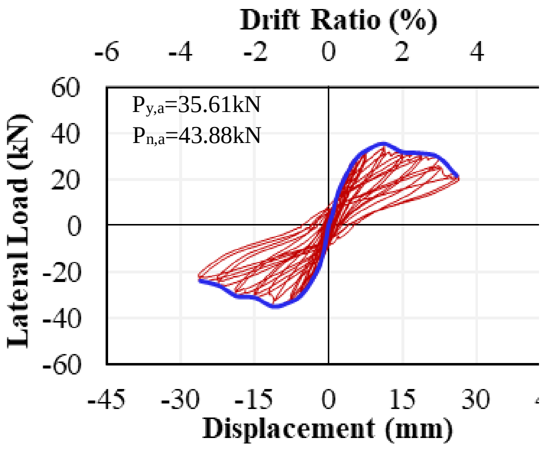

(d) - GDC3

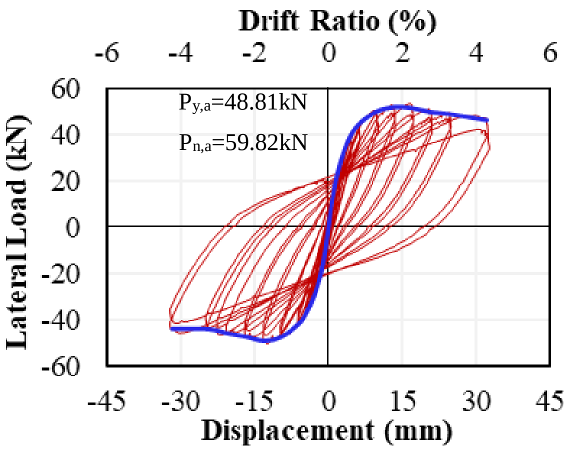

(e) - GDC4

Figure 4.8 Lateral load-displacement curves of the specimens.

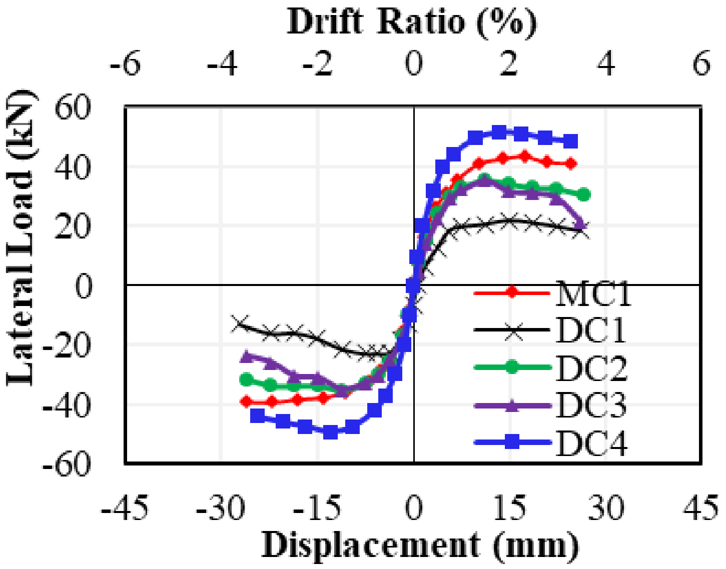

Figure 4.9 Envelope curves for all specimens.

Table 4.1 Seismic performance parameters of specimens.

Specimen	**f_{ck}**	**N**	**M_{max}**	**P_{max}**	**Δ_{max}**	**$\Delta_{0.4}$**	**K_e**	**P_y**	**Δ_y**	**$\Delta_{0.8}$**	**$\mu_{0.8}$**	**κ**
	MPa	**kN**	**kN.m**	**kN**	**mm**	**mm**	**kN/mm**	**kN**	**mm**	**mm**		
GMC1-Push	27.00	101.3	34.08	45.44	16.74	1.87	9.71	40.51	4.17	27.18	6.52	0.25
GMC1-Pull	27.00	101.3	-29.85	-39.81	-21.22	-1.63	9.66	-36.59	-3.79	-26.37	6.96	0.25
GDC1-Push	34.90	0.0	16.73	22.31	10.33	1.17	7.63	20.43	2.68	21.31	7.95	0.20
GDC1-Pull	34.90	0.0	-17.69	-23.59	-6.92	-1.27	7.42	-21.46	-2.89	-17.92	6.19	0.20

GDC2-Push	34.90	130.9	26.76	35.67	11.05	1.86	8.21	32.87	4.01	26.97	6.73	0.19
GDC2-Pull	34.90	130.9	-26.61	-35.48	-10.62	-1.50	9.49	-32.96	-3.47	-26.27	7.57	0.19
GDC3-Push	34.90	130.9	27.06	36.08	10.90	1.84	7.61	31.57	4.15	22.06	5.32	0.19
GDC3-Pull	34.90	130.9	-26.39	-35.18	-10.18	-1.39	10.11	-31.03	-3.07	-20.43	6.66	0.19
GDC4-Push	31.20	117.0	39.86	53.15	16.41	1.63	13.00	48.86	3.76	31.65	8.42	0.31
GDC4-Pull	31.20	117.0	-37.83	-50.44	-12.33	-1.45	13.63	-45.00	-3.30	-33.03	10.0	0.31

Note: M_{max} and Δ_{max} refer to the maximum moment generated by the applied loading and displacement at where lateral load equals P_{max}, respectively.

4.1.2.2. Structural Performance of CDW-Based Geopolymer Concrete Columns

In the second study, the hysteretic curves (cyclic lateral load vs. drift ratio curves) for all specimens are illustrated in **Figure 4.10**. The envelope curves in **Figure 4.11** are obtained by connecting the first hysteretic loop's peak points for each loading cycle. Performance parameters, including stiffness, ductility, and energy dissipation capacities, have been separately listed in **Table 4.2** for all specimens.

When the lateral load-displacement responses of the specimens are compared, demountable specimens exhibited a higher maximum lateral load capacity than their monolithic counterparts. The maximum lateral load capacities of the GMC-0.10, GMC-0.20, and GMC-0.30 for positive and negative directions, on absolute average, were 42.60, 47.95, and 47.25, respectively. Similarly, on absolute average, the maximum lateral load capacities for positive and negative directions of the GDC-0.10, GDC-0.20, and GDC-0.30 were 51.80, 71.45, and 76.60, respectively. As can be seen, specimens' lateral load capacity generally increased with increasing axial compression ratio on columns. On the other hand, the increase of the lateral load capacity due to the axial compression ratio for the demountable specimens was more significant than for the monolithic specimens. These observations could be attributed to the increasing axial compression ratio increased the friction force between the cracked faces of concrete, consequently improved the effectiveness of anchorage rods.

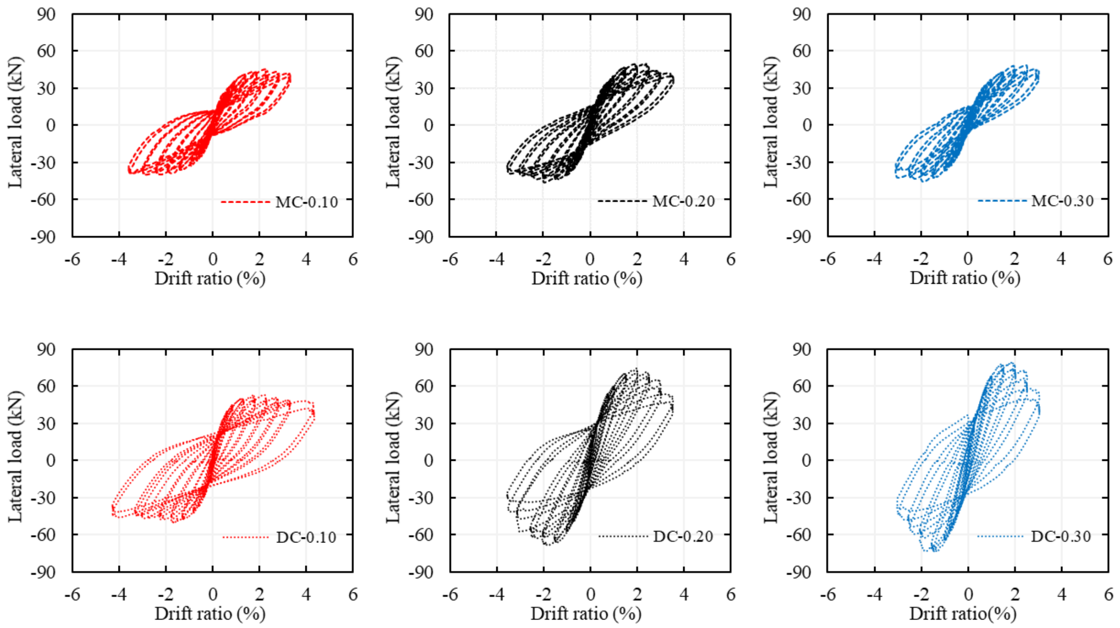

Figure 4.10 Lateral load-displacement curves of the specimens.

When the response of the specimens at push and pull directions was analyzed, slight differences in performance parameters were observed due to the minor variations in the installation of specimens. Demountable specimens with a 10% axial compression ratio showed no substantial drop in lateral load capacity throughout tests. Meanwhile, the drop in the lateral load capacity was more significant for demountable specimens with 20% and 30% axial compression ratios. But, monolithic specimens showed nearly similar load-displacement responses under varying compression loadings. When the maximum lateral load capacities of the monolithic and demountable specimens were compared, it was observed that demountable specimens had higher lateral load capacity than their monolithic counterparts. Demountable specimens with 10%, 20%, and 30% axial compression ratios had, on average, 22%, 49%, and 62% higher lateral load capacity than their monolithic counterparts, respectively. The main reason for the high lateral load capacities of the demountable specimens was the more robust loading transfer between the base and the longitudinal reinforcements due to the welding.

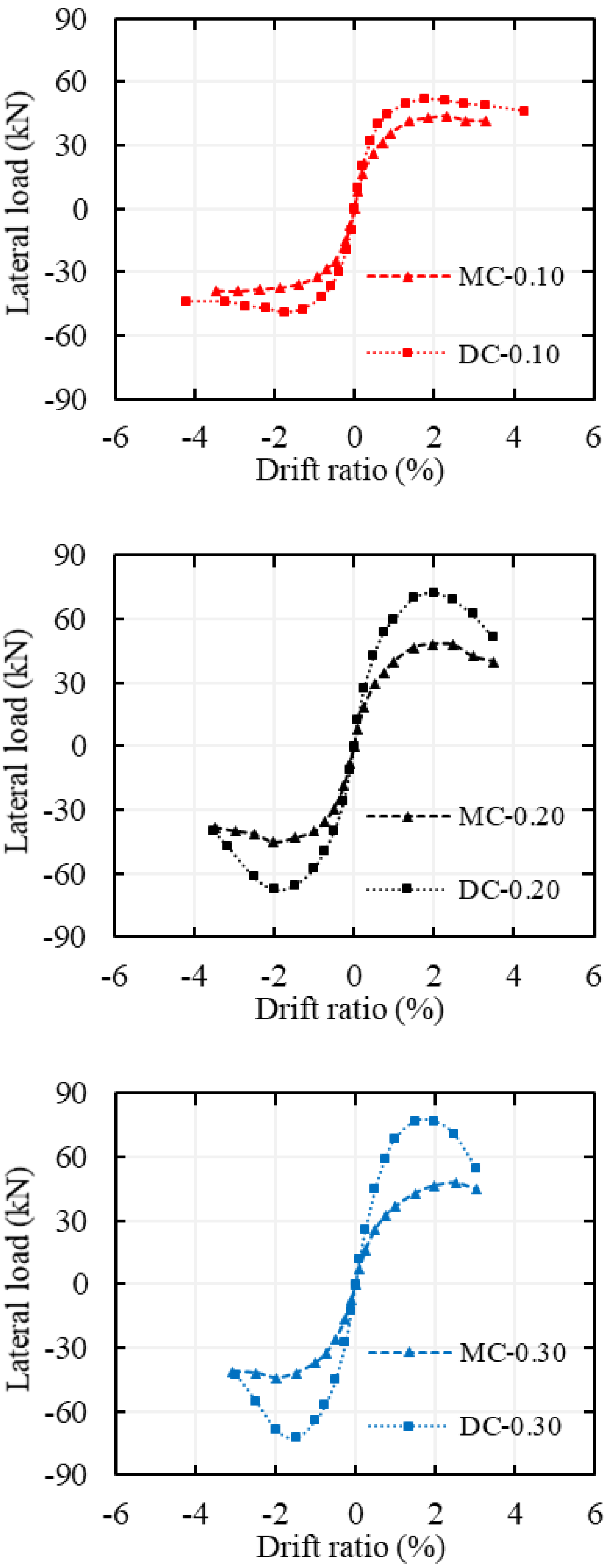

Figure 4.11 Envelope curves of the specimens.

Table 4.2 Summary of performance parameters obtained from the load-displacement relationship for all specimens.

Test ID	N	$P_{net, max}$	δ_{max}	$K_{initial}$	$K_{e, Park}$	$\delta_{y, Park}$	Ductility	Cumulative Energy	Dissipated Energy Ratio
	kN	kN	mm	kN/mm	kN/mm	mm	μ	J	κ
GMC-0.10 (push)	101.25	45.44	16.74	12.30	5.46	8.33	3.26	4626.82*	0.254
GMC-0.10 (pull)	101.25	-39.81	-21.22	12.17	5.28	7.54	3.50	4626.82*	0.254
GMC-0.20 (push)	202.50	49.90	17.24	10.94	5.84	8.55	3.02	5649.30*	0.305
GMC-0.20 (pull)	202.50	-46.04	-14.57	11.33	6.64	6.93	3.84	5649.30*	0.305
GMC-0.30 (push)	303.75	48.65	18.40	9.31	5.07	9.60	2.60	4921.91*	0.211*
GMC-0.30 (pull)	303.75	-45.82	-14.30	10.32	5.53	8.29	2.80	4921.91*	0.211*
GDC-0.10 (push)	117.00	53.15	16.41	15.62	8.74	6.08	5.20	6059.26*	0.310
GDC-0.10 (pull)	117.00	-50.44	-12.33	16.05	8.49	5.94	5.56	6059.26*	0.310
GDC-0.20 (push)	234.00	74.41	14.53	17.44	9.12	8.16	2.76	9613.37*	0.425
GDC-0.20 (pull)	234.00	-68.50	-13.66	15.13	8.48	8.07	2.88	9613.37*	0.425
GDC-0.30 (push)	351.00	79.83	13.99	15.82	10.55	7.57	2.49	11483.69*	0.450*
GDC-0.30 (pull)	351.00	-73.39	-11.05	18.08	10.33	7.11	2.40	11483.69*	0.450*

Note: * calculated value at 3% drift ratio. N: applied axial load, $P_{net, max}$: maximum lateral load capacity, δ_{max}: displacement corresponding to P_{max}, $K_{initial}$: initial stiffness, $K_{e, Park}$: effective stiffness calculated according to the method proposed by Park [152], $\delta_{y, Park}$: yield displacement calculated according to the method proposed by Park [152].

4.1.2.3. Damage Characteristics and Seismic Response of Demountable RC Column Base Joints

In the final study, the hysteretic responses of all specimens are illustrated in **Figure 4.12**, where the vertical axis denotes the net lateral load (P_net), and the horizontal axis represents the drift ratio (Δ). In **Figure 4.12**, the observed failures are also marked in order to ease the comparison of the damage accumulation for each specimen. In addition, the maximum points of the first hysteretic loop for each loading cycle are connected to obtain the envelope curves shown in **Figure 4.13**. The obtained performance parameters including applied axial loading N, maximum lateral load capacities (P_{max}), displacement corresponding to P_{max} (Δ_{max}), initial stiffness (K_i), etc., have been separately listed in **Table 4.3** for all specimens. It was seen that the specimens' maximum lateral load capacities increased with increasing axial loading when the load-displacement responses of the specimens were investigated. On the other hand, the higher axial loading on the columns led to a more rapid reduction in the lateral load capacity after reaching the maximum lateral load capacity. The bolted specimens with axial compression ratios of 10%, 20%, and 30% have, on average, 21%, 17%, and 23% higher maximum lateral load capacity than their monolithic counterparts, respectively. The main reasons for the high lateral load capacities of the bolted joints are anchorage rods that were used in the plastic hinge zone and more robust loading transfer between the base and the longitudinal reinforcements due to welding. The degradation in the lateral load capacities of the specimens in repeated loading cycles was small, particularly before reaching the drift ratio at the P_{max}. This finding implies that the specimens exhibited good resistance to degradation in their lateral load capacities throughout the repeated loading cycles, both before and after reaching the drift ratio at P_{max}.

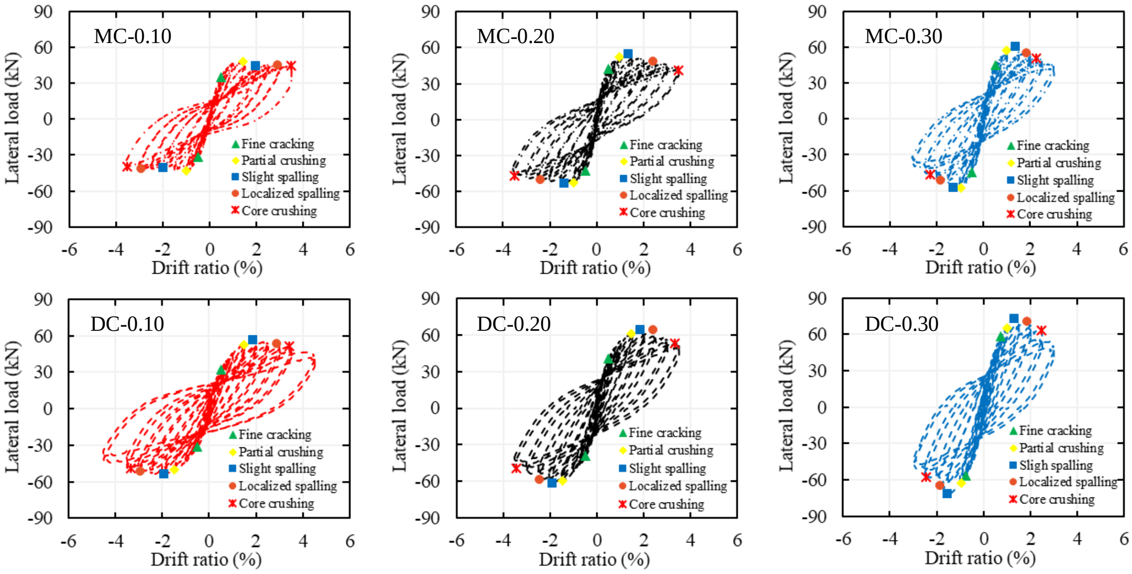

Figure 4.12 Lateral load-drift ratio curves of the specimens

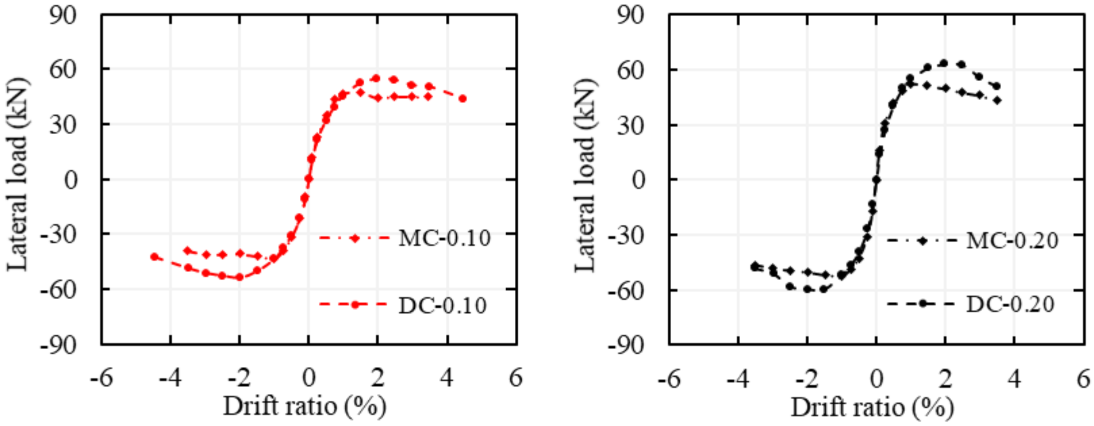

Figure 4.13 Envelope curves of the specimens

Table 4.3 Summary of performance parameters obtained from the load-displacement relationships

Test ID	**N**	**P_{max}**	**Δ_{max}**	**K_i**	**$K_{e,\text{ Park 1989}}$**	**$\Delta_{y,\text{ Park 1989}}$**	**Ductility**	**Cumulative energy**	**Dissipated energy ratio**
	kN	**kN**	**mm**	**kN/mm**	**kN/mm**	**mm**	**$\mu_{\text{Park 1989}}$**	**J**	**κ**
CMC-0.10 (+)	107.25	47.90	10.78	16.02	9.56	5.01	5.27	5622.75*	0.311
CMC-0.10 (-)	107.25	-43.27	-7.35	13.16	8.51	5.09	5.33	5622.75*	0.311
CMC-0.20 (+)	214.50	54.32	10.36	21.75	11.75	4.62	5.62	6916.91*	0.311
CMC-0.20 (-)	214.50	-53.40	-10.24	23.08	12.39	4.31	6.35	6916.91*	0.311
CMC-0.30 (+)	321.75	60.40	10.22	20.69	11.92	5.07	3.60	8010.12*	0.397*
CMC-0.30 (-)	321.75	-57.42	-7.28	20.32	12.32	4.66	3.66	8010.12*	0.397*
CDC-0.10 (+)	113.25	56.30	13.97	14.49	6.66	8.45	3.84	6563.68*	0.281
CDC-0.10 (-)	113.25	-54.20	-14.27	14.69	6.23	8.70	3.70	6563.68*	0.281
CDC-0.20 (+)	226.50	64.47	13.79	18.55	9.09	7.09	3.70	8367.57*	0.337
CDC-0.20 (-)	226.50	-61.49	-14.16	19.21	8.33	7.38	3.50	8367.57*	0.337
CDC-0.30 (+)	339.75	72.84	9.98	20.34	10.95	6.65	2.95	10653.42*	0.391*
CDC-0.30 (-)	339.75	-71.64	-11.59	19.23	10.55	6.79	2.53	10653.42*	0.391*

Note: * Value calculated at 3% drift ratio. $K_{e,\text{ Park 1989}}$: effective stiffness, $\Delta_{y,\text{ Park 1989}}$: displacement corresponding to yielding value.

4.1.3. Displacement ductility

The displacement ductility (μ) is crucial in determining whether a specimen provides sufficient seismic performance. The displacement ductility reflects the plastic deformation capacity of the specimens and is calculated based on **Eq. (4.1**) In order to determine the yield displacement, an equivalent elastoplastic relationship with a reduced stiffness proposed by Park [152] was adopted based on the envelope curves of the specimens. According to the Park method, initial stiffness is a secant stiffness that passes through 75% of the maximum net lateral load. The intersection of the horizontal line at maximum net lateral load and the inclined line characterizes the yield displacement ($\delta_{y,Park}$). Additionally, δ_u is the displacement corresponding to the point on the envelope curve where residual strength equals 80% of the maximum net lateral load. The parameters used to calculate the ductility of specimens are illustrated in **Figure 4.14**.

$$\mu = \frac{\delta_u}{\delta_{y,\ Park}} \tag{4.1}$$

where δ_u refers to the displacement when the load drops to 80% of its maximum value, and $\delta_{y,\ Park}$ refers to the yield displacement that was determined with the method proposed by Park [152].

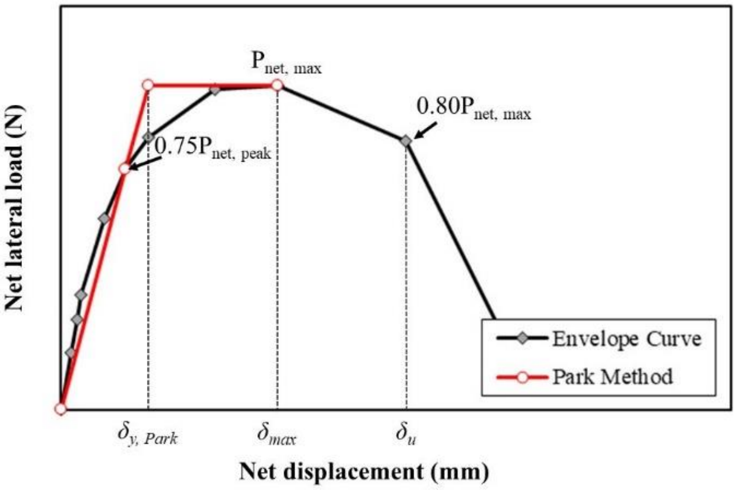

Figure 4.14 Park Method with parameters.

The cyclic displacement ductility ratio ($\mu_{0.8}$) is also a critical parameter for determining whether a specimen has adequate seismic performance. The displacement ductility ratios which represent the specimens' plastic deformation capacity in pull and push directions are calculated using **Eq. (4.2)**.

$$\mu_{0.8} = \frac{\Delta_{0.8}}{\Delta_y} \tag{4.2}$$

where Δ_y and $\Delta_{0.8}$ respectively refer to displacements where lateral load equals yield capacity (P_y) and residual capacity of 80% of P_{max}.

4.1.3.1. Fully Demountable Column Base Connections Design

From **Table 4.1**, it is apparent that the ductility for each direction of loading differs for each specimen but the difference is not more than 20%. The specimens GMC1, GDC2, and GDC3 exhibit similar values of ductility. On the other hand, specimen GDC4 has greater displacement ductility than their counterparts, which proves the better seismic performance. The only specimen with comparable ductility in the push direction to specimen GDC4 is specimen GDC1 but this specimen has zero axial load, which increases the ductility of RC members inherently. The results of the ductility ratio show that all the proposed connection details of the specimens can be considered to be a high ductile connection. However, it should be noted that ductile responses of specimens GDC1, GDC2, and GDC3 are mainly due to the plastic rotation taking place at the footing level. This behavior is not desired as it will cause permanent damage not to the precast elements, resulting in problems related to the replacing of damaged structural elements without major intervention.

4.1.3.2. Structural Performance of CDW-Based Geopolymer Concrete Columns

Displacement ductility of the columns connections was generally diminishing with increasing axial compression ratio on columns. The displacement ductility of the demountable specimens with 20% and 30% axial compression ratios was relatively lower than the monotonic counterparts while a demountable specimen with a 10% axial compression ratio had slightly high ductility than a monotonic counterpart. As seen in **Table 4.2**, all specimens had a higher ductility ratio than 2 so all specimens would be classified as having moderate ductility demand [153]. Also, it should be noted that displacement ductilities of specimens could be improved by changing the reinforcement details of columns.

4.1.3.3. Damage Characteristics and Seismic Response of Demountable RC Column Base Joints

As listed in **Table 4.3**, the displacement ductility of the specimens generally decreased as the axial compression load increased. The bolted specimens had lower displacement ductility compared to their monolithic counterparts. The ductility factors of bolted specimens CDC1, CDC2, and CDC3 were, respectively, 29%, 40%, and 25% below that of monolithic specimens CMC1, CMC2, and CMC3, which resulted due to that bolted specimens had lower stiffnesses compared with its corresponding monolithic specimens. The reduction in stiffness observed in the bolted specimens can be primarily attributed to deformations occurring at the columns' end plates and bolts when transferring loads from the longitudinal rebars to the foundation. According to FEMA 356 [153], ductility values greater than 4 are classified as high whereas ductility values between 2 and 4 are categorized as moderate. Therefore, monolithic test specimens with ACR less than 0.30

could be attributed to having high ductility whereas bolted specimens and monolithic test specimens with ACR = 0.30 could be called as having moderate ductility.

4.1.4. Energy dissipation capacity

One of the seismic performance parameters of structural systems is the energy dissipation capacity that occurs due to inelastic deformations, which leads to a reduction in energy transmission to other structural elements. The cumulative energy dissipation capacity was an area enclosed by the hysteresis load-displacement cycle loops.

4.1.4.1. Fully Demountable Column Base Connections Design

According to **Table 4.1**, specimen GDC1 shows relatively poor energy dissipation ability as compared to the monolithic counterpart, specimens GDC2 and GDC3 exhibit relatively similar energy dissipation capacities that are comparable to the monolithic specimen. The specimen GDC4 exhibit better energy dissipation capacity than other demountable specimens and monolithic specimens. This is due to the larger lateral load capacity of the connection and the enhanced plastic hinge zone of the column (i.e., longer plastic hinge length), by employing the steel detailing (i.e., rigid end plate, steel jacketing, and anchorage rods).

To compare the cumulative energy capacities of the specimens without considering the lateral load capacity of the specimens, actual dissipated energy is divided by the ideal dissipated energy to calculate relative energy dissipation capacities (κ) (**Eq. ((4.3))**. The relative energy dissipation ratio of the specimens with respect to the increasing level of drift ratio is given in **Figure 4.15**. According to the ACI 374.1-05 [154], the relative energy dissipation ratio of the connections used in the frame must be greater than or equal to 0.125 at a 3.5% drift ratio cycle. The results shown in **Figure 4.15** indicate that all of the specimens tested met this requirement. On the other hand, the specimen GDC1, GDC2, and GDC3 have the lower relative energy dissipation ratio than GMC1. However, the relative energy dissipation ratio of the specimen GDC4 is superior than the rest of the specimens including the control specimen, i.e., GMC1, which proves more ductile response of the specimen GDC4.

$$\kappa = \frac{E_{act}}{E_{id}} = \frac{A_h}{(E_1 + E_2)(\theta'_1 + \theta'_2)} \qquad \textbf{(4.3)}$$

where E_{act} and E_{id} respectively refer to actual and ideal dissipated energy. The value A_h refers to the dissipated energy during the i^th^ cycle. E_1 and E_2 respectively refer to the absolute lateral load under positive and negative loading at the i^th^ cycle. And θ'_1 and θ'_2 refer to lateral top displacements these occur during the unloading of the specimen with a slope equal to the initial stiffness of the specimen at E_1 and E_2, respectively.

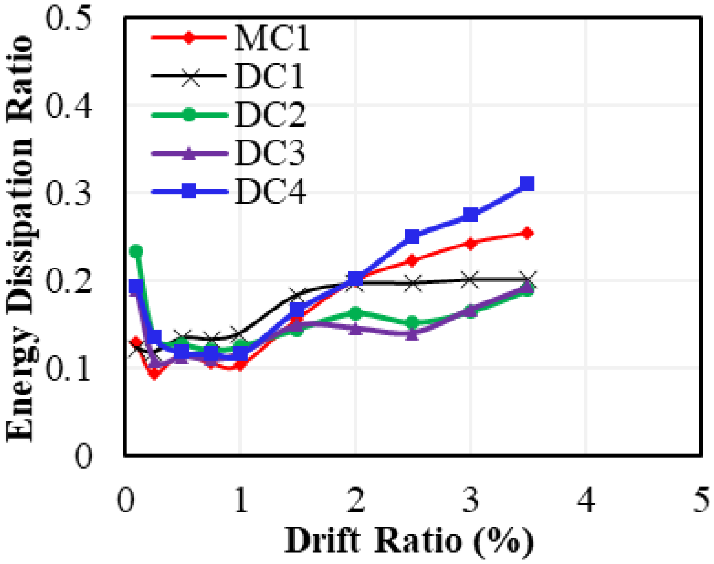

Figure 4.15 Relative energy dissipation ratio curves for all connections.

4.1.4.2. Structural Performance of CDW-Based Geopolymer Concrete Columns

The cumulative energy dissipation capacities of the specimens with respect to the increasing level of drift ratio are illustrated in **Figure 4.16**. The energy absorption capacities of the demountable specimens were higher than their monolithic counterparts. The differences in energy absorption capacities of the connections could result from the reinforcement details of the demountable specimens, resulting in a larger lateral load capacity of the connection and the enhanced plastic hinge zone of the column. Additionally, it was possible to correlate the axial compression ratio with the energy dissipation capacity of the specimens. In general, the energy dissipation capacity of the specimens increased with increasing axial compression ratio.

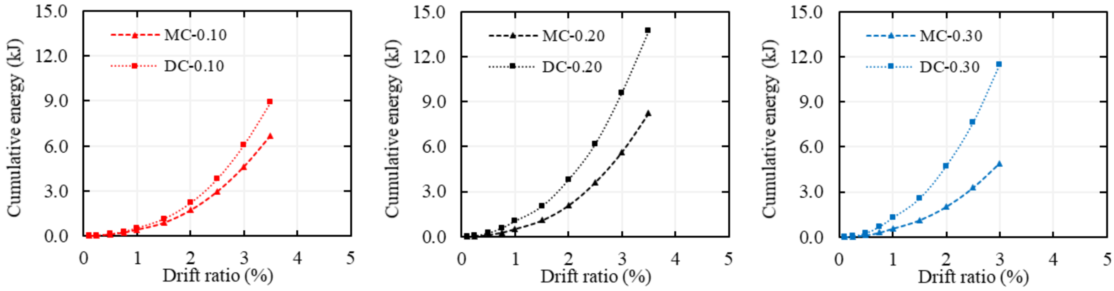

Figure 4.16 Cumulative energy dissipation capacity of the specimens. [154]

Figure 4.17 demonstrates the energy dissipation ratio of the specimens with respect to the drift ratio. As previously discussed, typical energy dissipation ratios for reinforced concrete modules at 3.00% drift are around 30%, and ACI 374.1-05 requires a minimum of 0.125 at 3.5% drift for frame connections [154]. As can be seen in **Figure 4.17**, all tested specimens satisfied the acceptance criteria. Also, it is observed that the energy dissipation ratio of the demountable specimens was greater than that of the monolithic counterparts.

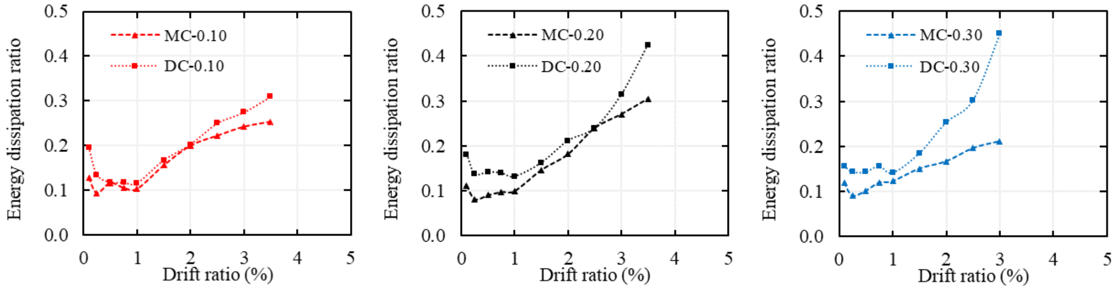

Figure 4.17 Energy dissipation ratio of specimens

4.1.4.3. Damage Characteristics and Seismic Response of Demountable RC Column Base Joints

Figure 4.18 presents the cumulative energy dissipation capacities of the specimens with respect to the increasing level of drift ratio. The monolithic specimens had lower energy absorption capacities compared to the bolted specimens. The differences in energy absorption capacities between the monolithic and bolted specimens could be attributed to the reinforcement details of the bolted joints, which led to a higher lateral load capacity and an improved plastic hinge zone of the column. Additionally, the energy dissipation capacity of the specimens increased with increasing axial compression ratio.

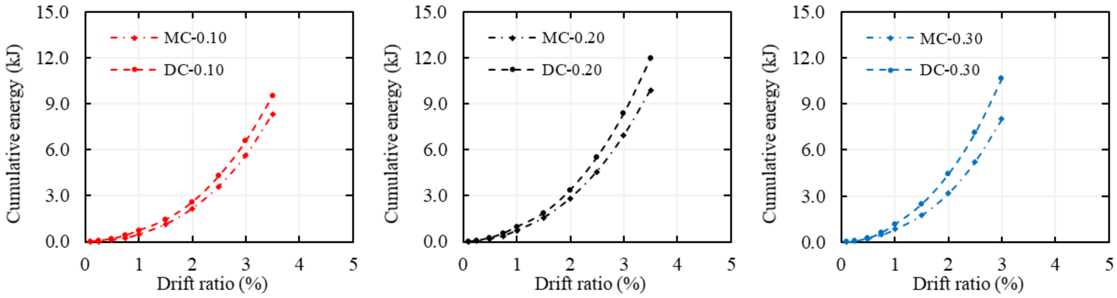

Figure 4.18 Cumulative energy dissipation capacity of the specimens

The relative energy dissipation ratio (κ) is a parameter proposed by ACI 374.1-05 [154] to eliminate the effects of additional reinforcement and concrete strength on the energy dissipation capacity. As previously noted, ACI 374.1-05 specifies a minimum energy dissipation ratio of 0.125 at 3.5% drift. As shown in **Figure 4.19**, all examined specimens except test specimens with ACR = 0.30 satisfied this acceptance requirement. On the contrary, all tested specimens have close values to the typical energy dissipation ratio at a drift ratio of 3.00%. In addition, the energy dissipation ratio of the bolted specimens was found to be comparable to that of their monolithic counterparts. Furthermore, it was seen that increasing axial loading improved the energy dissipation ratio for both types of specimens until ACR reaches 30%.

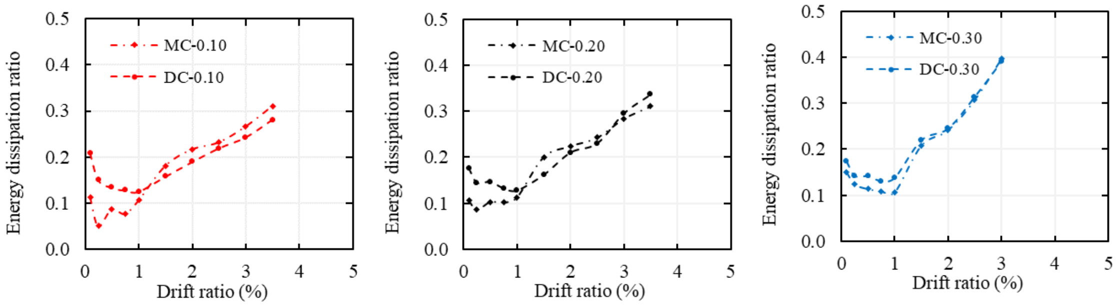

Figure 4.19 Energy dissipation capacity ratio of the specimens.

4.1.5. Stiffness degradation

Stiffness degradation is a critical parameter for evaluating the seismic performance and serviceability of reinforced concrete members, as it reflects the loss of stiffness and strength due to the development of inelastic deformations (e.g., cracking, concrete crushing) under cyclic lateral loading.

This section compares the stiffness degradation behavior of demountable and monolithic specimens based on three separate experimental studies. In each study, secant stiffness and stiffness degradation ratios were calculated using similar methods, enabling meaningful comparison. All specimens satisfied the minimum stiffness retention requirement at 3.5% drift ratio as defined by ACI 374.1-05, underscoring the structural reliability of the proposed demountable systems.

The stiffness degradation ratio of the i^{th} cycle was calculated as the ratio of the secant stiffness of the i^{th} cycle (K_i) to the secant stiffness of 1st cycle (K_1) (**Eq. (4.4**). The secant stiffness of the i^{th} cycle (K_i) was calculated using the envelope curves of the specimens as the ratio of the summation of lateral load capacities to the summation of the lateral displacements corresponding to the lateral load capacities for pull and push directions of the i^{th} cycle (**Eq. (4.5)**).

$$SDR = \frac{K_i}{K_1} \tag{4.4}$$

in which

$$K_i = \frac{|P_i| + |-P_i|}{|\delta_i| + |-\delta_i|} \tag{4.5}$$

Also, all specimens satisfied the ACI 374.1-05 [154] requirement, which stipulates secant stiffness at a drift ratio of 3.5% must be higher than 0.05 times the secant stiffness at an initial drift ratio.

4.1.5.1. Fully Demountable Column Base Connections Design

The effective lateral stiffness (K_e) of the specimens is calculated and obtained results are presented in **Table 4.1**. As seen in **Table 4.1**, the maximum effective lateral stiffness belongs to specimen GDC4 whereas the minimum effective lateral stiffness is measured for specimen GDC1. In addition, the second-highest effective lateral stiffness belongs to the monolithic specimen which indicates that the proposed connection details of specimen GDC4 improved the performance.

$$K_e = \frac{|P_{0.4}|}{|\Delta_{0.4}|} \tag{4.6}$$

where $P_{0.4}$ and $\Delta_{0.4}$ are the load equal to 40% of maximum lateral load capacity (P_{max}) and displacement corresponding to $P_{0.4}$, respectively.

The comparison of secant stiffness curves of the specimens is presented in **Figure 4.20 (a)**, and it is evident that the demountable specimens except specimen GDC4 exhibited slightly less stiffness than specimen GMC1. The stiffness curves of specimens GDC2 and GDC3 nearly coincide with the stiffness curve of specimen GMC1, on the other hand, stiffness of the specimen GDC4 is larger than the monolithic counterpart.

The calculated stiffness degradation ratios of the specimens are shown in **Figure 4.20 (b)**. The stiffness degradation curves of the specimens are similar and rapidly reduced between 0% drift ratio to 1% drift ratio, and reduction rates of stiffness degradation gradually decreased as increased drift ratio. The stiffness degradation of specimen GDC1 is, on the other hand, more visible than in the others. This can be explained by the lack of axial loading.

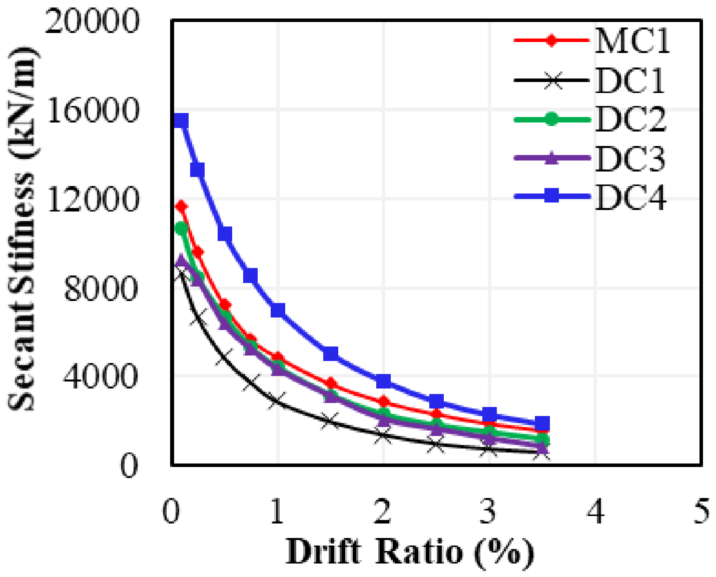

a)

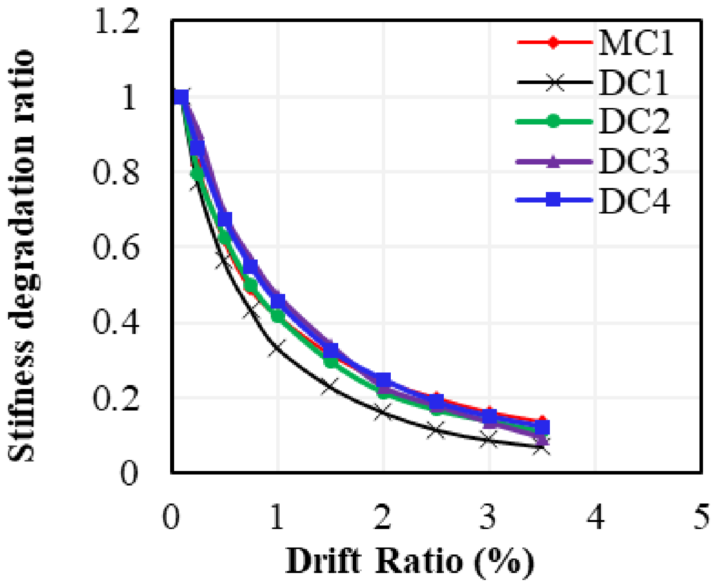

b)

Figure 4.20 Secant stiffness (a) and stiffness degradation ratio (b) curves of the specimens.

4.1.5.2. Structural Performance of CDW-Based Geopolymer Concrete Columns

The obtained secant stiffness curves of the specimens are presented in **Figure 4.21**. The secant stiffness of demountable specimens was bigger than secant stiffness of the monolithic specimens.

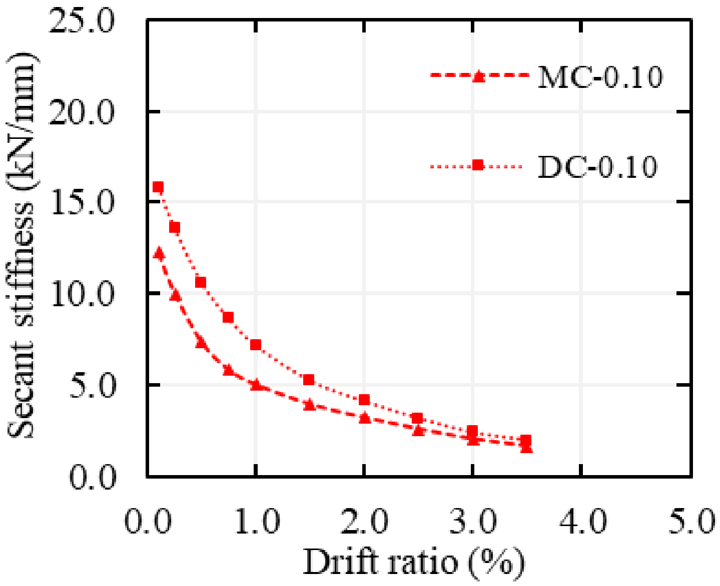

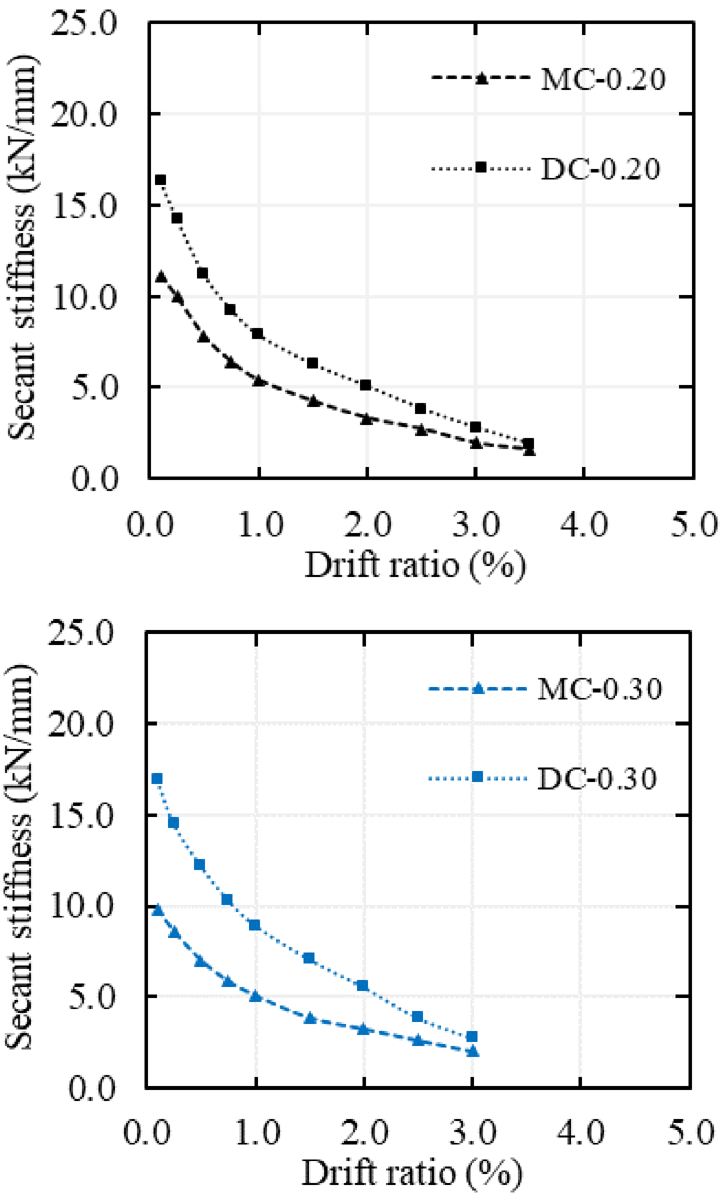

Figure 4.21 Secant stiffness curves of the specimens.

The calculated stiffness degradation ratios of the specimens with respect to the increasing level of drift ratio are depicted in **Figure 4.22**. Between 0% and 1% drift ratio, the change in stiffness degradation ratio was more visible, and as the drift ratio increased, the rate of reduction of stiffness degradation gradually decreased. The stiffness degradation ratio of the monolithic and demountable specimens was nearly identical. At a 1% drift ratio, specimens retained nearly half their secant stiffness.

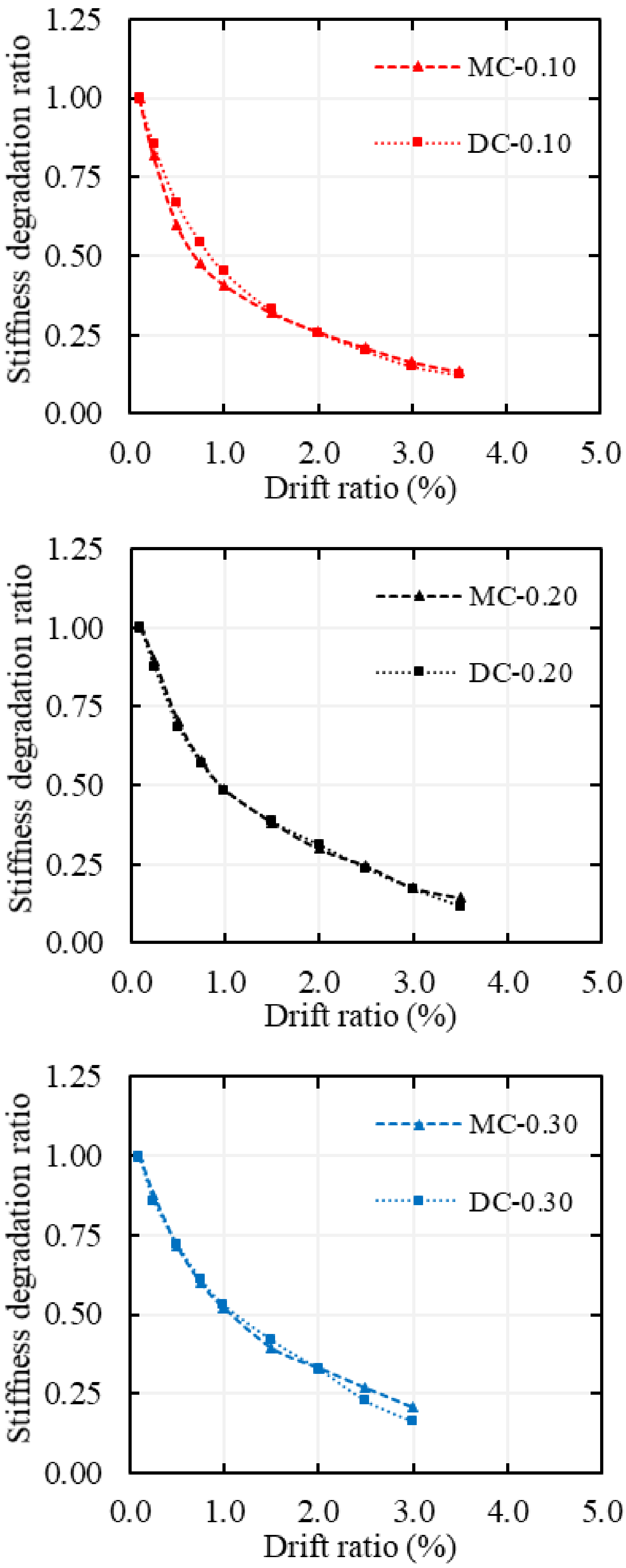

Figure 4.22 Stiffness degradation ratio curves of the specimens.

4.1.5.3. Damage Characteristics and Seismic Response of Demountable RC Column Base Joints

The secant stiffness curves of the specimens are shown in **Figure 4.23**. The obtained secant stiffness values for bolted and monolithic specimens were similar under the same loading. The initial secant stiffness of the bolted specimens is directly proportional to the applied lateral loading while it is not possible to correlate the initial secant stiffness of the monolithic specimens with applied lateral loading.

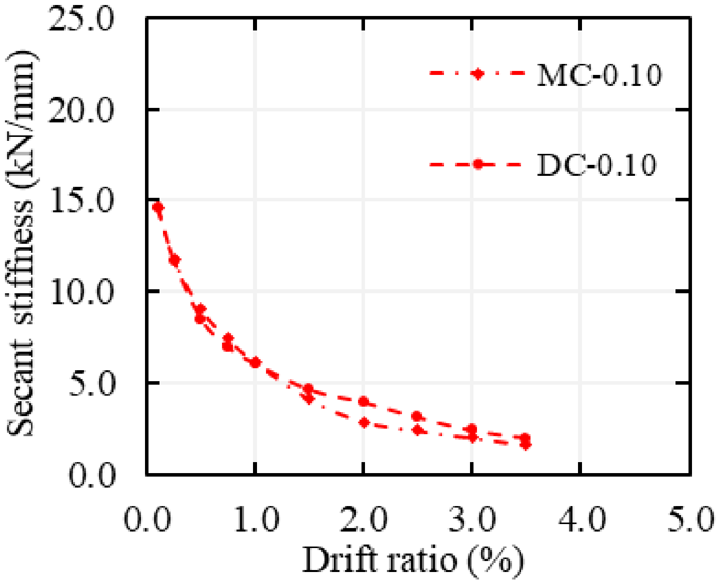

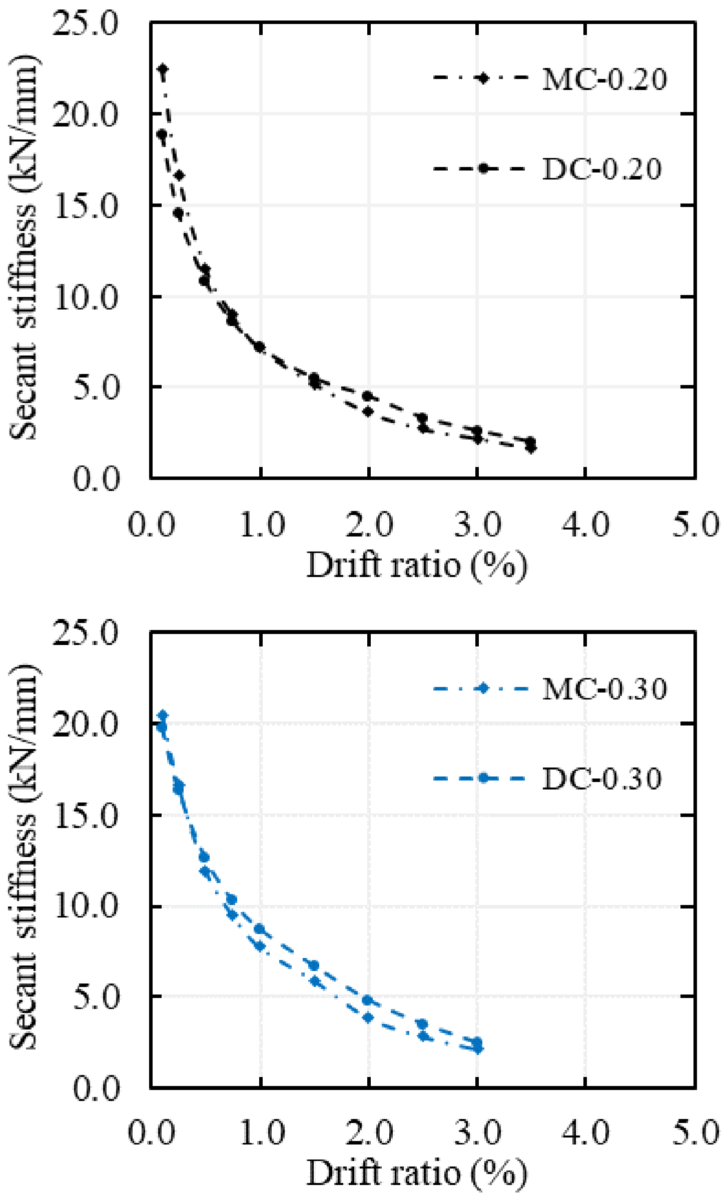

Figure 4.23 Secant stiffness curves of the specimens

Figure 4.24 shows the stiffness degradation ratios of the specimens as the drift ratio increases. The reduction in stiffness degradation ratio is more noticeable between 0% and 1% drift ratio, and as the drift ratio increases, the rate of reduction in stiffness degradation gradually slows down. At a 1% drift ratio, the secant stiffness of the conventional concrete specimens was reduced by approximately 60%. The paths of the stiffness degradation ratio of the monolithic and bolted specimens are generally similar.

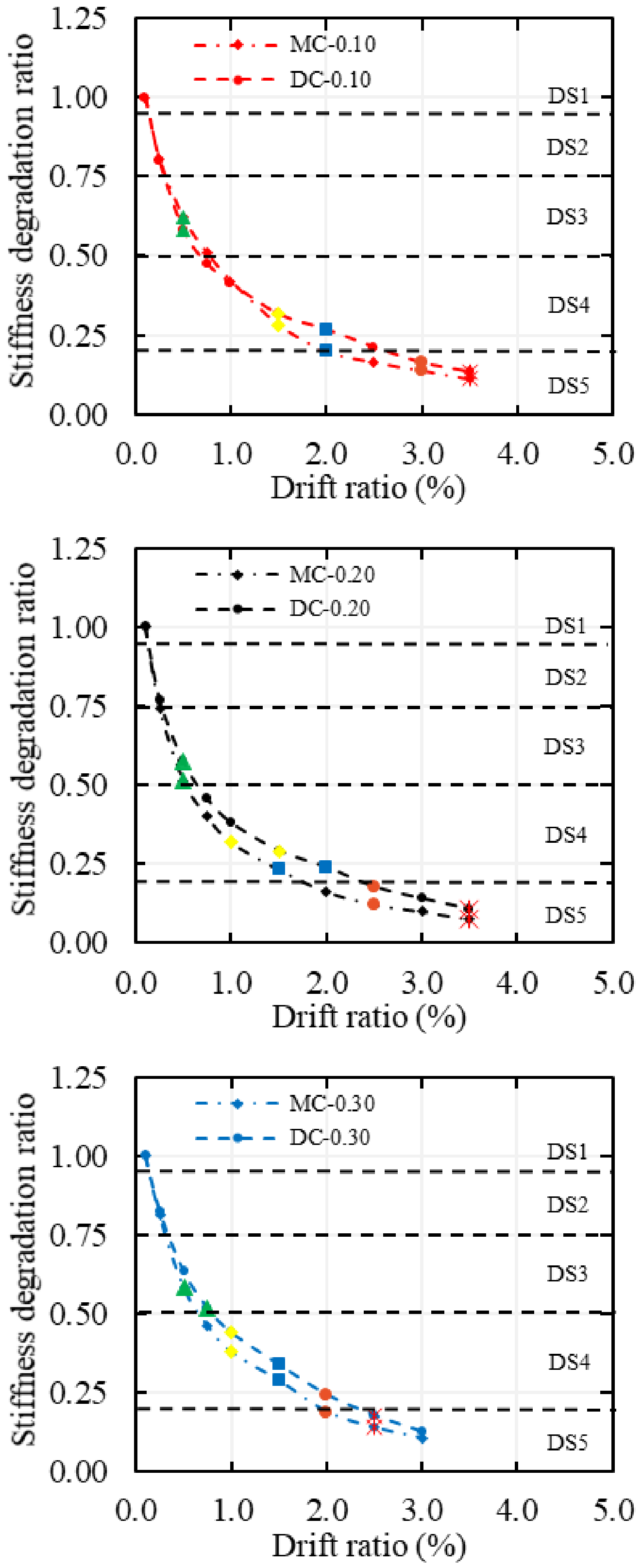

Figure 4.24 Stiffness degradation ratio curves of the specimens and JBDPA's (2015) reduction factors for damage states

4.1.6. Moment-curvature curves

Another way to compare the seismic performance of the specimens is to examine the moment-curvature relationships. The curvature values were determined at three regions (bottom, middle, and top regions) of the confinement zone by LVDTs mounted on the columns for this purpose, as shown in **Figure 3.48** using **Eq. (4.7)**. The gage lengths of the bottom, middle, and top regions were 50mm, 100mm, and 100mm, respectively. Based on the measured curvature values, a weighted average of the curvature values was calculated according to the measuring height of the regions. The initial curvature stiffness of the specimens was obtained from the slope of the first cycle of the moment-curvature curves. Meanwhile, the bending moment developed in connection could be estimated as the product of the net lateral loading and the clear span using **Eq. (4.8)**.

$$\phi_{(i)-(i+3)} = \frac{D_i - D_{i+3}}{w_{(i)-(i+3)} \times h_i} \qquad for\ i = 5, 6, and\ 7 \tag{4.7}$$

where D_i refers to the displacement measurement obtained from DT_i, and h_i refers to the height between the DT_i and DT_{i+3}.

$$M = P_{net} \times L \tag{4.8}$$

4.1.6.1. Fully Demountable Column Base Connections Design

In this study, curvature values are obtained in three zones (bottom, middle, top) as depicted in **Figure 4.25.** For monolithic specimen GMC1, curvature values of the bottom zone are much higher than the other zones which indicated that elastic energy absorption mostly occurred at the bottom of the column. This can be attributed to the crack propagation at the bottom of the column due to the low compressive strength of GMC1.

In specimens GDC1 to GDC3, the deformations concentrate on a small area that is in between the footing and the column. In addition, the curvature values of the middle and top zones of the plastic hinge region are negligible with respect to the curvature values of the bottom zone of the plastic hinge region, as shown in **Figure 4.25**. For specimen GDC4, curvature values of the middle and top zones have similar magnitudes and relatively larger than curvature values of the bottom zone of the plastic hinge region. On the other hand, for the demountable specimens and specimen GMC1, curvature values of the bottom zone are relatively larger than that of the bottom and middle zones. That indicates that the damage is spread on the plastic zone due to the proper steel detailing (i.e. steel jacket and anchorage rods) that provides an efficient load transfer mechanism from the column to the foundation. In addition, specimen GDC4 have higher maximum curvature value and higher curvature stiffness than the specimen GMC1. That can be attributed to the high reinforcement ratio in the confinement zone of the specimen GDC4.

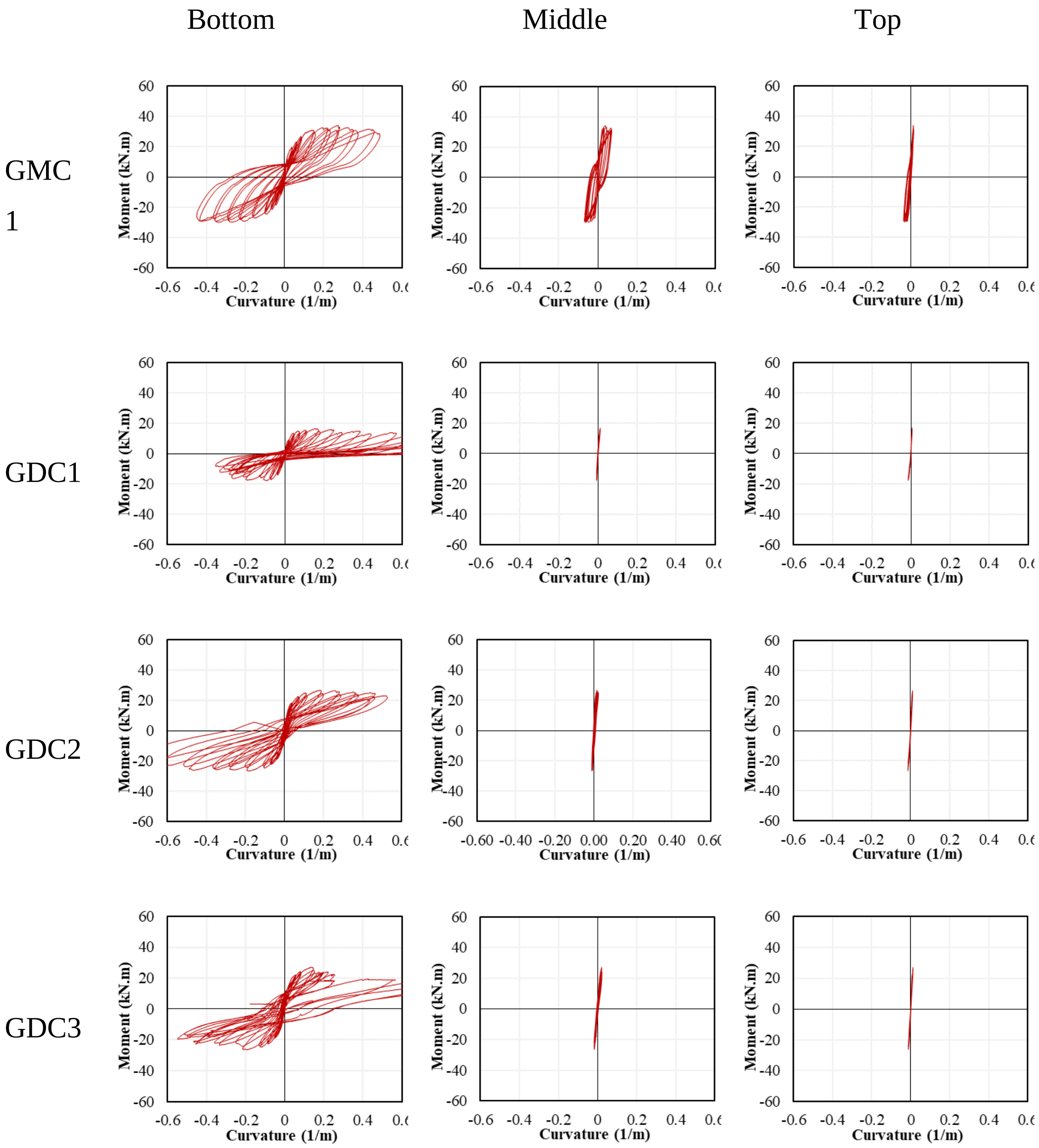

GDC4

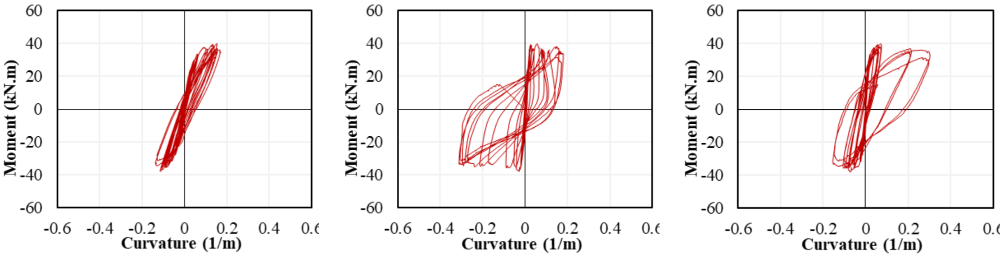

Figure 4.25 Moment-curvature curves of the specimens.

It should also be noted that this study investigates only the behavior of column base connections produced from CDW-based geopolymer. The performance of the elements produced from conventional concrete should also be studied in order to determine the effect of the use of geopolymer concrete, recycled aggregates, and CDW on structural performance. However, as an initial discussion and by referring other studies in the literature, it could be stated that the effect of the use of geopolymer is expected to be limited as far as load capacities are considered [23, 75]. However, the use of recycled aggregates most probably reduces the energy dissipation characteristics, flexural crack propagations and displacement capacities. This is mainly due to the secondary interfacial transition zone (ITZ) formation in recycled aggregates. Akbarnezhad et al. [87] claimed that the flexural ductility of beams depended on the bond strength between aggregate and paste. Since the most important factor affecting this bond strength is ITZ, a secondary ITZ formation is observed in mixtures with recycled aggregates due to formerly adhered mortar content surrounding the recycled aggregates. Therefore, the behavior of these elements should also be compared with conventional concrete counterparts. However, this subject is out of scope of this study.

4.1.6.2. Structural Performance of CDW-Based Geopolymer Concrete Columns

Figure 4.26 shows the hysteresis curves plotted for the moment-curvature for three regions in the confinement zone. Based on the obtained hysteresis curves for three regions, the weighted average curvatures were calculated and depicted in **Figure 4.27**. The obtained parameters for moment-curvature curves are listed in **Table 4.4** for the specimens. The maximum curvatures of the specimens occurred at the last cycle of the loading protocol. The demountable connections increased the maximum curvature of CDW-based geopolymer by an average of 29% (**Table 4.4**). Additionally, the demountable specimens had high curvature stiffness due to the high reinforcement ratio in the confinement zone. Also, the demountable specimens had higher energy dissipation capacity (area under the envelope of the moment-curvature curve) than their monolithic counterparts.

The contributions of the three regions on the weighted average curvature of the specimens were also compared. The curvature values of the monolithic CDW-based geopolymer concrete specimens were mainly provided in the bottom region while demountable specimens' curvatures were mainly provided in the middle and top regions. As illustrated in **Figure 4.26**, the contributions of the top and middle regions of the monolithic specimens on curvature value were negligible when compared to the bottom region. On the other hand, in the demountable specimens, the curvature values of the top region were generally higher than the curvature values of the lowest regions. These conclusions were also supported by crack and damage propagations observed during the tests. In the monolithic specimens, damage accumulations occurred in the bottom and middle regions. However, in the demountable specimens, damages and cracks spread over the three regions, especially the top regions, due to the effective load transfer mechanism and strengthened connection zone due to the proper steel detailing. This also proves more uniform energy dissipation in demountable members over the plastic hinge zone, limiting the maximum curvature demands throughout the plastic hinge zone.

Lastly, the effect of axial compression ratio on curvature is discussed. As seen in **Table 4.4**, with increasing axial compression ratio, initial curvature stiffness increased for specimens except specimen GMC-0.30. On the other hand, there is no clear correlation between the axial compression ratio and the maximum curvature exhibited by test specimens.

Table 4.4 Summary of performance parameters obtained from the moment-curvature relationship for all specimens.

Test ID	M_{max}	**Maximum Curvature**	**Initial Curvature Stiffness**	**Area under Envelope of M-φ Curve**	**Ultimate Curvature Region**
	kN.m	**10^{-3}/m**	**(kN.m) / (1/m)**	**(kN.m) × (1/m)**	**mm**
GMC-0.10 (push)	34.08	126.23	2412.41	3.63	0-50
GMC-0.10 (pull)	-29.85	-128.39	2332.47	3.32	0-50
GMC-0.20 (push)	37.42	164.28	2753.30	5.23	0-50

GMC-0.20 (pull)	-34.53	-139.93	2540.01	4.06	0-50
GMC-0.30 (push)	36.48	104.26	2196.86	3.15	0-50
GMC-0.30 (pull)	-34.37	-128.64	2185.14	3.62	0-50
GDC-0.10 (push)	39.86	160.56	2968.46	5.64	150-250
GDC-0.10 (pull)	-37.83	-177.13	2959.33	5.81	50-150
GDC-0.20 (push)	55.80	166.12	3003.76	7.38	150-250
GDC-0.20 (pull)	-51.37	-245.83	3650.63	10.40	150-250
GDC-0.30 (push)	59.87	111.30	3463.72	5.37	150-250
GDC-0.30 (pull)	-55.05	-159.42	4038.09	7.36	150-250

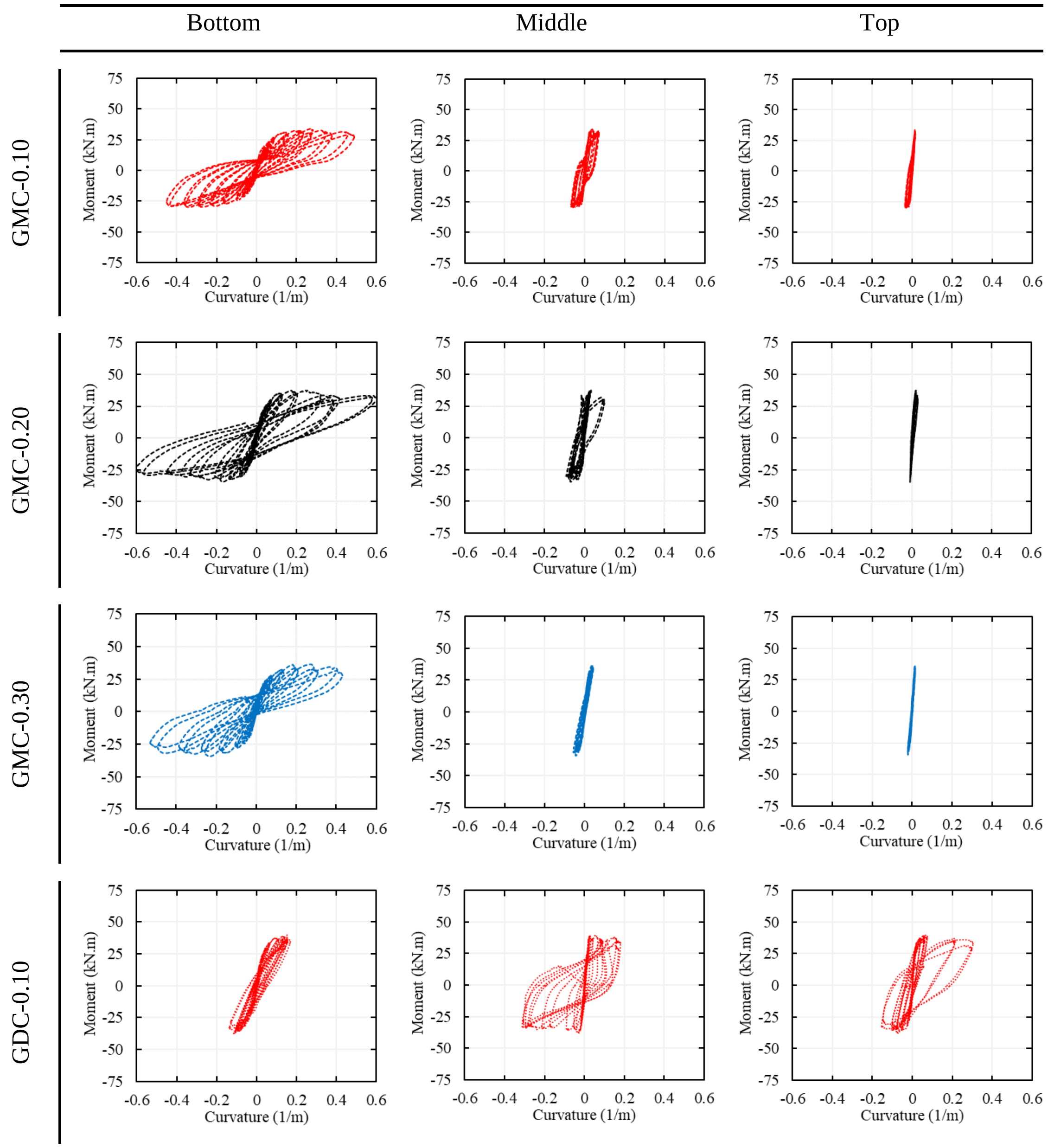

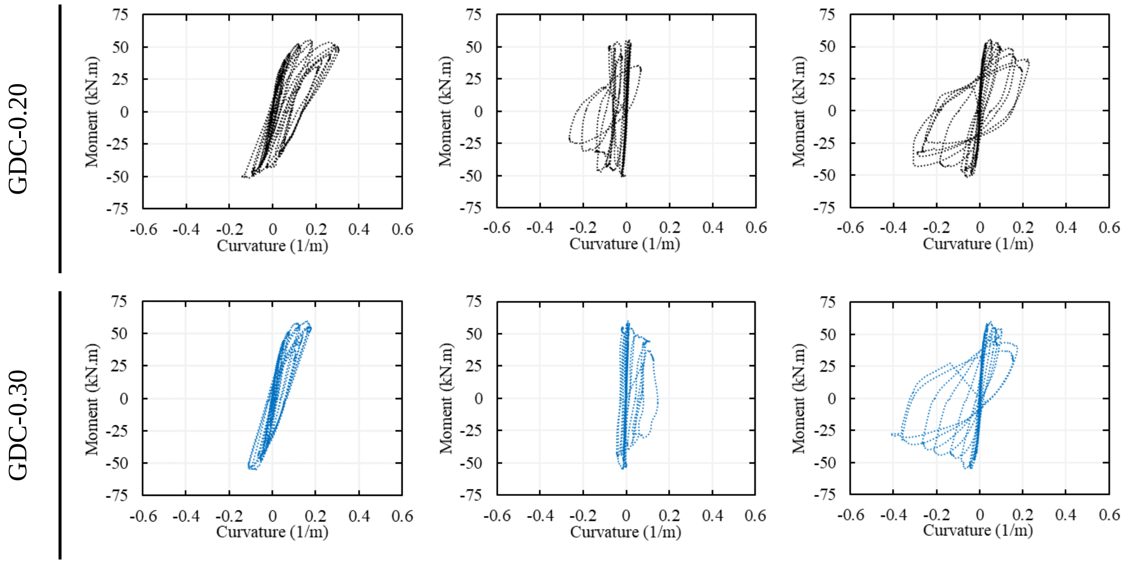

Figure 4.26 Moment versus curvature curves for three regions in the confinement zone of the specimens.

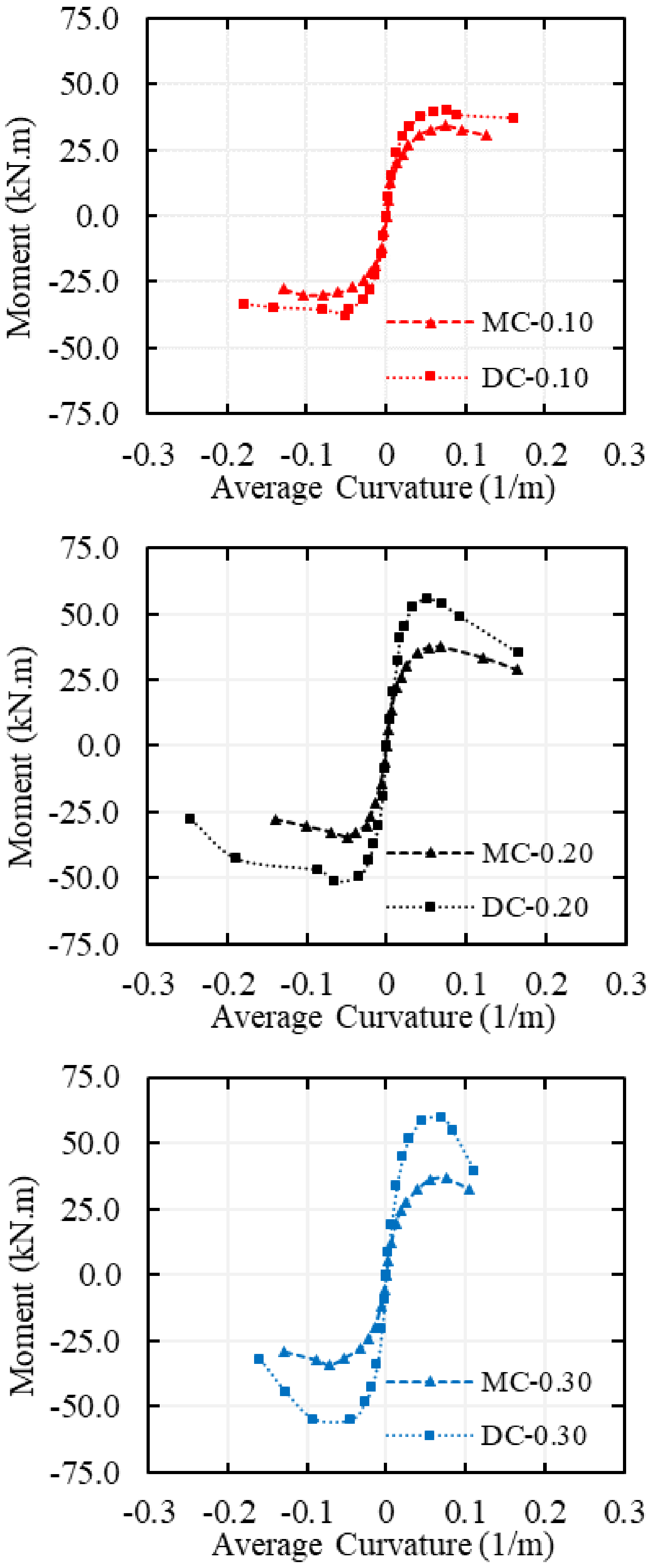

Figure 4.27 Envelope curves of the moment versus average curvature curves of the specimens.

4.1.6.3. Damage Characteristics and Seismic Response of Demountable RC Column Base Joints

Figure 4.28 illustrates the hysteresis curves of moment-curvature plotted for three different regions in the confinement zone. Using these curves, weighted average curvatures were calculated and displayed in **Table 4.5**. The values of various parameters obtained from the moment-curvature curves for all specimens are listed in **Table 4.5**. The maximum curvatures of the specimens were recorded during the last cycle of the loading protocol. The bolted specimens resulted in an average increase of 9% in the maximum curvature of CDW-based compared to the monolithic specimens. The high reinforcement ratio in the confinement zone contributed to the higher curvature stiffness of the bolted joints. Additionally, the bolted joints exhibited a higher energy dissipation capacity, which is represented by the area under the envelope of the moment-curvature curve, compared to their monolithic counterparts.

The comparison of the contributions of three regions to the weighted average curvature of the specimens was also conducted. The monolithic specimens showed that the middle region provided most of the curvature values, while the bolted joints provided higher curvature values in the top region, as shown in **Figure 4.28**. Furthermore, the contributions of the top region of the monolithic specimens on the weighted average curvature were insignificant compared to the middle region. In contrast, the bolted joints had generally higher curvature values in the top region than in the bottom regions. These conclusions were supported by the observed crack and damage propagations during the tests. The bottom and middle regions showed damage accumulations in the monolithic specimens. However, damages and cracks were distributed over the three regions, especially the top region, in the bolted joints, due to the efficient load transfer mechanism and strengthened connection zone due to proper steel detailing. This also resulted in more uniform energy dissipation in bolted specimens over the plastic hinge zone, limiting the maximum curvature demands throughout the plastic hinge region.

Table 4.5 Summary of performance parameters obtained from the moment-curvature relationship for all specimens

Test ID	M_{max}	Maximum curvature	Initial curvature stiffness	Energy dissipation capacity	Ultimate curvature region
	kN.m	10^{-3}/m	kN.m / 1/m	kN.m × 1/m	
CMC-0.10 (+)	35.93	122.81	2796.42	3.85	50-150
CMC-0.10 (-)	-32.45	-163.93	2326.70	4.75	50-150
CMC-0.20 (+)	40.74	128.65	5298.83	4.54	50-150
CMC-0.20 (-)	-40.05	-163.97	3712.11	5.85	50-150
CMC-0.30 (+)	45.30	126.43	4977.82	4.73	50-150
CMC-0.30 (-)	-43.07	-120.54	6167.97	4.21	50-150
CDC-0.10 (+)	42.23	137.03	4819.92	5.09	150-250
CDC-0.10 (-)	-40.65	-163.02	4312.03	5.85	150-250
CDC-0.20 (+)	48.35	135.83	5918.27	5.74	150-250
CDC-0.20 (-)	-46.12	-152.29	4931.83	6.02	150-250
CDC-0.30 (+)	54.63	158.85	6672.04	7.26	150-250
CDC-0.30 (-)	-53.73	-155.75	9369.18	6.86	150-250

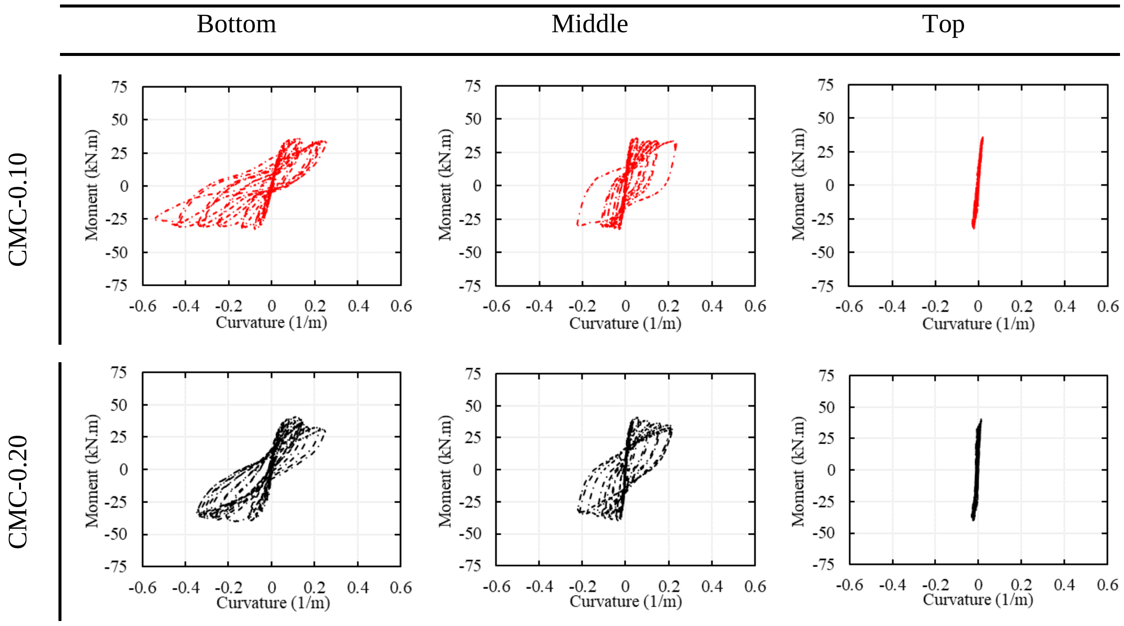

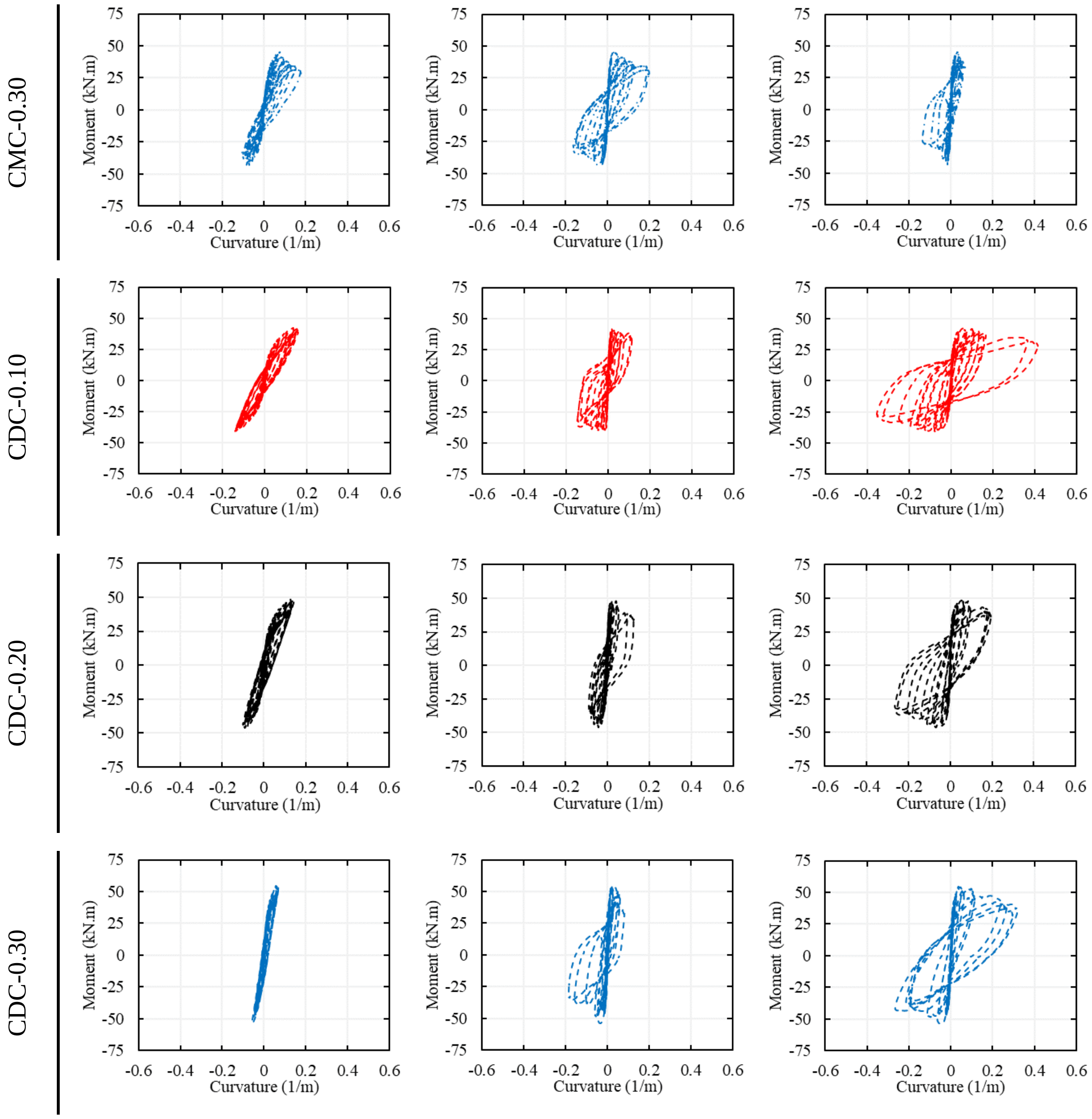

Figure 4.28 Moment versus curvature curves for three regions in the confinement zone of the specimens

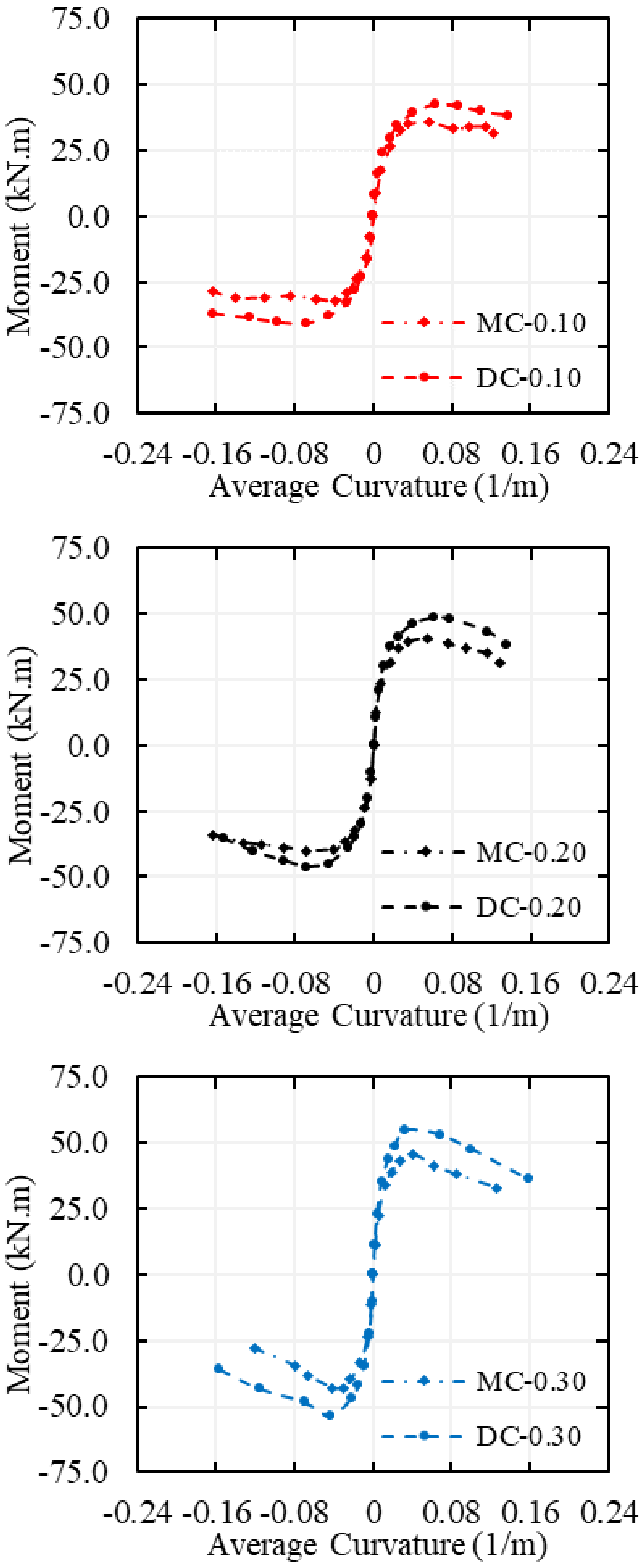

Figure 4.29 Envelope curves of the moment versus average curvature curves of the specimens

The ACI318 [77] and TS500 [76] equations were used to calculate the design axial load capacity and design moment capacity. Additionally, the nominal moment and axial load capacities were predicted using the stress-strain model for concrete proposed by Mander et al. [155], which is a fiber model that doesn't include material factors. The results of these calculations were tabulated in **Table 4.6** and shown in **Figure 4.30** as axial load-moment interaction curves. The fiber model provided the most accurate prediction of the moment and axial load capacities for both bolted and monolithic specimens. On average, the percentage errors of the ACI318 (TS500) predictions for monolithic specimens with axial compression ratios of 10%, 20%, and 30% were -14.49% (-21.15%), -23.87% (-26.09%), and -41.44% (-32.75%), respectively. Similarly, the percentage errors of the ACI318 (TS500) predictions for bolted specimens with axial compression ratios of 10%, 20%, and 30% were 1.11% (-6.45%), -18.23% (-12.79%), and -38.79% (-25.96%), respectively. The obtained results show that capacity predictions given by ACI318 [77] are generally more conservative than those given by TS500 [76]. The performance of TS500 predictions is slightly better than the performance of ACI318 predictions, especially for higher axial compression ratios. The capacity prediction errors of the design codes generally increased as the axial compressive ratio increased for both bolted and monolithic specimens. Moreover, the design code prediction errors were generally higher for monolithic specimens than for bolted specimens. Therefore, it can be concluded that the current design code equations for monolithic conventional reinforced concrete products resulted in nearly similar estimation performance for bolted specimens.

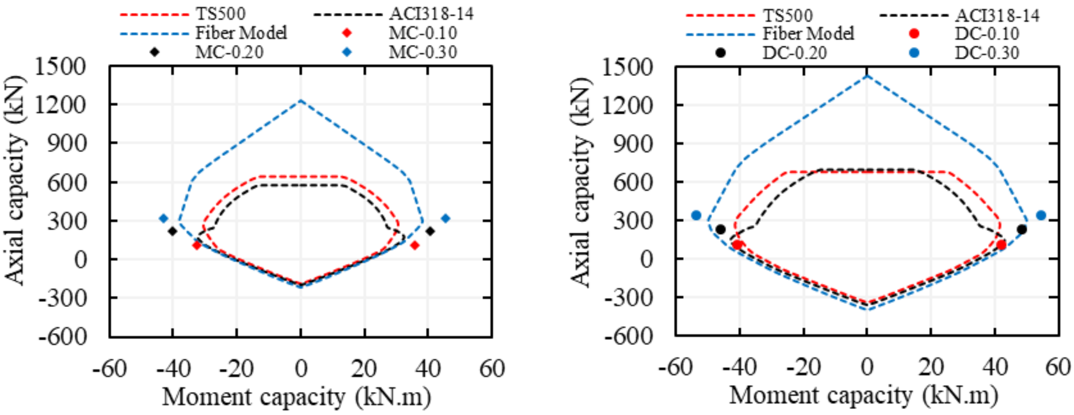

Figure 4.30 Comparison of experimental results with analytically predicted results

Table 4.6 Comparison of experimental results with predicted results

Test ID	N	Test	Fiber Model		ACI318-14		TS500	
		M_{max}	M	Error	M	Error	M	Error
	kN	kN.m	kN.m	%	kN.m	%	kN.m	%
CMC-0.10 (+)	107.25	35.93	29.94	-16.66	29.16	-18.83	26.89	-25.15
CMC-0.10 (-)	107.25	-32.45	-29.94	-7.75	-29.16	-10.15	-26.89	-17.14
CMC-0.20 (+)	214.50	40.74	35.37	-13.19	30.75	-24.52	29.86	-26.72
CMC-0.20 (-)	214.50	-40.05	-35.37	-11.69	-30.75	-23.22	-29.86	-25.46
CMC-0.30 (+)	321.75	45.30	37.70	-16.78	25.86	-42.92	29.69	-34.45
CMC-0.30 (-)	321.75	-43.07	-37.70	-12.46	-25.86	-39.96	-29.69	-31.05
CDC-0.10 (+)	113.25	42.23	44.42	5.21	41.88	-0.81	38.75	-8.23
CDC-0.10 (-)	113.25	-40.65	-44.42	9.28	-41.88	3.04	-38.75	-4.67
CDC-0.20 (+)	226.50	48.35	49.07	1.48	38.60	-20.16	41.17	-14.85
CDC-0.20 (-)	226.50	-46.12	-49.07	6.40	-38.60	-16.29	-41.17	-10.73
CDC-0.30 (+)	339.75	54.63	49.31	-9.75	33.16	-39.29	40.11	-26.57
CDC-0.30 (-)	339.75	-53.73	-49.31	-8.23	-33.16	-38.28	-40.11	-25.34

4.1.7. Influence of axial compression load ratio

According to the findings of the third study, the axial compression ratio can change the seismic performance of the CBJs by affecting the magnitude of the principal compressive stress. An increase in axial compression ratio helps close the cracks and reduces the number of visible cracks on the columns. With increasing the axial compression, the area of the concrete crushing and spalling was enlarged from the edges to the middle sections of both the front and back faces of the columns. When the obtained test results were analyzed, as can be seen in **Table 4.6** and **Figure 4.30**, an increase in axial compression ratio typically results in a higher lateral load capacity, energy dissipation, secant stiffness, initial curvature stiffness, and maximum curvature (for only bolted specimens) but less displacement capacity and displacement ductility. The displacement ductility of monolithic (bolted) specimens decreased from 5.30 (3.77) to 3.63 (2.74) with the increased axial compression ratio from 0.1 to 0.3. Additionally, there is no clear connection between the axial compression ratio and the maximum curvature of the specimens. Also, similar to the observation of Barrera et al. [156], an increase in axial compression ratio loading led to an increase in the plastic hinge length.

4.1.8. Plastic hinge characteristics

The third study revealed that cracked cross-sections exhibit substantially higher curvature values compared to uncracked sections, indicating that cracking significantly influences the curvature distribution along the structural element [157]. The plastic hinge region can be identified as the section of the member where significant plastic deformations (i.e., cracking, concrete crushing, and spalling) occur under load. Similarly, Ho and Pam [158] described the plastic hinge region as concrete spalling, longitudinal reinforcement buckling, transverse steel yielding, and damages in core concrete. The plastic hinge region allows for energy dissipation and redistribution of stresses, thereby enhancing structural performance and preventing sudden failure.

It is preferred to have plastic deformations concentrated at the ends of columns or piers. This approach minimizes damage to the superstructure and foundation while facilitating easier inspection and repair of any inelastic-related damage [159]. Mahini and Ronagh [160] stated that care should be taken to make sure that plastic hinges within the beam are sufficiently distanced away from the joint. Similarly, ASCE/SEI 41-17 [161] recommends shifting plastic hinge locations away from the joint region to reduce stress in the welded connection, thereby reducing the possibility of brittle fracture. For bolted specimens, the connection of the concrete columns to the steel end plate is critical so it could lead to an inevitable bond failure of the joint. Therefore, the eight anchorage rods used and the end of the columns are encased with steel jacketing, to enhance the bond resistance and shear strength. Moreover, due to the effect of the anchorage rods and the steel jacketing, the plastic hinge zone started from 50 mm away from the column end, and the plastic hinge length was increased.. Thus, joint failure was prevented and the loading capacity and ductility were enhanced. It should be noted that plastic hinge relocation should be carefully applied and other measures should be taken.

In this study, visual evaluation of cover spalling was used to estimate the plastic hinge region on the specimen’s columns, and estimated plastic hinge regions were verified with moment-curvature responses. It was observed that the upper part of the columns suffered minor damage during the loading process, and the plastic deformation including, cracks, concrete crushing and spalling, and buckling of longitudinal reinforcement was concentrated bottom end of the columns. Because the right (push) side of the columns experienced damage earlier due to the columns being subjected to cyclic lateral loading, the plastic hinge length in the push direction was different from the plastic hinge length in the pull direction. Therefore, the physical plastic hinge length, L_{pr}, was determined by averaging the measurements of the length of the plastic deformation zone taken on both the right and left sides. The experimental results have revealed that plastic hinge length increases with increasing the axial compression and longitudinal reinforcement ratio. Other researchers [156, 162, 163] have also made similar observations regarding the relationship between axial compression ratio/longitudinal reinforcement ratio and the length of the plastic hinge.

Over the past few decades, numerous researchers have proposed a wide range of models for predicting the plastic hinge length of RC columns. In numerical modeling, it is important to determine the efficiency of the proposed models for the bolted dry joints. To compare the experimental plastic hinge length with the predicted plastic hinge length, equivalent plastic hinge length ($L_{p,e}$) which also considers yield penetration are calculated using **Eq. (4.9)** proposed by Hines et al. [164]. The physical and equivalent plastic hinge lengths for each specimen are summarized in **Table 4.7**. The comparison of the equivalent plastic hinge lengths with the predicted plastic hinge lengths is tabulated in **Table 4.8**. It was seen that equivalent plastic hinge length is best predicted with the model proposed by Ning and Li [163] with a mean of -7%.

$$L_{p,e} = \frac{L_{pr}}{2} + L_{pb} \qquad \textbf{(4.9)}$$

where L_{pb} = plastic hinge length due to yield penetration into the base, i.e., $L_{pb} = 0.022 f_y d_b$. **Eq. (4.9)** was relied on the assumption that plastic deformation follows a linear distribution from the upper part to the lower part within the physical plastic hinge zone.

Table 4.7 Measured and equivalent plastic hinge lengths for all specimens

Plastic hinge length	**Models**	**CMC-0.10**	**CMC-0.20**	**CMC-0.30**	**CDC-0.10**	**CDC-0.20**	**CDC-0.30**
Physical	L_{pr}	155	170	197	195	205	200
Equivalent	$L_{p,e} = \frac{L_{pr}}{2} + 0.022 f_y d_b$	178	185	199	198	203	200

Table 4.8 Comparison of equivalent plastic hinge length with the predicted plastic hinge lengths

Reference - Year	Models	Prediction error (%)							
		CMC-0.10	CMC-0.20	CMC-0.30	CDC-0.10	CDC-0.20	CDC-0.30	Mean	Std. Dev.
[165] - 1987	$0.08Z + 6d_b$	-33	-35	-40	-39	-41	-40	-38	3
[166] - 1992	$0.08Z + 0.022f_y d_b$	-10	-13	-19	-19	-21	-20	-17	4
[167] - 1993	h (under high axial loads)	41	35	26	26	23	25	29	6
[168] - 2001	$0.12Z + 0.014\alpha_{sl} f_y d_b$	-13	-17	-23	-22	-24	-23	-20	4
[169] – 2005	$0.077Z + 8.16d_b$	-22	-25	-30	-30	-31	-30	-28	3
[170] - 2008	$0.05Z + 0.1\frac{f_y d_b}{\sqrt{f_c}}$	-31	-34	-38	-39	-41	-40	-37	4
[162] - 2008	$\left(0.3\frac{P}{P_0{}'} + 3\frac{A_s}{A_g} - 0.1\right)Z + 0.25H \geq 0.25H$	-65	-66	-59	-68	-62	-52	-62	6
[171] - 2009	$0.9\left(1 + 0.5\frac{P}{P_0{}'}\right)k_1\left(\frac{Z}{h}\right)^{0.25} h\ for\ \frac{P}{P_0} > 0.2$ $0.25h\ for \frac{P}{P_0{}'} \leq 0.2$	-65	-66	17	-68	-69	11	-40	38
[172] - 2010	$0.2h\left[1 + \min(9, {}^{Z}/_{h})/3\right]$	-44	-46	-50	-49	-51	-50	-48	3
[163] - 2016	$(0.042 + 0.072P/P_0)Z + 0.298h + 6.407d_b$	-1	-2	-6	-11	-11	-7	-7	4
[173] - 2005	$\frac{Z}{30} + 0.2h + 0.11\alpha_{sl}\frac{f_y d_{bl}}{\sqrt{f_c}}$	-11	-15	-20	-21	-23	-22	-19	4
	$0.1Z + 0.17h + 0.24\alpha_{sl}\frac{f_y d_{bl}}{\sqrt{f_c}}$	68	61	50	49	45	47	53	8
[149] - 2018	$h/2$	-30	-33	-37	-37	-38	-38	-35	3

Note: Z is the distance from the critical section to the point of contra-flexure, d_b is the maximum diameter of tension reinforcement, d_{bl} is the mean diameter of tension reinforcement, $f_y$is the yield strength of tension reinforcement (in MPa), f_c is the concrete compressive strength (in MPa), h is the section depth, α_{sl} is the coefficient for slip (which equals 1 if considering the bar pullout effect or 0 if not), P_0 is the axial load capacity in terms of $f_c \times A_g$; $P_0{}'$ is the nominal axial load capacity $(0.85f_c(A_g - A_s) + f_y A_s)$; A_s area of longitudinal reinforcements, A_g is the cross-sectional area, $k_1 = 0.9 - \left(\frac{0.3}{23.5}\right)(f_c - 11.7), (0.6 \leq k_1 \leq 0.9)$.

4.1.9. Damage assessment

4.1.9.1. Qualitative Damage States and Descriptions

In the third study, after the second cycle of each level of the drift ratio, all components of the specimen were photographed using the camera. The obtained photographs were used to quantification of visible damages such as cracking, concrete spalling and crushing, core crushing, and reinforcement buckling. Damage states (degree) of the test specimens were estimated using predefined criteria from detected visible damages. Typically, the damage state of a column is categorized into five different levels: insignificant, slight, moderate, severe, or extreme. These classifications provide a qualitative assessment of the extent of damage observed in the column. A summary of the proposed qualitative damage state definitions of RC columns by researchers is given in **Table 4.11**. Additionally, the standards proposed several performance levels and defines damage descriptions for these performance levels (**Table 4.9**). With the help of the proposed qualitative damage descriptions, damage descriptions for these five levels were determined and then corresponding drift ratios were calculated (**Table 4.10**). These five damage states (DS) given in **Table 4.10** are also depicted in **Figure 4.24**.

In general, the observed failure modes and damage states of bolted specimens were similar to these of the monolithic counterparts. The first visible fine cracks initiated between drift ratios of 0.50-0.75%. The minor flexural cracks and partial concrete crushing initiated at column ends around 1.00% drift ratios. The concrete crushing and slight spalling were observed at a drift ratio of 1.50–2.00%, generally, leading to achieving maximum lateral load capacities. Similar to the observation of Barrera et al. [156], the maximum lateral loading capacity of the specimens was generally achieved due to the spalling of the concrete cover. Cover concrete crushing, spalling of crushed concrete, and exposure of reinforcement were observed at drift ratios of 2.00-3.00%. Finally, the specimens failed due to the crushing of the concrete confined zone followed by the buckling of the longitudinal rebar on the column at drift ratios of 3.00-4.50%.

Table 4.9 Qualitative damage descriptions for different performance levels

	Performance level			
Reference	**Immediate Occupancy**	**Damage Control**	**Life Safety**	**Structural stability (Collapse prevention)**
ATC-40 [174]	Very limited flexural and shear cracking with no spalling. No	Limited flexural and shear cracking with little or no spalling. No	Hinges have formed in the lower portions of the building, causing spalling above and below beam-column	Hinges have formed in the lower portions of the buildings causing significant spalling above and below beam-column

	permanent horizontal offset. Gravity capacity maintained.	permanent horizontal offset. Gravity capacity maintained.	joints. Permanent horizontal offset approaching 2.0% inter-story drift with small areas marginally higher. Gravity capacity maintained.	joints and pulverizing of concrete within the core. Permanent horizontal offset approaching 3.5% inter-story drift with small areas marginally higher. Gravity capacity is maintained throughout nearly all of the structure.
FEMA 356 [153] - FEMA 273 [175]	Minor hairline cracking. Limited yielding is possible at a few locations. No crushing (strains below 0.003). (No permanent drift)	-	Extensive damage to beams. Spalling of cover and shear cracking (<1/8" width) for ductile columns. Minor spalling in non-ductile columns. Joint cracks <1/8" wide. (Permanent drift limit 1.0%)	Extensive cracking and hinge formation in ductile elements. Limited cracking and/or splice failure in some non-ductile columns. Severe damage in the short columns. (Permanent drift limit 4.0%)

Table 4.10 Observed relationship between damage states and drift ratio

Damage state	Qualitative damage description	CMC-0.10	CMC-0.20	CMC-0.30	CDC-0.10	CDC-0.20	CDC-0.30
Insignificant DS1	No damage or visible fine flexural cracks.	0.50%	0.50%	0.50%	0.50%	0.50%	0.75%
Slight DS2	Minor flexural cracks, visible shear cracks, partial crushing of concrete.	1.0-1.5%	1.00%	1.00%	1.50%	1.50%	1.00%
Moderate DS3	Moderate cracks, concrete crushing, slight spalling.	2.00%	1.50%	1.50%	2.00%	2.00%	1.50%
Severe DS4	Extensive cracking, localized spalling, obvious exposure of reinforcements.	3.00%	2.50%	2.00%	3.00%	2.50%	2.00%
Extreme DS5	Crushing of core concrete - reinforcement buckling and rupturing.	3.5-4.5%	3.5-4.5%	2.5-3.0%	3.5-4.5%	3.5-4.5%	2.5-3.5%

Table 4.11 A summary of proposed qualitative damage state definitions of RC columns.

Reference - Year	Damage state Insignificant damage, DS1	Slight damage, DS2	Moderate damage, DS3	Severe damage, DS4	Extreme damage, DS5
[176] - 1985	Sporadic occurrence of cracking.	Minor cracks, partial crushing of concrete.	Extensive large cracks, spalling of concrete in weaker elements.	Extensive crushing of concrete, disclosure of buckled reinforcements.	Total failure or partial collapse.
[177] - 2000	Barely visible cracks.	Reinforcement yielding, crack width is less than 1.0 mm.	Crack width ranges from 1.0 – 2.0 mm, diagonal cracks, concrete cover spalling (spalled region length <1/10 cross-section depth).	Wide cracks (crack width > 2.0 mm), diagonal cracks extend over 2/3 cross-section depth, length of the spalled is greater than ½ cross-section depth.	Cracks in core concrete (crack width > 2.0 mm), buckling of main reinforcing bars, rupture of transverse reinforcement, crushing of core concrete (expansion of concrete > 5%)
[178] - 2004	Visible narrow cracks on a concrete surface (crack width < 0.2 mm).	Visible clear cracks on a concrete surface (crack width ≈ 0.2 -1.0 mm).	Local crush of concrete cover, remarkable wide cracks (crack width ≈ 1.0 - 2.0 mm).	Remarkable crush of concrete with exposed reinforcing bars, spalling off of concrete cover (crack width > 2.0 mm).	Buckling of reinforcing bars, cracks in core concrete, visible vertical and/or lateral deformation in columns and/or walls.
[179]- 2010	Flexural cracks.	Minor spalling, possible shear cracks.	Extensive cracks, spalling	Visible lateral and/or longitudinal reinforcing bars	Imminent failure (i.e., onset of compressive failure of core concrete)
[180] - 2013	No damage or localized minor shear cracking along the column.	Insignificant damage, shear cracking throughout column, yielding of reinforcement, and initial de-bonding of concrete cover.	Severe cracking along the column, localized concrete cover spalling.	Severe concrete cover spalling, exposed reinforcement, onset of concrete core crushing.	Total concrete core crushing, reinforcement buckling and/or rupturing.
[181]- 2013	-	Flexural damage: Flexural cracks (<2 mm), limited yielding, no spalling. Shear damage: Hairline-minor shear cracks (<0.5 mm).	Flexural damage: Spalling of concrete cover. Shear damage: Moderate shear cracking (>0.5 mm).	Flexural damage: Buckling of compressive reinforcement, core concrete disintegration, fracture of tensile reinforcement, yielding or fracture of transverse reinforcement because of core expansion. Shear damage: Severe shear cracking (>1 mm), stirrup yielding, or fracture.	-
[182] - 2015	Visible narrow cracks on a concrete surface, crack width less than 0.2 mm.	Visible clear cracks on a concrete surface with cracks width 0.2-1.0 mm.	Crack width 1.0-2.0 mm, minor spalling of concrete.	Many wide cracks (width >2.0 mm), severe spalling of concrete, obvious exposure of reinforcement.	Crushing of core concrete, buckling of reinforcement, visible vertical and/or lateral deformation in columns.
[183] - 2017	Onset of hairline cracks.	Minor spalling, no exposed reinforcement.	Excessive spalling, exposed reinforcement.	Spalling over full hinge region, no buckling of longitudinal bars, loss of horizontal bearing capacity.	Buckling of main reinforcement, rupture of transverse reinforcement, crushing of core concrete, loss of vertical bearing capacity.

4.1.9.2. Quantitative Damage States and Descriptions

Qualitative (visual observation-based) damage indications, such as crack width and concrete cover spalling, are frequently subject to the engineer's discretion [184]. So, to provide a quantitative description of the seismic damage assessment of specimens, researchers have suggested various models for determining the damage index, which can be expressed as a function of drift ratio [185], stiffness [186, 187], ductility [188], energy dissipation [189], fatigue effect [190], acceleration [191], fundamental period [192], combined [193], etc. These models aim to capture multiple aspects of structural behavior and provide a comprehensive assessment of the level of damage and the damage-related cost caused by seismic events.

One of the most common and widely accepted damage index models has been proposed by Park and Ang [193]. The proposed damage index model is based on ductility and energy dissipation and calculated using **Eq. (4.10)**. To ensure comparability with previous studies, the present study utilizes the P&A damage index model to calculate the damage to the columns.

$$DI_{P\&A} = \frac{\delta}{\delta_{u,m}} + \beta \frac{\int dE}{P_y \delta_{u,m}} \qquad \textbf{(4.10)}$$

where DI represents the damage index of the RC members, Δ represents the maximum lateral displacement in the loading cycles, $\delta_{u,m}$ represents the maximum displacement capacity under monotonic loading, P_y represents the yield capacity, $\int dE$ represents the hysteretic energy absorbed by the element for a cycle with amplitude δ, and β represents the non-negative parameter considering the effect of cyclic load, which is determined by experiments or empirical models. Cosenza et al. [194] reported the value of β can vary between –0.3 and 1.2 with a median value of 0.15. In this study, to calculate the value of β, an empirical model proposed by Park and Ang [193] was used (as shown in **Eq. (4.11)**).

$$\beta = (-0.447 + 0.24n_0 + 0.073\lambda + 0.314\rho_l) \times 0.7^{\rho_t} \qquad \textbf{(4.11)}$$

here, n_0 represents the normalized axial stress (P/P_0, replaced with 0.2 if n_0<= 0.2), λ represents the shear span ratio (Z/h, replaced with 1.7 if λ<= 1.7), ρ_l represents the longitudinal steel ratio as a percentage (replaced with 0.75% if ρ_l<=0.75%), and ρ_t represents the confinement ratio as a percentage.

It is important to mention that the values of δ, P_y, and $\int dE$ in this model can be derived from the test results of the specimens. However, the value of $\delta_{u,m}$ was estimated using the empirical formula (as shown in **Eq. (4.12)**) specified in Eurocode 8 [173] for calculating the ultimate drift ratio.

$$\begin{aligned}\frac{\delta_{u,m}}{Z} &= \theta_{u,m} \\ &= \frac{1}{\gamma_{el}} 0.016 \times 0.3^{n_0} \left[\frac{\max(0.01, \omega^*)}{\max(0.01, \omega)} f_c\right]^{0.225} [\min(9, \lambda)]^{0.35} 25^{\alpha \rho_{sx} \frac{f_y}{f_c}} (1.25)^{100\rho_d}\end{aligned} \tag{4.12}$$

where γ_{el} is equal to 1.0 to simulate monotonic response, ω and ω^* refer to the ratio of tension (including web reinforcements) and compression reinforcement respectively, ρ_{sx} refers to the transverse reinforcement ratio, f_{yt} refers to the yield stress of transverse reinforcement, ρ_d refers to the diagonal reinforcement ratio, and α refers to the confinement effectiveness ratio derived from the following expression:

$$\alpha = \left(1 - \frac{s_h}{2b_w}\right)\left(1 - \frac{s_h}{2h_c}\right)(1 - \frac{\sum b_i^2}{6b_w h_c}) \tag{4.13}$$

Where s_h refers to the stirrup spacing, b_w and h_c refer to the width and height of the confined concrete core respectively, b_i refers to the centerline spacing of longitudinal reinforcement (index by i) laterally restrained by a stirrup corner.

In the P&A damage index model, the relationship between the damage index value and the state of damage in specimens is established using a scale ranging from 0 to 1. A value of 1 indicates a failure state, while a value of 0 represents an undamaged state of the specimens. Intermediate values within the range of 0 to 1 indicate various levels of damage, progressing from the undamaged state toward the failure state. **Table 4.12** illustrates the relationship between damage states and damage index. Additionally, according to Park et al. [176], the overall damage index may tentatively be defined as follows: $DI_{P\&A} \leq 0.4$ represents reparable damage; $DI_{P\&A} > 0.4$ represents damage beyond repair; and $DI_{P\&A} \geq 1.0$ represents total collapse.

Table 4.12 Ranges of the damage index for different damage states taken from study of Park et al. [176]

Damage state	Qualitative damage description	Damage index
Insignificant damage	Sporadic occurrence of cracking	$0.00 \leq DI_{P\&A} < 0.10$
Slight damage	Minor cracks, partial crushing of concrete	$0.10 \leq DI_{P\&A} < 0.25$
Moderate damage	Extensive large cracks, spalling of concrete in weaker elements	$0.25 \leq DI_{P\&A} < 0.40$
Severe damage	Extensive crushing of concrete, disclosure of buckled reinforcements	$0.40 \leq DI_{P\&A} < 1.00$
Extreme damage	Total failure or partial collapse	$DI_{P\&A} \geq 1.00$

Proposed limits for damage states by Park et al. [176] were compared with the values of damage indices for observed damage states in **Figure 4.31**. Description of damage states in **Table 4.12** are similar to that of damages states in **Table 4.10** except that the description of DS4 and DS5 damage states in **Table 4.10** corresponded to the severe damage state in **Table 4.12**. The obtained results showed that damage states: DS1, DS2, DS3, DS4, and DS5, were observed at, on average, damage indices of 0.15, 0.34, 0.49, 0.73, and 0.97, respectively. As can be seen, the proposed limits by Park et al. [176] are generally conservative and inadequate. With the limited knowledge from experimental results in this study, damage index limits for damages states were calculated using statistical methods as follows: $DI_{P\&A}$≤0.25 representing DS1, 0.25≤$DI_{P\&A}$≤0.40 representing DS2, 0.40≤$DI_{P\&A}$≤0.60 representing DS3, 0.60≤$DI_{P\&A}$≤0.80 representing DS4, and $DI_{P\&A}$≥0.80 representing DS5.

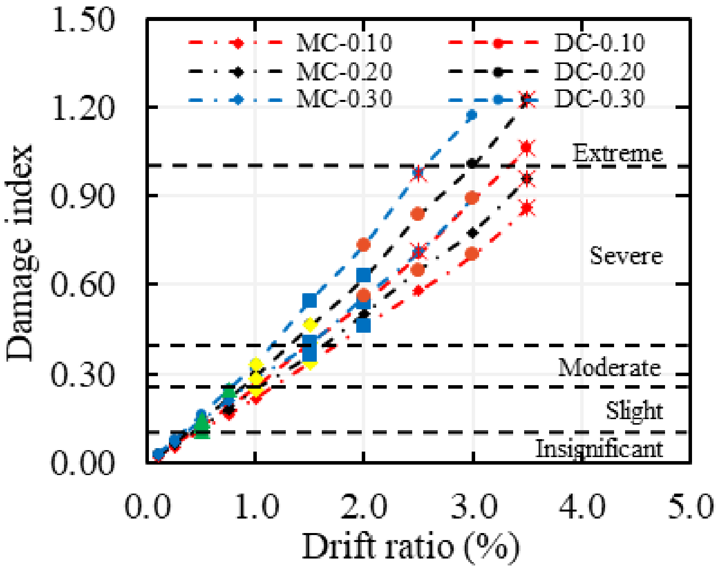

Figure 4.31 Damage index values of the specimens and proposed limits for damage states by Park et al. [176].

Japanese guideline (JDBPA, [182]) and Chiu et al. [195] proposed reduction factors for stiffness and strength according to the observed damage states. Chiu et al. [195] proposed a modified model that provides conservative estimations in addition to the original model. The proposed reduction factors concerning the damage states are tabulated in **Table 4.13**. To assess the stiffness degradation changes of the specimens, observed damage states with stiffness degradation ratios of the specimens concerning the drift ratio are drawn in **Figure 4.24**. Additionally, reduction factors for stiffness which is proposed by JBDPA [182] are highlighted. As shown in **Figure 4.24**, the initial crack formation (DS1*) led to a stiffness reduction of up to 50%. A slight spalling of a concrete cover (DS3*) caused a reduction in stiffness by 65-80%. When cracking and crushing of the confined concrete zone of a specimen (DS4*) was observed, stiffness reduced to approximately 10% of initial stiffness. Based on the results, it was found that the reduction factors suggested by both JBDPA [182] and the original model of Chiu et al. [195] yielded conservative estimations. However, the modified model of Chiu et al. [195] demonstrated good accuracy in estimating the observed values.

Table 4.13 Suggested reduction factors for flexural failure dominant RC beams/columns

Reference - Year	**Reduction factor for**	**DS1***	**DS2***	**DS3***	**DS4***	**DS5***
[182] - 2015	Stiffness	0.95	0.75	0.50	0.20	0.00
	Strength	0.95	0.75	0.50	0.20	0.00
[195] – 2020 (Modified)	Stiffness	1.00	0.60	0.35	0.15	0.00
		(0.65)	(0.40)	(0.25)	(0.10)	(0.00)
	Strength	1.00	1.00	1.00	0.75	0.00
		(1.00)	(1.00)	(1.00)	(0.60)	(0.00)

Note: * definition of damage states is given in JBDPA [182].

4.1.10. Code-Based Capacity Predictions of Specimens Made with CDW-based Geopolymer Concrete

The design axial load capacity and design moment capacity were calculated by **Eq. (4.14)** and **(4.15)** based on definitions and limits in ACI318 [77] and TS500 [76]. In these calculations, the nominal moment and axial load capacities were calculated based on a stress-strain model for concrete proposed by Mander et al. [155]. While calculating the design axial load and moment capacities of the columns, the maximum limits for allowable axial load capacity by seismic and design codes were considered. Additionally, a model named as fiber model that does not include strength reduction factors or material factors (Φ=1) and is not restricted by maximum axial load limits, was calculated.

$$N = \Phi \sum_{i=1}^{nc} \sigma_i A_i + \Phi \sum_{j=1}^{ns} \sigma_{ej} A_j \tag{4.14}$$

$$M = \Phi \sum_{i=1}^{nc} \sigma_i A_i y_i + \Phi \sum_{j=1}^{ns} \sigma_{ej} A_j \, y_j \tag{4.15}$$

where Φ refers to the strength reduction factor for ACI 318 (0.65 to 0.90 based on strain), or the material factor for TS500 (1.50 for concrete, 1.15 for reinforcement), σ_i and σ_j refer to stress at the centroid of i^{th} concrete fiber and centroid of j^{th} longitudinal reinforcement, respectively, A_i and A_j refer to area of i^{th} concrete fiber and of j^{th} longitudinal reinforcement, respectively, y_i and y_j refer to ordinates of i^{th} concrete fiber and of j^{th} longitudinal reinforcement, and nc and ns refer to number concrete fibers and of longitudinal reinforcements.

The calculated axial load-moment interaction curves are tabulated in **Table 4.14** and presented in **Figure 4.22**. As can be seen, the moment and axial load capacities of demountable and monolithic geopolymer concrete specimens were predicted best by the fiber model. The percentage errors of ACI318-19 (TS500) predictions for monolithic specimens with 10%, 20%, and 30% axial compression ratios, on average, were 10.62% (17.62%), 17.09% (19.51%) and 29.59% (18.67%), respectively. Similarly, the percentage errors of ACI318-19 (TS500) predictions for demountable specimens with 10%, 20%, and 30% axial compression ratios, on average, were -9.13% (-0.93%), 27.05% (21.98%) and 41.30% (29.13%), respectively. It is obvious that ACI318 [77] provides more conservative capacity predictions than the TS500 [76]. It can be inferred that the prediction performance of TS500 [76] is slightly better than the prediction performance of ACI318 [77], especially for a high axial compressive ratio. Also, it was seen that capacity prediction errors of the design codes are generally increased with increasing axial compressive ratio for the demountable and monolithic specimens. Additionally, capacity prediction errors of the design codes were higher for the demountable specimens than for the monolithic specimens. Consequently, it can be stated that the current codes' equations for conventional reinforced concrete products resulted in similar estimation performance for CDW-based geopolymer concrete products. However, there was a slight lack of conservatism.

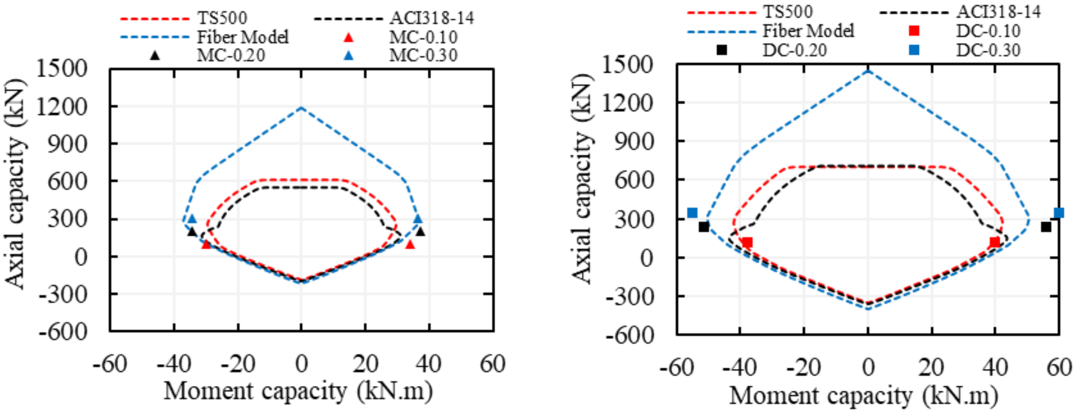

Figure 4.32 Comparison of experimental results with analytically predicted results.

Table 4.14 Comparison of experimental and predicted results.

		Test	**Fiber Model**		**ACI318-14**		**TS500**	
Test ID	***N***	***M_{max}***	***M***	**Error**	***M***	**Error**	***M***	**Error**
	kN	**kN.m**	**kN.m**	**%**	**kN.m**	**%**	**kN.m**	**%**
CMC-0.10 (push)	101.25	34.08	29.34	13.90	28.45	16.52	26.22	23.06
CMC-0.10 (pull)	101.25	-29.86	-29.34	1.72	-28.45	4.71	-26.22	12.18
CMC-0.20 (push)	202.50	37.43	34.35	8.21	29.78	20.43	28.91	22.74
CMC-0.20 (pull)	202.50	-34.53	-34.35	0.51	-29.78	13.76	-28.91	16.27
CMC-0.30 (push)	303.75	36.49	36.73	-0.66	24.92	31.70	28.79	21.10
CMC-0.30 (pull)	303.75	-34.37	-36.73	-6.87	-24.92	27.49	-28.79	16.23
CDC-0.10 (push)	117.00	39.86	44.86	-12.54	42.36	-6.27	39.18	1.71
CDC-0.10 (pull)	117.00	-37.83	-44.86	-18.58	-42.36	-11.98	-39.18	-3.57
CDC-0.20 (push)	234.00	55.81	49.66	11.02	39.03	30.06	41.74	25.20
CDC-0.20 (pull)	234.00	-51.38	-49.66	3.34	-39.03	24.03	-41.74	18.75
CDC-0.30 (push)	351.00	59.87	49.79	16.84	33.67	43.77	40.65	32.11
CDC-0.30 (pull)	351.00	-55.04	-49.79	9.54	-33.67	38.83	-40.65	26.15

4.1.11. Design methodology for Connection DC4

According to the test results, the connection types GDC1-GDC3 failed to well-matured plastic hinging in the column. Therefore, it is recommended to use DC4 connection as proper seismic column base connection. The design philosophy of this connection is thoroughly based on enforcing the plastic deformations in the RC column. Thus, the steel plates and connection bolts are designed to remain elastic. For the design methodology of the proposed connection DC4 is as follows:

- Perform both flexure and shear design of the RC column as per any reinforced concrete standard (i.e., ACI318, Eurocode 2, TS500, etc.),
- Add eight threaded bars having the same diameter as the smallest longitudinal reinforcement of the RC column,
- Determine the plastic hinge length of the RC column and take the length of the threaded bars as two times the calculated plastic hinge length,
- Design thickness of the base plate, stiffeners at the steel base plate and bolts using general rules and methods for steel base connections.

In this procedure, the column internal forces are transferred to the base plate and the bolts are designed by firstly determining the position of the neutral axis at the base plate level. The strain profile at the base plate level is assumed to be linear (**Figure 4.33**) and hence the bolt axial forces are related to their positions relative to the neutral axis location. For simplification, bearing stress profile at the compression side of the base plate is assumed constant. After that, thickness of the base plate is determined by checking the flexural stress demands with the yield strength of the selected steel. The stress demands on the base plate could be reduced by applying stiffeners to the base plate (i.e., to reduce the required thickness of the base plate).

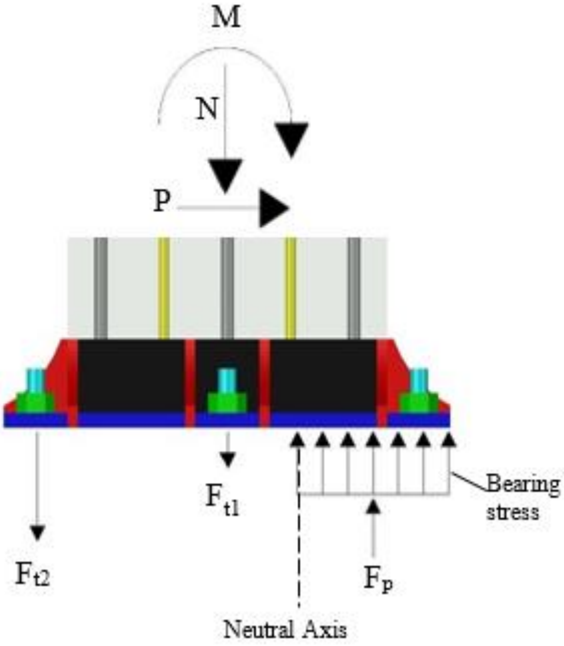

Figure 4.33 Example free body diagram used to design demountable connection

4.2. Summary of beam-to-column connection tests

4.2.1. General Behavior of the Demountable Beam-to-Column Connection

The demountable beam-to-column connection exhibited stable and controlled behavior under both bending and shear loading scenarios. The connection was designed as a simple support that restrained in-plane and out-of-plane deflections while allowing free rotation under vertical loading. No initial signs of instability or slip were observed during the early loading stages, confirming the proper fit and engagement of the steel socket mechanism.

The mechanical interlocking system, resembling a lock-and-key configuration between the T-shaped profiles on the beam and the steel socket on the column, performed as intended.

4.2.2. Flexural Behavior and Crack Development

Under monotonic flexural loading, the connection allowed sufficient rotation at the interface without any signs of local failure in the steel socket or surrounding concrete. The first flexural cracks appeared near the end of the beam under 50 kN vertical loading. As the loading increased, additional flexural cracks propagated toward the midspan.

Until the target deflection, minor deformations were observed in main body of the beam, but no yielding or buckling occurred. If the three-point flexural test applied, the beam would showed yielding of longitudinal reinforcement near midspan.

The load–displacement response of the system displayed a ductile trend, with gradual stiffness degradation beyond the yield point and stable post-yield behavior until ultimate load.

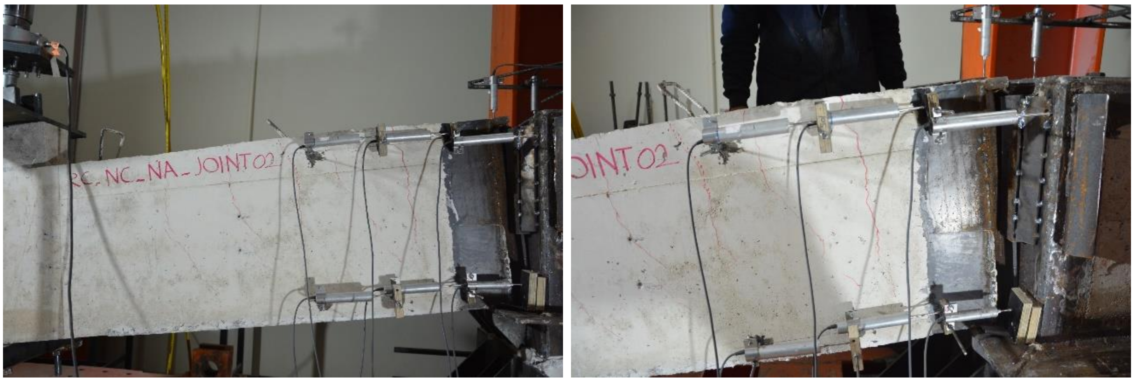

Figure 4.34 First cracks on the demountable beam connection

At a vertical load of 65 kN, tearing began to occur in the UPN profiles located at the upper part of the steel plates on the column. The load–displacement response of the system displayed a ductile trend, with gradual stiffness degradation beyond the yield point and stable post-yield behavior until ultimate load.

Figure 4.35 Failure states of the beam-to-column connection

4.2.3. Shear Performance of the Connection Interface

A separate shear test was conducted to evaluate the performance of the steel socket and the shear transfer elements between the beam and the column. The shear force was applied through an I-shaped steel profile that transferred the load directly to the equal angle sections located beneath the steel socket.

No LVDTs were used during the shear test; instead, the applied force was monitored via a high-capacity load cell. The connection successfully resisted the applied shear loads without noticeable slippage or local failure in the angle profiles or welds.

The use of stiffeners in the angle sections contributed significantly to the integrity and stiffness of the connection under shear.

Up to approximately 300 kN of loading, no deformation was observed in the connection.

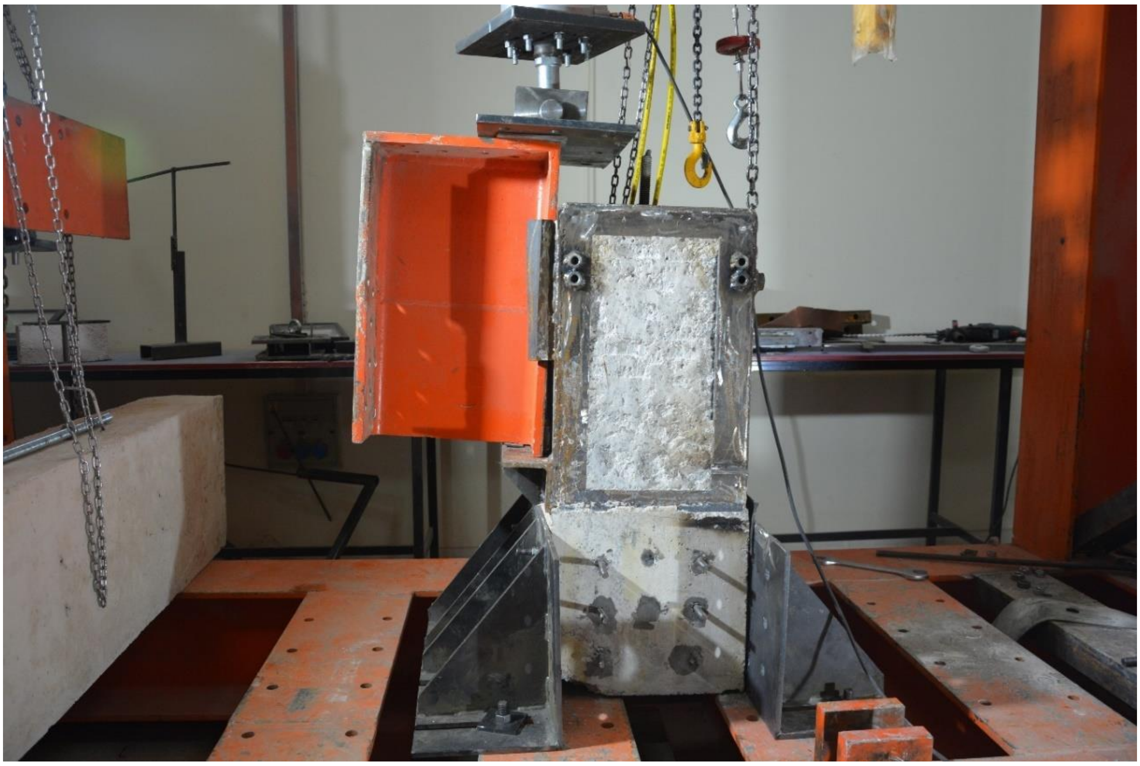

Figure 4.36 Shear test of the beam-to-column connection

4.2.4. Load–Displacement Behavior and Rotation Capacity

The load–displacement behavior of the final design demountable beam under flexural loading indicated sufficient energy absorption and deformation capacity. The ultimate load was reached without any sudden loss of stiffness, and the beam-to-column connection maintained structural continuity throughout the test. Because of the limited LVDT deflection capacity, ultimate deflection capacity cannot be captured.

The total rotation capacity of the beam at the interface was measured indirectly from the relative displacements, and the connection allowed for several degrees of rotation before failure. This confirms the intended performance of the demountable interface as a flexible yet reliable rotational joint under gravity loads.

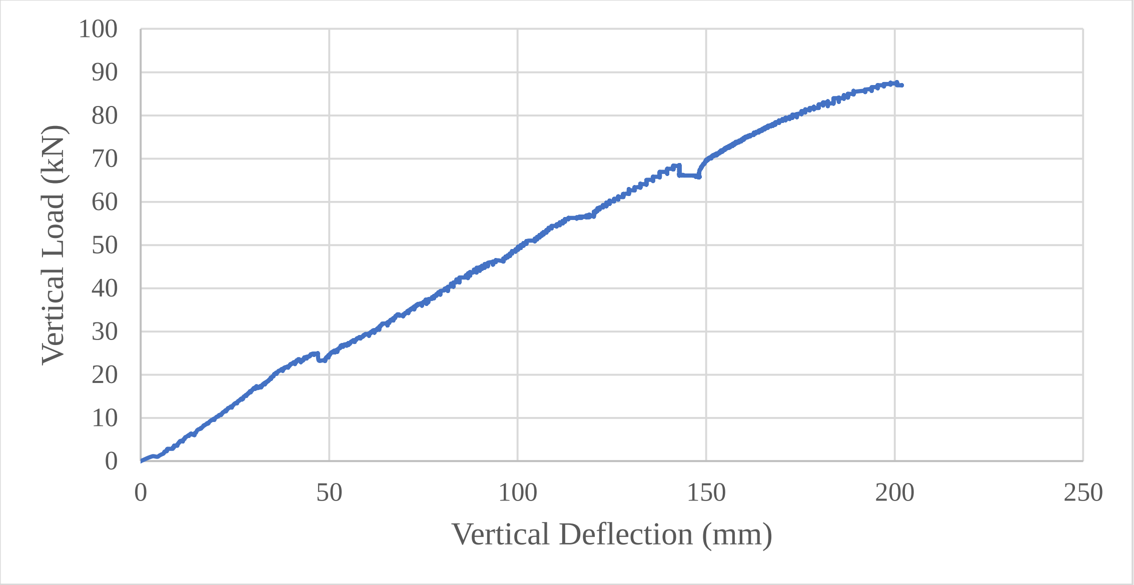

4.2.5. Summary of Observations

- The demountable connection successfully emulated simple support behavior while providing adequate rotational freedom and shear resistance.
- Both flexural and shear tests demonstrated ductile behavior with no signs of brittle or premature failure.
- The steel socket and lock-and-key system allowed for easy assembly without compromising performance.
- The observed crack patterns and load responses were consistent with pin-supported beam behavior, validating the structural efficiency of the demountable design.
- The use of encased steel elements, stiffeners, and threaded rods improved the connection's robustness.

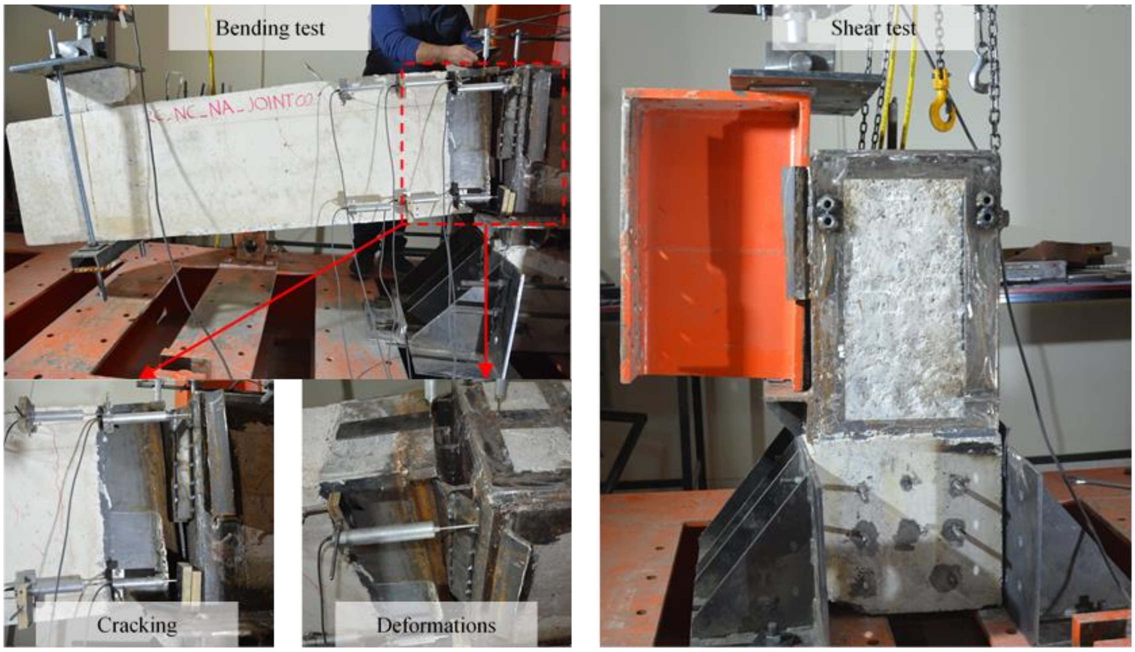

Figure 4.37 Observed failure states of the beam-to-column connection tes

4.3. Summary of slab-to-beam connection tests

4.3.1. General Observations

The demountable slab-to-beam connection was subjected to monotonic vertical loading until failure or target displacement. The specimen exhibited stable flexural behavior during the early stages of loading. Initial cracking was observed at the bottom face of the mid span, indicating the onset of flexural tension failure. No sudden or brittle failure occurred throughout the test.

No visible signs of slip were recorded at the connection interface, suggesting that the demountable mechanism provided sufficient engagement between the slab and the supporting beam.

4.3.2. Crack Pattern and Failure Mode

The first flexural cracks (labeled as 1 and 10) were observed on both sides of the mid-span at a load of 27141 N and a displacement of 7.38 mm. These cracks appeared at approximately 30% of the ultimate load, marking the onset of flexural behavior. As the load increased to 35,809 N and the mid-span displacement reached 10 mm, additional cracks progressively developed toward the support regions in sequential order as illustrated at below figure.

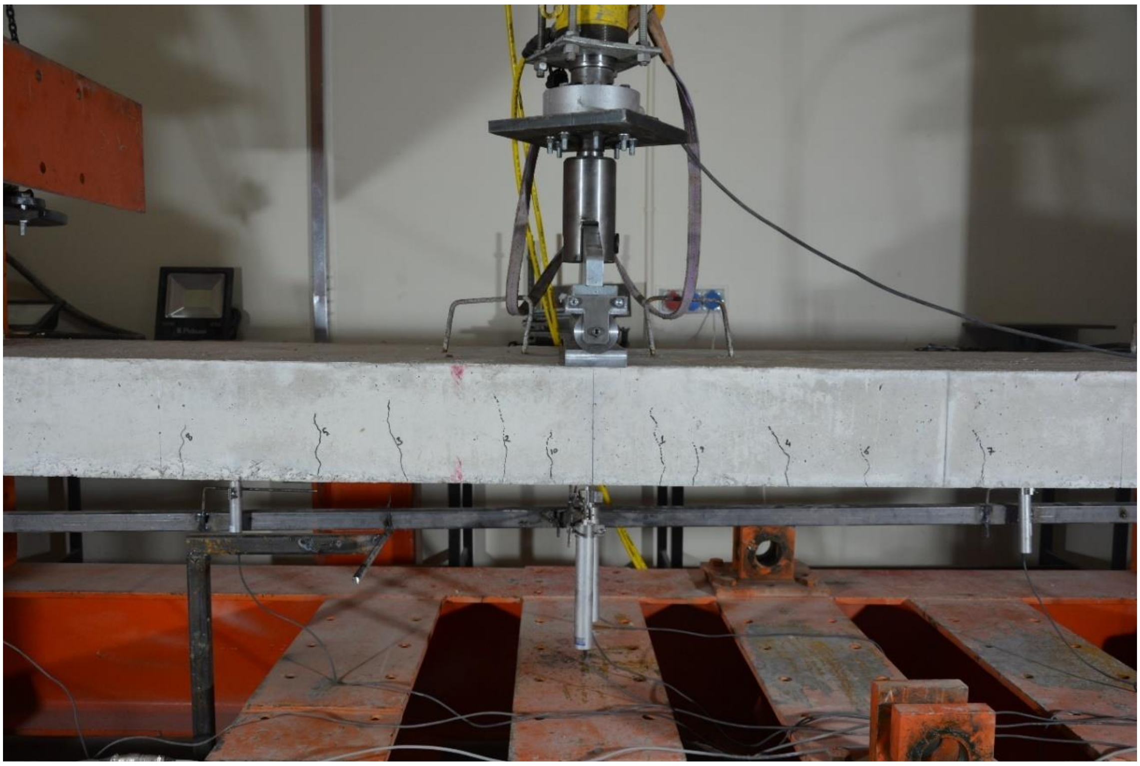

Figure 4.38 Initial cracking of the demountable slab

As the load increased, additional flexural cracks developed symmetrically towards the supports. At higher load levels, diagonal cracks also appeared near the slab mid span, indicating the activation of shear mechanisms.

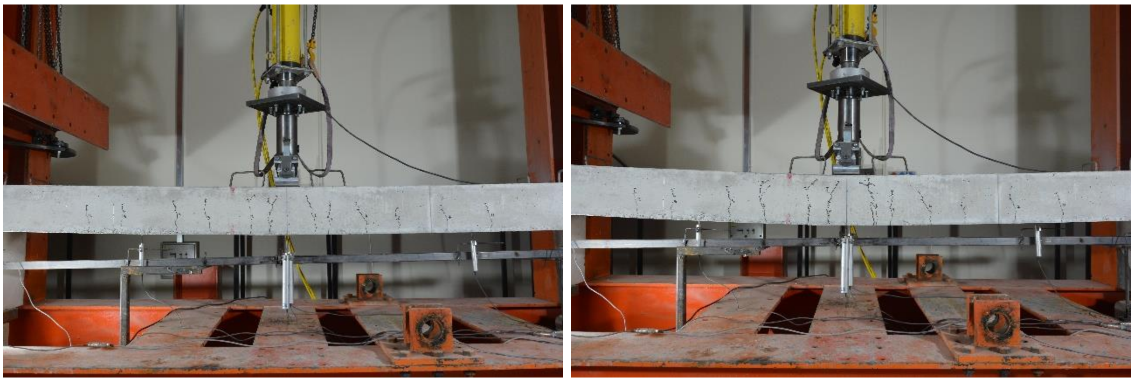

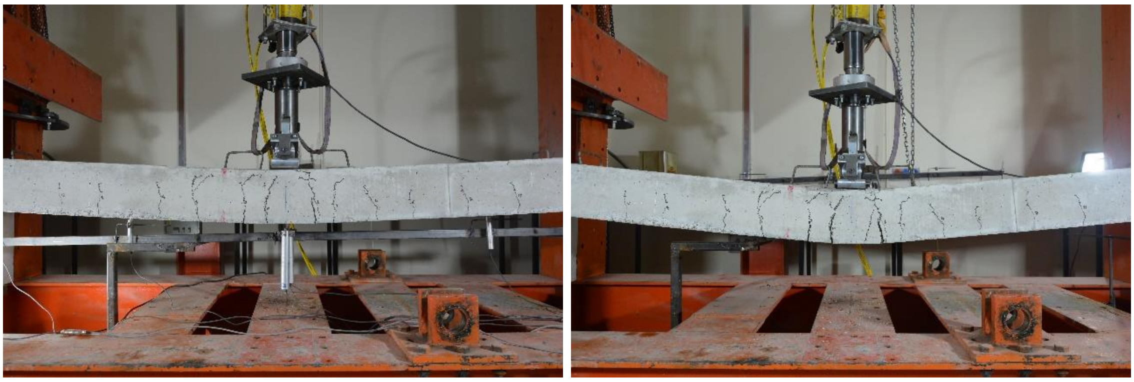

Figure 4.39 Crack propagation of the demountable slab

The failure mode was predominantly flexural, with concrete crushing observed at the top fiber near the loading point and yielding of bottom reinforcement. No signs of connection failure or detachment between the slab and the beam were observed.

Figure 4.40 Failure of the demountable slab

4.3.3. Load–Displacement Behavior

Ductility was evaluated as the ratio of the ultimate displacement to the yield displacement, resulting in a ductility index of higher than 5. This indicates a satisfactory deformation capacity for demountable systems designed with conventional reinforcement.

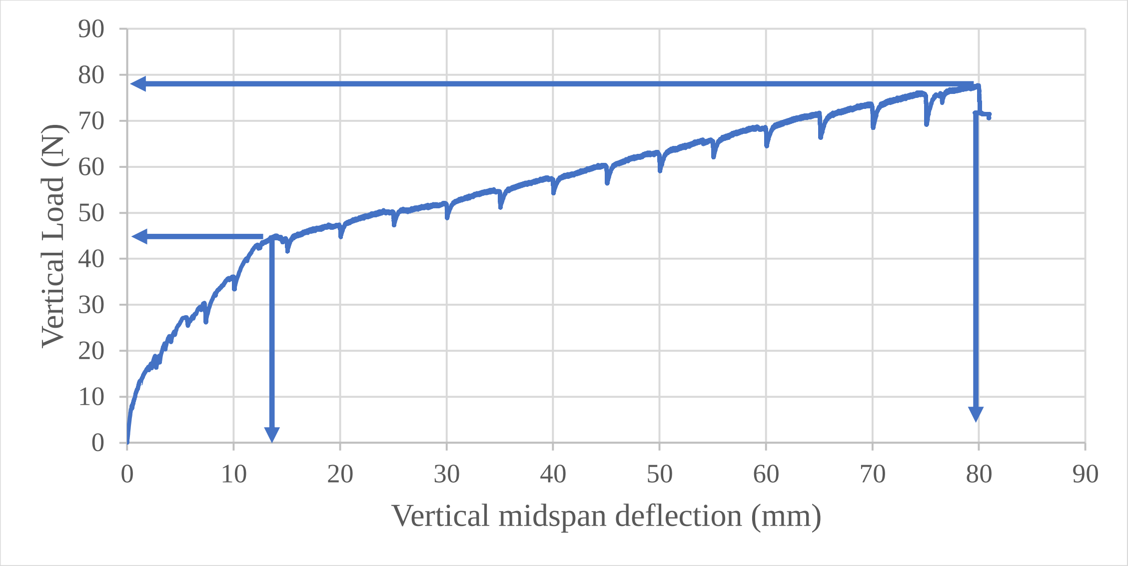

Figure 4.41 Load–displacement behavior of the demountable slab

4.3.4. Shear vs. Flexural Behavior

Although some inclined cracks developed near the midspan at later stages of loading, the observed failure mode was predominantly flexural. No shear failure plane was detected. This confirms that the connection detailing was effective in preventing premature shear failure and allowed the development of plastic hinges in the intended region.

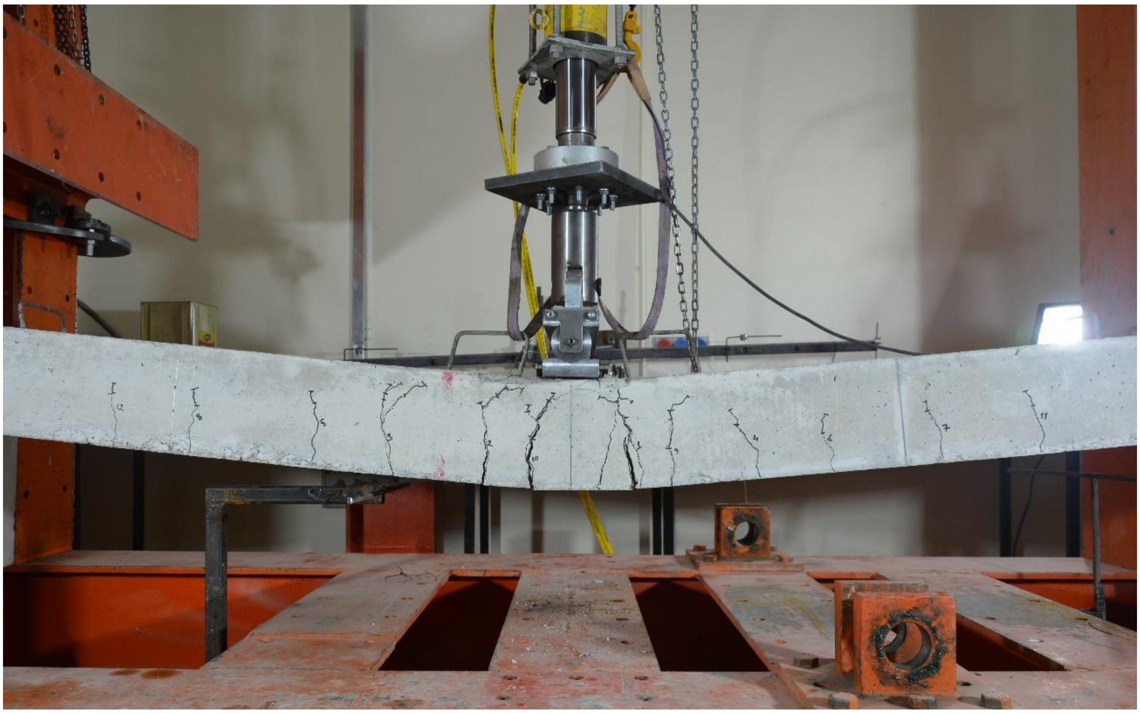

Figure 4.42 Crack behavior of the demountable slab

It is important to note that a certain amount of displacement was intentionally allowed at the supports. In the experimental setup, this was achieved by placing 10 mm-thick elastomeric pads beneath the supports. This design choice helped absorb dynamic effects transmitted through the supports and protected the high-strength threaded rods from premature failure under fluctuating loads.

Figure 4.43 Elastomeric pads usage in the demountable slap-to-beam connection

4.3.5. Summary of Findings

The test specimen did not show a reduction in capacity up to 80 mm deflection that was too higher than the serviceability limits, so the serviceability limit was used to calculate the capacity of the specimen. The recommended deflection limit for the slab by TS500 [76] is equal to the L/240, which corresponds to a deflection of 14.3 mm and an applied load of 44.5 kN.

The beam-to-slab specimen exhibited flexural cracks, crushing, and spalling through the loading line and rotation at the slab-to-beam connection zones (as illustrated in **Figure 4.44**). The observed flexural cracks mainly accumulated in the mid-span of the slab and were widened with increasing load/deflection. The width of the observed cracks at the mid-span of the slab is significant due to the higher moment in the mid-span. At the connection zones, there were no cracks and deformation observed, but the slab easily rotated due to simple support conditions due to the proper load transfer mechanism between slab to beam.

In summary, the demountable slab-to-beam connection exhibited sufficient flexural strength, ductile behavior, and stable crack development under monotonic loading. The connection mechanism ensured full engagement without relative slip, validating its structural reliability for reuse in sustainable construction applications.

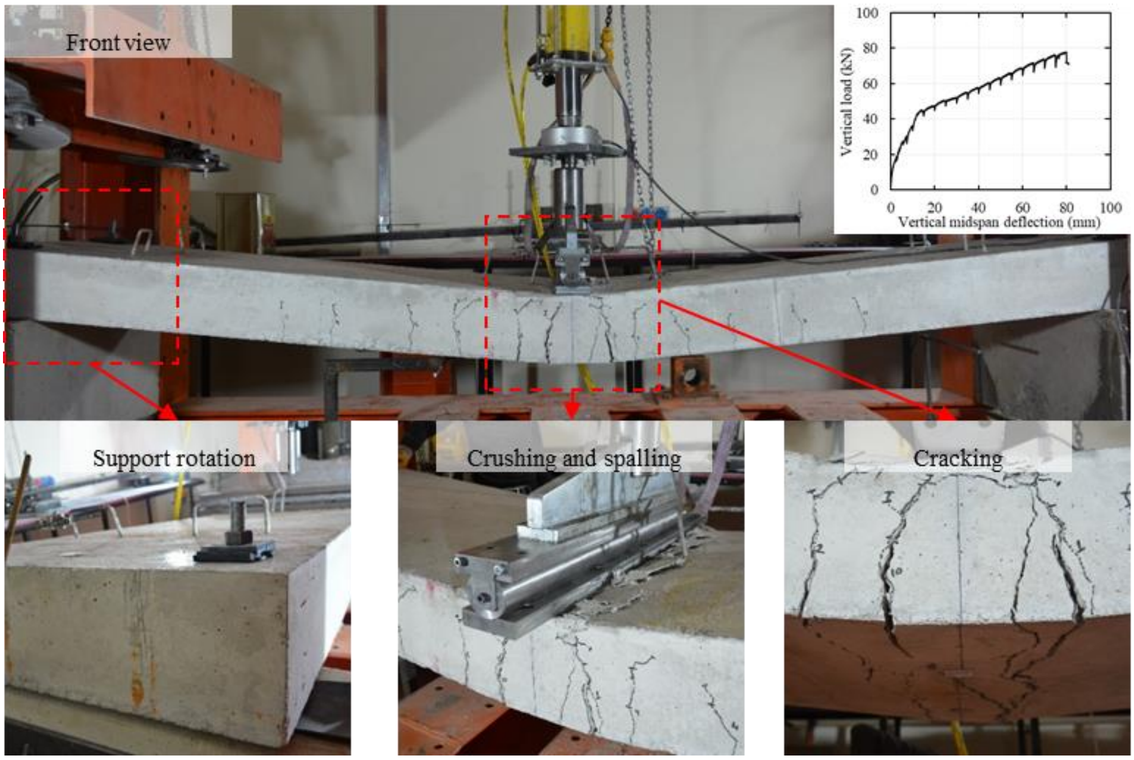

Figure 4.44 Observed failure states of the slab-to-beam connection test

FULL-SCALE ECO-FRIENDLY DEMOUNTABLE BUILDING APPLICATION

5.1. Introduction

In the previous chapters, the structural behavior of demountable precast elements produced with CDW-based geopolymer concrete was comprehensively investigated through a series of experimental studies, including quasi-static cyclic tests on column, beam, and slab components. These studies demonstrated that well-detailed demountable systems can exhibit seismic performance comparable to or exceeding that of monolithic systems while offering environmental and economic advantages in long term usage.

In this chapter, a full-scale one-bay, ~300 m2, modular frame structure is designed, and assembled using the predesigned connections and material configurations identified in the previous experiments. The aim is to demonstrate the real-world applicability, constructability, and structural efficiency of an eco-friendly demountable system under practical conditions. To further elaborate on the motivation and environmental considerations for this chapter, the following section presents the background from previous literature.

The chemical and physical properties of source materials, such as metakaolin, fly ash, and slag, can vary depending on the production process, potentially having a significant impact on the performance of the final geopolymer-based product. Additionally, the feasibility of sourcing these materials can vary depending on the intended production location, and cost considerations may make it challenging for different manufacturers, even within the same country, to acquire the required source material. These factors contribute to the limited widespread use of geopolymers, in comparison to traditional Portland cement (PC), in the production of construction materials such as concrete and bricks. Despite these drawbacks, Duxson et al. [9] indicate that fly ash-based geopolymers require 60% less energy for production and result in a minimum of 80% fewer CO_2 emissions compared to ordinary Portland cement. These findings underscore the substantial environmental advantages of utilizing fly ash-based geopolymers, including significant energy efficiency gains and a noteworthy reduction in carbon dioxide release. This highlights the potential of geopolymers as a sustainable and eco-friendly alternative for construction, offering a greener choice when compared to conventional cement.

By substituting Portland cement with alternative materials, not only can the overall release of CO2 and energy consumption be reduced, but it also enables the efficient utilization of waste materials generated by the industry and/or construction sites. To achieve the production of environmentally friendly and sustainable geopolymeric binders and increase the feasibility of source materials, it is necessary to not only use CDW as a filler material but also leverage the inert portion of CDW. Recognizing the ease of availability of CDW globally, some studies [19, 20, 147, 196] have been conducted to explore the use of CDW-based source materials for geo-polymerization in the manufacturing of various construction materials, which shows desired mechanical, chemical, and durability performances.

One of the other significant opportunities to mitigate significantly the environmental impact of construction and demolition activities is the reuse of structural elements once a structure has completed its service life. The problem with the conventional prefabricated and traditional construction is mainly the same. These structures generally built with fixed connections (i.e., wet joint in prefabricated construction) as no versatile connection other than fixed connections that performs well under the effect of large lateral load demands like earthquakes and wind load effects exist. When these structures reach the end of its service life, even though the steel and concrete materials remain functional, the building is typically destructively demolished. the building is typically destructively demolished. The demolished structures have no use other than being waste or being used as landfills. The most of the waste steel are recycled through energy-intensive melting processes, while the remaining waste materials are either sent to landfills or recycled to a limited extent. Facilitating the reusability of structural elements has the potential to achieve a remarkable reduction of more than 50% in the embodied energy of structures while also providing clients with the added benefit of preserving the value of their assets. The prefabrication method, where structures are designed and constructed with reuse in mind after their service life, can be a solution to reduce resource and waste generation during the design, construction, operation, and demolition processes. Furthermore, this method has the potential to reduce the environmental, social, and economic impact due to construction and demolition activities. The use of precast methods offers several additional advantages, including rapid construction speed, design flexibility, cost efficiency, and reduced energy and material consumption.

Connections between the structural elements in precast buildings directly affect the reusability of the structural members, and that can be either “wet” which needs on-site concrete casting, or “dry”, which does not require any on-site concrete placement. The dry connections, which are often constructed with bolts, give structural elements of precast buildings with demountability. Several studies on the development and assessment of the structural feasibility and structural performance of dry connections are available. Several investigations have been conducted to explore the behavior of various types of precast RC beam-to-column [101, 103-105, 107], and RC bolted column-to-column [24, 108-111] connections.

Based on the aforementioned information, a more energy-efficient and environmentally friendly alternative for structural elements could be achieved by the utilization of demountable precast elements with CDW-based geopolymer concrete. This approach not only reduces waste, CO2 emission, and energy consumption due to the production of Portland cement and C&D activities but also promotes sustainability in the construction industry by reusing and relocating structural elements at any time. For these purposes, in the first part of this study, geopolymer concrete that utilized CDWs as inert and filler materials after crushing and grinding operations was developed and tested. The structural performance of the developed geopolymer concrete was compared with that of conventional concrete. The connection details that enable rapid assembly and disassembly of precast elements directly on the construction site were developed. The developed connections for precast concrete units, including columns, beams, and slab details, were tested under varied loading conditions to determine the structural performance of the units. Obtained knowledge from the laboratory experiments was converted into a practical, full-scale eco-friendly demountable precast building application under real-world conditions. So, for the first time, the demountable precast building was successfully constructed, and a revolutionary construction approach that leverages demountable prefabricated elements constructed entirely from sustainable materials and assembled effortlessly by the cradle-to-cradle design philosophy is introduced.

In the second part of this study, sustainability analysis on a developed geopolymer concrete and demountable precast building is performed. Then, crucial aspects that should be considered in the design and construction phases by contractors to engineers for assisting successfully implementing reusable structural elements are mentioned. Generation & minimization & handling & recovery of CDW were assessed because of the state of Türkiye. Opportunities and challenges in constructing prefabricated structures in Türkiye were investigated.

5.2. Details on the case study building

The real-life site implementation of the demountable precast building was realized in a forest in the Beytepe Campus of Hacettepe University, Ankara, Türkiye. The building was designed as a complex building that was constructed on a 26.3 × 11.3 m plan area, including a cafeteria, lounge, storage room, bathrooms, dressing rooms, and office rooms (as shown in **Figure 5.1**). All structural members (i.e., columns, beams, and slabs) were fabricated and cured in a precast concrete plant. The all produced precast elements are demoulded after three days for ambient temperature curing. The precast elements are wrapped with a blanket and a plastic cover. After that, the precast elements were cured by watering twice a day for the first week and once a day until the assembly day. Then, the precast elements were transferred from the plant to the construction site with the help of an articulated lorry. The plant was located approximately 20 km distance away from the construction site. In total, 24 columns, 37 beams, and 19 slabs were produced and used to construct the demountable precast building. Connection details of the elements of the building frame are illustrated in **Figure 5.2**, and detailed dimensions of the precast structural elements are tabulated in **Table 5.1**.

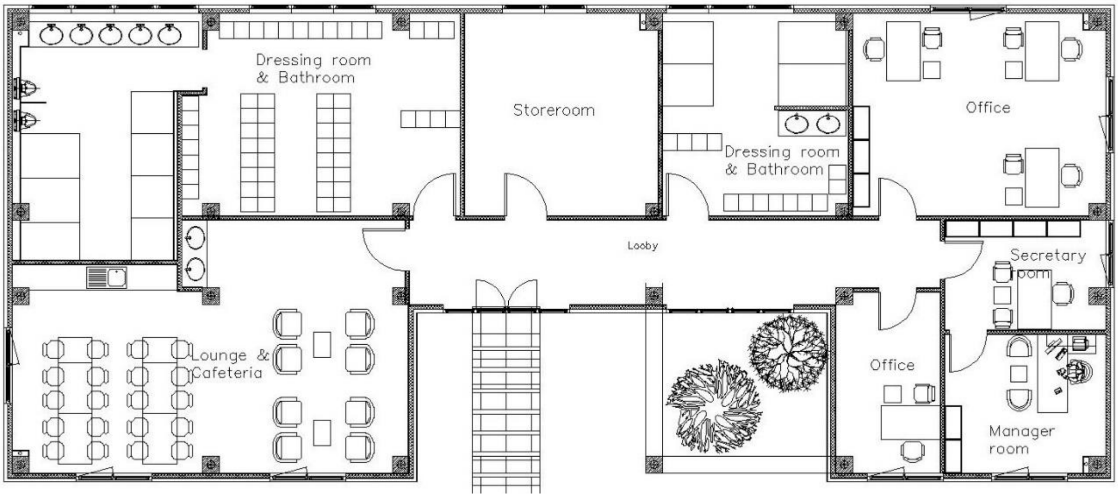

Figure 5.1 Plan view of the building

Table 5.1 Structural precast elements used for the construction of the demountable precast building

Structural element	Constant dimension	Dimensions×number of elements
Slabs	200 mm thick	5450×2350×#4, 5450×2250×#4, 5450×2200×#2, 5450×2000×#4, 6900×2000×#3, 6900×2250×#2
Beams	300×500 mm	1600×#6, 3600×#6, 4100×#18, 5600×#7
Columns	400×400 mm	3200×#24

The construction of the building started with the construction of a 0.35 m thick mat foundation. A thin layer of aggregates was separated on the finished soil surface to obtain a flat workable area, and then 50 mm thick leveling concrete was cast. Above the leveling concrete, 12 mm diameter reinforcements were placed in longitudinal and transverse directions with two rows as the bottom and top reinforcements. Before the casting, twelve 24-mm-diameter threaded rods with two adjusting steel plates for connecting each column were placed in the foundation. After the hardening of the concrete of the foundation, the demountable columns, which had a cross-sectional dimension of 0.40 × 0.40 m and height of 3.2 m, were placed and bolted to the foundation in less than two hours with the help of a mobile crane. The demountable column was reinforced with eight longitudinal reinforcements of 16 mm diameter and 22 stirrups of 10 mm diameter through the length. Then, demountable beams of 0.30 × 0.50 m cross-sectional dimensions were placed in between every two columns by simply sliding through the beam-to-column connection in less than 3 hours with the help of a mobile crane. The demountable beam was reinforced with six longitudinal reinforcements of 20-mm diameter, and stirrups of 10-mm diameter, whose numbers depended on the length of the beam. Final structural elements, demountable slabs, which were reinforced with 12 mm diameter reinforcements in two rows (top and bottom) at longitudinal and transverse directions, were bolted to beams with the help of the 24 mm diameter threaded rods. The assembly of the columns, beams, and slabs was completed in two days. The cross-sectional dimensions and reinforcement ratio of the produced columns, beams, and slabs were intentionally designed to be larger than the typical one-story building's beams and columns. The main reason for this was the potential change in the required capacities of the members for reusing after the end of the service life of the building.

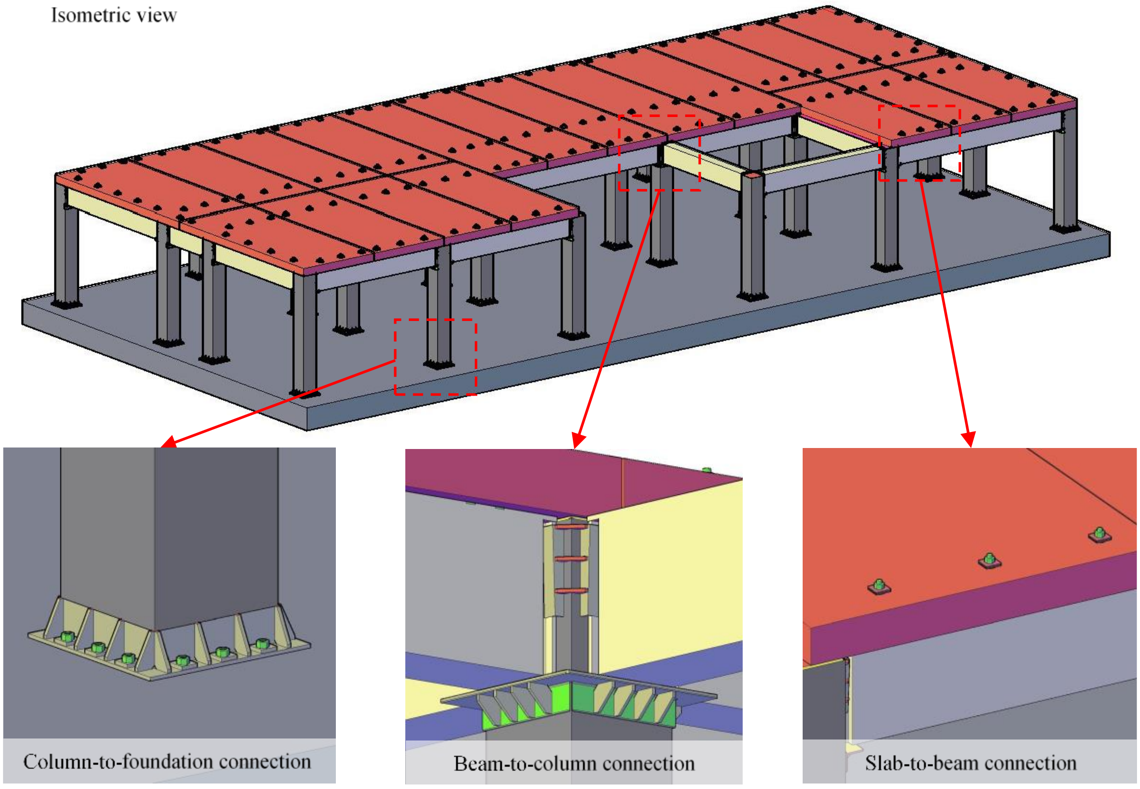

Figure 5.2 Connection details of the elements of the building frame

To complete the building envelope, precast panels constructed from cold-formed steel members and sheathed with wood-fiber cement composite boards on both sides were used. The utilization of composite boards as sheathing offers not only weather protection and stability but also improves the shear capacity and stiffness of the precast panels [197]. In between composite boards, thermal insulating material was placed. The duration of the assembly of a single precast panel was 20 minutes, and the assembly of all precast panels was completed in two days. The total duration of construction of the building, without considering the duration of the construction of the foundation, is four days. Rendered three-dimensional sketch of the completed demountable precast building is given in **Figure 5.3**

Figure 5.3 Rendered three-dimensional view of the demountable precast building

The seismically efficient load-transfer mechanism and ease of installation of the precast building were obtained using proper connections between structural elements. The column-to-foundation and slab-to-beam connections were obtained with bolts. On the other hand, the beam-to-column connection does not need the bolts because it is easily placed due to the employing simple lock and key model. Column-to-foundation connection resists movement, and rotations of columns end in all directions, so no additional structural elements are needed to satisfy stability and strength of the building under the seismic loadings. The beams only transfer the gravity and shear loads that are coming from slabs and claddings to the columns. The moment-free connection type for beam-to-column connections is preferred because of the structural simplicity, flexibility in design, providing uniform load distribution, construction efficiency (ease of maintenance and replacement), versatility, etc. The slabs were designed to be one-way concrete slabs so it provides structural efficiency, increased span length, flexibility in design, etc. The step-by-step construction stages of the demountable precast building envelope are summarized in **Figure 5.4**. In addition, all the construction stages of the case study building are summarized in short videos.

Figure 5.4 Step-by-step construction stages of the demountable precast building envelope

5.3. Results and discussion

5.3.1. Sustainability analysis

5.3.1.1. Concrete case

The cement is most commonly used structural binder material in the construction industry, leading to a high amount of carbon dioxide released during its production. In the production of 1 ton of cement, approximately 0.9 tons of carbon dioxide is released environment. The total amount of cement production worldwide is estimated at 4.1 billion metric tons. In China, estimated cement production was calculated as 2.1 billion metric tons, which makes China the world’s leading cement producer, followed by India, Vietnam, the USA, and Türkiye. Türkiye is the fifth leading cement-producing country in the globe, and the estimated production of cement is 85 million metric tons per year [198]. Türkiye exports 18.5 million tons (22%) of total produced cement to more than 80 countries. To minimize cement production-related carbon dioxide emissions, eco-friendly binders as an alternative to cement should be employed in structures. Although efforts to develop environmentally friendly building materials generally emphasize the lower environmental impact and energy consumption qualitatively, the environmental impact and energy consumption values of the developed green products should be quantitatively calculated. In this context, the Material Sustainability Index (MSI) plays a prominent role in analyzing sustainability parameters (e.g., carbon footprint, embodied energy, etc.) of newly developed products [199]. By calculating the carbon emissions and energy consumption of each component used in the developed product throughout its lifecycle until it becomes a final product, it is possible to quantitatively demonstrate how superior it is as an alternative in terms of sustainability compared to market products. To calculate the carbon footprint and embodied energy of the developed CDW-based geopolymer concrete and the Portland cement-based concrete produced for comparison within the scope of the study, life cycle inventory data for each component was obtained through comprehensive literature analyses and data from the devices used in the laboratory-scale experiments. The findings obtained are presented in **Table 5.2**.

Table 5.2 Life cycle inventory of the materials

Material	**Global warming intensity (kg.CO_2-eq/t)**	**Embodied energy (MJ/t)**	**Reference**
Hollow brick	96.9	675	[20]
Red clay brick	96.9	675	[20]
Roof tile	96.9	675	[20]
Concrete	96.9	675	[20]
Glass	96.9	675	[20]
Slag	70	1300	[200]
Fly ash	8	100	[201]
Recycled Aggregate	13.84	112.5	[20]
Normal Aggregate	6.20	120	[202]
Sodium hydroxide	633	3500	[203]
Sodium silicate	430	4600	[204]
Calcium hydroxide	938	4464	[205]
Water	-	-	[206]
Portland cement	1000	5500	[207]

Following the collection of life cycle inventory data, the findings obtained from the global warming intensity and embodied energy calculations for the production of 1 m^3 CDW-based geopolymer concrete and Portland cement-based concrete with similar compressive strengths are presented in **Figure 5.5** and **Figure 5.6**, respectively. According to the global warming intensity results presented in **Figure 5.5**, the production of 1 m^3 of CDW-based geopolymer concrete resulted in approximately 316 kg.CO_2-eq of carbon emissions, while the production of 1 m^3 of Portland cement-based concrete yielded approximately 327 kg.CO_2-eq of carbon emissions. It can be observed that the highest contributions to carbon emissions in CDW-based geopolymer concrete were attributed to sodium silicate at 30%, sodium hydroxide at 22%, and calcium hydroxide at 14.8% as alkali activators. Furthermore, the crushing and grinding processes of CDW-based components in the laboratory were responsible for 28.8% of the total carbon emissions. Although CDW-based geopolymer concrete and Portland cement-based concrete have similar carbon emissions, this can be attributed to the absence of industrial-scale crushing and grinding processes for CDW-based components, resulting in higher values when using laboratory-scale units. Additionally, it is expected that CDW-based geopolymer concrete's carbon emissions could significantly decrease with further optimization of alkali activators in future studies in the literature.

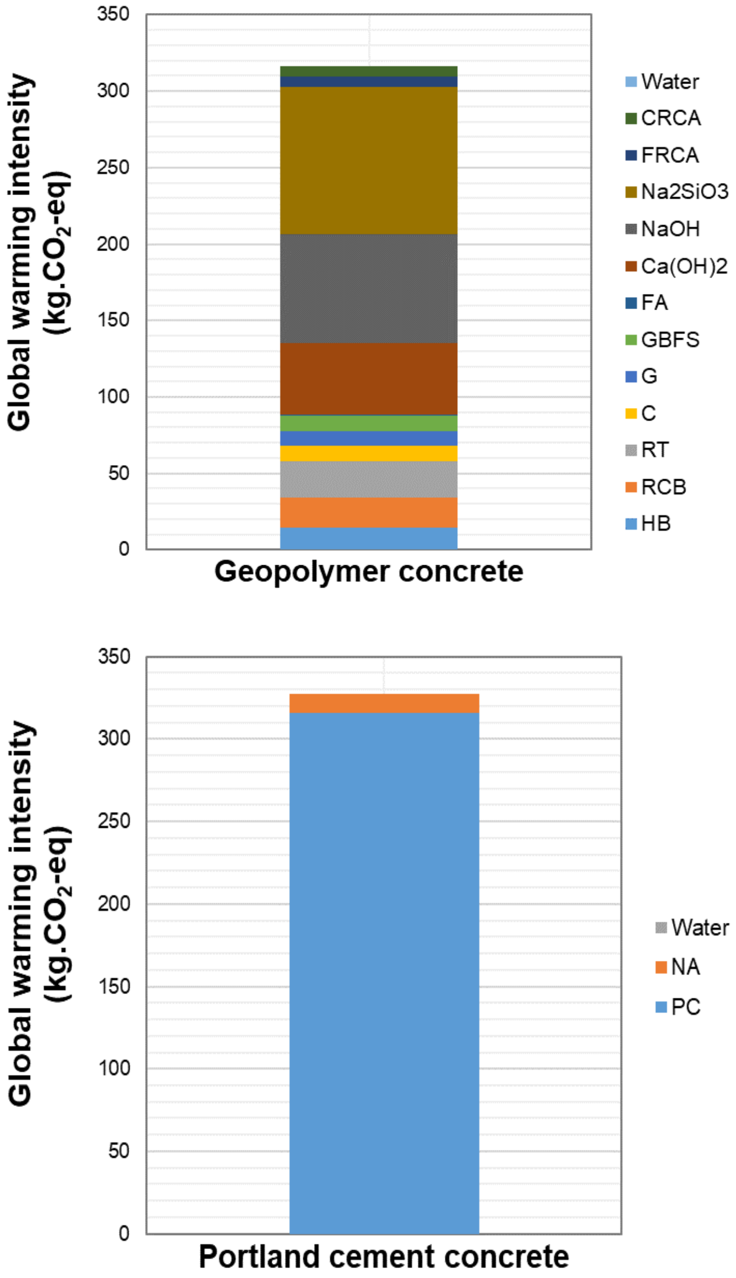

Figure 5.5 Global warming intensity values of CDW-based geopolymer concrete and Portland cement concrete for 1 m^3 production

According to the embodied energy values presented in **Figure 5.6**, the energy consumption attributed to the components of CDW-based geopolymer concrete is 2498 MJ, while for Portland cement-based concrete, it is 1958 MJ. The results show that, to some extent, Portland cement-based concrete has a slightly more advantageous position in terms of embodied energy, although it differs slightly from the carbon emission values. As previously explained, this can be attributed to the higher energy consumption per unit for CDW-based component processing at the laboratory scale compared to the industrial scale. Additionally, similar to carbon emissions, sodium silicate has the highest contribution to energy consumption. When analyzing the embodied energy values of CDW-based geopolymer concrete as shown in **Figure 5.6** (a), it becomes apparent that roughly 70% of this energy is derived from alkali activators. While the utilization of such elevated levels of alkalis is indispensable for the activation of CDWs, which inherently exhibit low reactivity, it concurrently results in substantial energy consumption. From a technical perspective, there are two viable approaches to diminish the embedded energy content of CDW-based geopolymers. One option involves enhancing the reactivity of CDWs through processes like calcination at around 900 °C, albeit this leads to a notable increase in energy consumption. Consequently, the most optimal strategy can be replacing alkalis, such as Na_2SiO_3, with materials characterized by lower embedded energy values, exemplified by silica fume, renowned for its high silica content [196]. Furthermore, it should be noted that if CDW recycling processes transition to an industrial scale, there will be a significant reduction in embedded energy values.

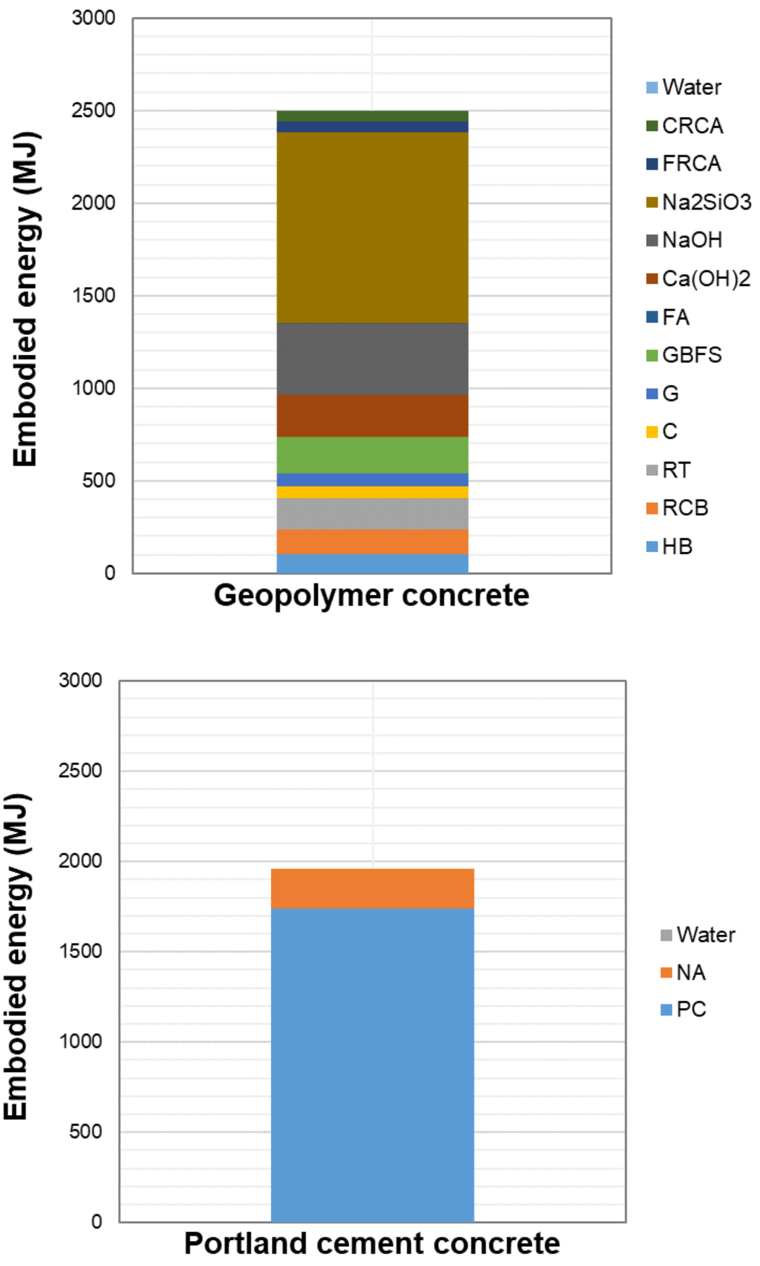

Figure 5.6 Embodied energy values of CDW-based geopolymer concrete and Portland cement concrete for 1 m^3 production

5.3.1.2. Building case

To assess the environmental impact of the demountable precast building, we first conducted a quantity take-off analysis, which is presented in **Table 5.3**. The structural precast members were fabricated using various materials, including geopolymer concrete, reinforcement, steel profiles, steel plates, bolted connection parts, pipes, elastomers, and arc welding. Although steel molds were employed to shape the structural members, we did not include them in the calculations since they can be reused heaps of times.

Table 5.3 Quantity take-off of the eco-friendly demountable precast building

Material	**Building Element**	**Quantity**
Geopolymer concrete	Slab (200 mm thick)	47.750 m^3
	Beams (300×500 mm)	21.000 m^3
	Columns (400×400 mm)	12.200 m^3
	Total	**80.950 m^3**
Reinforcement	Slab (200 mm thick)	4491.560 kg
	Beams (300×500 mm)	3076.470 kg
	Columns (400×400 mm)	1481.080 kg
	Total	**9049.110 kg**
Steel Profiles (NPU120, L100×100×10)	Slab connection	-
	Beam connection	1503.791 kg
	Column connection	1026.288 kg
	Total	**2530.079 kg**
Steel Plate	Slab connection	265.426 kg
	Beam connection	1738.815 kg
	Column connection	2998.008 kg
	Total	**5002.249 kg**
Threaded rod, lengthening nut, standard nut, washer (Ø24 8.8 grade)	Slab connection	**-**
	Beam connection	**-**
	Column connection	**-**
	Total	**247, 154, 748, 442**
2 mm thick Ø50 PVC pipe	Slab connection	**34.200 m**
	Beam connection	**-**
	Column connection	**-**
	Total	**34.200 m**
Arc welding	Slab connection	2.660 kg
	Beam connection	27.706 kg
	Column connection	33.499 kg
	Total	**63.865 kg**
Elastomer	Slab connection	0.167 m^3
	Beam connection	0.001 m^3
	Column connection	0.046 m^3
	Total	**0.214 m^3**

The life cycle inventory of components such as steel, arc welding, and PVC pipes other than geopolymer concrete (GPC) of the demountable building manufactured with CDW-based geopolymer concrete was obtained from literature studies, and the values are presented in **Table 5.4**.

Table 5.4 Life cycle inventory values of components used in the demountable building

Materials	Global warming intensity ($kg\ CO_2$)	Embodied energy (MJ)	Reference
Geopolymer concrete ($1m^3$)	316	2498	Current Study
Steel (1 ton)	2380	29000	[208]
PVC Pipe (1 kg)	3.4	68	[209]
Arc welding (1m)	0.21	2.63	[209]

Due to their relatively small quantities used in the components of the demountable building production, such as threaded rods, lengthening nuts, standard nuts, washers, and elastomers, they were neglected in the sustainability analysis for global warming intensity and embodied energy calculations. The sustainability analysis calculations took into account the usage of 80.95 m^3 of geopolymer concrete, 16.59 tons of steel, 34.2 m of PVC pipes, and 63.87 kg of arc welding in the demountable building production. As a result of the sustainability analysis, the total global warming intensity and embodied energy values for the demountable building are presented in **Figure 5.7**. According to the obtained data, the total global warming intensity value for the demountable building is 65.24 $t.CO_2$-eq, while the total embodied energy value is calculated as 686.7 GJ. In terms of global warming intensity, steel has the highest contribution, with approximately 60%, while geopolymer concrete accounts for about 39% of the total emissions. In the embodied energy aspect, steel’s share is 70%, while geopolymer concrete’s share is 29.4%. The manufacturing of demountable connections for structural members had a considerable impact on the calculated global warming intensity and embodied energy of the building, accounting for approximately 27% and 32% of the respective values. These findings highlight the significant environmental influence of demountable connections in the overall life cycle of the precast building. On the other hand, it should be considered that enabling the reusability of structural elements at the end of their service has the potential to reduce their environmental impact. Moreover, conducting optimization works for reducing the steel employed in connection could further mitigate the environmental impact.

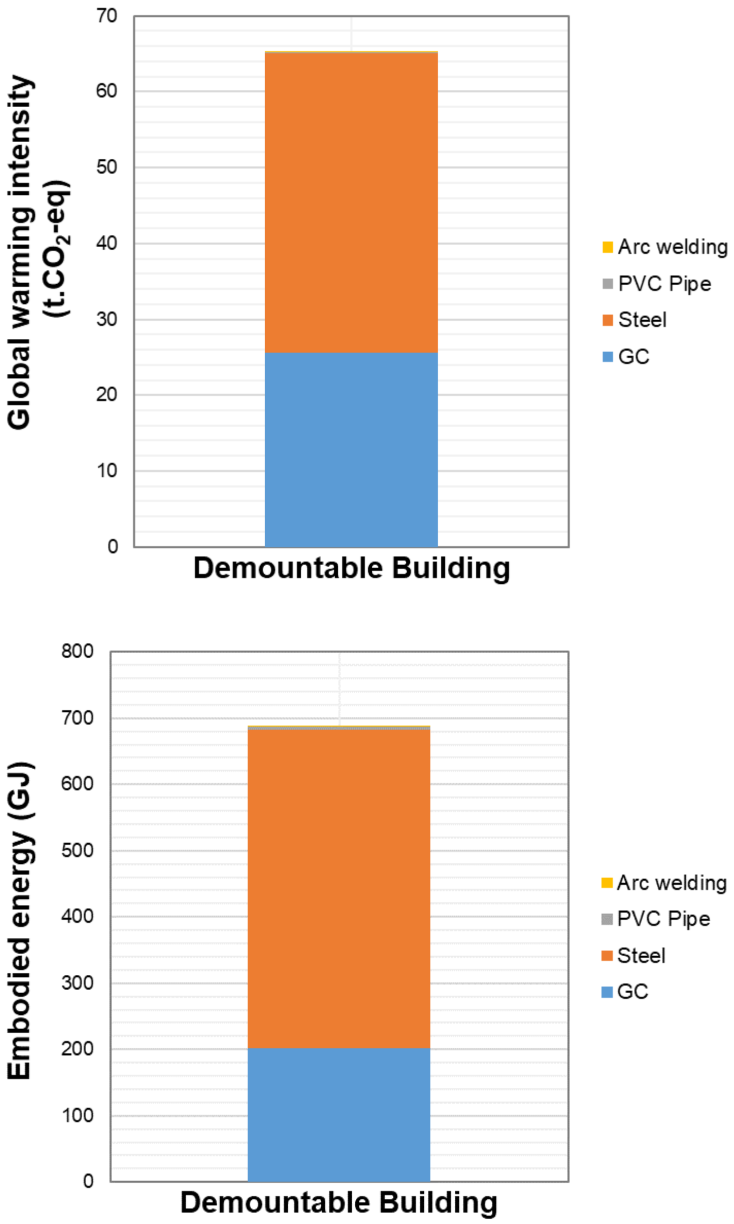

Figure 5.7 Global warming intensity and embodied energy values of demountable building

5.3.2. Cost analysis

In this section, an economic comparison was provided between CDW-based geopolymer concrete and traditional Portland cement-based concrete. According to the results presented in **Figure 5.8** . On the other hand, the cost of ready-mix concrete with a C35 class in Turkey is approximately €145. It is important to note that transportation costs and landfill tax for CDW have to be included in the cost calculations of Portland cement concrete as an alternative cost. The average landfill tax in Europe is around €90 per ton and the transportation cost of CDW material is approximately €15 per 100km. Thus, the cost of 1 m^3 of Portland cement concrete considering the expenses related to waste disposal taxes and the transportation of CDWs to waste sites is €334, which is significantly larger than the cost of geopolymer concrete. Additionally, as emphasized in the previously mentioned carbon emissions and energy consumption values, further optimization of activator combinations and/or the substitution with certain industrial by-products will significantly reduce geopolymer costs. Consequently, a more fair comparison about the cost of different concrete alternatives indicated that the CDW-based geopolymer concrete is a good and feasible candidate to Portland cement concrete if the environmental aspects are also (i.e., alternative costs) taken into consideration.

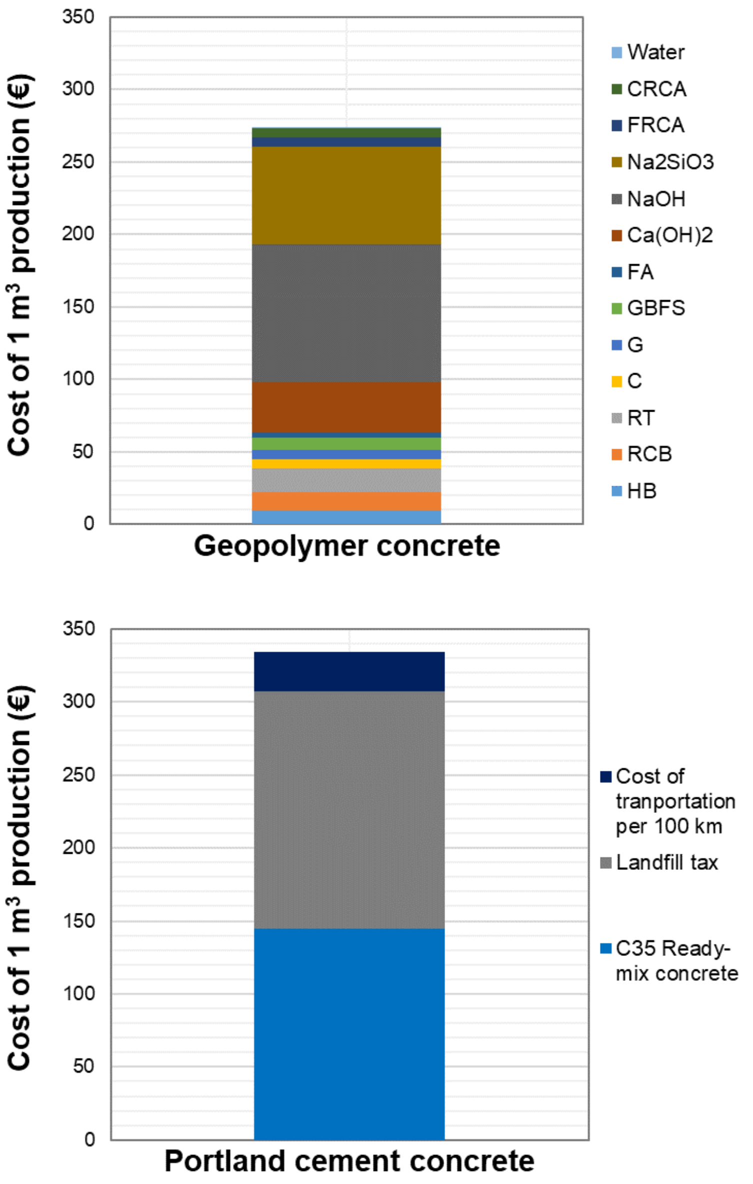

Figure 5.8 Cost of 1 m^3 production of geopolymer concrete and Portland cement concrete

5.3.3. Critical considerations for developing reusable structural elements

The crucial aspect for successfully implementing reusable structural elements lies in ensuring that the structural system can be easily assembled, dismantled, and re-assembled at the end of its life. This can be easily achieved by employing simple connections with/without bolts. As beam-to-column connections employ a simple lock and critical model, and as column-to-base and slab-to-beam connections, bolted connections provide reusability of the structural elements. Even though reusable connections reduce deficiencies due to labor works in the in-situ assembly stage, the complexity of the connections has the potential to increase deficiencies that originated from labor works.

Several key considerations should be taken into account during or before manufacturing reusable structural elements. Precise production of reusable structure components is crucial, requiring the use of steel molds throughout the manufacturing process. Careful welding is necessary during the fabrication of steel molds to prevent deformations caused by the weld cooling process. Logical determination of error margins is essential to strike a balance. Excessive margins can compromise the translational stiffness of the building and hinder effective load transfer between structural elements. On the other hand, insufficient margin can lead to assembly difficulties during the final stages of construction.

To ensure water and wind insulation, elastomer-like materials should be used between structural elements. Bolts can be employed to securely tighten the connection with these elastomer-like materials at critical points of the structure. The use of elastomer-like materials between structural elements helps prevent steel parts from crushing concrete during an earthquake, as the steel has a higher elastic modulus. During the assembly of the elements, spaces at the connections should be filled with elastomer-like materials to facilitate load transfer. Proper surface leveling is crucial, as even a small leveling error at the base can result in significant errors at the top of the structure.

Reusable structure manufacturing requires special attention to electric and water plumbing, which may increase labor requirements. However, this becomes less problematic over time due to repetition and experience gained. Transportation of reusable structures can be challenging due to the weight of the concrete structural elements. High-load capacity cranes are necessary in the production, storage, and construction areas, resulting in increased costs and initial investment. Care must be taken during transportation and placement to avoid breakage at corners and edges, which are susceptible to damage even from minor impacts.

Engineers/designers should keep in mind that the cost of the reusable connections should be optimized to compete with the cast-in-situ counterparts. For instance, instead of restraining a large number of the degrees of freedom of the connections to stabilize the building, a reduced number of degrees of freedom should be restrained to reduce a material quantity, employing other structural elements, such as steel wire for bracing.

After the development of reusable connections, an optimization process should be applied to reduce the material quantity. Welding and labor work for the fabrication of the connections should be minimized. However, reusable connections should be designed such that failure mechanisms can be observed out of the connection regions for enhanced structural integrity. Additionally, in the development of the hybrid (concrete-steel) connections, the cost of the steelworks, including material and manufacturing costs, dominates the total cost. So, the percentage of steel in connection should be reduced by replacing it with more economically efficient materials, such as high-strength concrete and composite materials. Moreover, standardization and mass construction of the reusable connection can save time and cost.

5.3.4. CDW management in Türkiye

The total waste generated in the EU amounted to 2,135 million tons, and the construction and demolition sector contributed to 37.5% (800.63 million tons of excavated soils and CDW) of total waste generation in 2020, the highest rate of other sectors [210]. In the U.S., the expected amount of waste generated by the construction sector was 600 million tons in 2018 [211] (U.S. E.P.A., 2018), and the construction sector in China produced 1-1.13 billion tons of waste in 2014 [212]. In Türkiye, the amount of municipal waste generated in 2020 was calculated as 104.8 million tons. However, the contribution of the construction and demolition sector to total waste generation is not mentioned [213]. But, in one of the most populated cities of Türkiye (i.e., Ankara), 37.1 million tons of excavated soil and CDW were generated, and 13.4 million tons of that was stored in landfills [214]. It can be assumed that 20-40% of the generated waste corresponds to the CDW generation, and so the total generated CDW per capita can be calculated as 1965 kg. When Türkiye’s total population is considered, approximately 164 million tons of CDW may have been generated in Türkiye in 2020. The main factors of the huge amount of CDW generation in Türkiye could be listed as:

(i) Use of high-volume and high-mass construction material usage in existing old structures as structural and non-structural elements (highly dependent on building age),

(ii) Growth in the construction sector,

(iii) Slum clearance,

(iv) Collapse of structures which do not take engineering services,

(v) Uncontrolled modification in structures,

(vi) Rapid urbanization,

(vii) Error and changes during design and construction phases, etc.

Also, on 6th February of 2023, two successive catastrophic earthquakes hit the Türkiye province Kahramanmaraş and led to destruction in eleven provinces in Türkiye. Approximately 260,000 buildings suffered severe damage and collapse, which may have resulted in the generation of approximately 200-250 million tons of CDW. The amount of the generated CDW makes its environmental and economic effects significant, so CDW should be carefully stored and recovered.

The demolition method (traditional or selective) generally determines whether CDW is stored due to mixed CDW making the recovery hard. Selective demolition, whose initial cost is more expensive than traditional ones, can sell processed mass materials as a filling material for less price and reuse the obtained materials in new projects, thus reducing the stored materials in landfills. On the other hand, different from demolition, deconstruction refers to actions that systematically dismantle structures, resulting in recovering the maximum amount of valuable components [215]. In Türkiye, regulation on control of excavated soil and CDW [216] came into force in 2004. According to the regulation, recycling of CDWs, especially their reuse as infrastructure material, and selective demolition methods are taken as bases. The detailed rules for waste prevention, recovery, and proper storage for excavated soils and CDW are also presented in the regulation.

The CDW storage and recovery cost is highly dependent on country policies (landfill tax, subvention, etc.), type of facility, transportation from site to landfill, and container/crane cost. The landfill storage tax varies from one country to another. However, the cost of it plays a crucial role in determining the demolition method and whether it will be recovered. In Türkiye, landfill taxes are determined by municipalities. In order the find approximated landfill taxes in Türkiye, landfill taxes determined by six metropolitan municipalities (Ankara 7₺, Antalya 12₺, İstanbul 24₺, İzmir 9₺, Kayseri 6₺, Kocaeli 9-18₺) were considered. The average landfill taxes in Türkiye were calculated as 12₺ (0.4$)

per ton. When the landfill tax of different countries compared to Türkiye’s landfill tax (as shown in **Table 5.5**), it was observed that the landfill tax in Türkiye was too lower than the other countries. This stimulated some of the contracting companies and owners to select traditional methods and store the CDW in landfills. To increase the recovery rate, reduce the environmental effects, reduce stored CDW, encourage selective demolition, and increase the economic contribution, of CDW in Türkiye, landfill taxes could be increased, and recovery should be encouraged and rewarded by municipalities.

Table 5.5 Landfill tax of the CDW for different countries

Country	Unit price per tonne	Source	Year
Germany	8.00 (for brick waste) 148.00 € (for mixed CDW)	CDW management in Germany [217]	2015
The U.S.	58.94 $	Analysis of MSW Landfill Tipping Fees [218]	2022
The U.K.	3.25 £ (for a lower rate) 102.10 £ (for a standard rate)	Guidance landfill tax rates [219]	2023
Portugal	29.88-57.60 €	CDW management in Portugal [220]	2015
Denmark	49.00-64.00 €	CDW management in Denmark [221]	2015
France	1.00-8.00 € (for inert waste) 80.00-120.00 € (for non-inert non-hazardous)	CDW management in France [222]	2015
Finland	100.00-170.00 € (for mixed CDW) 20.00– 90.00 (for sorted CDW)	CDW management in Finland [223]	2015
Greece	10.00-48.50 €	CDW management in Greece [224]	2015
Netherland	3.50-4.50 €	Zhang et al. (2020) [225]	2016
Türkiye	0.40 $	Current study	2023

According to European standards [226], buildings and common structures, and large-scale public works are expected to have a service life of at least 50 and 100 years, respectively. However, the general public often expects structures to endure indefinitely due to the ever-growing urban population. Unfortunately, the reality is that many structures built in the latter half of the previous century are already approaching the end of their service lives, experiencing deterioration caused by the combined influences of mechanical and environmental loads [227]. This necessitates repair, maintenance, and renovation efforts to address the degraded components. However, these interventions often lead to increased traffic congestion, fuel consumption, and greenhouse gas emissions, while many of the solutions employed are not long-lasting and ultimately result in the complete demolition and reconstruction of the structure.

The construction year of the buildings provides an important insight into building construction quality. Türkiye's earthquake code (TEC) which determines buildings' construction quality and earthquake resistance, was revised eight times in total with the 2018 earthquake regulation, which came into force in 2019. Before 1998 TEC, ribbed reinforcements and plant-mixed concrete were not popular, so concrete quality and adhesion between the concrete and reinforcement were low. And also, major corrections were applied to Türkiye's Earthquake Hazard Map in 1996. Moreover, the construction inspection law came into force in 2001. Considering all these negativities, the risk of most of the buildings built in 1998 and before is very high.

The clear information on building stock in Türkiye is not valid. In Türkiye's mostly populated city Istanbul, total building stocks comprise reinforced concrete (82.5%), masonry (15.4%), tunnel formwork (1.0%), timber (0.65%), prefabricated (0.26%), and steel (0.16%) structures [228]. To make an inference the proportion of households by construction year of the residential buildings was used (illustrated in **Figure 5.9**). Taking into account that 25% of all households reside in buildings that are over 33 years old, and considering that Türkiye had a total of 32.7 million houses as per TÜİK data from 31st December, 2017, it can be estimated that around 8.2 million houses may be vulnerable to seismic activity due to not being constructed according to current earthquake codes. Consequently, there is a pressing need for building restructuring, which may involve demolition, reinforcement, and new construction activities. However, such endeavors inevitably lead to the generation of substantial amounts of CDW.

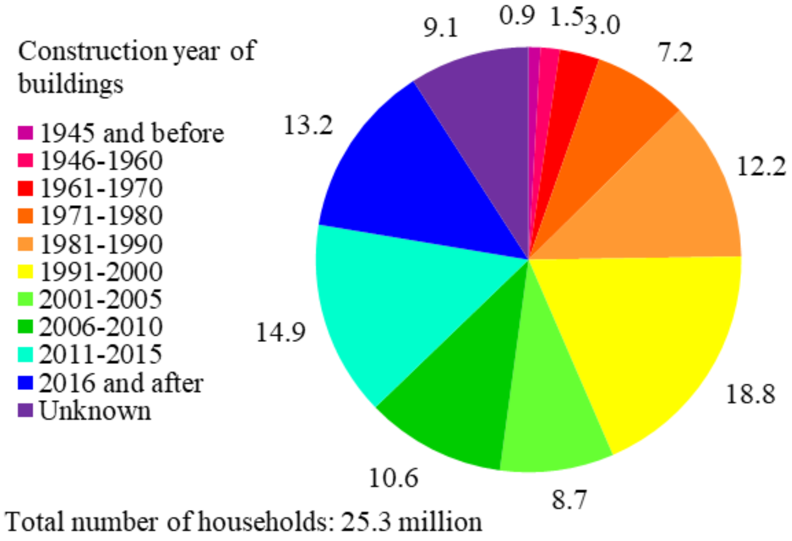

Figure 5.9 Proportion of households by construction year of residential buildings in Türkiye, 2021 [229]

As evident from the examples discussed in the previous section, effective management of CDW is a major environmental concern for communities worldwide, given its long-term impacts. Improper disposal of CDW in uncontrolled landfills not only incurs environmental and financial costs but also poses health risks. To mitigate these issues, it is crucial to implement rational CDW management practices, including recycling and storage strategies. Sustainable approaches to reusing and recycling unavoidable CDW are crucial for achieving substantial benefits both in economic and environmental terms. By diverting CDW from clean landfills, the production of new materials and the associated pollution of air and water can be reduced, thereby mitigating health impacts and lowering greenhouse gas emissions. Recycling CDW is generally more energy-efficient compared to the production of materials from virgin sources.

According to the given proportion of the building stock, different types of wastes are expected to be generated due to demolishing of the buildings that completed their service lives or exhibited insufficient seismic performances under expected earthquake loadings, as tabulated in **Table 5.6**. The proper handling of CDW plays a significant role in reducing the number of waste materials destined for clean landfills and minimizing the strain on diminishing natural resources. The compliance of the works carried out during the construction and demolition of the building with the regulations should be strictly controlled, and in case of non-compliance, it should be severely penalized. Selective demolition of structures and use of the CDWs should be promoted by regulations.

Table 5.6 Potential types of CDWs

Structural elements materials	Walls	Insulation	Openings	Finishes	Roof	Other
Steel, concrete, timber, stone, mudbrick, brick	Bricks, briquette, stone, OSB, Boards	XPS, rockwool, glasswool	Glass, PVC, Aluminum, wood	Tiles, plasterboards, floorboard, plaster	Wood, Steel	PVC pipes, iron pipes, ceramics (washbasin, toilet bowl, etc.), etc.

5.3.5. Opportunities and challenges in prefabrication

There is a constant increase in the population of the world that pushes pressure on the increased usage of the cement all over the world. Thus, the use of geopolymer concrete is very important as the Portland cement concrete construction not only causes greenhouse gas emissions due to the use of cement but also Portland cement concrete construction constantly generates CDW due to the limited service life of the material and the structure itself. Therefore, the sustainable construction sector could not be achieved by only reducing the use of cement in the concrete construction by replacing some of the ingredients with the recycled counterparts like recycled aggregates, use of geopolymer binders, etc. In addition, only replacement of conventional concrete with the geopolymer is not a solution to achieve a sustainable construction sector as the CDW is still generated in large amounts that requires emergent attention. For instance, earthquakes (e.g., Kahramanmaraş) caused an enormous amount of CDW generation due to collapsed buildings and heavily-damaged buildings that should be demolished. This enormous amount of CDW could not be handled with usual landfill operations. Therefore, the CDW-based geopolymer concrete is a good alternative to build structures to replace the heavily-damaged or collapsed buildings and to dispose of the CDW simultaneously. In addition, the prefabrication of buildings decreases the construction and demolition waste by up to 52% [230], due to reusing the building components at the end of the service life of the structure and reducing the on-site waste generation due to the decreased on-site construction time. Therefore, the proposed demountable precast construction alternative with fully CDW – based geopolymer is a rational step towards having a sustainable construction sector.

Prefabrication in Türkiye gained prominence after the 1960s. As per the Turkish Precast Concrete Association (TPCA), there are currently 109 prefabrication companies, with 51 of them being affiliated with TPCA. Prefabrication, respectively, is preferred for superstructures (72.5%), substructures (18.6%), landscaping (6.9%), and other purposes (2.0%). The prefabricated elements are mainly demanded by the private sector, with 85% of total products, then demanded by the public sector, with 15% of total products. In 2021, for prefabrication companies associated with TPCA, the proportion of total consumption of CEM I 32.5 – 42.5 and iron for reinforcements stood at 1.8% and 1.5%, respectively [231]. As can be understood from the given proportion, the prefabrication market has a lower share of the overall construction market in Türkiye. That could be attributed to the construction of housing and commercial buildings dominating the construction market. According to Oral et al. [232], 2003, the primary hurdle to meeting the demand for both housing and commercial buildings is the current financing system, which fails to facilitate the rapid financing necessary for prefabrication. Moreover, despite the rapid construction and high quality offered by prefabrication, several other factors hinder its widespread adoption. These include the reconditeness of the seismic performance of such structures, low labor costs, lack of experience of the labor, manufacturing process limits and architectural constraints of prefabrication, societal demand and perception, public construction policies, and limited competitive advantage due to a small number of companies operating in this sector.

Two recent catastrophic earthquakes in Kahramanmaraş on 6th February 2023 highlighted the significance of timely construction and the stringent seismic performance criteria for buildings. The urgent demand for residential structures to accommodate earthquake victims became evident. Although temporary container buildings were deployed to address immediate needs, there remained a requirement for permanent residential structures. Prefabrication assumes a vital role in fulfilling the need for permanent residential buildings, aiming to minimize the social, health, and economic impact of earthquakes.

CONCLUSIONS and RECOMMENDATIONS

The results of four independent studies are presented under their respective headings, followed by recommendations for future research in geopolymer concrete, sustainable construction, and demountable structural systems.

6.1. Conclusions of Fully Demountable Column Base Connections Design

In this study, 5 different specimens, representing 4 novel demountable connections and a reference monolithic specimen, are tested under cyclic lateral displacement excursions and constant axial loading to investigate and compare the seismic performance of the proposed demountable connections. For this purpose, ½ scaled specimens are manufactured from CDW-based geopolymer concrete. The results from the reference monolithic specimen are used to determine the viability and effectiveness of the developed connection details by comparing performance parameters that include maximum lateral load capacity, ductility, stiffness, energy dissipation capacity, stiffness degradation ratio, and moment-curvature response. Based on the obtained experimental results, the following conclusions are drawn:

- The damages of the reference monolithic specimen GMC1 is concentrated at the end of the column above the foundation surface, where concrete cracking, concrete spalling, and concrete crushing are successively observed.

- Specimen GDC1 produced from steel bars presents footing failure and unfavorable performance. The main damages appear at the column footing whereas limited cracks appear at the bottom of the column above the column footing. The specimen shows a lower maximum lateral load capacity, effective stiffness, and energy dissipation capacity when compared to the other specimens.

- Specimen GDC2 is produced from a rectangular grille that consists of steel plates and round bars and exhibits similar failure behavior to specimens GDC1 and GDC3. The damages are observed at the column footing, with only a few cracks appearing at the bottom of the column above the footing. Therefore, specimen GDC2 shows lower maximum lateral load capacity, stiffness, energy dissipation, and energy dissipation ratio.

- Specimen GDC3, which is created from a rectangular grille made of steel plates, does not demonstrate satisfactory performance when compared to the corresponding monolithic specimen GMC1 as far as the observed damage patterns are considered. The damage in the specimen accumulated at the joint footing level and no plastic hinging is observed at the column base. Specimen GDC3 shows a similar maximum lateral load capacity to specimen GDC2 while having lower ductility.

- Observed failure modes of the specimen GDC1, GDC2, and GDC3 proved that the lateral load and displacement capacity of these specimens are governed by the connection not the column element. This could be attributed to the fact that the load-transfer mechanism between the column and the footing does not show the expected performance. Additional detailing modifications can improve the performance, which can affect the development of the plastic hinge. Moreover, seismic performance of all these specimens are worse than monolithic specimen GMC1. The seismic performance of specimen GDC4 are significantly better than that of the monolithic specimen GMC1 and all other investigated demountable specimens, including the maximum lateral load capacity, ductility, initial stiffness, energy dissipation capacity, and moment-curvature response. The plastic deformation and damage are observed at the end of the column where outside the connection region and distributed along 200 mm, indicating that damage and deformation can be controlled in out-of-joint and connection strength can be determined from member strength. This can be attributed to the use of a steel jacket and anchorage rods, which increase the connection between the end plate and column. Therefore, connection details of specimen GDC4 can be safely used as a monolithic connection in seismic regions for both beam and column applications.

6.2. Conclusions of Structural Performance of CDW-Based Geopolymer Concrete Columns

In this study, 6 specimens, representing 3 demountable and 3 monolithic connections for CDW-based geopolymer concrete, were tested under constant axial loading and cyclic lateral displacement excursions. Three different axial compression ratios including 10%, 20%, and 30% were used for axial loading. Performance parameters such as failure mode, ultimate lateral load capacity, displacement ductility, energy dissipation capacity, stiffness degradation, and curvature distribution of demountable and monolithic connection test specimens were compared to investigate the efficiency of CDW-based geopolymer concrete connections under varied axial loadings. Based on the results and discussions of this study, the following conclusions can be drawn:

- The demountable specimens exhibited a better level of performance parameters including maximum lateral load capacity, energy dissipation capacity, initial curvature stiffness, and maximum curvature than their monolithic counterpart. On the other hand, under the high axial loadings, demountable specimens had relatively lower ductility.

- The monolithic and demountable specimens had similar crack propagation and failure modes. However, damages were spread along a height of the confinement zone of the column of demountable specimens, while the damage was concentrated at the ends of the column of monolithic specimens.

- The reduction in lateral load capacity initiated with concrete crushing and spalling for both demountable and monolithic specimens. The failure of demountable specimens was caused by the crushing of the confined concrete zone followed by a buckling of longitudinal reinforcements. The failure of the monolithic specimens, on the other hand, was caused by only the crushing of confined concrete zone.

- The hysteresis moment-curvature curves for three regions demonstrated that demountable connection details helped to distribute deformation evenly and so improved the plastic hinge length of the connection, enhancing the deformation capacity of the specimens.

- As the main parameter considered, the axial compression ratio had a significant effect on the seismic performance of specimens. Experimental results showed that the increase in axial compression ratio led to an increase in lateral load capacity, energy dissipation capacity, energy dissipation ratio, and initial curvature stiffness however decreased the ductility, of both types of specimens.

- The comparison of the experimental results with the numerical predictions indicated that the equations and assumptions in the current numerical practice for conventional reinforced concrete products provide conservative estimations for CDW-based geopolymer concrete products.

- The ultimate moment capacity prediction of current codes was similar to each other, although the prediction of TS500 equations was slightly better. The absolute average percentage errors of ACI318-19 (TS500) predictions for monolithic and demountable specimens were 19.11% (18.60%), and 30.16% (21.80%), respectively.

6.3. Conclusions on the Damage Characteristics and Seismic Response of Demountable RC Column Base Joints

In this study, to evaluate the seismic performance and to assess damage characteristics of bolted CBJs, six specimens, representing three bolted joints and three monolithic joints, were tested under combined cyclic lateral load and static axial compression load. The obtained test results were compared with capacity predictions of current codes. In addition, modifications to the damage index limits of Park and Ang [193] for five DS levels (i.e., insignificant, slight, moderate, severe, and extreme) were proposed for both monolithic and bolted CBJs specimens. These limits along with the displacement and energy dissipation comparisons with the damage states would be useful for the performance-based design of bolted CBJs in precast concrete frames. The effect of axial compression ratio and reinforcement details of bolted joints, characteristics of plastic hinges, and damage index and damage progression were investigated. Based on the results and discussions of this study, the following conclusions can be drawn:

- In all tested specimens, a ductile flexural failure was observed, characterized by the formation of a plastic hinge at the bottom of the column.

- The progression of the observed damage state was similar for all tested specimens: concrete cracking, cover crushing, concrete spalling, core crushing, and longitudinal reinforcement buckling.

- The bolted CBJs exhibited a similar or better level of seismic performance except for displacement ductility than their monolithic counterpart.

- In all specimens, as an axial compression ratio increased from 0.10 to 0.30, lateral load capacity, energy dissipation, secant stiffness, initial curvature stiffness, and maximum curvature (for only bolted specimens) increased but displacement capacity and displacement ductility decreased. Also, the stiffness degradation is not significantly affected by the axial compression ratio.

- The ultimate moment capacity prediction of current codes was similar to each other, although the prediction of TS500 equations was slightly less conservative for bolted joints. The prediction error for bolted specimens increased as increasing the axial compression ratio while prediction errors for monotonic specimens were approximately similar.

- In bolted CBJs, the plastic hinge length was elongated and relocated by 50 mm with the help of the anchorage rods and the jacketing, so joint failure was prevented and the loading capacity and ductility were enhanced.

- The plastic hinge lengths increased with increasing the axial compression and longitudinal reinforcement ratio and were well predicted with the model proposed by Ning and Li [163].

- According to the limited experimental study, proposed damage index limits for damage states by Park et al. [176] lead to conservative estimation, so P&A damage index limits for damage states are proposed.

- The modified model of Chiu et al. [195] demonstrated good accuracy in estimating stiffness reduction factors for damage states.

- The experimental evidence enables us to state that the proposed joint system for precast columns is effective in terms of seismic performance.

6.4. Conclusions of Case Study Building

This study investigates potential benefits of constructing a one-story demountable precast building from CDW-based geopolymer concrete in Ankara-Türkiye with considering issues, including (i) sustainability analysis of CDW geopolymer concrete and demountable precast building, (ii) critical considerations for development of the reusable precast structural elements, (iii) CDW management strategies, (iv) challenges and opportunities of prefabricated construction, and (v) potential benefits and future direction of the prefabrication. Drawing upon the results and discussions presented in this study, the following conclusions can be derived:

- As a result of the preliminary studies, CDW-based geopolymer concrete was developed with a compressive strength of 34.2 MPa, drying shrinkage of 3874 με, water absorption of 8.6%, porosity of 9.8% and chloride ion penetration of 2390 C after 28 days.

- CDW-based geopolymer concrete and Portland cement-based concrete exhibited similar carbon emissions. Still, the higher emissions in the former can be attributed to the absence of industrial-scale crushing and grinding processes for CDW-based components. While Portland cement-based concrete had a slightly more advantageous position in terms of embodied energy, further optimization of alkali activators and processing methods can significantly reduce emissions and energy consumption in CDW-based geopolymer concrete.

- Developed demountable connections for structural precast members, such as beams, columns, and slabs, exhibited sufficient structural performances under varied loading conditions to use in building precast buildings.

- The use of demountable connections for the construction of precast buildings reduces the construction time and labor cost of in-situ assembling. On the other hand, the use of a high amount of steel and welding in the manufacturing of demountable connections increases the demountable precast building cost.

- The implementation of demountable connections for structural members significantly influenced the calculated global warming intensity and embodied energy of the building, contributing to approximately 27% and 32% of the respective values, respectively.

- The estimated annual CDW generation in Türkiye is approximately 164 million tons. Additionally, when considering that approximately 25% of Türkiye’s total building stocks are vulnerable to seismic activities, it is inevitably expected that repair, maintenance, renovation, and rebuilding efforts increase the rate of CDW generation.

6.5. Future Direction and Suggestions

This section outlines strategies to reduce the environmental impact of construction and demolition activities and to increase the role of prefabrication in the construction industry.

Approximately two-thirds of Türkiye’s land area falls within first- and second-degree seismic zones, exposing a large portion of the population, about 71%, to significant earthquake risk. In response, it is essential to develop seismically resilient precast building systems that are also economically viable.

To enhance environmental sustainability, broader adoption of geopolymer concrete, an eco-friendly alternative to Portland cement, and greater utilization of construction and demolition waste (CDW) in concrete production and reusable structural components should be promoted through government incentives and private sector engagement.

Although CDW-based geopolymer concrete may offer limited environmental advantages in small-scale structures such as single-story buildings, future research should focus on industrial-scale processing techniques, including crushing and grinding of CDW. These steps are anticipated to reduce emissions and energy demands, thereby supporting more effective integration of CDW into the circular construction economy.

Given the complexity of geopolymer formulation, especially the environmental impact of alkali activators, further optimization is crucial. Sustainable alternatives such as using silica fume (high in silicon content) instead of sodium silicate, or incorporating slag in place of calcium hydroxide to form calcium-based geopolymer structures, should be explored.

In line with these considerations, several recommendations are provided below to guide future research and policy efforts aimed at promoting sustainability and expanding prefabrication in the construction sector:

- To increase the prefabrication market, share in the total construction market, Türkiye’s prefabrication sector should focus on the housing sector by developing innovative solutions for cost management and should be supported by public policies.

- The reuse of structural elements will not become a reality unless it becomes economically viable to construct mainstream structures in such a way. So, developed demountable connections for structural elements should be optimized.

- To make building construction more environmentally friendly and cost-effective, the structural system can be shifted from a beam-column frame to a shear wall panel system. Since every vertical element in such a system acts as a load-bearing member, there is no longer a need for high-strength connections to resist moments and shear forces, resulting in a more optimized structural design.

- The comprehensive training that enables the classification of buildings based on their Green Construction Performance, empowering owners and regulators to make informed decisions regarding rehabilitation, reshaping, and dismantling with a focus on maximizing recycling, should be organized.
- Türkiye faces the challenge of effectively managing a substantial volume of construction and demolition (C&D) waste generated. The temporary storage of mixed CDW in landfills has the potential to cause environmental and health hazards. It is crucial to enforce laws that mandate selective demolition and storage while imposing high landfill taxes as penalties for mixed demolition.

REFERENCES

[1] Y. Li, X. Zhang, Web-based construction waste estimation system for building construction projects, Automation in Construction, 35 (**2013**) 142-156.

[2] V.W.Y. Tam, X.F. Gao, C.M. Tam, C.H. Chan, New approach in measuring water absorption of recycled aggregates, Construction and Building Materials, 22 (**2008**) 364-369.

[3] C.-L. Peng, D.E. Scorpio, C.J. Kibert, Strategies for successful construction and demolition waste recycling operations, Construction Management & Economics, 15 (**1997**) 49-58.

[4] T. Fayyad, A. Abdalqader, Demountable reinforced concrete structures: a review and future directions, (**2020**).

[5] P.K. Aninthaneni, R.P. Dhakal, Demountable Precast RC Frame Building System for Seismic Regions, (**2016**).

[6] F.C. Rios, D. Grau, W.K. Chong, Reusing exterior wall framing systems: A cradle-to-cradle comparative life cycle assessment, Waste Management, 94 (**2019**) 120-135.

[7] H.H. Korkmaz, T. Tankut, Performance of a precast concrete beam-to-beam connection subject to reversed cyclic loading, Engineering Structures, 27 (**2005**) 1392-1407.

[8] IEA, Cement - fuels & technologies.

[9] P. Duxson, A. Fernández-Jiménez, J.L. Provis, G.C. Lukey, A. Palomo, J.S.J. van Deventer, Geopolymer technology: the current state of the art, Journal of Materials Science, 42 (**2006**) 2917-2933.

[10] J.L. Provis, S.A. Bernal, Geopolymers and Related Alkali-Activated Materials, Annual Review of Materials Research, 44 (**2014**) 299-327.

[11] M. Alhawat, A. Ashour, G. Yildirim, A. Aldemir, M. Sahmaran, Properties of geopolymers sourced from construction and demolition waste: A review, Journal of Building Engineering, 50 (**2022**).

[12] İ.R. Bayer, Influence of Retempering with Superplasticizer on Fresh and Hardened Properties of Prolonged Mixed Concretes Containing Supplementary Cementitious Materials, Tehnički vjesnik, 30 (**2023**) 1118-1125.

[13] P. Zhang, Z. Gao, J. Wang, J. Guo, S. Hu, Y. Ling, Properties of fresh and hardened fly ash/slag based geopolymer concrete: A review, Journal of Cleaner Production, 270 (**2020**).

[14] İ.R. Bayer, Graphene Oxide-Reinforced Cementitious Concrete Composites That Incorporates Silica Fume And Fly Ash, International Journal of Engineering Research and Development, 15 (**2023**) 526-534.

[15] H. Wu, J. Zuo, G. Zillante, J. Wang, H. Yuan, Construction and demolition waste research: a bibliometric analysis, Architectural Science Review, 62 (**2019**) 354-365.

[16] E. Özçelikci, A. Oskay, İ.R. Bayer, M. Şahmaran, Eco-hybrid cement-based building insulation materials as a circular economy solution to construction and demolition waste, Cement and Concrete Composites, 141 (**2023**).

[17] O. Sevim, E.H. Alakara, I. Demir, I.R. Bayer, Effect of magnetic water on properties of slag-based geopolymer composites incorporating ceramic tile waste from construction and demolition waste, Archives of Civil and Mechanical Engineering, 23 (**2023**).

[18] H. Ulugöl, A. Kul, G. Yıldırım, M. Şahmaran, A. Aldemir, D. Figueira, A. Ashour, Mechanical and microstructural characterization of geopolymers from assorted construction and demolition waste-based masonry and glass, Journal of Cleaner Production, 280 (**2021**).

[19] G. Yıldırım, A. Kul, E. Özçelikci, M. Şahmaran, A. Aldemir, D. Figueira, A. Ashour, Development of alkali-activated binders from recycled mixed masonry-originated waste, Journal of Building Engineering, 33 (**2021**).

[20] E. Ozcelikci, A. Kul, M.F. Gunal, B.F. Ozel, G. Yildirim, A. Ashour, M. Sahmaran, A comprehensive study on the compressive strength, durability-related parameters and microstructure of geopolymer mortars based on mixed construction and demolition waste, Journal of Cleaner Production, 396 (**2023**).

[21] AFAD, AFAD, 2023. 06 Şubat 2023 Pazarcık-Elbistan (Kahramanmaraş) Mw: 7.7 – Mw: 7.6 Depremleri Raporu. 140 s. (In Turkish), (**2023**).

[22] H. Huang, R. Hao, W. Zhang, M. Huang, Experimental study on seismic performance of square RC columns subjected to combined loadings, Engineering Structures, 184 (**2019**) 194-204.

[23] A. Aldemir, S. Akduman, O. Kocaer, R. Aktepe, M. Sahmaran, G. Yildirim, H. Almahmood, A. Ashour, Shear behaviour of reinforced construction and demolition waste-based geopolymer concrete beams, Journal of Building Engineering, 47 (**2022**).

[24] G. Wang, Y. Li, Z. Li, J.M. Ingham, Experimental and numerical study of precast concrete columns with hybrid bolted splice connections, Structures, 28 (**2020**) 17-36.

[25] Y.-T. Lu, Z.-X. Guo, Y. Liu, S.H. Basha, Performance of prefabricated RC column with replaceable Column-Base connection under cyclic lateral loads, Engineering Structures, 240 (**2021**).

[26] R. Nascimbene, L. Bianco, Cyclic response of column to foundation connections of reinforced concrete precast structures: Numerical and experimental comparisons, Engineering Structures, 247 (**2021**).

[27] S. Pul, M. Senturk, A. Ilki, I. Hajirasouliha, Experimental and numerical investigation of a proposed monolithic-like precast concrete column-foundation connection, Engineering Structures, 246 (**2021**).

[28] Y. Qing, C.-L. Wang, S. Meng, B. Zeng, Experimental study on the seismic performance of precast concrete columns with thread-bolt combination couplers, Engineering Structures, 251 (**2022**).

[29] Q. Zhou, Y. Liu, Y. Li, Load transfer mechanism of precast concrete piers with demountable connections, Engineering Structures, 261 (**2022**).

[30] R. Aktepe, S. Akduman, A. Aldemir, E. Ozcelikci, G. Yildirim, M. Sahmaran, A. Ashour, Fully demountable column base connections for reinforced CDW-based geopolymer concrete members, Engineering Structures, 290 (**2023**).

[31] S. Akduman, R. Aktepe, A. Aldemir, E. Ozcelikci, G. Yildirim, M. Sahmaran, A. Ashour, Structural performance of construction and demolition waste-based geopolymer concrete columns under combined axial and lateral cyclic loading, Engineering Structures, 297 (**2023**) 116973.

[32] K.L. Scrivener, V.M. John, E.M. Gartner, Eco-efficient cements: Potential economically viable solutions for a low-CO2 cement-based materials industry, Cement and Concrete Research, 114 (**2018**) 2-26.

[33] A. International, Standard Specification for Portland Cement, ASTM C150/C150MWest Conshohocken, PA, **2020**.

[34] R.M. Andrew, Global CO₂ emissions from cement production, Earth System Science Data, 10 (**2018**) 195-217.

[35] C.L. Sabine, R.A. Feely, N. Gruber, R.M. Key, K. Lee, J.L. Bullister, R. Wanninkhof, C.S. Wong, D.W. Wallace, B. Tilbrook, F.J. Millero, T.H. Peng, A. Kozyr, T. Ono, A.F. Rios, The oceanic sink for anthropogenic CO2, Science, 305 (**2004**) 367-371.

[36] F. Pacheco-Torgal, S. Jalali, Reusing ceramic wastes in concrete, Construction and Building Materials, 24 (**2010**) 832-838.

[37] C. Meyer, The greening of the concrete industry, Cement and Concrete Composites, 31 (**2009**) 601-605.

[38] D. McKelvey, V. Sivakumar, A. Bell, G. McLaverty, Shear strength of recycled construction materials intended for use in vibro ground improvement, Proceedings of the Institution of Civil Engineers - Ground Improvement, 6 (**2002**) 59-68.

[39] J. Davidovits, The need to create a new technical language for the transfer of basic scientific information, (**1982**).

[40] J. Davidovits, Geopolymers - Inorganic Polymeric New Materials, Journal of Thermal Analysis, 37 (**1991**) 1633-1656.

[41] X.W. Jan Wastiels, Stephane Faignet, Georges Patfoort, Mineral polymer based on fly ash, J Resour Manage Technol, 22 (**1994/9**) 135-141.

[42] J. Davidovits, High-alkali cements for 21st century concretes, Special Publication, 144 (**1994**) 383-398.

[43] J. Davidovits, Geopolymer chemistry and applications, Geopolymer Institute, (**2008**).

[44] S.-D. Wang, X.-C. Pu, K. Scrivener, P. Pratt, Alkali-activated slag cement and concrete: a review of properties and problems, Advances in cement research, 7 (**1995**) 93-102.

[45] A. Gruskovnjak, B. Lothenbach, L. Holzer, R. Figi, F. Winnefeld, Hydration of alkali-activated slag: comparison with ordinary Portland cement, Advances in Cement Research, 18 (**2006**) 119-128.

[46] Z.J. Li, S.F. Liu, Influence of slag as additive on compressive strength of fly ash-based geopolymer, Journal of Materials in Civil Engineering, 19 (**2007**) 470-474.

[47] C. Gunasekara, D.W. Law, S. Setunge, Long term permeation properties of different fly ash geopolymer concretes, Construction and Building Materials, 124 (**2016**) 352-362.

[48] K. Neupane, "Fly ash and GGBFS based powder-activated geopolymer binders: A viable sustainable alternative of portland cement in concrete industry", Mechanics of Materials, 103 (**2016**) 110-122.

[49] Y.H.M. Amran, R. Alyousef, H. Alabduljabbar, M. El-Zeadani, Clean production and properties of geopolymer concrete; A review, Journal of Cleaner Production, 251 (**2020**).

[50] C. Kurt, J. Bittner, Sodium hydroxide, Ullmann's encyclopedia of industrial chemistry, (**2000**).

[51] J. Van Deventer, J. Provis, Alkali-activated materials: state-of-the-art report, RILEM TC, (**2014**).

[52] A. Fernández-Jiménez, F. Puertas, Effect of activator mix on the hydration and strength behaviour of alkali-activated slag cements, Advances in cement research, 15 (**2003**) 129-136.

[53] S.D. Wang, K.L. Scrivener, P.L. Pratt, Factors Affecting the Strength of Alkali-Activated Slag, Cement and Concrete Research, 24 (**1994**) 1033-1043.

[54] K. Dombrowski, A. Buchwald, M. Weil, The influence of calcium content on the structure and thermal performance of fly ash based geopolymers, Journal of Materials Science, 42 (**2007**) 3033-3043.

[55] M. Yazdani, K. Kabirifar, B.E. Frimpong, M. Shariati, M. Mirmozaffari, A. Boskabadi, Improving construction and demolition waste collection service in an urban area using a simheuristic approach: A case study in Sydney, Australia, Journal of Cleaner Production, 280 (**2021**).

[56] R.A. Robayo-Salazar, W. Valencia-Saavedra, R.M. de Gutiérrez, Construction and Demolition Waste (CDW) Recycling-As Both Binder and Aggregates-In Alkali-Activated Materials: A Novel Re-Use Concept, Sustainability, 12 (**2020**) 5775.

[57] S. Akduman, Experimental Investigations on the Flexure Behaviour of Reinforced Geopolymer Beams Produced from Recycled Construction Materials, (**2021**).

[58] J. Tan, Ö. Cizer, B. Vandevyvere, J. De Vlieger, H. Dan, J. Li, Efflorescence mitigation in construction and demolition waste (CDW) based geopolymer, Journal of Building Engineering, 58 (**2022**).

[59] M. Vafaei, A. Allahverdi, P. Dong, N. Bassim, M. Mahinroosta, Resistance of red clay brick waste/phosphorus slag-based geopolymer mortar to acid solutions of mild concentration, Journal of Building Engineering, 34 (**2021**).

[60] J. Fořt, E. Vejmelková, D. Koňáková, N. Alblová, M. Čáchová, M. Keppert, P. Rovnaníková, R. Černý, Application of waste brick powder in alkali activated aluminosilicates: Functional and environmental aspects, Journal of Cleaner Production, 194 (**2018**) 714-725.

[61] D.M.J. Sumajouw, D. Hardjito, S.E. Wallah, B.V. Rangan, Fly ash-based geopolymer concrete: study of slender reinforced columns, Journal of Materials Science, 42 (**2006**) 3124-3130.

[62] P.K. Sarker, Analysis of geopolymer concrete columns, Materials and Structures, 42 (**2008**) 715-724.

[63] K.H. Mo, U.J. Alengaram, M.Z. Jumaat, Structural performance of reinforced geopolymer concrete members: A review, Construction and Building Materials, 120 (**2016**) 251-264.

[64] M. Albitar, M.S. Mohamed Ali, P. Visintin, Experimental study on fly ash and lead smelter slag-based geopolymer concrete columns, Construction and Building Materials, 141 (**2017**) 104-112.

[65] T.T. Tran, T.M. Pham, H. Hao, Experimental and analytical investigation on flexural behaviour of ambient cured geopolymer concrete beams reinforced with steel fibers, Engineering Structures, 200 (**2019**).

[66] P. Saranya, P. Nagarajan, A.P. Shashikala, Behaviour of GGBS-dolomite geopolymer concrete short column under axial loading, Journal of Building Engineering, 30 (**2020**).

[67] D.Q. Pham, T.N. Nguyen, S.T. Le, T.T. Pham, T.D. Ngo, The structural behaviours of steel reinforced geopolymer concrete beams: An experimental and numerical investigation, Structures, 33 (**2021**) 567-580.

[68] K. Neupane, S.A. Hadigheh, Sodium hydroxide-free geopolymer binder for prestressed concrete applications, Construction and Building Materials, 293 (**2021**).

[69] P. Saranya, P. Nagarajan, A.P. Shashikala, Seismic performance of geopolymer concrete beam-column joints under reverse cyclic loading, Innovative Infrastructure Solutions, 6 (**2021**).

[70] Y. Mao, Y. Du, H.J. Hwang, J. Su, X. Hu, Y. Liu, C. Shi, Seismic performance of interior beam-column joints using reinforced slag-based geopolymer concrete, Earthquake Engineering & Structural Dynamics, 52 (**2022**) 285-307.

[71] A.S. Albidah, Shear behviour of metakaolin-fly ash based geopolymer concrete deep beams, Engineering Structures, 275 (**2023**).

[72] C.-L. Peng, D.E. Scorpio, C.J. Kibert, Strategies for successful construction and demolition waste recycling operations, Construction Management and Economics, 15 (**1997**) 49-58.

[73] X.-S. Shi, Q.-Y. Wang, X.-L. Zhao, F.G. Collins, Structural behaviour of geopolymeric recycled concrete filled steel tubular columns under axial loading, Construction and Building Materials, 81 (**2015**) 187-197.

[74] P. Kathirvel, S.R.M. Kaliyaperumal, Influence of recycled concrete aggregates on the flexural properties of reinforced alkali activated slag concrete, Construction and Building Materials, 102 (**2016**) 51-58.

[75] Ş. Akduman, O. Kocaer, A. Aldemir, M. Şahmaran, G. Yıldırım, H. Almahmood, A. Ashour, Experimental investigations on the structural behaviour of reinforced geopolymer beams produced from recycled construction materials, Journal of Building Engineering, 41 (**2021**).

[76] Turkish Standard (TS500), Design and Construction Rules of Reinforced Concrete Structures Turkish Standards Institute, Ankara, Turkey, **2000**.

[77] ACI Committee (ACI 318), Building code requirements, structural concrete and Commentary, American Concrete Institute, Michigan, USA, **2019**.

[78] L. Ferreira, J. de Brito, M. Barra, Influence of the pre-saturation of recycled coarse concrete aggregates on concrete properties, Magazine of Concrete Research, 63 (**2011**) 617-627.

[79] R. Kumar, Influence of recycled coarse aggregate derived from construction and demolition waste (CDW) on abrasion resistance of pavement concrete, Construction and Building Materials, 142 (**2017**) 248-255.

[80] J. De Brito, N. Saikia, Recycled aggregate in concrete: use of industrial, construction and demolition waste, Springer Science & Business Media ,**2012**.

[81] M. Etxeberria, E. Vázquez, A. Marí, M. Barra, Influence of amount of recycled coarse aggregates and production process on properties of recycled aggregate concrete, Cement and Concrete Research, 37 (**2007**) 735-742.

[82] S.C. Kou, C.S. Poon, D. Chan, Influence of fly ash as a cement addition on the hardened properties of recycled aggregate concrete, Materials and Structures, 41 (**2007**) 1191-1201.

[83] A. Domingo, C. Lázaro, F.L. Gayarre, M.A. Serrano, C. López-Colina, Long term deformations by creep and shrinkage in recycled aggregate concrete, Materials and Structures, 43 (**2009**) 1147-1160.

[84] L. Evangelista, J. de Brito, Mechanical behaviour of concrete made with fine recycled concrete aggregates, Cement and Concrete Composites, 29 (**2007**) 397-401.

[85] W. Li, S.H. Xu, The building junk status quo research, Construction Technology 2(**2007**) 480–483.

[86] D.R. Hack, D.P. Bryan, Aggregates. Industrial Minerals and Rocks, 7 ed., Society for Mining, Metallurgy and Exploration, Littleton, Colorado, **2006**.

[87] A. Akbarnezhad, K.C.G. Ong, M.H. Zhang, C.T. Tam, T.W.J. Foo, Microwave-assisted beneficiation of recycled concrete aggregates, Construction and Building Materials, 25 (**2011**) 3469-3479.

[88] J. Liu, K. Ma, J. Shen, J. Zhu, G. Long, Y. Xie, B. Liu, Influence of recycled concrete aggregate enhancement methods on the change of microstructure of ITZs in recycled aggregate concrete, Construction and Building Materials, 371 (**2023**) 130772.

[89] W. Li, J. Xiao, Z. Sun, S. Kawashima, S.P. Shah, Interfacial transition zones in recycled aggregate concrete with different mixing approaches, Construction and Building Materials, 35 (**2012**) 1045-1055.

[90] H. Sezen, A.S. Whittaker, Seismic Performance of Industrial Facilities Affected by the 1999 Turkey Earthquake, Journal of Performance of Constructed Facilities, 20 (**2006**) 28-36.

[91] H.M. Elsanadedy, Y.A. Al-Salloum, M.A. Alrubaidi, T.H. Almusallam, N.A. Siddiqui, H. Abbas, Upgrading of precast RC beam-column joints using innovative FRP/steel hybrid technique for progressive collapse prevention, Construction and Building Materials, 268 (**2021**).

[92] A. Belleri, E. Brunesi, R. Nascimbene, M. Pagani, P. Riva, Seismic Performance of Precast Industrial Facilities Following Major Earthquakes in the Italian Territory, Journal of Performance of Constructed Facilities, 29 (**2015**).

[93] E. Brunesi, R. Nascimbene, S. Peloso, Evaluation of the Seismic Response of Precast Wall Connections: Experimental Observations and Numerical Modeling, Journal of Earthquake Engineering, 24 (**2018**) 1057-1082.

[94] E. Brunesi, S. Peloso, R. Pinho, R. Nascimbene, Shake-Table Testing of a Full-Scale Two-Story Precast Wall-Slab-Wall Structure, Earthquake Spectra, 35 (**2019**) 1583-1609.

[95] E. Brunesi, S. Peloso, R. Pinho, R. Nascimbene, Cyclic tensile testing of a three-way panel connection for precast wall-slab-wall structures, Structural Concrete, 20 (**2019**) 1307-1315.

[96] S. Ravasini, B. Belletti, Robustness-oriented conceptual design of precast concrete frame structures, International fib Symposium on the Conceptual Design of StructuresSwitzerland, **2021**.

[97] S. Ravasini, B. Belletti, E. Brunesi, R. Nascimbene, F. Parisi, Nonlinear Dynamic Response of a Precast Concrete Building to Sudden Column Removal, Applied Sciences, 11 (**2021**).

[98] H.H. Ghayeb, N.H.R. Sulong, H.A. Razak, K.H. Mo, Z. Ismail, H. Hashim, M. Gordan, A review of the seismic performance behaviour of hybrid precast beam-to-column connections, Archives of Civil and Mechanical Engineering, 23 (**2022**) 35.

[99] Z.B. Haber, K.R. Mackie, H.M. Al-Jelawy, Testing and Analysis of Precast Columns with Grouted Sleeve Connections and Shifted Plastic Hinging, Journal of Bridge Engineering, 22 (**2017**) 04017078.

[100] J.-J. Fan, D.-C. Feng, G. Wu, S. Hou, Y. Lu, Experimental study of prefabricated RC column-foundation assemblies with two different connection methods and using large-diameter reinforcing bars, Engineering Structures, 205 (**2020**) 110075.

[101] M. Senturk, S. Pul, A. Ilki, I. Hajirasouliha, Development of a monolithic-like precast beam-column moment connection: Experimental and analytical investigation, Engineering Structures, 205 (**2020**).

[102] J.D. Nzabonimpa, W.-K. Hong, J. Kim, Experimental and non-linear numerical investigation of the novel detachable mechanical joints with laminated plates for composite precast beam-column joint, Composite Structures, 185 (**2018**) 286-303.

[103] P.K. Aninthaneni, R.P. Dhakal, J. Marshall, J. Bothara, Experimental investigation of “dry” jointed precast concrete frame sub-assemblies with steel angle and tube connections, Bulletin of Earthquake Engineering, 18 (**2020**) 3659-3681.

[104] E. Baran, M. Mahamid, M. Baran, M. Kurtoglu, I. Torra-Bilal, Performance of a moment resisting beam-column connection for precast concrete construction, Engineering Structures, 246 (**2021**).

[105] K. Ding, Y. Ye, W. Ma, Seismic performance of precast concrete beam-column joint based on the bolt connection, Engineering Structures, 232 (**2021**).

[106] W. Huang, G. Hu, X. Miao, Z. Fan, Seismic performance analysis of a novel demountable precast concrete beam-column connection with multi-slit devices, Journal of Building Engineering, 44 (**2021**).

[107] I. Torra-Bilal, M. Mahamid, E. Baran, Cyclic behaviour of precast beam-to-column connections: An experimental and numerical investigation, Structures, 35 (**2022**) 939-957.

[108] J.D. Nzabonimpa, W.-K. Hong, Structural performance of detachable precast composite column joints with mechanical metal plates, Engineering Structures, 160 (**2018**) 366-382.

[109] J. Liu, Y. Xue, C. Wang, J. Nie, Z. Wu, Experimental investigation on seismic performance of mechanical joints with bolted flange plate for precast concrete column, Engineering Structures, 216 (**2020**).

[110] J. Chen, J. Liu, P. Hu, H. Sun, X. Hu, Experimental and numerical investigation on seismic behavior of detachable precast concrete column joints with bolted flange plate, Journal of Building Engineering, 49 (**2022**).

[111] J.-Y. Hu, W.-K. Hong, S.-C. Park, Experimental investigation of precast concrete based dry mechanical column-column joints for precast concrete frames, The Structural Design of Tall and Special Buildings, 26 (**2017**).

[112] P.K. Aninthaneni, R.P. Dhakal, Demountable Precast Concrete Frame–Building System for Seismic Regions: Conceptual Development, Journal of Architectural Engineering, 23 (**2017**).

[113] L. Fan, J. Wei, Y. Chen, J. Feng, P. Sareh, Shear Performance of Large-Thickness Precast Shear Walls with Cast-in-Place Belts and Grouting Sleeves, ASCE-ASME Journal of Risk and Uncertainty in Engineering Systems, Part A: Civil Engineering, 9 (**2023**) 04023005.

[114] W. Fan, Y. Chen, J. Li, Y. Sun, J. Feng, H. Hassanin, P. Sareh, Machine learning applied to the design and inspection of reinforced concrete bridges: Resilient methods and emerging applications, Structures, 33 (**2021**) 3954-3963.

[115] Z. Wang, T. Liu, Z. Long, J. Wang, J. Zhang, A machine-learning-based model for predicting the effective stiffness of precast concrete columns, Engineering Structures, 260 (**2022**).

[116] T.-D. Nguyen, R. Cherif, P.-Y. Mahieux, J. Lux, A. Aït-Mokhtar, E. Bastidas-Arteaga, Artificial intelligence algorithms for prediction and sensitivity analysis of mechanical properties of recycled aggregate concrete: A review, Journal of Building Engineering, 66 (**2023**).

[117] M. Ye, J. Jiang, H.M. Chen, H.Y. Zhou, D.D. Song, Seismic behavior of an innovative hybrid beam-column connection for precast concrete structures, Engineering Structures, 227 (**2021**) 111436.

[118] J.D. Nzabonimpa, W.K. Hong, S.C. Park, Experimental investigation of dry mechanical beam–column joints for precast concrete based frames, The Structural Design of Tall and Special Buildings, 26 (**2017**) e1302.

[119] P.K. Aninthaneni, R.P. Dhakal, J. Marshall, J. Bothara, Nonlinear Cyclic Behaviour of Precast Concrete Frame Sub-Assemblies With "Dry" End Plate Connection, Structures, 14 (**2018**) 124-136.

[120] Q. Zhou, Y. Liu, Y. Li, Load transfer mechanism of precast concrete piers with demountable connections, Engineering Structures, 261 (**2022**) 114287.

[121] J.D. Nzabonimpa, W.K. Hong, J. Kim, Mechanical connections of the precast concrete columns with detachable metal plates, The Structural Design of Tall and Special Buildings, 26 (**2017**) e1391.

[122] Z. Li, Y. Qi, J. Teng, Experimental investigation of prefabricated beam-to-column steel joints for precast concrete structures under cyclic loading, Engineering Structures, 209 (**2020**).

[123] R. Zhang, Y. Zhang, A. Li, T.Y. Yang, Experimental study on a new type of precast beam-column joint, Journal of Building Engineering, 51 (**2022**) 104252.

[124] C. Yang, A. Li, L. Xie, Development of design method for precast concrete frame with dry-connected rotational friction dissipative beam-to-column joints, Journal of Building Engineering, 45 (**2022**) 103563.

[125] E. Brunesi, R. Nascimbene, D. Bolognini, D. Bellotti, Experimental investigation of the cyclic response of reinforced precast concrete framed structures, Pci Journal, 60 (**2015**) 57-79.

[126] I.N. Psycharis, H.P. Mouzakis, Shear resistance of pinned connections of precast members to monotonic and cyclic loading, Engineering Structures, 41 (**2012**) 413-427.

[127] G. Magliulo, M. Ercolino, M. Cimmino, V. Capozzi, G. Manfredi, FEM analysis of the strength of RC beam-to-column dowel connections under monotonic actions, Construction and Building Materials, 69 (**2014**) 271-284.

[128] D.A. Bournas, P. Negro, F.J. Molina, Pseudodynamic tests on a full-scale 3-storey precast concrete building: Behavior of the mechanical connections and floor diaphragms, Engineering Structures, 57 (**2013**) 609-627.

[129] P. Negro, D.A. Bournas, F.J. Molina, Pseudodynamic tests on a full-scale 3-storey precast concrete building: Global response, Engineering Structures, 57 (**2013**) 594-608.

[130] E.A.B. Aguiar, E.K. Bellucio, M.K. El Debs, Behaviour of grouted dowels used in precast concrete connections, Structural Concrete, 13 (**2012**) 84-94.

[131] B. Zoubek, T. Isakovic, Y. Fahjan, M. Fischinger, Cyclic failure analysis of the beam-to-column dowel connections in precast industrial buildings, Engineering Structures, 52 (**2013**) 179-191.

[132] G.D. Kremmyda, Y.M. Fahjan, S.G. Tsoukantas, Nonlinear FE analysis of precast RC pinned beam-to-column connections under monotonic and cyclic shear loading, Bulletin of Earthquake Engineering, 12 (**2014**) 1615-1638.

[133] G.D. Kremmyda, Y.M. Fahjan, I.N. Psycharis, S.G. Tsoukantas, Numerical investigation of the resistance of precast RC pinned beam-to-column connections under shear loading, Earthquake Engineering & Structural Dynamics, 46 (**2017**) 1511-1529.

[134] H.-K. Kang, D.J. Lee, Special precast beam-column connection using pure dry cast method, World Congress on Advances in Structural Engineering and Mechanics, (**2013**).

[135] P. Aninthaneni, R. Dhakal, J. Marshall, J. Bothara, Experimental investigation of dry beam-column moment connections for demountable precast concrete frame

buildings, Proc., New Zealand Society for Earthquake Engineering Annual Conf.(NZSEE), **2016**.

[136] J. Navarro-Rubio, P. Pineda, A. García-Martínez, Sustainability, prefabrication and building optimization under different durability and re-using scenarios: Potential of dry precast structural connections, Sustainable Cities and Society, 44 (**2019**) 614-628.

[137] A. Baghdadi, M. Heristchian, L. Ledderose, H. Kloft, Experimental and numerical assessment of new precast concrete connections under bending loads, Engineering Structures, 212 (**2020**).

[138] Y. Bao, V.C. Li, Feasibility study of lego-inspired construction with bendable concrete, Automation in Construction, 113 (**2020**) 103161.

[139] C. Zhou, B. Tang, L.Y. Ding, P. Sekula, Y. Zhou, Z.K. Zhang, Design and automated assembly of Planetary LEGO Brick for lunar in-situ construction, Automation in Construction, 118 (**2020**) 103282.

[140] T. Ding, J. Xiao, Q. Zhang, A. Akbarnezhad, Experimental and numerical studies on design for deconstruction concrete connections: An overview, Advances in Structural Engineering, 21 (**2018**) 2198-2214.

[141] S. Pul, M. Senturk, A bolted moment connection model for precast column-beam joint, Proceedings of the 2nd World Congress on Civil, Structural, and Environmental Engineering, Barcelona, Spain, **2017**, pp. 2-4.

[142] P.K. Aninthaneni, R.P. Dhakal, J. Marshall, J. Bothara, Experimental investigation of dry beam-column moment connections for demountable precast concrete frame buildings, (**2016**).

[143] H. Rashidian-Dezfouli, P.R. Rangaraju, Comparison of strength and durability characteristics of a geopolymer produced from fly ash, ground glass fiber and glass powder, Materiales de Construcción, 67 (**2017**).

[144] G. Yildirim, E. Ozcelikci, M. Alhawat, A. Ashour, Development of Concrete Mixtures Based Entirely on Construction and Demolition Waste and Assessment of Parameters Influencing the Compressive Strength, in: A. Jędrzejewska, F. Kanavaris, M. Azenha, F. Benboudjema, D. Schlicke (Eds.) International RILEM Conference on Synergising Expertise towards Sustainability and Robustness of Cement-based Materials and Concrete Structures, Springer, **2023**, pp. 510-520.

[145] E. Ozcelikci, G. Yildirim, M. Alhawat, A. Ashour, M. Sahmaran, An Investigation into Durability Aspects of Geopolymer Concretes Based Fully on Construction and Demolition Waste, in: A. Ilki, D. Çavunt, Y.S. Çavunt (Eds.) Building for the Future: Durable, Sustainable, Resilient, Springer Nature Switzerland, Cham, **2023**, pp. 377-386.

[146] G. Baronio, L. Binda, Study of the pozzolanicity of some bricks and clays, Construction and Building Materials, 11 (**1997**) 41-46.

[147] G. Yildirim, A. Ashour, E. Ozcelikci, M.F. Gunal, B.F. Ozel, Development of Geopolymer Binders with Mixed Construction and Demolition Waste-Based Materials, Ioci 2022, **2022**.

[148] I. Garcia-Lodeiro, A. Palomo, A. Fernández-Jiménez, D.E. Macphee, Compatibility studies between N-A-S-H and C-A-S-H gels. Study in the ternary diagram Na2O–CaO–Al2O3–SiO2–H2O, Cement and Concrete Research, 41 (**2011**) 923-931.

[149] Turkish Earthquake Code (TEC2018), Specifications for the Buildings to Be Constructed in Disaster Areas, Prime Ministry Disaster and Emergency Management Authority, Ankara, Turkey, **2018**.

[150] ACI Committee (ACI 374.2R-13), Guide for Testing Reinforced Concrete Structural Elements under Slowly Applied Simulated Seismic Loads, American Concrete Institute, Farmington Hills, **2013**.

[151] American Standard (E2126-11), Standard Test Methods for Cyclic (Reversed) Load Test for Shear Resistance of Vertical Elements of the Lateral Force Resisting Systems for Buildings, American Society for Testing and Materials (ASTM), West Conshohocken, PA, USA, **2011**.

[152] R. Park, Evaluation of ductility of structures and structural assemblages from laboratory testing, Bulletin of the New Zealand Society for Earthquake Engineering, 22 (**1989**) 155-166.

[153] Federal Emergency Management Agency (FEMA 356), Prestandard and commentary for the seismic rehabilitation of buildings, Washington, DC, **2000**.

[154] ACI Committee (ACI 374.1-05), Acceptance criteria for moment frames based on structural testing and commentary, American Concrete Institute, Farmington Hills, **2005**.

[155] J.B. Mander, M.J.N. Priestley, R. Park, Theoretical Stress-Strain Model for Confined Concrete, Journal of Structural Engineering, 114 (**1988**) 1804-1826.

[156] A.C. Barrera, J.L. Bonet, M.L. Romero, P.F. Miguel, Experimental tests of slender reinforced concrete columns under combined axial load and lateral force, Engineering Structures, 33 (**2011**) 3676-3689.

[157] C. Jiang, Y.-F. Wu, G. Wu, Plastic Hinge Length of FRP-Confined Square RC Columns, Journal of Composites for Construction, 18 (**2014**).

[158] J.C.M. Ho, H.J. Pam, Inelastic design of low-axially loaded high-strength reinforced concrete columns, Engineering Structures, 25 (**2003**) 1083-1096.

[159] Y.C. Kurama, S. Sritharan, R.B. Fleischman, J.I. Restrepo, R.S. Henry, N.M. Cleland, S.K. Ghosh, P. Bonelli, Seismic-Resistant Precast Concrete Structures: State of the Art, Journal of Structural Engineering, 144 (**2018**).

[160] S.S. Mahini, H.R. Ronagh, Strength and ductility of FRP web-bonded RC beams for the assessment of retrofitted beam–column joints, Composite Structures, 92 (**2010**) 1325-1332.

[161] ASCE Standard (ASCE/SEI 41-17), Seismic Evaluation and Retrofit of Existing Buildings, American Society of Civil Engineers, Reston, Virginia, **2017**.

[162] S. Bae, O. Bayrak, Plastic hinge length of reinforced concrete columns, ACI Structural Journal, 105 (**2008**) 290-300.

[163] C.-L. Ning, B. Li, Probabilistic Approach for Estimating Plastic Hinge Length of Reinforced Concrete Columns, Journal of Structural Engineering, 142 (**2016**).

[164] E.M. Hines, J.I. Restrepo, F. Seible, Force-displacement characterization of well-confined bridge piers, ACI Structural Journal, 101 (**2004**) 537-548.

[165] M.J.N. Priestley, R. Park, STRENGTH OF DUCTILITY OF CONCRETE BRIDGE COLUMNS UNDER SEISMIC LOADING, ACI Structural Journal, 84 (**1987**) 61-76.

[166] T. Paulay, M.J.N. Priestley, Seismic design of reinforced concrete and masonry building, John Wiley & Sons, New York, USA, **1992**.

[167] S.A. Sheikih, S.S. Khoury, Confined concrete columns with Stubs, ACI Structural Journal, 90 (**1993**) 414-431.

[168] T.B. Panagiotakos, M.N. Fardis, Deformations of reinforced concrete members at yielding and ultimate, ACI Structural Journal, 98 (**2001**) 135-148.

[169] Y. Lu, X. Gu, J. Guan, Probabilistic Drift Limits and Performance Evaluation of Reinforced Concrete Columns, Journal of Structural Engineering, 131 (**2005**) 966-978.

[170] M.P. Berry, D.E. Lehman, L.N. Lowes, Lumped-plasticity models for performance simulation of bridge columns, ACI Structural Journal, 105 (**2008**) 270-279.

[171] Four Discussions from the May/June **2008** ACI Structural Journal - Plastic Hinge Length of Reinforced Concrete Columns.)Paper by Sungjin Bae and Oguzhan Bayrak). Discussion by N. Subramanian. Disc. 105-S28, ACI Structural Journal, 106.

[172] D. Biskinis, M.N. Fardis, Flexure-controlled ultimate deformations of members with continuous or lap-spliced bars, Structural Concrete, 11 (**2010**) 93-108.

[173] CEN. Eurocode 8: Design of structures for earthquake resistance – Part 3: Assessment and retrofitting of building, Comite Europeen de Normalisation, Brussels, **2005**.

[174] Applied Technology Council (ATC-40), Seismic Evaluation and Retrofit of Concrete Building. , Redwood City, California, **1996**.

[175] Federal Emergency Management Agency (FEMA 273), NEHRP Guidelines for the Seismic Rehabilitation of Buildings Buildings, Washington, DC, **1997**.

[176] Y.J. Park, A.H.S. Ang, Y.K. Wen, Seismic Damage Analysis of Reinforced Concrete Buildings, Journal of Structural Engineering, 111 (**1985**) 740-757.

[177] Y. Hose, P. Silva, F. Seible, Development of a Performance Evaluation Database for Concrete Bridge Components and Systems under Simulated Seismic Loads, Earthquake Spectra, 16 (**2000**) 413-442.

[178] Y. Nakano, M. Maeda, H. Kuramoto, M. Murakami, Guideline for Post-Earthquake Damage Evaluation and Rehabilitation of RC Buildings in Japan, 13th World Conference on Earthquake EngineeringVancouver, BC, **2004**.

[179] A. Vosooghi, M.S. Saiidi, “Seismic Damage States and Response Parameters for Bridge Columns.” Structural Concrete in Performance-Based Seismic Design of Bridges, SP-271, P. F. Silva and R. Valluvan, eds., American Concrete Institute, Farmington Hills, MI, pp. 29-46, (**2010**) 29-46.

[180] Q. Li, A. Belarbi, Damage assessment of square RC bridge columns subjected to torsion combined with axial compression, flexure, and shear, KSCE Journal of Civil Engineering, 17 (**2013**) 530-539.

[181] P.E. Mergos, A.J. Kappos, A combined local damage index for seismic assessment of existing RC structures, Earthquake Engineering & Structural Dynamics, 42 (**2013**) 833-852.

[182] JBDPA. Guideline for post-earthquake damage evaluation and rehabilitation (2015 revision) (in Japanese), Tokyo, **2015**.

[183] G. Xing, O.E. Ozbulut, T. Lei, B. Liu, Cumulative seismic damage assessment of reinforced concrete columns through cyclic and pseudo-dynamic tests, The Structural Design of Tall and Special Buildings, 26 (**2017**).

[184] A. Moshref, M. Khanmohammadi, M. Tehranizadeh, Assessment of the seismic capacity of mainshock-damaged reinforced concrete columns, Bulletin of Earthquake Engineering, 15 (**2016**) 291-311.

[185] M.A. Sozen, Review of Earthquake response of reinforced concrete buildings with a view to drift control, State-of-the-Art in Earthquake Engineering, Turkish National Committee on Earthquake EngineeringIstanbul, **1981**, pp. 383-418.

[186] H. Banon, D. Veneziano, Seismic safety of reinforced concrete members and structures, Earthquake Engineering & Structural Dynamics, 10 (**1982**) 179-193.

[187] A. Ghobarah, H. Abou-Elfath, A. Biddah, Response-based damage assessment of structures, Earthquake Engineering & Structural Dynamics, 28 (**1999**) 79-104.

[188] G.H. Powell, R. Allahabadi, Seismic damage prediction by deterministic methods: Concepts and procedures, Earthquake Engineering & Structural Dynamics, 16 (**1988**) 719-734.

[189] W. Krätzig, I. Meyer, K. Meskouris, Damage evolution in reinforced concrete members under cyclic loading, Structural safety and reliability american society of civil engineersSan Francisco, CA, **1989**, pp. 795–804.

[190] J.B. Mander, J.-T. Cheng, Renewable Hinge Detailing for Bridge Columns, Pacific Conference on Earthquake EngineeringMelbourne November 20-22, **1995**.

[191] A. Elenas, Correlation between seismic acceleration parameters and overall structural damage indices of buildings, Soil Dynamics and Earthquake Engineering, 20 (**2000**) 93-100.

[192] T.H. Kim, K.M. Lee, Y.S. Chung, H.M. Shin, Seismic damage assessment of reinforced concrete bridge columns, Engineering Structures, 27 (**2005**) 576-592.

[193] Y.J. Park, A.H.S. Ang, Mechanistic Seismic Damage Model for Reinforced Concrete, Journal of Structural Engineering, 111 (**1985**) 722-739.

[194] E. Cosenza, G. Manfredi, R. Ramasco, The use of damage functionals in earthquake engineering: A comparison between different methods, Earthquake Engineering & Structural Dynamics, 22 (**1993**) 855-868.

[195] C.K. Chiu, H.F. Sung, T.C. Chiou, Quantification of the reduction factors of seismic capacity for damaged RC column members using the experiment database, Earthquake Engineering & Structural Dynamics, 50 (**2020**) 756-776.

[196] H. Ilcan, O. Sahin, Z. Unsal, E. Ozcelikci, A. Kul, N. Cağatay Demiral, M. Ozkan Ekinci, M. Sahmaran, Effect of industrial waste-based precursors on the fresh, hardened and environmental performance of construction and demolition wastes-based geopolymers, Construction and Building Materials, 394 (**2023**).

[197] R. Aktepe, S. Akduman, B. Guldur Erkal, Experimental investigation on lateral behavior of novel hybrid cold-formed steel walls with composite sheathing, Journal of Constructional Steel Research, 202 (**2023**).

[198] U.S.G.S, Cement Statistics and Information - Cement, **2023**.

[199] G. Keoleian, A.M. Kendall, M.D. Lepech, V.C. Li, Guiding the design and application of new materials for enhancing sustainability performance: Framework and infrastructure application, MRS Proceedings, 895 (**2005**).

[200] H. Yu, Y. Yi, C. Unluer, Heat of hydration, bleeding, viscosity, setting of Ca(OH)2-GGBS and MgO-GGBS grouts, Construction and Building Materials, 270 (**2021**).

[201] M. Kumar, S. Prashant, M.V. Kamath, Enhancing the sustainability of high strength concrete in terms of embodied energy and carbon emission by incorporating sewage sludge and fly ash, Innovative Infrastructure Solutions, 7 (**2022**).

[202] M. Nisbet, M.G. Van Geem, J. Gajda, M.L. Marceau, Environmental life cycle inventory of Portland cement and concrete, World Cement, 28 (**1997**).

[203] O. Mahmoodi, H. Siad, M. Lachemi, S. Dadsetan, M. Sahmaran, Optimization of brick waste-based geopolymer binders at ambient temperature and pre-targeted chemical parameters, Journal of Cleaner Production, 268 (**2020**).

[204] M. Fawer, M. Concannon, W. Rieber, Life cycle inventories for the production of sodium silicates, The International Journal of Life Cycle Assessment, 4 (**1999**).

[205] A. Sagastume Gutiérrez, J. Van Caneghem, J.B. Cogollos Martínez, C. Vandecasteele, Evaluation of the environmental performance of lime production in Cuba, Journal of Cleaner Production, 31 (**2012**) 126-136.

[206] R. Jones, M. McCarthy, M. Newlands, Fly ash route to low embodied CO2 and implications for concrete construction, World of Coal Ash (WOCA) Conference **2011**, pp. 1-14.

[207] L. Barcelo, J. Kline, G. Walenta, E. Gartner, Cement and carbon emissions, Materials and Structures, 47 (**2013**) 1055-1065.

[208] W. Chen, S. Yang, X. Zhang, N.D. Jordan, J. Huang, Embodied energy and carbon emissions of building materials in China, Building and Environment, 207 (**2022**).

[209] M.V.P. Migo-Sumagang, M.C. Maguyon-Detras, M. Gummert, C.G. Alfafara, M.G. Borines, J.A. Capunitan, N. Van Hung, Rice-Straw-Based Heat Generation System Compared to Open-Field Burning and Soil Incorporation of Rice Straw: An Assessment of Energy, GHG Emissions, and Economic Impacts, Sustainability, 12 (**2020**).

[210] Eurostat, Eurostat Statistics for Waste Flow Generation European Commision, **2020**.

[211] U.S. Environmental Protection Agency, Construction and Demolition Debris: Material-Specific Data. , Environmental Protection Agency, **2023**.

[212] W. Lu, Estimating the Amount of Building-Related Construction and Demolition Waste in China, Proceedings of the 18th International Symposium on Advancement of Construction Management and Real Estate, **2014**, pp. 539-548.

[213] Turkish Statistical Instute (TÜİK), Waste Statistics, **2020**.

[214] Minister of Environment, Urbanisation and Climate Change, Ankara Province Environmental Report, **2020**.

[215] A. Tatiya, D. Zhao, M. Syal, G.H. Berghorn, R. LaMore, Cost prediction model for building deconstruction in urban areas, Journal of Cleaner Production, 195 (**2018**) 1572-1580.

[216] Minister of Environment and Forest, Regulation on Control of Excavated Soil, Construction and Demolition Wastes, Turkey, **2004**.

[217] European Commission, Construction and Demolition Waste management in Germany, **2015**.

[218] Environmental Research and Education Foundation (EREF), Analysis of MSW Landfill Tipping Fees – 2022, **2023**.

[219] Guidance Landfill Tax rates - Updated April 2023, **2023**.

[220] European Commission, Construction and Demolition Waste management in Portugal, **2015**.

[221] European Commission, Construction and Demolition Waste management in Denmark, **2015**.

[222] European Commission, Construction and Demolition Waste management in France, **2015**.

[223] European Commission, Construction and Demolition Waste management in Finland, **2015**.

[224] European Commission, Construction and Demolition Waste management in Greece, **2015**.

[225] C. Zhang, M. Hu, X. Yang, B. Miranda-Xicotencatl, B. Sprecher, F. Di Maio, X. Zhong, A. Tukker, Upgrading construction and demolition waste management from downcycling to recycling in the Netherlands, Journal of Cleaner Production, 266 (**2020**).

[226] CEN. Eurocode: Basis of structural design, Comite Europeen de Normalisation, Brussels, **2005**.

[227] P.K. Mehta, R.W. Burrows, Building durable structures in the 21st century, Concrete international, 23 (**2001**).

[228] Disaster and Emergency Management Presidency (AFAD), Istanbul Province Disaster Reduction Plan, **2022**.

[229] Turkish Statistical Instute (TÜİK), Building and Housing Qualifications Survey, **2021**.

[230] L. Jaillon, C.S. Poon, Y.H. Chiang, Quantifying the waste reduction potential of using prefabrication in building construction in Hong Kong, Waste Manag, 29 (**2009**) 309-320.

[231] Turkish Precast Concrete Association (T.P.C.A.), Precast concrete by numbers, **2021**.

[232] E.L. Oral, G. Mıstıkoglu, E. Erdis, JIT in developing countries—a case study of the Turkish prefabrication sector, Building and Environment, 38 (**2003**) 853-860.